Investigation of Structural, Magnetic and Electrochemical Parameters of Spinel Ferrites and its Composites for Energy Storage Application

Thesis Submitted For the Award of the Degree of

DOCTOR OF PHILOSOPHY

In

(**Physics**)

By

Hamnesh Mahajan

(11919191)

Supervised by:

Dr. A. K. Srivastava

LOVELY PROFESSIONAL UNIVERSITY

PUNJAB

2022

DECLARATION

I declare that the thesis entitled "**Investigation of Structural, Magnetic, and Electrochemical Parameters of Spinel Ferrites and its Composites for Energy Storage Application"** has been prepared by me under the guidance of Dr. A. K. Srivastava, Professor, Department of Physics, School of Computer Science and Engineering, Lovely Professional University. No part of this thesis has formed the basis for the award of any degree or fellowship previously.

Hamnesh Mahajan

(Reg. No.: 11919191)

Department of Physics

School of Physical Sciences

Lovely Professional University

Jalandhar-Delhi, G.T. Road (NH-1), Phagwara

Punjab (INDIA)-144411

Date:

CERTIFICATE

I certify that **Mr. Hamnesh Mahajan** has prepared his thesis entitled "**Investigation of Structural, Magnetic, and Electrochemical Parameters of Spinel Ferrites and its Composites for Energy Storage Application",** for the award of Ph.D. degree in Physics of the **Lovely Professional University,** under my guidance. He has carried out the work at the **Department of Physics, School of Physical Sciences, Lovely Professional University**.

A. K. Srivastava

(Supervisor)

Department of Physics

School of Computer Science and Engineering

Lovely Professional University

Jalandhar-Delhi, G.T. Road (NH-1), Phagwara

Punjab (INDIA) -144411

Date:

<u>ACKNOWLEDGEMENT</u>

I thank God for bestowing me with the blessing of being a learner, for keeping me a knowledge seeker. May this little knowledge lead me and those who are directly or indirectly associated with me on the righteous path, here and hereafter.

I cordially express my profound regards and gratitude to my research supervisor Dr. A.K. Srivastava, who always paid attention and gave masterly advice to overcome my delusions and hurdles. His expert comments and suggestions made this work meaningful.

I am very much obliged to all my mentors and would like to express my gratitude, especially to my friend Anjori Sharma, Ibrahim Mohammed, Manisha Thakur, and Simrandeep Kour who have helped me in and out in all possible ways and I would take this opportunity to thank them wholeheartedly.

I express my sincere thanks to all faculty members of the Physics Department for their help and support during this period. My special thanks are due to the other research scholars, all the members of the technical and non-technical/non-teaching staff especially Nitin Kumar Yadav and Ramesh Kumar of the Physics Department, and Manoj Kumar of the Chemistry Department for their affection and kind co-operation. I consider it an appropriate occasion to record my deep sense of affection for my well-wisher's sisters and brothers who prayed for my success.

Finally and most importantly, I would like to thank my parents who are always there for me and without them this piece of work was impossible. I shall always be indebted to them for their unstinted support, be it financially, morally, or inspirationally. May the Almighty God give them a happy life and bless them with good health.

Date: **Hamnesh Mahajan**
                                                                                                          (Reg. No.: 11919191)

ABSTRACT

The development of alternative energy storage systems is undoubtedly one of the greatest challenges faced by our modern society as a result of emerging energy requirements and environmental concerns over fossil fuels. Recently, supercapacitors have gained much attention owing to their high power density than batteries, energy density than conventional capacitors, flexibility, long life, and low cost. In order to make the efficient usage of these stationary energy storage devices, state-of-the-art research on new and advanced electrode materials is highly needed. Recognition of nano-materials for supercapacitors has given the new extended platform to the researchers in order to develop appropriate electrode materials that can deliver excellent specific capacitance. The main focus of this doctoral thesis is to develop high-performing supercapacitor electrodes through simple and cost-effective methods suitable for industrial and commercial use. The materials reported herein are spinel ferrite, conducting polyaniline, and spinel ferrite-polyaniline nanocomposite to produce a synergistic impact for the energy storage supercapacitor application.

In the present research work, the two different series of the doped spinel ferrites have been prepared by employing the facile and minimal cost sol-gel auto-combustion approach. The two prepared spinel ferrite series are mentioned below:

- A pristine zinc doped magnesium spinel ferrite, $Mg_{1-x}Zn_xFe_2O_4$ (x = 0.0, 0.2, and 0.4), sintered at 800 ^{o}C for 6 h.

- A pristine manganese doped cobalt-zinc spinel ferrite, $Mn_xCo_{0.5-x}Zn_{0.5}Fe_2O_4$ (x = 0.0, 0.1, 0.2, 0.3, and 0.4), sintered at 1200 ^{o}C for 6 h.

These above prepared doped series were initially analyzed to examine the basic characteristics viz. structurally, morphological, elemental, and magnetic which are essential for its utilization as a supercapacitor electrode material. The various techniques like X-ray Diffraction (XRD), Fourier Transform Infrared Spectroscopy (FTIR), Field Emission Scanning Electron Microscopy (FESEM), Energy Dispersive X-ray Analysis (EDX), and Vibrating Sample Magnetometer (VSM) were employed to investigate the above-said characteristics.

Owing to the large surface area, appropriate pore size, pore size dissemination, and the presence of the functional group in the prepared $Mn_xCo_{0.5-x}Zn_{0.5}Fe_2O_4$ (x = 0.0, 0.1, 0.2, 0.3, and 0.4) in contrast to the $Mg_{1-x}Zn_xFe_2O_4$ (x = 0.0, 0.2, and 0.4), the $Mn_xCo_{0.5-x}Zn_{0.5}Fe_2O_4$ have been preferred as a promising active material for supercapacitor.

One of the vital steps for the preparation of the spinel ferrite by the sol-gel technique is the sintering. The sintering temperature plays a significant part in influencing the various structural properties viz. phase, crystallinity, crystallite size, density, porosity, etc. In order to track down the reasonable sintering temperature, out of the five prepared manganese doped samples, the sample at x = 0.3 concentration i.e. $Mn_{0.3}Co_{0.2}Zn_{0.5}Fe_2O_4$ is favored, and sintered at three different temperatures viz. 750, 950, and 1150 ^{o}C for examining the single phase. The lower temperature (750 and 950 ^{o}C) yields spinel and hematite peaks whereas the higher temperature (1150 ^{o}C) yields a single spinel phase. Moreover at 1150 ^{o}C excellent morphological, elemental, and magnetic characteristics have been exhibited by the $Mn_{0.3}Co_{0.2}Zn_{0.5}Fe_2O_4$ spinel ferrite.

Based on the above investigation, further spinel ferrite nanocomposite with conducting polymer polyaniline has been prepared. The facile chemical oxidative polymerization was employed for the preparation of polyaniline, which is then physically blended with prepared $Mn_{0.3}Co_{0.2}Zn_{0.5}Fe_2O_4$ spinel ferrite to form the $Mn_{0.3}Co_{0.2}Zn_{0.5}Fe_2O_4$-polyaniline nanocomposite. The prepared nanocomposite was examined for the structural, morphological, elemental, and electrochemical characteristics by employing the X-ray Diffraction (XRD), Fourier Transform Infrared Spectroscopy (FTIR), Field Emission Scanning Electron Microscopy (FESEM), Energy Dispersive X-ray Analysis (EDX), Cyclic voltammetry (CV), Galvanostatic charge-discharge (GCD), and Electrochemical impedance spectroscopy (EIS).

The electrochemical activity of the novel $Mn_{0.3}Co_{0.2}Zn_{0.5}Fe_2O_4$-polyaniline nanocomposites is manifested to be higher as compared to their counterparts on account of synergistic impact, continual movement of electrons towards the electrode, and multiple redox reactions.

PAPER PUBLISHED AND COMMUNICATED

1. **Hamnesh Mahajan**, Sachin Kumar Godara, A. K. Srivastava, Synthesis and Investigation of Structural, Morphological, and Magnetic Properties of the Manganese Doped Cobalt-Zinc Spinel Ferrite, J. Alloys Compd. 896 (2021) 162966. https://doi.org/10.1016/j.jallcom.2021.162966.

2. **Hamnesh Mahajan**, Shammi Kumar, Anjori Sharma, Ibrahim Mohammed, Manisha Thakur, Amarjeet Kaur, A. K. Srivastava, Effect of Sintering Temperature on Structural, Morphological, and Magnetic Properties of $Mn_{0.3}Co_{0.2}Zn_{0.5}Fe_2O_4$ Ferrite, J. Sol-Gel Sci. Technol. 105 (2023) 388-404. https://doi.org/10.1007/s10971-022-06022-5.

3. **Hamnesh Mahajan**, Shammi Kumar, Anjori Sharma, Ibrahim Mohammed, Manisha Thakur, Simrandeep Kour, Amarjeet Kaur, Ajeet Kumar Srivastava, Structural, Morphological, and Electrochemical Investigation of $Mn_{0.3}Co_{0.2}Zn_{0.5}Fe_2O_4$-Polyaniline Nanocomposite for Supercapacitor Application, J. Mater. Sci.: Mater. Electron. (2022) 1-14. https://doi.org/10.1007/s10854-022-09335-x.

4. Anjori Sharma, **Hamnesh Mahajan**, Ibrahim Mohammed, Sachin Kumar Godara, A. K. Srivastava, Enhanced Dielectric and Magnetic Properties of Garnet-Spinel Ferrite Composite for Microwave Device Application, Appl. Phys. A, 2022 (under review).

5. Anjori Sharma, **Hamnesh Mahajan**, Ibrahim Mohammed, Amarjeet Kaur, Neha Aggarwal, Sukhleen Bindra Narang, Ajeet Kumar Srivastava, Investigation of Miniaturization Parameter and Losses of YIG/MgCdCoFe Composite for Antenna Applications in Ku Band, Mater. Res. Bull., 2022 (under review).

6. Ibrahim Mohammed, J. Mohammed, Anjori Sharma, **Hamnesh Mahajan**, Shweta Sharma, Manisha Thakur, Amarjeet Kaur, Neha Aggarwal, Structural, Morphological, Optical, Magnetic, and Microwave Properties of La^{3+}-Mn^{2+} substituted Zn_2-Y- Type Barium-Strontium Hexaferrite, Chin. J. Phys. (2022) 0577-9073. https://doi.org/10.1016/j.cjph.2022.06.025.

7. Simrandeep Kour, Nitish Kumar, **Hamnesh Mahajan**, Rupam Mukherjee, Influence of the Sintering Temperature on Impedance and Modulus Spectroscopic Studies of Nickel-Substituted Cobalt Ferrite, J. Mater. Sci.: Mater. Electron. 34 (2023) 594. https://doi.org/10.1007/s10854-023-10030-8.

CONFERENCE PROCEEDINGS

1. **Hamnesh Mahajan**, A. K. Srivastava, Structural, Morphological, and Magnetic Investigation of the Zinc Substituted Magnesium Spinel Ferrite, AIP Conf. Proc., 2022 (Accepted Manuscript).

2. Ibrahim Mohammed, J. Mohammed, Anjori Sharma, **Hamnesh Mahajan**, Amarjeet Kaur, A. K. Srivastava, Influence of Mn^{2+}-Substitution on the Structural, Morphological and Magnetic Properties of Co2Y Strontium Hexaferrites, Mater. Today: Proc., 2022, ISSN: 2214-7853. https://doi.org/10.1016/j.matpr.2021.12.514.

POSTER PRESENTATIONS

1. **Hamnesh Mahajan** and A. K. Srivastava, Investigation of Structural Magnetic Studies of the Zinc Doped Magnesium Spinel Ferrite, International Conference on "Recent Advances in Fundamental and Applied Sciences" (RAFAS-2021), 25-26 June, 2021, Lovely Professional University, Punjab.

2. **Hamnesh Mahajan**, Amarjeet Kaur, A. K. Srivastava, Effect of Sintering Temperature on Structural, Morphological, and Magnetic Properties of $Mn_{0.3}Co_{0.2}Zn_{0.5}Fe_2O_4$ Ferrite, ACS and ECS Sponsored International Conference on Technologies for Smart Green Connected Societies (ICTSGS-2021), 29-30 November, 2021, Yamagata University, Japan.

ORAL PRESENTATION

1. **Hamnesh Mahajan**, Amarjeet Kaur, and A. K. Srivastava, Effect of Mn Doping on Structural, Morphological, and Magnetic Properties of Co-Zn Spinel Ferrite, International Conference on Materials for Emerging Technologies (ICMET-21), 18-19 February, 2022, Lovely Professional University, Punjab.

PAPER AWARD

1. Best Paper Award of the Conference Theme: Materials Science and Nanomaterials on the Topic Influence of Mn^{2+}-Substitution on the Structural, Morphological and Magnetic

Properties of Co2Y Strontium Hexaferrites in the International Conference on Recent Advances in Mechanical Engineering and Nanomaterials (ICRAMEN-2022), 19-20 February, 2022, Research Association of Masters of Engineering, Maharashtra, India.

COURSE AWARDS

1. Attended and Awarded Elite Class NPTEL Certificate for Successfully Completing the 12 Week Course from July-October (2021) on Experimental Physics-1 by Indian Institute of Technology Kharagpur (Funded by Ministry of Human Resource Development, Govt. of India).

2. Attended and Awarded Elite Class NPTEL Certificate for Successfully Completing the 4 Week Course from January-February (2022) on Introduction to Probability and Statistics by Indian Institute of Technology Madras (Funded by Ministry of Education, Govt. of India).

WORKSHOP

1. Boxberg Sponsored Workshop on "Manuscript Writing" by SPAST Foundation, 23-24 April (2022), Hyderabad, India.

LIST OF SYMBOLS

Symbol	Description
ω	Angular frequency
K_1	Anisotropy constant
i_{pa}	Anodic peak current
E_{pa}	Anodic peak voltage
H	Applied magnetic field
N_A	Avogadro's number
B	Benzenoid ring
T_B	Blocking temperature
μ_B	Bohr magneton
θ	Bragg's angle
D_b	Bulk density
C	Capacitance
i_{pc}	Cathodic peak current
E_{pc}	Cathodic peak voltage
ΔE	Change in energy
R_{ct}	Charge transfer resistance
H_c	Coercivity
A	Cross-sectional area
D	Crystallite size
I	Current
I_m	Current density
I (V)	Current response
I/E	Current to voltage converter
^oC	Degree Celsius
2θ	Diffraction angle
Δt	Discharging time
δ	Dislocation density
l	Distance between electrodes

$\vec{E}$	Electrostatic field
E	Energy density
R_{ES}	Equivalent series resistance
ν	Frequency
β	Full width at half maximum
α-Fe_2O_3	Hematite
j	Imaginary number
Z	Impedance
L	Inductance
d	Interplanar spacing
a_o	Lattice constant
ϵ	Lattice strain
m	Loaded mass
M-H curve	Magnetic hysteresis curve
n_B	Magnetic moment
μ'	Magnetic permeability
M	Magnetization
M_B	Magnetization of octahedral site
M_A	Magnetization of tetrahedral site
m	Mass of pellet
M-O	Metal-oxygen bond
(hkl)	Miller indices
MW	Molecular weight
Z	Number of molecules in the unit cell
ν_2	Octahedral band
B-site	Octahedral site
R_s	Ohmic resistance
1-D	One-dimensional
n	Order of the diffraction
m:n	PANI redox state ratio
%	Percentage

π	pi (3.14)
h	Planck constant
P	Porosity
ΔV	Potential window
P	Power density
Q	Quinonoid ring
r	Radius of pellet
M_r	Remnant magnetization
M_s	Saturation magnetization
υ	Scan rate
K	Shape factor of crystallite
C_s	Specific capacitance
S	Specific surface area
R	Squareness ratio
$ν_1$	Tetrahedral band
A-site	Tetrahedral site
t	Thickness of pellet
3-D	Three-dimensional
2-D	Two-dimensional
V	Voltage
V_{cell}	Volume of the unit cell
W	Warburg impedance
D_x	X-ray density
λ	X-ray wavelength

LIST OF ACRONYMS AND ABBREVIATIONS

Acronym and Abbreviations	Description
AC	Alternating current
ASTM	American Standards for Testing of Materials
APS	Ammonia persulphate solution
AR	Analytical reagent
At.	Atomic
AFM	Atomic force microscope
ATR	Attenuated total reflection
BET	Brunauer-Emmett-Teller
via	by way of
CSA	Camphor sulphonic acid
CNT	Carbon nanotube
COP	Chemical oxidative polymerization
CP	Chronopotentiometry
CE	Common era
CPE	Constant phase element
I-V	Current-Voltage Characteristics
CV	Cyclic voltammetry
DRS	Diffuse reflectance spectra
EDLC	Electric double-layer capacitor
EIS	Electrochemical impedance spectroscopy
ESCs	Electrochemical supercapacitors
EM	Electromagnetic
EB	Emeraldine base
ES	Emeraldine salt
EDX	Energy-dispersive X-ray analysis
Eq.	Equation
ESR	Equivalent series resistance

etc.	Et cetera
fcc	Face centered cubic
FM-PM	Ferromagnetic-paramagnetic transitions
FESEM	Field emission scanning electron microscopy
FETEM	Field emission transmission electron microscope
Fig.	Figure
eg.	for example
FTIR	Fourier transform infrared spectroscopy
GCD	Galvanostatic charge-discharge
GO	Graphene oxide
HRTEM	High-resolution transmission electron microscopy
HC	Hybrid capacitor
HMF	Hyperfine magnetic field
IR	Infrared
ICDD	International Centre for Diffraction Data
IEA	International Energy Agency
JCPDS	Joint Committee Powder Diffraction Standards
LB	Leucoemeraldine
LEDs	Light-emitting diodes
Ltd.	Limited
LSV	Linear sweep voltammetry
MRI	Magnetic resonance imaging
MOF	Metal-organic framework
min.	minute
Mol.	Molecular
MWCNT	Multiwall carbon nanotube
viz.	namely
NF	Nano ferrite
NSFs	Nano spinel ferrite
NC	Nanocomposite
NCs	Nanocomposites

NP	Nanoparticle
NPs	Nanoparticles
NFMR	Natural ferromagnetic resonance
NMP	n-methyl-2-pyrrolidone
PB	Pernigraniline
PL	Photoluminescence
P-E loop	Polarization-electric field hysteresis loop
PEDOT	Poly(3,4-ethylenedioxythiophene)
PANI	Polyaniline
PET	Polyester fabric
Ppy	Polypyrrole
Pth	Polythiophene
PVDF	Polyvinylidene fluoride
pH	Potential of hydrogen
Pvt.	Private
PC	Pseudocapacitor
RE	Rare earth
rGO	Reduced graphene oxide
SEM	Scanning electron microscopy
SAED	Selected area electron diffraction
SS	Stainless steel
SC	Supercapacitor
SCs	Supercapacitors
SQUID	Superconducting quantum interference device
SFD	Switching field distribution
i.e.	that is
TGA	Thermogravimetric analysis
TG-DSC	Thermogravimetry-Differential scanning calorimetry
TG-DTA	Thermogravimetry-Differential thermal analysis
TEM	Transmission electron microscopy
UV-VIS	Ultraviolet-visible

VSM	Vibrating sample magnetometer
Wt.	Weight
EXAFS	X-ray absorption fine structure
XRD	X-ray diffraction
XANES	X-ray near edge structure
XPS	X-ray photoelectron spectroscopy

LIST OF UNITS

Unit	Description
A	Ampere
Å	Angstrom
cm	centimeter
cc	Cubic-centimeter
emu	electromagnetic unit
eV	electron-Volt
erg	ergon
F	Farad
GHz	Giga-Hertz
g	gram
h	hour
K	Kelvin
kg	kilo-gram
KHz	Kilo-Hertz
KOe	Kilo-Oersted
kW	kilo-Watt
MHz	Mega-Hertz
m	meter
μHz	micro-Hertz
μm	micro-meter
mA	milli-Ampere
mF	milli-Farad
mL	milli-liter
mm	milli-meter
mV	milli-Volt
mW	milli-Watt
mWh	milli-Watt-hour
M	Mole

nm	nano-meter
Oe	Oersted
Ω	ohm
s	second
S	Siemens
TWh	Tera-Watt-hour
W	Watt
Wh	Watt-hour

LIST OF FIGURES

LIST OF TABLES

Table of Contents

CHAPTER-1

Introduction

1.1. Preamble

Energy plays a very crucial role in our day-to-day life. From 7,323 TWh in 1980 to 23,845 TWh in 2019, global electricity consumption has expanded dramatically in recent decades. According to the World Energy and Climate Statistics - Year Book 2021, worldwide energy usage fell by 1.1 % in 2020, the first drop since 2009. The global economy is largely reliant on energy generation, storage, and transportation. Energy production is heavily reliant on non-renewable fossil fuels such as coal, oil, and gas, according to the International Energy Agency [1]. Furthermore, it is widely accepted that the increase in greenhouse gas concentrations in the atmosphere during the 1950s is largely due to the combustion of fossil fuels, which is driving global climate change [2]. Population growth, the depletion of fossil fuel reserves, and the harmful effects of greenhouse gases on the ecosystem and climate all pose a severe danger in the future decades. As a result, switching from fossil fuels to renewable energy sources and ecologically friendly technology is critical for long-term growth [3]. Renewable energy sources such as solar and wind, among others, cannot be employed for commercial or residential use since supply interruptions might result in huge losses [4]. As a result, the comprehensive approach toward clean energy emerges in modern civilization, as does the necessity to investigate new storage and conversion technologies as the global economy grows [5]. Energy-storage systems are becoming increasingly important in this respect, and have been hailed as the most promising among numerous renewable energy storage technologies due to their high efficiency, adaptability, and flexibility. The currently used energy storage and conversion devices as mentioned in Fig. 1.1 are fuel cells, batteries, capacitors, and supercapacitors (SCs) [6,7]. Unlike fuel cell and batteries which converts chemical energy into electrical energy, conventional capacitor deals with the physical separation of electric charge across the dielectric medium such as ceramic, polymer film, or oxide layer [8]. In a conventional capacitor, the maximum energy storage is not possible due to the small surface area. Therefore the researchers are too much concentrating on finding those devices which have high energy storage capacity and which can deliver maximum power [9]. In light of this, the SCs are one of the best contenders for all of the above energy storage devices.
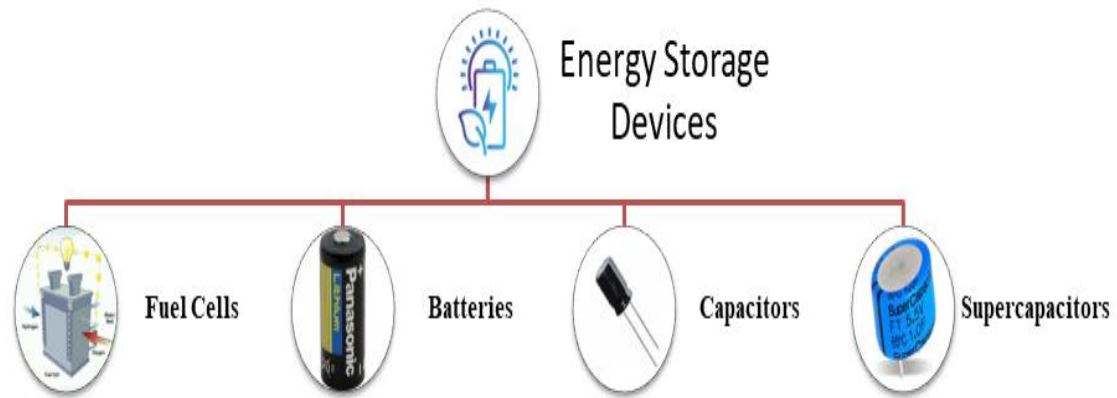
Fig. 1.1. Energy storage and conversion devices.

Because of their increased energy density (E), fuel cells and batteries are mostly exploited in high-energy applications. Low power density (P), limited cycle life, high cost, complicated device manufacturing process, and a lack of safety are some of their drawbacks. Conventional capacitors have a high power density and a long cycle life, but they have a lower energy density than batteries and fuel cells. Thus, electrochemical supercapacitors (ESCs) are regarded as one of the most intriguing energy storage technologies capable of bridging the gap between batteries and ordinary capacitors, as seen in the Ragone plot in Fig. 1.2 [10].
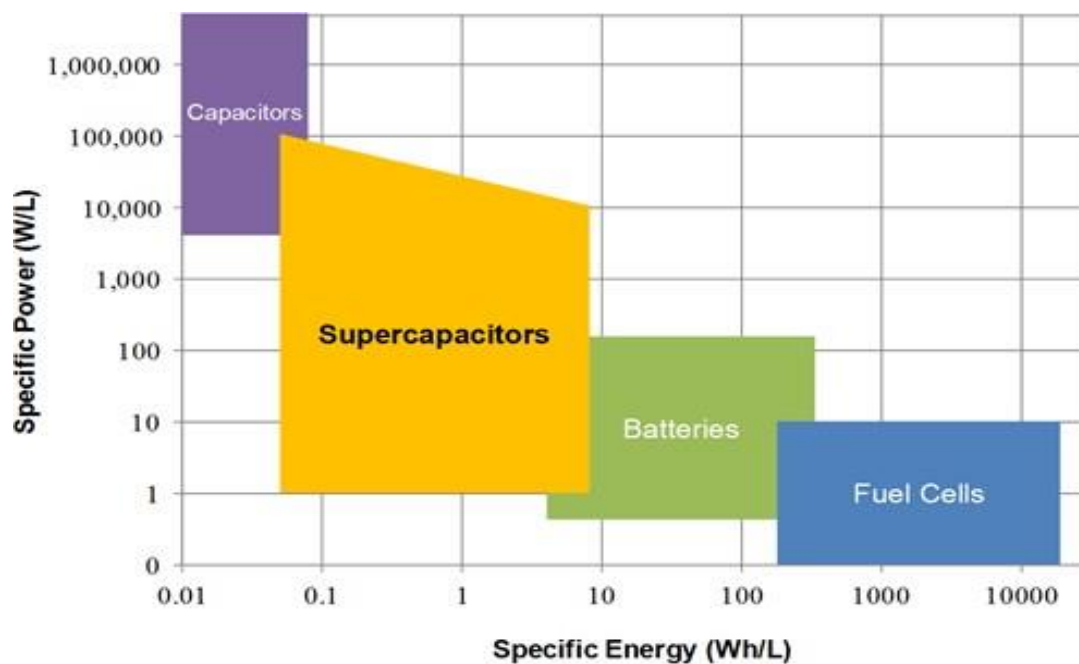
Fig. 1.2. Ragone plot of specific power versus specific energy for supercapacitors [11].

The electrochemical supercapacitors (ESCs) have superior energy and power density, excellent cyclic life, rapid charge-discharge rate, superb reversibility, longer shelf life, fast dynamic response, minimum equivalent series resistance (ESR), economic, featherweight, pliable, highly efficient, operational safety, and eco-friendly character [12-14]. Owing to the above-mentioned characteristics of the ESCs it seems to have its application in mobile phones, laptops, notebook computers, smartwatches, memory backup, digital cameras, electric as well as hybrid electric vehicles, energy power systems, urban rail transit, toys, headphones, calculators, etc. [15]. Because ESCs have magnificent power density, they may quickly release stored energy, making them ideal for short-term applications that require high electricity bursts [16].

1.2. Supercapacitor

In comparison with conventional capacitors, supercapacitors (SCs) are specifically constructed capacitors with large capacitance and energy density values. Relatively small, the SCs can provide capacitance in the tens, hundreds, or even thousands of farad range. They not only can hold a lot of charges, but they can also withstand thousands of charge-discharge cycles without breaking down. That's why SCs, are usually called ultracapacitors [17]. Due to its high capacitance value, it can store much more electric energy between its plates. The SCs are more like an electrochemical device similar to the electrolytic capacitor but in this, no chemical reactions are involved for the storage of electric energy. As an electrostatic field ($\vec{E}$), the SCs store a huge amount of charge. The construction of the SCs is somewhat like electrolytic capacitors and it consists of the porous electrodes (cathode as well as the anode), electrolyte, and separator as depicted in Fig. 1.3. These porous electrodes have the ability to attract a large quantity of charge. The electrolytes employed in SCs can be solid, liquid, or gel, and they play an important part in the SCs redox processes [18]. The electrodes in the SCs are separated by a separator (paper membrane) that is permeable to charge carriers but prevents direct shorting between them. SCs store charge in a completely different way than conventional capacitors. The polarization of the dielectric material is responsible for charge storage in conventional capacitors. The electrolyte of SCs, on the other hand, does not act as a dielectric. It is solely responsible for supplying charge carriers to the electrodes. However, the charge is stored on electrodes through the buildup of opposing charge carriers. The electrolyte affects the internal or equivalent series resistance (ESR) of the SCs. According to

Eq. (1.1), the higher the power density (P) of the SCs, the lower the resistance (R) given by the electrolyte [19].

$$P = \frac{V^2}{4R_{ES}}$$
(1.1)

Here P, V, and R signify the power density, applied voltage, and equivalent series resistance respectively [20].
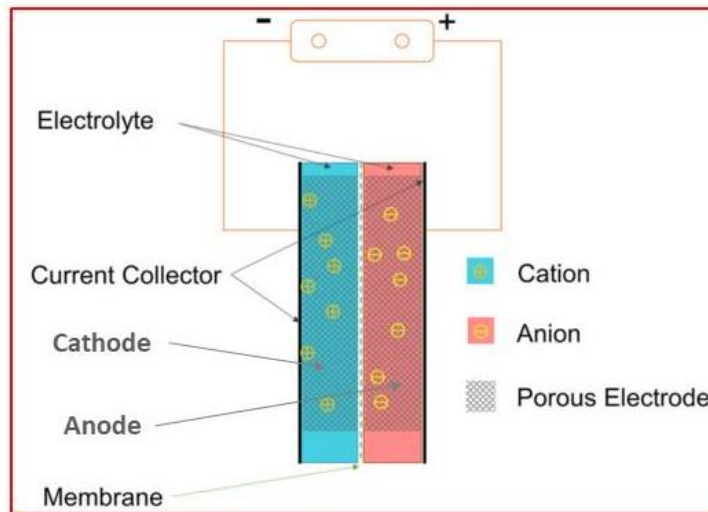
Fig. 1.3. Construction of the supercapacitor [21].

1.2.1. Principle and Working of the Supercapacitor

In a supercapacitor (SC), the energy storage principle can either be pure charge storage on the interface of electrode-electrolyte electrochemically or it can be a transfer of the charge to the redox molecule layers on the surface of the electrode [22].

The supercapacitor (SC) works similar to the conventional capacitor, both electrostatic and electrolytic, with only minor differences in technical features. It comprises two exceptionally permeable or porous electrodes, a paper membrane that isolates positive and negative plates called a separator; these terminals are electrically associated with an ionic liquid called the electrolyte. Whenever the voltage is supplied to the negative electrode, positive ions from the electrolyte are attracted to it, and vice versa. These ions accumulate on the electrode surface, thereby reducing the distance (l) between the electrodes [23]. As a result, the capacitance (C) of the SC is extremely high. Because the C of the SC is inversely related to the l between the electrodes ($C = \frac{A}{l}$), where A and l are the cross-sectional areas and separation distance between the two electrodes respectively.

4

An electrostatic field ($\vec{E}$) is created between the current collectors due to the buildup of opposing charges. The SC is charged until the $\vec{E}$ between the current collectors equals and opposes the applied voltage. Till the supply voltage lowers or reverses polarity, the charge carriers are held by the current collectors. When the supplied voltage is reduced, the current collectors return a corresponding number of charge carriers to the electrolyte. During such an operation, an equivalent current travels in the opposite direction through the SC. The SC goes through a similar charging and discharging cycle when the polarity changes, as seen in Fig. 1.4 [24]. The SC has a ten-times higher specific capacitance (C_s) and energy density (E) than an electrolytic capacitor and a hundred-times higher C_s and E than an electrostatic capacitor [25].
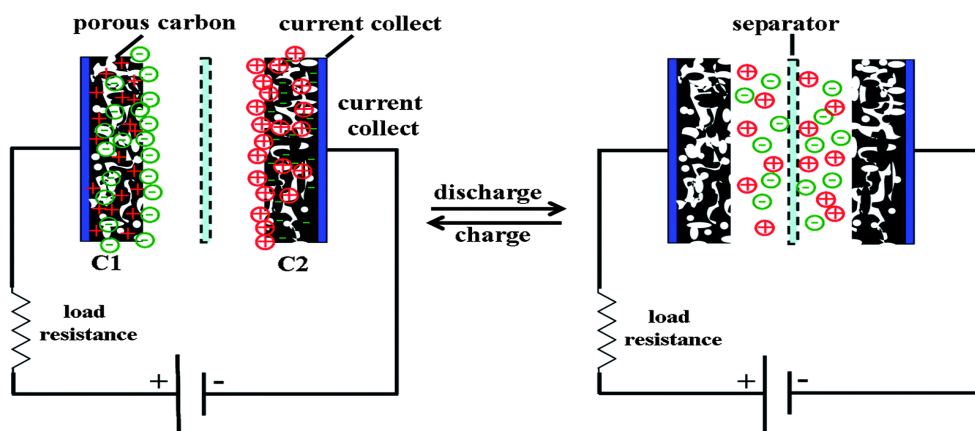
Fig. 1.4. Working of the supercapacitor [26].

1.2.2. Types of the Supercapacitors

The supercapacitors (SCs) may be categorized into three major types viz. electrical double layer capacitor, pseudocapacitor, and hybrid capacitor [27] as shown in Fig. 1.5, based on what kind of charge storage strategy and active material are utilized.
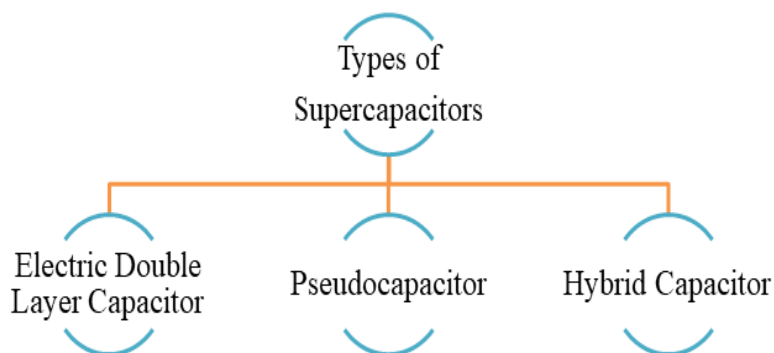
Fig. 1.5. Types of the supercapacitors.

5

(a) Electric Double-Layer Capacitor

The electric double-layer capacitor (EDLC) uses carbon-based material (viz. carbon nanotubes, carbon aerogel, activated carbon, carbon fiber cloth, graphene, etc.) as an active material for the electrode, an electrolyte, and a separator. The charge storage in EDLC is due to electrostatically or by a non-faradic mechanism where no charge is transferred in between the electrolyte and electrode [28,29]. Whenever a voltage is supplied to an electrode, a charge builds on the electrode's surface, and ions in the electrolyte solution begin diffusing over the separator into the pores of the electrode with the opposite charge. The design of the electrode is in such a way, that it prevents ion recombination, resulting in a double layer of charge at each electrode. The development of a double layer, together with an increase in surface area and a reduction in the distance (d) between the two electrodes, culminates in an EDLC with a higher energy density (E) than a conventional capacitor [30].

(b) Pseudocapacitor

The construction of the pseudocapacitor (PC) is similar to EDLC but uses conducting polymer [polyaniline (PANI), polythiophene (PTh), poly(3,4-ethylenedioxythiophene) (PEDOT), and polypyrrole (PPy)] and metal oxides (Fe_2O_3, Co_3O_4, ZnO_2, MnO_2, RuO_2, NiO, V_2O_5, SnO_2, $CoFe_2O_4$, etc.) as an active material for the electrode. Charge storage in PC is mostly accomplished by a faradic mechanism, where a charge is transferred between the electrolyte and electrode. Under potential deposition, intercalation, and reduction-oxidation processes are used to store charge in the PC, allowing it to reach higher specific capacitance (C_s) and energy densities (E) than an EDLC. The reduction-oxidation reaction occurs in the PC, just as it does in batteries, resulting in poor cycling stability and low power density (P) [31,32].

(c) Hybrid capacitor

A hybrid capacitor (HC) combines an EDLC with a PC. When EDLC and PC storage are combined, the drawbacks of the combining components are overshadowed, resulting in larger specific capacitance (C_s). HC is mainly composed of two electrodes, which possess different materials and have superior electrochemical performance than the SCs employing the same electrode material [33,34].

1.3. Materials for the Supercapacitor Electrode

The electrode materials have a major impact on the supercapacitors (SCs) electrochemical performance. Owing to the types of the SCs as discussed earlier, three

distinct types of electrode materials are being used for energy storage applications in the SCs: carbon-based, metal oxides, and conducting polymer. Electrical conductivity, specific surface area, surface functionality, pore size distribution, and pore shape and structure are all important material properties that impact the electrochemical performance of the SCs [35].

1.3.1. Carbon-Based Materials

The active carbon-based material viz. carbon nanotubes, carbon aerogel, activated carbon, carbon fiber cloth, graphene, etc. were extensively utilized as electrode materials in supercapacitor (SC) fabrication. The reasons for this include (a) minimal cost, (b) large surface-to-volume ratio, (c) well-established electrode fabrication technology, and (d) easy availability. Carbon materials utilize an electrochemical double layer produced at the electrode-electrolyte interface as a storage mechanism. As a result, with carbon-based materials, capacitance is mostly determined by the surface area available to electrolyte ions [36]. In the case of carbon materials, having a large specific surface area leads to a high capacity for charge buildup at the electrode-electrolyte interface. Surface functionalization must be addressed when enhancing specific capacitance (C_s) for carbon materials, in addition to pore size and high specific surface area [37]. The carbon-based SC electrodes, with high conductivity and stability, typically offer great cyclic stability and high power density (P). Furthermore, due to the limitations of the energy storage strategy, the energy density (E) of carbon-based electrodes for SCs is typically low.

1.3.2. Metal Oxides

Various metal oxides viz. Fe_2O_3, Co_3O_4, ZnO_2, MnO_2, RuO_2, NiO, V_2O_5, SnO_2, etc. were examined for the energy storage application. Owing to their magnificent activity and superior inherent electrochemical characteristics, these metal oxides have outstanding electrochemical performance in the supercapacitors (SCs). However, they still face issues like scarcity of natural resources, poor conductivity, and exorbitant costs. Out of these above-specified metal oxides, RuO_2 was observed to be the most amazing active material for pseudocapacitor (PC) electrodes which exhibits reverse charge-discharge properties, and excellent specific capacitance (C_s), and extremely high electrical conductivity. Despite that, there emerge a few difficulties with the utilization of RuO_2 as an active material for electrodes because it is highly toxic and too much expensive [38]. Moreover, the single transition metal oxides have lower C_s and lower electrical conductivity which needs to be

improved. These above troubles can be eliminated by the utilization of the mixed metal oxides viz. cobaltite (MCo_2O_4), aluminate (MAl_2O_4), spinel ferrite (MFe_2O_4), etc. These mixed metal oxides have been contemplated as possible contestants for superior SCs in light of the fact that they exhibit magnificent electrochemical performance due to the synergetic impact of different metal cations [39]. One of the most outstanding known, mixed metal oxides is the spinel ferrite (MFe_2O_4) because it imparts surprising properties viz. electrochemical stability, different oxidation states, electronic, magnetic, optical, and catalytic [40]. Furthermore, these spinel ferrites are easily available, have minimal cost, massive productivity, are ecologically innocuous, and are convenient to synthesize on an industrial scale.

1.3.3. Conducting Polymers

Due to their ease of synthesis and minimal cost, a variety of conductive polymers have been studied as supercapacitor (SC) electrode materials [41]. When compared to carbon-based electrode materials, conducting polymers have a higher conductivity and specific capacitance (C_s), as well as lower equivalent series resistance (ESR). For conducting polymers various arrangements or configurations of the electrodes were utilized. The n-p type arrangement, which has one n-doped and one p-doped electrode, offers high energy densities (E), yet the shortage of n-doped electrodes of the conducting polymer has prevented pseudocapacitor (PC) from achieving their full potential [42]. The reversible redox reaction was utilized to store and release charge in the conducting polymers. Ions are transported to the polymer backbone when oxidation takes place, which is also called doping. However, ions are released back into the solution when reduction takes place, which is also called de-doping [43]. In conducting polymer the mechanical stress caused by redox reactions restricts the stability of the material during numerous charge-discharge cycles [44]. Owing to the minimal cost, high conductivity, excellent energy storage capacity, and ease of synthesis, polyaniline (PANI) is perhaps the most encouraging SC electrode material out of the various existing conducting polymers [viz. polyaniline (PANI), polythiophene (PTh), poly(3,4-ethylenedioxythiophene) (PEDOT), and polypyrrole (PPy)] [45]. Swelling and shrinking of PANI are prone to a substantial loss in performance owing to recurrent charge-discharge cycles. PANI has been proven to be more stable when combined with metal oxides or carbon-based materials which also enhance the value of C_s [46].

However, these above specified active materials have their own shortcomings such as

lower E of carbon-based material, low electronic conductivity of metal oxides, and low cyclic stability of the conducting polymers. These above-specified properties can be enhanced by preparing the various binary nanocomposites (NCs) viz. metal oxide-carbon, conducting polymer-carbon, and metal oxide-conducting polymer. Out of these binary NCs, the metal oxide (spinel ferrite)-conducting polymer (PANI) NC was favored as an active material for PC electrodes in light of their faradic reactions [47].

1.4. Ferrite

Thales, a Greek philosopher who made advances in the area of magnetism in the sixth century, saw a magnet as an attractive substance. Magnesia in Asia Minor was called after the ferrous oxide (Fe_3O_4) rock known as magnetite, which occurs naturally and has mutual attracting characteristics. William Gilbert presented the first magnetic substance for compass as an iron needle in CE 1600. Ferrites were first utilized in 1930, and various experts, notably Snoek [48], have focused on their magnetic, electrical, and structural characteristics. The ferrites are insulators with moderate permittivity and high electric resistivity, high magnetic permeability, low eddy currents, and low dielectric loss [49]. Ferrites are the only material that exhibits such a broad range of characteristics, making them suitable for usage in a variety of fields and applications [50].

1.4.1. Classification of Ferrites

The crystal structure of the ferrites can be utilized to categorize them, as per the majority of the investigation done on ferrites by the researcher's group. Subsequently in fact talking, the ferrites are categorized into four main types: spinel, hexagonal, garnet, and ortho as illustrated in Fig. 1.6.

Fig. 1.6. Classification of ferrites.

Each one of these ferrites comprises Fe_2O_3 as the basic formula. These four ferrites are unique, concerning one another by the structure as well as by properties and applications and have been explained one by one in detail below [51].

(a) Spinel Ferrite

Spinel ferrites are in fact a prototype of naturally occurring ferrites, i.e., $FeO \cdot Fe_2O_3$. The spinel structure is derived from the mineral spinel ($MgAl_2O_4$ or $MgO \cdot Al_2O_3$), which crystallizes in the cubic system. This crystal structure was first determined by Bragg and by Nishikawa. Analogous to the mineral spinel, the magnetic spinel has the general formula $MO \cdot Fe_2O_3$ or MFe_2O_4 where M is the divalent metal ion. The smallest cell of the spinel lattice that has cubic symmetry contains eight "molecules" of MFe_2O_4. The relatively large sized oxygen ions (radius about 1.4 Å form fcc lattice, and the much smaller metal ions [radii from about 0.7 to 0.8 Å]) occupy the spaces between them. In this cubic close-packed structure, two kinds of interstitial sites occur: the tetrahedral and the octahedral sites, which are surrounded by four and six oxygen ions, respectively.

(b) Hexagonal Ferrite

This class of magnetic oxides suggests the magnetoplumbite structure, which comes from the mineral of the same name. The hexagonal ferrites are get defined by $MFe_{12}O_{19}$, where, M is usually Ba, Sr, or Pb. The symmetry of the magnetoplumbite structure is hexagonal. Thus, it has a major preferred axis called the c-axis and a minor axis called the a-axis. The preferred direction is used for a good advantage in permanent magnet material. Most of these compounds are ferrimagnetic, but some are antiferromagnetic. The best known compounds in this class are $BaFe_{12}O_{19}$, $SrFe_{12}O_{19}$, and $PbFe_{12}O_{19}$.

(c) Garnet Ferrite

These are the ferrites that accommodate a large trivalent rare earth ions of large magnetic moments. Garnet ferrites reveal the structure of the silicate mineral garnet. Magnetic garnets crystallize in the dodecahedral or 12-sided structure related to the mineral garnet. The general formula is $M_3Fe_5O_{12}$. It is to be noted that all the metal ions are trivalent in contrast to the other classes. In the important magnetic garnets, M is usually yttrium (Y) or one of the rare earth ions. The crystal structure and the unit cell dimensions of the rare-earth iron garnets were first reported by Bertaut and Forrat and then by Geller and Gilleo.

(d) Ortho Ferrite

Apart from the spinel, hexagonal, and garnet ferrites, the next important structure is the ortho ferrites or perovskites. The formula is $RFeO_3$ where, R is yttrium or a rare earth ion.

These are also cubic ferrites but of slightly distorted perovskite structure. Perovskite structure is the name given to the atomic arrangement of the oxides of formula RMO_3, e.g., $BaTiO_3$, $PbTiO_3$ etc. This structure is often acquired by a material, which has a complicated molecular arrangement consistent with cubic symmetry. The structure is orthorhombic rather than cubic. The canting or nonparallel alignment of the antiferromagnetic coupled ions leads to weak ferromagnetism in the perovskite structured materials. These compounds present the structure which is formed by the superposition of a canted spin antiferromagnetic sub lattice M and sub lattice R. The rare earth iron perovskites are also known as "ortho ferrite". They were first studied by Forestier and Guillot Guillain and then by Pauthenet and Blum. They observed that these rare earth iron perovskites have a parasitic ferromagnetic moment at room temperature.

Out of these above ferrites, spinel ferrite has pulled in the focal point of numerous scientists in light of its immense scope of utilizations in high-performance energy storage supercapacitors (SC).

1.4.2. Spinel Ferrite and its Crystal Structure

Bragg and Nishikawa were the first to notice the spinel structure. When spinel ferrite crystallizes in the space group Fd-3m, it forms a cubic structure [52].
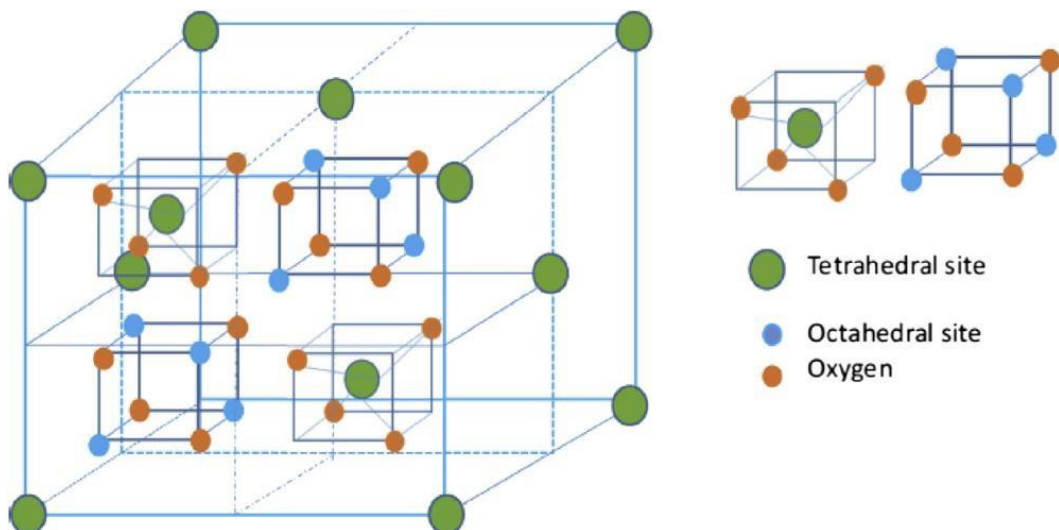
Fig. 1.7. Spinel ferrite unit cell crystal structure [53].

The structure of the spinel consists of 32 oxygen anions packed closely together to develop a complete structural unit cell. These oxygen anions are arranged in a face-centered cubic (fcc) pattern, leaving two types of voids between them: A or tetrahedral site, which is

surrounded by 4 oxygen anions, and B or octahedral site, which is surrounded by 6 oxygen anions. Spinel ferrite consists of 8 small cubes of MFe_2O_4 known as formula units or octants in a single crystallographic unit cell (where M is a divalent metal cation). There are 64 A or tetrahedral sites in each unit cell of spinel ferrite, 8 of which are occupied and 32 B or octahedral sites, 16 of which are occupied. The ionic circumstances within just two neighboring octants are depicted, with the octant on the left showing A or tetrahedral site and the octant on the right showing B or octahedral site. Each octant in the spinel ferrite has 4 oxygen anions on the body diagonals and at the tetrahedron's corners. Fig. 1.7 manifests the crystal structure of spinel ferrite.

1.4.3. Classification of Spinel Ferrites

The generic formula $M_x^{2+}Fe_{1-x}^{3+}[M_{1-x}^{2+}Fe_{1+x}^{3+}]O_4^{2-}$ is used to represent spinel ferrites. The cations which are outside the square bracket are represented by A or tetrahedral sites and the cations which are inside the square brackets are represented by B or octahedral sites. Here x is the inversion factor that decides the classification of spinel ferrites. The spinel ferrites may be categorized into three categories based on the distribution of metal cations, as shown in Fig. 1.8, viz. normal, inverse, and mixed [54].
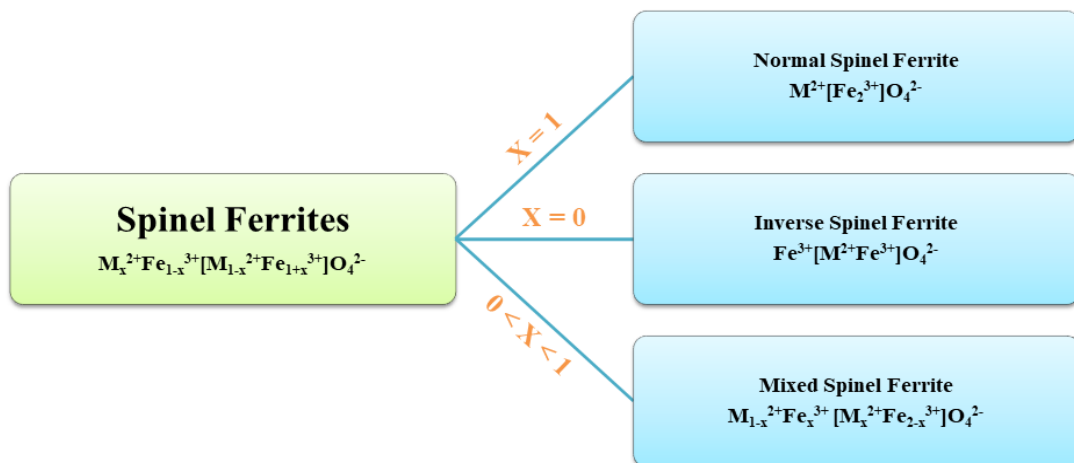
Fig. 1.8. Classification of spinel ferrites.

(a) Normal Spinel Ferrite

The normal spinel ferrite structural formula is denoted by $M^{2+}[Fe_2^{3+}]O_4^{2-}$. All divalent metal cations (M^{2+}) occupy A or tetrahedral sites, whereas trivalent metal cations (Fe^{3+}) occupy B or octahedral sites in the normal spinel ferrite. Zinc ferrite ($ZnFe_2O_4$) belongs to the category of the normal spinel ferrite.

(b) Inverse Spinel Ferrite

The inverse spinel ferrite structural formula is denoted by $Fe^{3+}[M^{2+}Fe^{3+}]O_4^{2-}$. All divalent metal cations (M^{2+}) occupy B or octahedral sites, while trivalent metal cations (Fe^{3+}) equally occupy A or tetrahedral and B or octahedral sites in the inverse spinel ferrite. Nickel ferrite ($NiFe_2O_4$) and cobalt ferrite ($CoFe_2O_4$) belongs to the category of inverse spinel ferrite.

(c) Mixed Spinel Ferrite

The mixed spinel ferrite structural formula is denoted by $M_{1-x}^{2+}Fe_x^{3+}[M_x^{2+}Fe_{2-x}^{3+}]O_4^{2-}$. Both divalent metal cations (M^{2+}) and trivalent metal cations (Fe^{3+}) occupy A or tetrahedral and B or octahedral sites in the mixed spinel ferrite. Manganese ferrite ($MnFe_2O_4$) belongs to the category of mixed spinel ferrite.

1.4.4. Spinel Ferrite Synthesis Method

The properties of the spinel ferrite viz. structural, morphological, optical, electrical, magnetic, electrochemical, etc. relied heavily on the synthesis method. Several methods viz. ceramic, co-precipitation, solid-state, hydrothermal, microwave, spray pyrolysis, and sol-gel can be utilized for the synthesis of the spinel ferrite as depicted in Fig. 1.9.
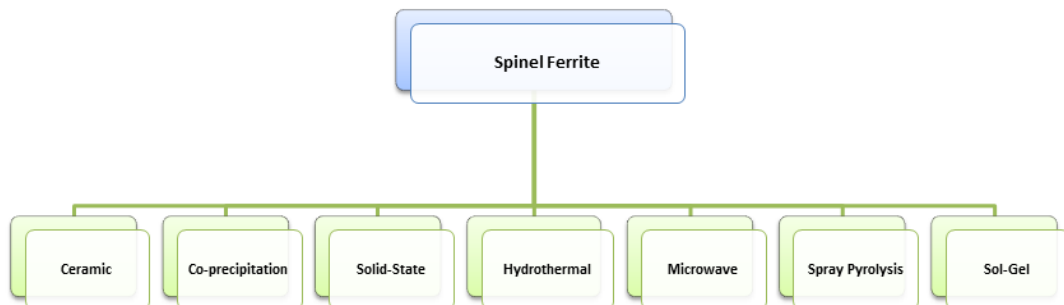
Fig. 1.9. Methods for the synthesis of spinel ferrite.

The sol-gel procedure is favored over the other procedures stated above, owing to its minimal cost, nanosized structure formulation of the product, formulation of thin films, massive production, decrement of the crystallization temperature, homogeneity, formulation of the porous product, the minimum time for the synthesis of product, and formulation of the immaculate product. Furthermore, the use of distilled water as a solvent in the sol-gel makes this procedure ecologically benign [55].

1.4.5. Sol-Gel Auto Combustion Method

The most extensively utilized and facile method for the synthesis of the nanoparticles

is the wet chemical method known as the sol-gel auto combustion method. It is mainly used for metal oxide synthesis. The popularity and wide acceptance of this method are attributed to its great advantages over other methods of synthesis such as the ceramic method, solid-state reaction method, co-precipitation method, and hydrothermal method. Sol-gel is a compelling method due to its properties such as controlled particle size and porosity, performed at low temperature, it is a cheap method because no complicated equipment is required, high homogeneity and it can be used to synthesize thin film. The beginning of this process as depicted in Fig. 1.10 is to convert monomers or starting material into colloidal solution (sol) which acts as a precursor for the further formation of a gel [56].
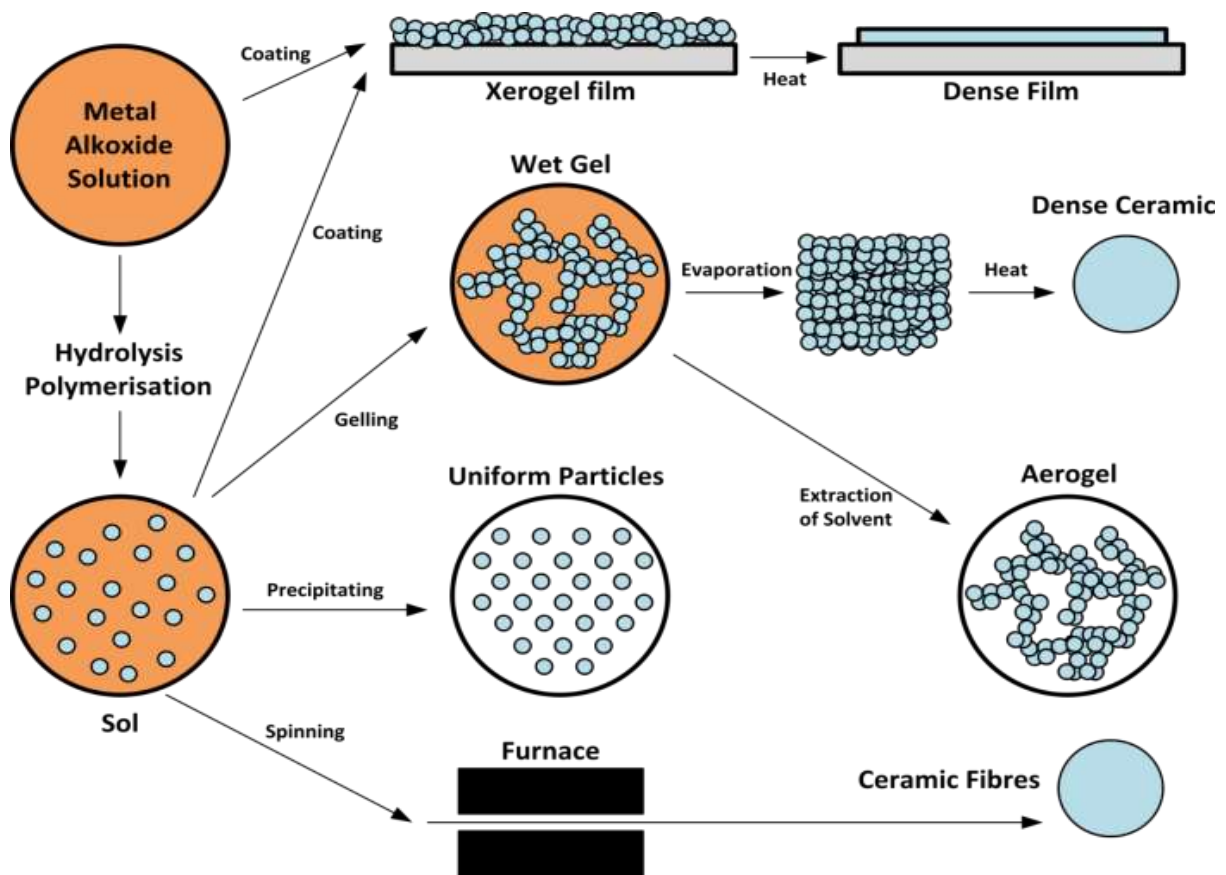
Fig. 1.10. Sol-gel auto combustion process [57].

The raw material such as metal nitrates or alkoxides is usually dissolved in a liquid medium such as ethylene glycol, distilled water, or a suitable acid to form a "sol" which is succeeded by aging and then heating of the sol to get what is named as "gel", further drying or heating the gel at higher temperatures evaporate the liquid medium and transform the gel into a "precursor". A sol is a colloid suspended in a liquid, however, a gel is a suspension that maintains its shape, thus the name "sol-gel". The hydrolysis, condensation, and

polymerization of monomers to produce particles and particle agglomeration, followed mostly by the creation of a network that spreads across the liquid media, resulting in the formulation of a gel using the sol-gel auto combustion method. Hydrolysis is a chemical breakdown of a compound when reacts with water whereas condensation is the conversion of a gas or vapor into liquid.

AR grade chemicals are employed for the production of spinel ferrites. The steps in the sol-gel auto combustion procedure for the production of spinel ferrite are manifested in Fig. 1.11.

Fig. 1.11. Steps in the sol-gel procedure for spinel ferrite production.

15

1.5. Polyaniline

With the introduction of polyacetylene during the year 1958, the phase of naturally conducting polymers began. Despite Alan J. Heeger's, Hideki Shirakawa, and Alan G. McDiarmid study is regarded as the innovative research in the area of conducting polymers, for which they were awarded the Nobel Prize in 2000, the origin of polyaniline (PANI) could be even earlier than that of polyacetylene and several other known conducting polymers. The "blue material" synthesized via electrolysis of aniline sulphate was firstly described by Dr. Henry Letheby, in 1862. While handling the synthesized blue material with a reducing agent it somewhat gets decolorized [58]. Owing to its dark colour it was extensively utilized for colouring the textile materials in the ancient era and designated as the aniline black. Subsequently, much study has been conducted in this sector to determine its potential application in a variety of fields. Among the various existing conducting polymers [viz. polyaniline (PANI), polythiophene (PTh), poly(3,4-ethylenedioxythiophene) (PEDOT), and polypyrrole (PPy)], PANI has sparked a lot of interest among researchers working on conversion and energy storage devices viz fuel cells, batteries, and supercapacitors (SCs). The superb electrical conductivity, excellent electrochemical activity, magnificent redox properties, minimal cost for infinite abundance, eco-friendly nature, huge pseudocapacitance (PC), and adaptability of PANI has enticed the researchers to serve it as an active material for SC electrodes [59]. PANI is also more thermally stable and therefore can be easily produced as a powder as well as a thin film. PANI structures are adaptable over a broad range of crystal structures, sizes, and shapes [60]. Despite the fact that PANI is a homopolymer, its chemical structure can comprise a benzenoid (B) ring, quinonoid (Q) ring, or both in varying quantities. As seen in Fig. 1.12, PANI occurs in three distinct oxidation states. The leucoemeraldine (LB) is a fully reduced state and comprises the B ring, in which atoms of the hydrogen are coupled to atoms of the nitrogen, whereas pernigraniline (PB) is a fully oxidized state and comprises the Q ring, in which no atoms of hydrogen is coupled to atoms of nitrogen. The m:n ratio in PANI chains determines the PANI redox state. The m:n ratio of B to Q ring, as seen in Fig. 1.12, ought to have 1:0 for LB (fully reduced) state, 0:1 for PB (fully oxidized) state, and 1:1 for emeraldine (EB) (partially oxidized) state [61]. The above-stated PANI states may be changed by changing the synthesis technique and doping amount. The PANI LB form is colourless, while the PB form is violet or blue in colour, and both are unstable in the environment. The emeraldine base (EB) which is blue in colour is a very valuable PANI form owing to its high thermal stability at ambient temperature. On

subsequent doping with an acidic solution in EB, the resultant PANI form is the emeraldine salt (ES) which is green in colour and is exceptionally conductive. When the ES is de-doped using a basic solution, the operation is reversible, and the ES becomes EB (redox procedure) [62]. However, when treated with an acidic solution, LB and PB remain an insulator. The conductivity of emeraldine can be increased by 10 orders of magnitude when it is treated with acidic solutions. Upon doping with 4 % HBr the PANI conductivity had incremented from 6.28×10^{-9} to 4.60×10^{-5} S/m [59].
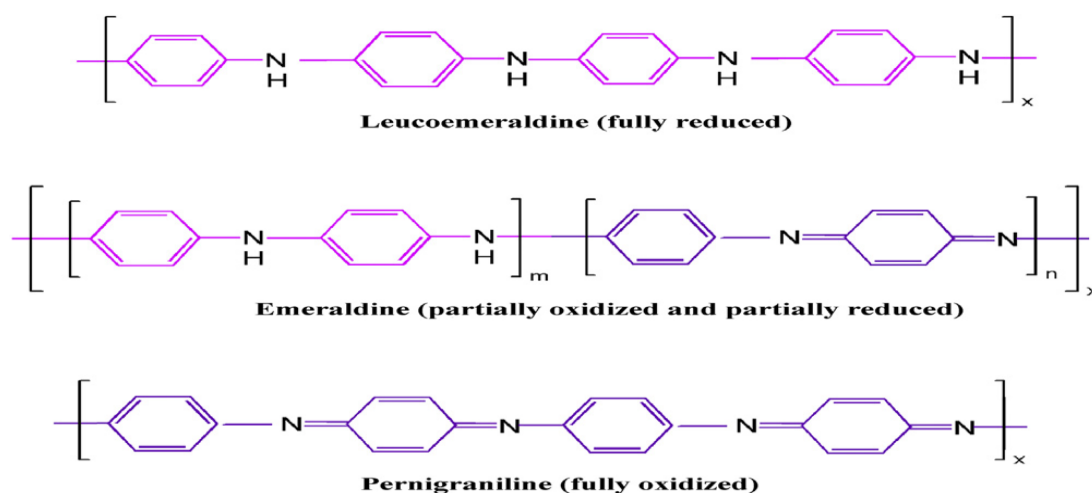
Fig. 1.12. Oxidation states of polyaniline [62].

To obtain the desired electrochemical performance, it is common practice to maintain equilibrium between B and Q rings in the ES. The ratio of peak intensities in the FTIR spectrum in which peaks near 1460 and 1560 cm^{-1} associates to B and Q respectively were utilized to evaluate the m:n ratio [62].
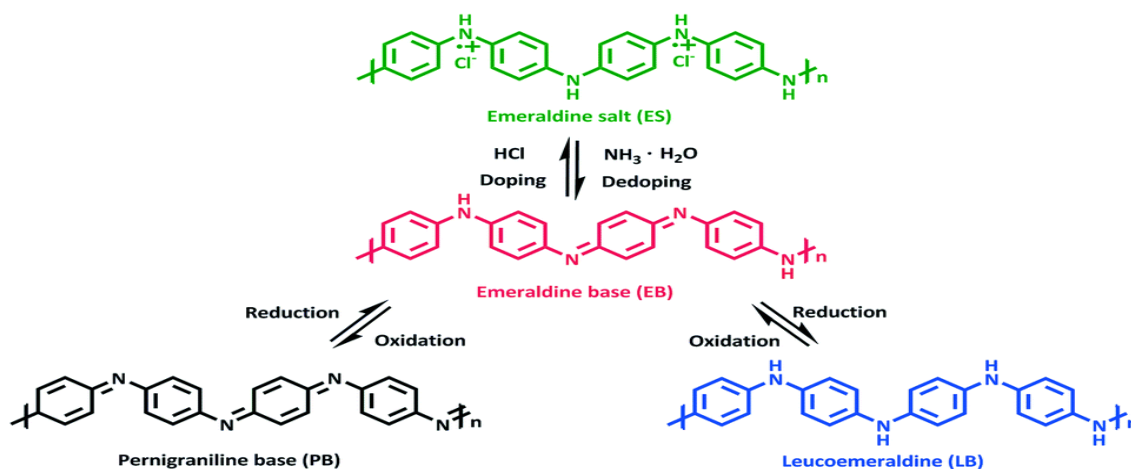
Fig. 1.13. Conversion between different forms of polyaniline [63].

17

To tailor the electrochemical activity of the PANI, the most significant phenomenon is doping. It should be noted that the dopant utilized in the PANI neither creates a chemical connection nor chemically reacts with the PANI chain. Nonetheless, it resides in proximity to the PANI chain, as manifested in Fig.1.13. The PANI band gap is lowered by relying on the dopant types and their polarities thereby improving conductivity. The redox approach may be utilized to transform distinct PANI forms into one another, as depicted in Fig. 1.13 [64]. The conductivity, microstructure, solubility, degree of crystallinity, molecular weight, and optical property of PANI are all influenced by the dopant: aniline and oxidant: aniline molar ratios.

1.5.1. Polyaniline Synthesis Method

The synthesis techniques of polyaniline (PANI) described by various research groups may be divided into two categories as presented in Fig. 1.14: (a) without using oxidant and (b) with using oxidant. The former part involves only electrochemical polymerization, while the latter part involves chemical oxidative polymerization (COP), interfacial polymerization, solid-state polymerization, enzymatic polymerization, microemulsion polymerization, plasma polymerization, electrospinning technique, and ultrasonic irradiation [62].
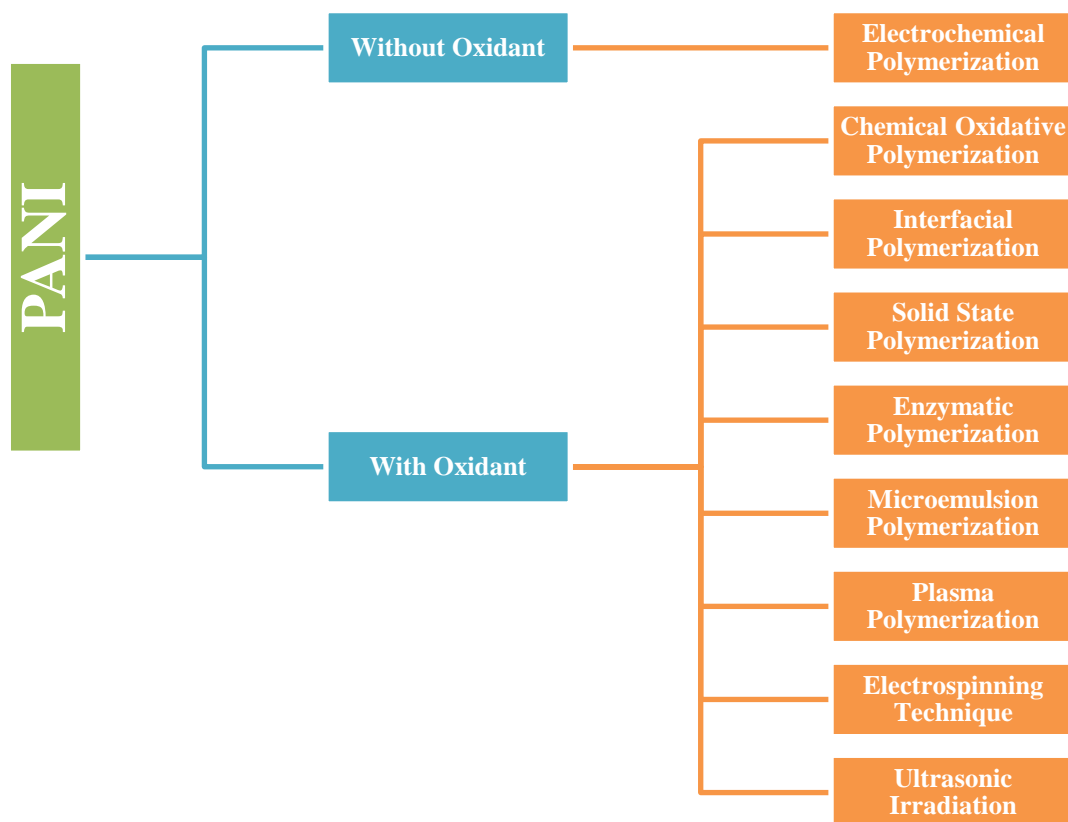
Fig. 1.14. Method for synthesis of polyaniline.

18

Out of the above mention techniques, the chemical oxidative polymerization (COP) technique is preferred and most widely used by virtue of the following properties [65-67]:

(a) The COP is a facile synthesis technique that yields immaculate PANI in bulk amounts.

(b) In COP the starting material used was cost-effective.

(c) The COP controls the growth and alignment of the PANI nanofibers.

(d) The COP will take less than 1 h to complete the polymerization of PANI.

(e) In the COP technique, the oxidant part could be cycled.

(f) Owing to the lower molecular weight of the oxidant, the dosage of the oxidant used in the COP is very small.

(g) Unlike other synthesis techniques, the PANI prepared by the COP technique can be deposited on both the conducting as well as non-conducting substrates.

(h) The PANI prepared by the COP technique doesn't require the nasty or toxic solvent for the preparation of PANI ink which is to be loaded on conducting substrate surface by utilizing spin or dip coating.

1.5.2. Chemical Oxidative Polymerization

As illustrated in Fig. 1.15, polyaniline (PANI) is produced in an aqueous environment utilizing the dopants (HCl) and an oxidant (APS) in chemical oxidation polymerization (COP) [68,69]. The oxidant might remove a proton from the aniline monomer at this stage without forming a bond with the final product.
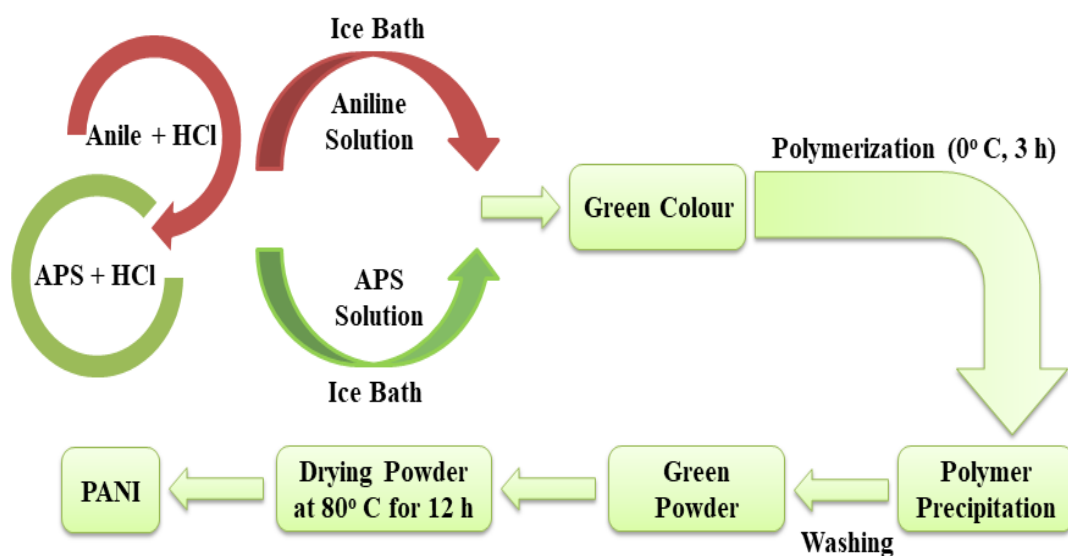
Fig. 1.15. Chemical oxidative polymerization method for preparation of polyaniline.

The monomer [aniline], oxidant [$K_3(Fe(CN)_6$, $(NH_4)_2S_2O_8$, $Ce(SO_4)_2$, H_2O_2, $NaVO_3$, KIO_3, $K_2Cr_2O_7$], and dopant [HCl, H_2SO_4] are involved for the chemical production of PANI. The most widely utilized and facile technique for the production of the PANI is the COP. In this technique, the monomer of aniline acts as a neutralizer by interacting with the doping reagent. The polymerization phenomenon occurs at different temperatures when the oxidizing reagent is added drop by drop to the aforementioned (anile+HCl) solution. After 3 h, the PANI polymerization is pretty much under completion, and the resulting PANI is still in aqueous form. The PANI residues are collected by filtering the PANI solution, which is then washed repeatedly with distilled water to obtain a pristine PANI. The resulting PANI residue is then further rinsed with acetone to render the colorless filtrate and assure that all non-reactive elements are eliminated. The final PANI is emeraldine salt (ES) having a slime-green colour which is unstable because of the presence of swords [70]. As a result, the ES state transforms to the emeraldine base (EB) state of PANI at ambient temperature, which itself is inherently stable, enabling these precipitates to reach equilibrium with an adequate quantity of ammonia (NH_4OH) [71].

1.6. Spinel Ferrite-Polyaniline Nanocomposite

Polyaniline (PANI) has shown tremendous interest in supercapacitors (SCs) owing to its minimal cost, ease of synthesis, adaptability, and magnificent specific capacitance (C_s) [72]. It solitary may be utilized to prepare an SC electrode for excellent C_s. The lower PANI stability, on the other hand, restricts its usage as an SC electrode. PANI in association with other well-known active materials viz. carbon materials or metal oxides can overcome PANI's inherent drawbacks. For the energy storage SCs, PANI is considered to be a candidate material, which demands additional research and product development. Furthermore, doping-dedoping of charged ions, during the reversible redox reactions in the pseudocapacitor (PC) undergoes the PANI to crack, shrink, and swell, thereby reducing the cyclic life [73]. Furthermore, owing to excessive oxidation, PANI can deteriorate at higher applied potentials, resulting in the PANI operating at low potentials. Such issues need the development of composite systems that combine PANI matrix with the additional well-known SC electrode materials (carbon materials or metal oxides). Out of the various known binary nanocomposites (NCs), metal oxide-PANI was most desirable for the PC electrode material by virtue of the faradic reactions. Numerous metal oxides had been investigated for the SC electrode material. To the best of our knowledge the mixed metal oxide viz. spinel ferrite had

been envisioned as a possible contestant for SC application as discussed earlier in section 1.3.2. This is an intriguing process of combining the amazing features of spinel ferrite and PANI into a single electrode [47]. This process enables the NC (spinel ferrite-PANI) materials to have synergistic effects that are not possible with individual constituents. The nanoparticles (NPs) of the spinel ferrite can be merged and deeply embedded with the PANI matrix in the NC electrode, resulting in improved electrical conductivity, porous structure, and structural stabilization thereby giving rise to superfluous storage of charge by virtue of kinetic operations and enhanced charge transportation.

1.6.1. Spinel Ferrite-Polyaniline Nanocomposite Synthesis Method

The researchers working on the conducting polymer PANI-based nanocomposite are predominantly employing two methods for its synthesis viz. in situ polymerization method and blending or direct compounding method as presented in Fig. 1.16 [74].
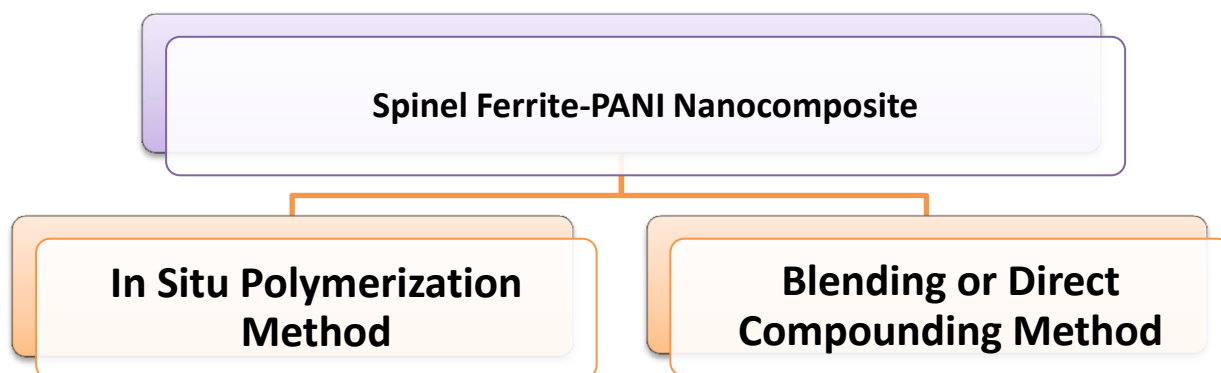
Fig. 1.16. Method for synthesis of spinel ferrite-polyaniline nanocomposite.

An appropriate method will be preferred depending upon the type of polymeric matrix, nanoparticles, and desired properties for the final products. The blending method is widely utilized for the synthesis of the PANI-based nanocomposite due to the facile synthesis, less time, and minimal cost. Moreover, it is very difficult in the blending method to attain a proper dispersion of the nanoparticles in the PANI matrix as compared to the in situ polymerization method.

1.6.2. Blending or Direct Compounding Method

Blending, sometimes known as direct compounding, is considered to be a facile and quick procedure to produce polymer nanocomposites (NCs). Solution, emulsion, melt,

mechanical, and physical are the commonly known blending procedures, as manifested in Fig. 1.17. These blending procedures deal with the direct insertion of nanoparticles (NPs) into the polymer matrix in the required proportion. The preforms of polymers and NPs are prepared separately in this case before being blended together to produce the NCs. Aside from the benefits, there are also drawbacks to this procedure, as it results in non-uniform dissemination of NPs inside the polymer matrix owing to NPs agglomeration [75]. Regardless of the drawbacks mentioned above, the blending procedures continue to be utilized for the production of polymer NCs.
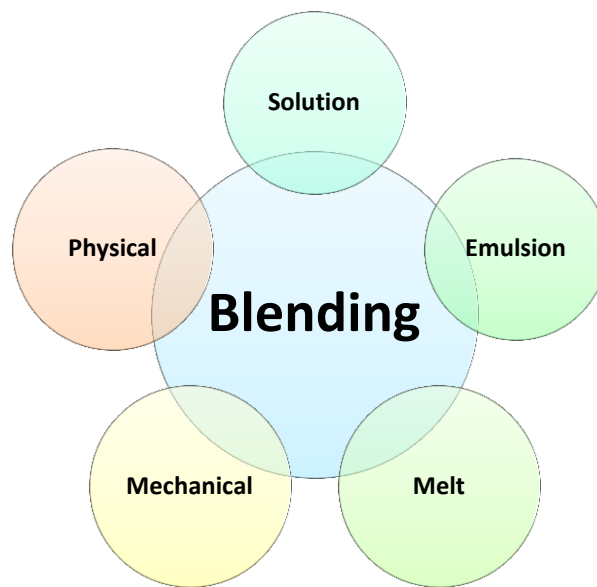
Fig. 1.17. Blending method for synthesis of the polymeric nanocomposite.

CHAPTER-2

Review of Literature, Research Gaps, and Objectives

2.1. Review of Literature

T. Dippong et al. (2022) had discussed the effect of Mn^{2+} substitution by Ni^{2+} on the structural, morphological, and magnetic characteristics of $Mn_{1-x}Ni_xFe_2O_4@SiO_2$ (x = 0, 0.25, 0.50, 0.75, 1.00) nanocomposites (NCs) produced using a modified sol-gel process. The formation of a SiO_2 matrix and ferrite is confirmed by Fourier transform infrared spectra, and X-ray diffraction patterns reveal the presence of poorly crystalline ferrite at low annealing temperatures and highly crystalline mixed cubic spinel ferrite with secondary phases at high annealing temperatures. With increasing Ni content and in accordance with Vegard's rule, the lattice parameters steadily drop as the crystallite size, volume, and X-ray density of $Mn_{1-x}Ni_xFe_2O_4@SiO_2$ NCs rise. The coercivity falls as the Ni concentration rises, while the saturation magnetization, remanent magnetization, squareness, magnetic moment per formula unit, and anisotropy constant all rise. For samples that were annealed at greater temperatures and had the same chemical formula, these parameters were bigger. While the NCs with high Mn content exhibit paramagnetic activity, the NCs with high Ni content exhibit superparamagnetic-like behaviour [76].

S. A. Al Kiey et al. (2022) had reported that due to the various oxidation states of the metal ions, metal ferrites possess exceptional electrochemical properties, making them intriguing materials for solving both the expanding environmental problems and sustainable energy conversion and storage. Thus the three nano-crystallites of transition metal ferrites viz. $CoFe_2O_4$, $CuFe_2O_4$, and $Co/CuFe_2O_4$ were prepared by employing citrate precursor's method. These materials were then used as electrode materials for supercapacitor applications. Mixed transition metal ferrite nanoparticles were examined using Fourier transform infrared (FT-IR), scanning electron microscopy (SEM), energy dispersive spectroscopy (EDX), transmission electron microscopy (TEM), Raman spectroscopy, and thermal analysis (TGA). The results showed how a single-phase spinel ferrite was formed, which was demonstrated by XRD data. The as-synthesized nanomaterial also displayed a spherical form with a size ranging from 30 to 50 nm, according to the particle shape and size data collected through TEM investigation. The outcome showed that the electrochemical performance of the ferrite

nanoparticles attained an impressive maximum specific capacitance of 893 F g^{-1} at a scan rate of 5 mV s^{-1} while employing a three-electrode configuration. Co-Cu ferrite demonstrated exceptional cycling stability over 3000 cycles with 90 % capacity retention at a current density of 1 A g^{-1}. Based on the aforementioned information, it can be concluded that the Co-Cu ferrite nanocomposites exhibit extraordinary electrochemical performance and hold promise as potential materials for supercapacitor electrodes [77].

S. Balideh et al. (2021) had prepared $Ni_{0.3}Co_{0.7}Dy_xFe_{2-x}O_4$ (x = 0:0, 0.02, 0.04, 0.06, 0.08, and 0.1) samples by utilizing the hydrothermal process, an annealing treatment, and NaOH as a solvent. The prepared samples underwent a 7-hour annealing process at 150. On structural, morphological, electrical, and magnetic characteristics, the effect of Dy doping was investigated. The structure, size, morphology, and magnetic characteristics of synthesized compounds were examined using X-ray diffraction, Fourier transform infrared spectroscopy, field emission scanning electron microscopy, an energy dispersive spectrometer, and a vibrating sample magnetometer (VSM). X-ray diffraction proved the presence of a ferrite phase. An increase in Dy doping has been seen to result in larger average crystallite and grain sizes. Two distinct, significant absorption bands at 500-600 cm^{-1} were visible in the Fourier transform infrared spectra. Particles with an average size ranging from 45 to 60 nm were seen by field emission scanning electron microscopy to have a consistent spherical form. The presence of the component elements Co, Ni, Fe, and Dy, with proportions that are extremely near to the stoichiometry of the chemical formula, was confirmed by examining the energy dispersive spectrometer analysis patterns. The characteristic magnetic behaviour of spinel ferrite nanoparticles was validated by magnetic measurements, and the magnetic hysteresis behaviour was enhanced over that described in other studies [78].

B. Nawaz et al. (2021) had developed $Ni_{0.5}Zn_{0.5}Fe_2O_4$ as electrodes with and without binders. Simple hydrothermal procedures are used to directly produce the binder-free electrode on nickel foam. X-ray diffraction is used to investigate the crystalline phase of both of these electrodes. Through the use of high resolution transmission electron microscopy (TEM) and scanning electron microscopy (SEM), their morphology has been studied. These techniques have shown a well-defined nanostructure that resembles tiny hexagonal platelets. Using energy dispersive spectroscopy (EDX), the chemical composition is confirmed. By using cyclic voltammetry (CV), Galvanostatic charge-discharge (GCD), and electrochemical impedance spectroscopy (EIS), their electrochemical characteristics are examined. Due to the

nickel foam's 3-D linked structure, the NZF@NF electrode has surpassed the NZF electrode based on a binder in terms of electrochemical performance. The NZF@NF electrode produced a high specific capacity of 504 F g^{-1} at a current density of 1 A g^{-1}, whereas its counterpart produced a specific capacity of 151 F g^{-1} at the same current density [79].

E. Samuel et al. (2021) had worked in synthesizing NiFe$_2$O$_4$ nanosheets over nickel nanocone decorated nickel foil via the electrodeposition method. The above formed NiFe$_2$O$_4$ nanosheets were confirmed by XRD characterization. This excellent NiFe$_2$O$_4$ C$_s$ was revealed to be 560 F g^{-1} and 483 F g^{-1} at 1 A g^{-1} and 5 A g^{-1} current densities, respectively, and brilliant cycling performance with capacitance retention of 95.3 % beyond 10,000 cycles, making it an appropriate binder-free NiFe$_2$O$_4$ nanostructure for advanced SC electrode material [80].

K. Sathiyamurthy et al. (2021) had employed a simple co-precipitation approach to prepare ZnFe$_2$O$_4$, CoFe$_2$O$_4$, and Co-doped ZnFe$_2$O$_4$. XRD was utilized to confirm the cubic spinel structure of the Co-doped ZnFe$_2$O$_4$ nanoparticles. The metal oxide's characteristic vibration mode was determined utilizing composite FTIR spectra. FE-TEM and FE-SEM corroborated the shape, exhibiting a spherical structure with an aggregation of the nanocomposite. EDX analysis indicates the elemental characteristics of the Co-doped ZnFe$_2$O$_4$ nanocomposite. A VSM was used to investigate the produced NC, which revealed the transition from paramagnetic to ferromagnetic activity. The C$_s$ of the three ferrites were estimated at a scan rate of 10 mV s^{-1}, and Co$_{0.5}$Zn$_{0.5}$Fe$_2$O$_4$ had a significantly enhanced C$_s$ of 218 F g^{-1}. The NC that has been prepared can be utilized in energy storage systems. The theoretical component was determined utilizing the density functional theory technique, which was then utilized to examine the physicochemical, nonlinear optics, and structural properties of CoZnFe$_2$O$_4$ NPs [81].

M. Safari et al. (2021) was using a two-step approach for Fe$_2$Co-MOF production viz. solvothermal procedure and then calcination. The occurrence of the cubic structure of CoFe$_2$O$_4$ and MIL-88A (Fe) structure of Fe$_2$Co-MOF has been validated by XRD patterns. As per FE-SEM micrographs, the calcination method transforms the morphology from spindle (Fe$_2$Co-MOF) into yolk-shell (CoFe$_2$O$_4$). As per BET analysis, the specific surface areas of Fe$_2$Co-MOF and CoFe$_2$O$_4$ are 36.0 and 29.2 m^2 g^{-1} respectively. VSM study found that CoFe$_2$O$_4$ had a high value of coercivity of 2500 Oe owing to the surface anisotropy. During morphological change, the optical band gap is decreased from 1.92 to 1.77 eV. GCD

curves at 1 A g^{-1} yield C$_s$ of 489.9 F g^{-1} (Fe$_2$Co-MOF/NF) and 192.6 F g^{-1} (CoFe2O4/NF). The Fe$_2$Co-MOF/NF exhibits more magnificent cyclic stability than their counterparts beyond 3000 cycles [82].

W. Raza et al. (2021) had synthesized for the first time, lanthanum cerium ferrite nanoparticles by employing a hydrothermal and co-precipitation approach. The structural along with the morphological characteristics of NPs were investigated employing XRD, SEM, TEM, and EDX. For CV, GCD, and EIS of J1 and J2 electrodes, a three-electrode setup in 6 M KOH electrolyte has been used. The excellent C$_s$ of 1195 F g^{-1} was achieved for J2 at 10 mV s^{-1} and had 92.3 % capacitive retention beyond 2000 cycles. The E and P densities for the J2 electrode at 5 A g^{-1} were noticed to be 59 Wh kg^{-1} and 9234 W kg^{-1}, respectively. As a consequence, the developed J2 electrode is a likely contender for supercapacitor use [83].

A. Anwar et al. (2021) had employed a co-precipitation method to prepare NiGd$_x$Fe$_{2-x}$O$_4$ NPs. The spinel cubic structure of NiGd$_x$Fe$_{2-x}$O$_4$ NPs was verified by XRD. Moreover, XRD spectra have also been utilized to determine the presence of metal cations in the A and B sites, bond lengths, hopping, and site radii. The M-O vibrations (stretching) at the A and B sites and spinel structure were corroborated by the FTIR spectra. The uneven shape of NiGd$_x$Fe$_{2-x}$O$_4$ nanoparticles was validated by the FESEM investigation. The elemental compositions were determined using EDX spectrographs. The dielectric characteristics were explored by employing Koop's model and Debye's theory. There was no discernible dielectric loss at higher applied frequencies (AC). Additionally, the electron exchange energy, magneto-crystalline anisotropy, and spin canting all aided in magnetic assessment. Owing to the low coercivity of NiGd$_x$Fe$_{2-x}$O$_4$, it can be extensively utilized in data storage systems having high frequency [84].

I. Petrila et al. (2021) had employed a sol-gel procedure to examine the influence of the sintering of Cu$_{0.5}$Zn$_{0.5}$Fe$_2$O$_4$ on the structural, electrical, and magnetic characteristics. XRD reveals the size of the crystallite and phase of the prepared samples. SEM and AFM reveal the impact of sintering on several aspects viz. size of the crystallite, homogeneity, and porosity. At ambient temperature, relative permittivity, relative permeability, and electrical conductivity were computed with frequency. Eventually, at varying levels of humidity, an evaluation of relative permittivity, electrical conductivity, and the temporal response has

been done. Consequently, the prepared sample would have the possibility to be used in humidity sensors [85].

S. A. Mazen et al. (2020) had prepared $Li_{0.25}Mn_{0.5-x}M_xFe_{2.25}O_4$ by the conventional ceramic method. The metal cations (M) viz. Co^{2+}, Ni^{2+}, and Cu^{2+} were doped at different concentrations (x = 0.0, 0.1, 0.3 and 0.5) to enhance the magnetic characteristics. The structural along with the magnetic characteristics of the prepared samples were examined by employing the XRD, SEM, and VSM. For all prepared samples the single-phase (spinel) was affirmed by the XRD. With increasing doping concentrations, the lattice parameter fell linearly. The crystallite sizes range from 60 to 101 nanometers. VSM tests demonstrated that different metal ions replacements had a significant impact on the M_s of $Li_{0.25}Mn_{0.5-x}M_xFe_{2.25}O_4$, which is attributable to the distribution of metal cations in the A and B sites. Owing to the enhanced magnetic characteristics of the $Li_{0.25}Mn_{0.5-x}Co_xFe_{2.25}O_4$ as compared to their counterparts, it can be eventually implemented in the magnetic recorders and microwave appliances. It was noticed that the prepared $Li_{0.25}Mn_{0.5}Fe_{2.25}O_4$, structural and magnetic characteristics can be tuned by the substitution of various divalent transition metal ions [86].

M. I. A. A. Maksoud et al. (2020) explored conducting polymers, carbon materials, transition metal sulphides, perovskite oxides, and spinel ferrite which are all utilized to make supercapacitors. The C_s of $ZnCo_2S_4$ (1269 F g^{-1}) were four times that of Zn-Co ferrite (296 F g^{-1}). The rapid ionic diffusion and the small R_{ct} of the $ZnCo_2S_4$ account for this. The excellent capacitive retention and the C_s were examined for the composite materials (metal sulphides or oxides with carbon or conducting polymer-based material). This seems to be owing to the active sites of sulphur and oxygen that will enhance electrolyte intake and, as a result, develop new active sites while cycling [33].

S. J. Uke et al. (2020) had synthesized Zn doped $MgFe_2O_4$ by sol-gel technique, as an electrode material for SC at varied Zn concentrations. The concentration of Zn in $MgFe_2O_4$ improves the SCs performance and raises the value of electric conductivity. The 2 wt. % Zn concentration in $MgFe_2O_4$ has been reported to be a high mesopores content with a modest surface area for ions to be accommodated. In 1 mol L^{-1} of Na_2SO_4 electrolyte, Zn doping in $MgFe_2O_4$ exhibited excellent C_s. The enhanced C_s of 484.6 F g^{-1} for 2 wt. % Zn in $MgFe_2O_4$ at 1 mA cm^{-2} was observed in the GCD investigation. P and E are determined to be 2 kW kg^{-1} and, 9 Wh kg^{-1} respectively. Furthermore, EIS demonstrates that 2 wt. % Zn doped $MgFe_2O_4$

has a lower resistance for intercalation and de-intercalation. The larger value of resistance is 1.2, and R_{ct} is 3.2, which is quite low, thus it's a great choice for SCs [87].

M. Barakzehi et al. (2020) had prepared at room temperature, a commonly utilized PET that is modified utilizing MIL-53(Al), via a layer-by-layer fabrication process. The rGO is then dipped into a GO solution and deposited on the surface of PET-MOF following chemical reduction. Finally, an in situ chemical polymerization method polymerizes pyrrole on the PET-MOF-rGO surface. The produced composite has been used as electrode material in an H_2SO_4 solution, yielding a C_s of 510 mF cm^{-2} at 1 mV s^{-1}. The improved electrode is used in symmetrical SCs that has a 3.5 F cm^{-3} (volumetric C_s), 64 mWh cm^{-3} (E), and 0.6 mW cm^{-3} (P). The fabricated SC maintains 85 % of its initial C_s beyond 1000 cycles after twelve months of storage under ambient temperature [88].

J. P. Cheng et al. (2020) had investigated the high activity and electrical conductivity of $NiCo_2O_4$ which has been regarded as an effective electrode material. $NiCo_2O_4$ (core-shell) structural composites have been produced, and the composites seem to have superior C_s than pure $NiCo_2O_4$. This research is aimed at the present state of composites (core-shell) that use $NiCo_2O_4$ as a scaffolding. In core-shell structures conductive polymers, sulphides, hydroxides, and metal oxides are explored in detail as shell materials. The structure (core-shell) produced on conductive substrates can prevent material agglomeration and allow electrolytes to penetrate more easily. The cores of $NiCo_2O_4$ act as conducting conduits to the shell materials, ensuring synergic impact, while the shell materials protect and stabilize the $NiCo_2O_4$ cores. The electrodes of the $NiCo_2O_4$ core were examined in terms of potential development paths and prospects [89].

R. Awata et al. (2020) had exploited in situ chemical oxidation polymerization, to prepare CSA substituted PANI-MWCNT in varied ratios for SC electrodes. The maximal C_s and E of the SC electrodes relying on PANI-MWCNTs (2 wt. %) over graphite sheet and Ni foam, were 1183 and 2053 F g^{-1} and 183.18 and 102.6 Wh kg^{-1}, respectively. For PANI-MWCNTs (2 wt. %), over the graphite sheet, the capacitive retention was reduced to 13 % beyond 1000 cycles and displayed outstanding cyclic stability of 100 % over Ni foam. Cyclic stability of PANI over the Ni foam, on the other hand, was about 50 %. Thus SC electrode of PANI-MWCNTs (2 wt. %) seems to be more reversible than pristine PANI [90].

S. Gul et al. (2020) had prepared $Al_xZnFe_{2-x}O_4$ nanoparticles using a facile and minimal cost co-precipitation technique. The single-phase formation was seen at around 600 °C, according to the thermal study. The genesis of the fcc structure was shown via structural investigation. Ionic exchange in the ferrite nanoparticles caused the crystallite size to shrink as the aluminium concentration rose. The unsubstituted and substituted zinc spinel ferrite nanoparticles had a generally spherical shape and a size of 100 nm, according to the morphological study. The replacement philosophy has a significant impact on magnetic characteristics. The saturation magnetization of the nanoparticles dropped as the aluminum concentration increased. The material was discovered to have significant resistance values after an electrical examination. The optical characteristics of the produced nanoparticles demonstrated that they were suitable for photocatalysis and could destroy organic-based contaminants in drinking water [91].

S. B. Somvanshi et al. (2020) reported surface, optical, spectral, thermal, and structural investigations of Gd^{3+} doped Zn-Mg ferrite NPs prepared by utilizing the sol-gel procedure. The fluctuation in thermal characteristics and spinel phase development with weight loss % in the obtained samples was analyzed using the TG-DTA technique. The nano-crystalline and spinel-phase formation of all prepared samples were validated by XRD spectra. A rising and falling trend in the lattice constant and crystallite size respectively was noticed with the addition of Gd^{3+}. FT-IR spectrum investigations confirmed the occurrence of two vibrational bands. The enhancement and decrement in the absorbance and bandgap energy respectively with the doping of Gd^{3+} were examined by the UV-VIS. The surface characteristics viz. pore size distribution, pores radius, pore-volume, surface area, etc. were investigated by the BET. All of the samples showed an increase in these surface characteristics due to Gd^{3+} doping. The current research emphasizes the importance of Gd^{3+} doped Zn-Mg ferrites NPs in MRI imaging and magnetic hyperthermia [92].

Y. Slimani et al. (2020) had utilized ultrasonic irradiation procedure for the preparation of $Ni_{0.4}Cu_{0.2}Zn_{0.4}Fe_{2x}Eu_xO_4$ (x = 0.00-0.10) ferrite NPs and thoroughly researched as a green and simple approach. Various properties viz. dielectric, electrical, magnetic, optical, morphology, and structure were examined on doping Eu^{3+} in NiCuZn ferrite NPs. The band gap in the range of 1.86-1.90 eV was evaluated utilizing the tauc plots. At ambient temperature, magnetization tests revealed superparamagnetic activity. A transition from superparamagnetic to ferromagnetic might be observed below the blocking temperature (T_B).

The decrement in the M_s was noticed with the doping of Eu^{3+}. The greatest fluctuation in dc conductivity was exhibited at the concentration of x = 0.02. The activation energy is shown to be significantly dependent on both the substitution ratios of Eu ions and the temperature regions [93].

M. F. Warsi et al. (2020) had prepared the nanoparticles using a cost-effective and simple surfactant-assisted co-precipitation method. Er-doped Ni-Co ferrites are substantially tailorable in terms of magnetic, electrical, physical, and structural characteristics. XRD investigation verified the cubic phase of these nanoparticles. Using hysteresis loops and dielectric tests, the nanoparticles were further evaluated for potential application studies. M_s was enhanced from 35.99 to 45.6 emu g^{-1} after Er^{+3} doping. Owing to the composition's substantial rise in saturation density and coercivity, it's a good candidate for use in high-density media recording device construction. Increased Er^{+3} concentrations in $Ni_{0.4}Co_{0.6}Fe_2O_4$ spinel ferrite nanoparticles resulted in a considerable improvement in AC conductivity [94].

S. Ikram et al. (2020) used a simple sol-gel auto combustion approach to successfully synthesis a series of $CoFe_{2-x-y}Tb_xDy_yO_4$ (x + y = 0.00-0.25). The produced sample's single-phase formation and nanocrystalline characteristics were verified by XRD analysis. The structure of the studied materials did not degrade up to 900 °C temperature, and now the phrase has evolved, according to time and temperature-dependent XRD observations. Dy^{3+} and Tb^{3+} ions were effectively integrated into Co ferrite NPs, as per the XPS investigation. XPS has also been used to validate the spinel structure of the prepared samples. The single domain and the magnetic soft characteristics of the prepared samples were avowed by the VSM study [95].

S. Ikram et al. (2020) had assessed the impact on the dielectric, magnetic, electrical, and structural characteristics of the doping of the rare earth metal cations. XRD scans and subsequent FTIR analyses verified the cubic spinel structure of all produced nano-ferrites. The type of dopant RE^{3+} ions has a substantial impact on the lattice constant, grain size, and crystallite size. Secondary phases on doping La exist for x > 0.2 owing to the La larger radius than the Ce. The spin order coupled with RE^{3+} ionic radius was affected by decreasing crystallite size, resulting in a reduction in magnetization. The decrement in the coercivity and increment in the permeability was examined for the dopant having a short radius. The dielectric constant, as well as dielectric loss, dropped with the decrement in the frequency.

These ferrites NPs were applicable for microwave and high-frequency appliances according to their described properties [96].

S. V. Bhandare et al. (2020) had utilized a glycine-aided sol-gel auto combustion technique to make nanocrystalline Co-Mg-Ni ferrite samples, which were then calcinated at 600 ^{o}C. The impact of substituting Mg for Ni relies on the presence of metal cation in the A and B sites. The ^{57}Fe-Mossbauer spectroscopy, magnetic characteristics, and rietveld refinement affirms the existence of Co in the A and B sites in the ratio of 2:3, Ni in the B site, and Mg in the A site. For maintaining the spinel structure of the prepared samples, only Fe^{3+} shifts their lattice sites, but sites of the Co^{2+}, Ni^{2+}, and Mg^{2+} remain unchanged when Mg^{2+} is substituted for Ni^{2+}. Thus when Mg^{2+} is substituted for Ni^{2+} in a $Co_{0.5}Ni_{0.5}Fe_2O_4$ sample, the cation distribution and magnetic characteristics change [97].

C. Murugesan et al. (2020) had employed the combustion reaction approach to successfully produce nanocrystalline $Mn_{1-x}Zn_xFe_2O_4$ mixed ferrites. The single spinel phase of all the prepared samples was avowed by the XRD. The spherical ferrite NPs were prepared, according to surface morphology studies. Furthermore, the SAED patterns reveal the produced ferrite's polycrystalline nature. The existence of O, Fe, Zn, and Mn in the states O 1s, Fe 2p, Zn 2p, and Mn 2p may be seen in the XPS spectra. With the doping of Zn, the decrement in the AC electrical conductivity, tan δ, and dielectric constant were noticed for x < 0.9. The enhancement in the activation energy from x = 0.0 to 0.8 was noticed. The prepared $Mn_{0.2}Zn_{0.8}Fe_2O_4$ NPs are beneficial for high-frequency applications [98].

R. P. Patil et al. (2020) had synthesized Mn-doped $LiFe_2O_4$ NPs by employing the sol-gel procedure. The prepared sample is sintered in air at various temperatures. FTIR, SEM, and XRD have been utilized for the examination of morphological and structural characteristics. All of the samples had a nanocrystalline single cubic phase structure, as per the XRD pattern. The SEM method is used to provide morphological investigations of produced nanocrystalline materials. It can be observed that when the sintering temperature rises, the average grain size grows dramatically. According to FT-IR investigations, the spinel phase forms at a higher sintering temperature [99].

K. Tanbir et al. (2020) studied the effects of Eu^{3+}, Sm^{3+}, and Gd^{3+} doping on the magnetic, optical, and structural characteristics of Ni-Co ferrite NPs produced via the facile co-precipitation route. XRD confirmed the development of single-phase (spinel) for all the

samples. Owing to the larger radius of the dopant, a decrement in the crystallite size was exhibited. The HR-TEM micrograph-derived mean particle size closely matched the X-ray diffraction data. At ambient temperature, the paramagnetic character of rare-earth ions decreases the superexchange interactions between sublattices. In contrast with the dopant, the Curie temperature, M_s, and coercivity were noticed to be lower than the pristine samples. The nano-size effect of the produced NPs is responsible for the enhancement in the bandgap (optical) [100].

N. Mechi et al. (2020) had used the sol-gel technique to produce $Ni_{0.4}Cd_{0.3}Zn_{0.3}Fe_2O_4$ ferrites at two different temperatures. The produced NPs exhibit spinel phase, according to Rietveld refinements of XRD patterns. With the enhancement in sintering temperature, the increment in the grain size and lattice constant was noticed. When the sintering temperature is raised, the maximum magnetization (M_s) increases, but coercivity (H_c) and remanence (M_r) decrease. An impedance study was utilized to examine the frequency and temperature dependency of electrical conductivity, electrical modulus, and electrical impedance. The conductivity of the samples increases as the sintering temperature rises. The presence of an electrical relaxation event and non-Debye nature may be seen in the changing of the imaginary component of the modulus. An electrical equivalent circuit was used to examine Nyquist representations. The obtained findings show that the grain boundary contribution is mostly responsible for the sample's conduction mechanism [101].

F. Hcini et al. (2020) had used the sol-gel technique to prepare $Cd_{0.5}Zn_{0.5}FeCrO_4$ at two different temperatures. The sintering impact on the electrical, magnetic, infrared, and structural characteristics of the prepared samples was examined. For all the prepared samples the development of the single-phase (spinel) was assured by the XRD. With the increment in the sintering temperature, the increment in the grain size and lattice constant was noticed. Moreover, the enhancement in the dielectric constant, electrical conductivity, M_s, and absorption band intensity was observed with the enhancement in the temperature. Owing to the same current carriers, the dc-conductivity and relaxation time revealed similar activation energies, thereby demonstrating the conduction and relaxation phenomenon [102].

M. A. Almessiere et al. (2020) had used sol-gel technique to prepare Eu doped Ni-Cu-Zn ferrite NPs. The single-phase (spinel) for all the prepared samples was affirmed by the XRD. The hyperfine magnetic field (HMF), quadrupole splitting, isomeric shift, and line-width disparity were all estimated using Mossbauer spectra. With the increment in the Eu doping,

the decrement in the HMF was noticed. The prepared NPs paramagnetic contribution grew as the Eu^{3+} level rose. The suggested NSF's S-parameters were measured using the co-axial approach. Natural ferromagnetic resonance (NFMR) occurrences allowed for significant EM energy absorption in the range of 2.5-9.5 GHz. Furthermore, the frequency features of the NSF's were greatly altered by the rise in Eu substitution. The resonant amplitude changed abnormally (more than four times). The findings indicate that the prepared materials are applicable for radio-electronic gadgets [103].

R. R. Chilwar et al. (2019) had employed a chemical spray approach to preparing a thin film of Al^{3+} doped $LiFe_2O_4$. The single-phase (spinel) development of the prepared sample was assured by XRD pattern analysis. The decrement in the lattice constant was noticed with the doping of Al^{3+}. FTIR study exhibits the effective integration of the dopant in the $LiFe_2O_4$. The agglomerated spherical-shaped grain was perceived in the FESEM. The bandgap lies in the range of 2.36 and 2.04 eV, which is estimated utilizing the Tauc plot. With increasing Al^{3+} content, the saturation magnetization (M_S) drops, but the coercivity (H_C) increases. With increasing Al^{3+} concentrations, the dielectric characteristics deteriorated [104].

P. Bandyopadhyay et al. (2019) had employed a facile hydrothermal approach to preparing porous 3-D Zn-Ni-Co oxide/$NiMoO_4$ over Ni foam for SC. The hierarchical porous Zn-Ni-Co oxide/$NiMoO_4$ exhibits excellent reversible Faradaic reaction, by having quick ions mobility, porous structure, stability, and magnificent conductivity. It was perceived that the asymmetric SC exhibits an excellent life span, C_s, and quick charge-discharge rate if Fe_2O_3/rGO and Zn-Ni-Co oxide/$NiMoO_4$ were utilized as an anode and cathode material respectively [105].

Y. Z. Cai et al. (2019) had altered the composition ratio, to produce rGO-$NiFe_2O_4$ nano-hybrids with $NiFe_2O_4$ dispersed over a 2-D rGO substrate. $NiFe_2O_4$ levels might interfere with the ideal condition of transportation of ions and conduction of the electron, thereby lowering C_s. The weight capacitance of the G-N3 (30 wt. % $NiFe_2O_4$) SC electrode is four times that of pristine $NiFe_2O_4$ at 0.5 A g^{-1}. Furthermore, this G-N3 SC electrode has excellent rate performance as well as long-term cycle stability. Quantitative electrochemical kinetics experiments are also used to investigate a surface capacitive storage mechanism. The findings suggest that nanoscale tailoring may be a more reliable route to developing novel SC electrodes [106].

J. Bhagwan et al. (2019) had applied a facile, rapid, and cost-effective combustion process was used to synthesize zinc cobaltate (ZCO) nanoparticles. To achieve acceptable crystallinity and a suitable morphology in ZCO, several calcination temperatures were utilized. The impact on the electrochemical activity of the SC with the temperature was examined. The excellent C_s at 1 A g^{-1} for optimized sample yields to be 843 F g^{-1}. The aqueous asymmetric supercapacitor was made using the optimum sample. The P and E at 1 A g^{-1} for asymmetric SC were evaluated to be 716 W kg^{-1} and 26.28 Wh kg^{-1} respectively. The parallel-connected 14 LEDs and fan were operated with the two asymmetric SCs connected in series. Based on the foregoing findings, optimized ZCO appears to be favorable for the SC electrode [107].

J. Acharya et al. (2019) had utilized a facile sonochemical technique to prepare the SC electrode material ($CoFe_2O_4$-MWCNTs). The prepared material had 3D porous morphology as exhibited by the FESEM owing to which there is quick mobility of the ions in between the electrode and the electrolyte. The prepared material had magnificent capacitive retention, excellent rate capability, and high C_s. Moreover, the electrochemical activity of the SC is remarkably higher when AC and $CoFe_2O_4$-MWCNTs were utilized as the negative and the positive electrode respectively. At 3 mA cm^{-2}, the C_s were noticed to be 81 F g^{-1} and beyond 2000 cycles, there exist excellent capacitive retention (92 %) with P and E to be 319 W kg^{-1} and 26.67 Wh kg^{-1} respectively [108].

T. Das et al. (2019) had successfully prepared a novel hybrid ternary ($CuFe_2O_4$-Acetylene black-PANI) nanocomposite. The prepared material characteristics were examined by the EDX, SEM, UV, FTIR, and XRD. The ternary system's linked structure encouraged various electrochemical processes. The C_s of the prepared material at 0.5 A g^{-1} are estimated to be 732.35 F g^{-1}. The prepared SC exhibits the C_s of 192.64 F g^{-1} at 0.5 A g^{-1}. The P and E of the prepared sample were noticed to be 3165.25 W kg^{-1}, and 26.757 Wh kg^{-1} respectively. Because of the synergistic effects between separate components, ternary composites provide intriguing outcomes and are favorable for the SCs. To determine the resistances of electrode material, an EIS study was performed [109].

H. Javed et al. (2019) used a co-precipitation approach to make $Ni_{0.65}Zn_{0.35}Nd_xFe_{2-x}O_4$ nanoparticles. The electromagnetic and structural characteristics of the prepared samples can be tuned with doping (RE). The electric, magnetic, spectral, and structural behavior of the prepared samples was examined utilizing I-V measurements, VSM, FTIR, and XRD.

Excluding x = 0.075, for all the prepared samples the development of the single-phase (spinel) was avowed by the XRD. The nonlinear trend in the magnetic, electric and structural study was perceived with the doping of Nd^{3+}. The vibrations in the prepared samples were explained by the FTIR [110].

B. J. Rani et al. (2018) had employed a facile co-precipitation procedure for the production of Co-doped $ZnFe_2O_4$. The electrochemical, optical, and structural characteristics of the prepared samples are highly swayed by the dopant. The active modes were precisely defined in the prepared samples as detected by the Raman results. The occurrence of vacancies in the produced samples was corroborated by the PL spectra. The doping of the Co, as well as the spinel phase in the prepared samples, was confirmed by the FTIR. The increment in the C_s was noticed from 319.37 to 377.81 F g^{-1} with the Co doping [111].

M. Chandel et al. (2018) had utilized the facile in-situ approach for the production of $CuFe_2O_4$-rGO NC. Density functional theory was employed to examine the interaction of rGo with $CuFe_2O_4$ inside the prepared NC. The excellent C_s of the NC were exhibited, due to their synergic action. The prepared NC in the weight % ratio of 96:04 showed remarkable catalytic efficiency. This efficiency was much greater than that of pristine $CuFe_2O_4$ in each of these processes. The prepared NC also outperformed pristine $CuFe_2O_4$ in terms of super-capacitance. The C_s of the NC at 2 A g^{-1} were estimated to be 797 F g^{-1} and hold excellent capacitive retention (92 %) beyond 2000 cycles [112].

S. Hcini et al. (2018) had exploited the sol-gel approach for the production of $Ni_{0.4}Cd_{0.3}Zn_{0.3}Fe_2O_4$ and investigated the critical, magneto-caloric, magnetic, and structural characteristics of the temperature. The increment in the size of the crystal and lattice constant was perceived with the increase in the temperature. In the prepared samples the transitions from FM-PM are noticed in the magnetic investigation. The enhancement in the relative cooling power, entropy, Curie temperature, and magnetization was manifested with the enhancement in the temperature. Owing to the enhancement in the size of the crystal, there arises variability in the critical exponents [113].

F. M. Ismail et al. (2018) had successfully worked in preparing $Mn_{0.5}Zn_{0.5}Fe_2O_4$ spinel ferrite for the first time for high-performance supercapacitor electrodes. The $Mn_{0.5}Zn_{0.5}Fe_2O_4$ spinel ferrite so formed has a mesoporous nanostructure, narrow pore size dissemination, and high surface to volume ratio. The electrode prepared by utilizing $Mn_{0.5}Zn_{0.5}Fe_2O_4$ exhibits a

very high value of C_s (783 Fg^{-1}) in 0.5 M H_2SO_4 and has a very high coulombic efficiency. The P and E at 1.0 A g^{-1} for the $Mn_{0.5}Zn_{0.5}Fe_2O_4$ are 899.7 W kg^{-1} and 15.8 Wh kg^{-1} respectively, which is comparatively larger than the P and E of $MnFe_2O_4$ and $ZnFe_2O_4$. This makes $Mn_{0.5}Zn_{0.5}Fe_2O_4$ a favorable material for high-performance SC applications [114].

N. Arsalani et al. (2018) had prepared $MnFe_2O_4$ nanoparticles using a simple hydrothermal process and subsequently inserted them in a PANI matrix by in situ polymerization. The prepared NC characteristics were examined utilizing FESEM, FTIR, and XRD. At 1 A g^{-1} the excellent C_s of NC (371 F g^{-1}) are exhibited in contrast with the pristine PANI (312 F g^{-1}). Furthermore, the synthesized NC exhibits magnificent cyclic life with better capacitive retention (86.7 %) beyond 2000 cycles [39].

A. Shokri et al. (2018) had utilized a simple co-precipitation approach to preparing $Co_xSn_{1-x}Fe_2O_4$ NPs. The optical, morphological, magnetic, and structural characteristics of the prepared samples were examined utilizing DRS, EDX, FESEM, VSM, FTIR, and XRD. The development of the cubic spinel structure was verified by XRD and FTIR findings. With the doping of the Co, the lattice constant first increments (up to x = 0.25) and then decrements (above x = 0.25). For x < 0.25 and x > 0.25, the shifting of the υ_1 peak towards the lower and higher wavenumber respectively was perceived in the FTIR. For x = 0.50 the value of anisotropy constant, M_r, and M_s were extremely higher and then decrements above x = 0.50 [115].

X. Feng et al. (2018) had applied a simple hydrothermal approach to synthesize hierarchical $CoFe_2O_4$-$NiFe_2O_4$ NC. In contrast to their counterparts, the prepared NC at 1 A g^{-1} exhibits excellent C_s of 269 F g^{-1} and has magnificent capacitive retention (81 %) beyond 10000 cycles. The superb electrochemical activity of the prepared NC makes it favorable for SC of the future [116].

H. Kennnaz et al. (2018) had employed a facile hydrothermal and co-precipitation procedure to prepare $CoFe_2O_4$. The development of the single-phase (spinel) in the prepared samples was avowed by the XRD. The particle size (average) in the nanoscale range of 11 to 26 nm was perceived by the HRTEM and FESEM. The prepared $CoFe_2O_4$ (hydrothermal) exhibits H_c and M_s at ambient temperature to be 750 Oe and 63 emu g^{-1} respectively. Moreover, at 0.5 A g^{-1} excellent C_s (429 F g^{-1}) were perceived with 98.8 % efficiency (coulombic) beyond 6000 cycles, which makes $CoFe_2O_4$ a promising material for SC application [117].

V. Vignesh et al. (2018) had utilized a facile and minimal cost co-precipitation technique for the production of $MnFe_2O_4$. The 3.5 M KOH had been utilized for the electrochemical investigation and it was revealed that at 0.2 A g^{-1}, the excellent C_s (245 F g^{-1}) with capacitive retention of 105 % beyond 10,000 cycles. The P and E were perceived to be 1207 W kg^{-1} and 12.6 Wh kg^{-1} respectively and thus make $MnFe_2O_4$ a favorable material for SC [118].

S. R. Bhongale et al. (2018) had utilized the oxalate co-precipitation approach to prepare $Mg_xCd_{1-x}Nd_{0.03}Fe_{1.97}O_4$ using a unique microwave sintering procedure. Sintering of the prepared sample was done in a microwave oven for 10 minutes. The structural characteristics of the prepared sample were investigated utilizing FTIR, SEM, and XRD. The development of the spinel structure in the prepared sample was assured by the XRD. In spite of the 4 absorption peaks, two sharp peaks were noticed near 400 and 600 cm^{-1} in the FTIR study. The magnetic characteristics of the produced samples are reliant on the grain size, and per the VSM analysis. The processed sample's superior magnetic characteristics make them ideal for use as a recording medium. The microwave sintering process allows for the rapid production of spinel ferrites [119].

E. R. Kumar et al. (2018) had prepared the pure phase of $Ni_{0.8}Co_{0.2}Fe_2O_4$ using egg white as a bio-template and by simple evaporation process. The prepared nanoparticles act as a binder for emulsifying, foaming, and gelling properties which are controlled by egg white. Core-shell interactions appear to impact the magnetic behavior of the current ferrite system. In the current ferrite system, the anisotropy function must be understood in order to account for the overall magnetic behaviour. Koop's hooping mechanism may be used to explain the dielectric behaviour. As there isn't any assurance that Fe^{2+} ions exist, they are generated quickly as a result of the heat treatment for electron hooping [120].

M. N. Akhtar et al. (2018) utilized the sol-gel process to successfully synthesize $Ni_{0.8}Zn_{0.2}Ce_xFe_{2-x}O_4$. The decrement in the porosity, X-ray density, and bulk density was manifested with the doping of the Ce^{3+}. The distribution of the cations in the A and B sites (viz. unshared edges, shared edges, bond length, and cation radii) were examined by the XRD. With increased Ce^{3+} concentration, crystallite and grain size decreased. On Ce^{3+} doping, the decrement in the M_s by 61 % was manifested by the VSM examination. Whereas doping Dy^{3+} in $CoFe_2O_4$, results in a 40 % drop in M_s. In addition, Ce doped Cu ferrite showed a 46 % increase in M_s. The utilization of Ce^{3+} doped Ni-Zn nano ferrites for switching applications was shown using switching field distribution (SFD) measurements.

The relationship between Ce^{3+} content and assessed attributes revealed that these prepared samples can be applied in a wide range of technical and industrial areas [121].

F. S. Omar et al. (2017) had synthesized $ZnCo_2O_4$ spinel nanoparticles by the hydrothermal method which were then physically blended with Polyaniline (PANI) to form PANI-$ZnCo_2O_4$ spinel NCs. The PANI-$ZnCo_2O_4$ spinel NCs formation was confirmed by XRD, FTIR, and FESEM analysis. It has been revealed that the substitution of PANI in the $ZnCo_2O_4$ spinel NPs increases the conductivity, specific capacitance, and the rate of the capability. This enhancement in the above characteristics accounts for the augmentation of the redox site and the synergistic effect of the PANI- $ZnCo_2O_4$ spinel nanocomposites which will ultimately lead to an increase in the effective charge transportation. The PANI- $ZnCo_2O_4$ spinel NCs achieve excellent E and P which is 13.25 Wh kg^{-1} and 375 W kg^{-1} respectively as well as excellent cycling life with the coulombic efficiency of 90 % beyond 3000 cycles [122].

R. S. Yadav et al. (2017) had procured a hot press sintering procedure for the preparation of $Co_{1-x}Zn_xFe_2O_4$. The development of the spinel structure for the prepared sample was avowed by the XRD. Smaller ferrite nanoparticles grew and densified faster than bigger ferrite nanoparticles, according to the scanning electron micrographs. In the prepared samples, magnetic characteristics are reliant on the grain size at the ambient temperature which was examined by the SQUID. The high M_s (82.47 emu g^{-1}) was noticed for the $Co_{0.5}Zn_{0.5}Fe_2O_4$. The prepared samples, grain size, and density impact on the ac conductivity, dielectric characteristics, and hardness had also been explored [123].

M. A. Mousa et al. (2017) had successfully prepared the ternary NC which consists of Nanoferrite (Fe_3O_4, $NiFe_2O_4$, $CoFe_2O_4$), graphene, and PANI. This ternary NC so formed was then characterized for its structural and electrochemical properties. The development of the single-phase (spinel) in the prepared samples was avowed by the XRD. The fiber structure of PANI was confirmed by TEM micrographs which is very useful for the transfer of electrolyte ions. It has been analyzed that the ternary NCs so formed show an excellent performance than individual and binary NCs. These ternary NCs at 1 A g^{-1} have a very high value of C_s i.e. 1123 F g^{-1}. The magnificent P and E of the prepared NC at 1 A g^{-1} were perceived to be 2680 W kg^{-1} and 240 Wh kg^{-1} respectively along with the capacitive retention of 98.2 % beyond 2000 cycles [124].

A. E. Elkholy et al. (2017) had employed a facile co-precipitation procedure for the

preparation of $MnCoFeO_4$. The prepared sample characteristics were examined by the N_2 desorption-adsorption, FTIR, HRTEM, XRD, and EDX. The prepared samples at 1 mV s^{-1} exhibit excellent C_s (675 F g^{-1}). The P and E at 1.5 A g^{-1} were perceived to be 337.50 W kg^{-1} and 18.85 Wh kg^{-1} respectively. The cyclic stability had been explored by employing GCD and EIS. After 1000 GCD cycles, the supercapacitive performance had just 7.14 % deterioration, showing good long-term stability [125].

P. Thakur et al. (2017) had employed the co-precipitation approach to preparing $Mn_{0.5}Zn_{0.5}Fe_2O_4$. The prepared sample crystallite size (average) at 1373, 1173, and 973 K was evaluated to be 67.42, 39.02, and 11.38 nm respectively. The secondary phase Fe_2O_3 was removed during sintering at 1373 K, revealing a single-phase cubical spinel structure. The spinel structure of the prepared samples was assured by the existence of the two sharp bands near 400 and 600 cm^{-1}. The production of homogeneous nanoparticles may be seen in FESEM pictures. The peak of the absorption spectra shifts to a higher wavelength from 214 nm to 285 nm as the sintering temperature rises. The redshift in the PL and decrement in the bandgap energy were noticed with the sintering temperature [126].

S. A. Ansari et al. (2017) had employed a facile chemical oxidative polymerization process to prepare an M-MoS$_2$-PANI NC. The prepared M-MoS$_2$-PANI NC exhibits excellent C_s in contrast with its counterparts. Owing to the synergic activity and MoS$_2$-PANI interface connection in the NC, magnificent cyclic stability was noticed at 10 A g^{-1}. The structural integrity is also compromised during the cycling test as a result of this. With an accessible and scalable production technique, the prepared NC had enhanced electrochemical activity and offers a lot of promise for SC application [127].

N. S. Arul et al. (2017) had applied a simple chemical precipitation approach to preparing pristine ZnS NPs, MnS NPs, and ZnS-MnS NCs. The prepared NCs at 2 mV s^{-1} exhibit excellent C_s of 884 F g^{-1}. The prepared NC-based SC manifests superb P and E which is to be 7.78 kW kg^{-1} and 91 Wh kg^{-1} respectively. Moreover, the synthesized NC has magnificent cyclic stability after 5000 cycles. Thus owing to the excellent C_s, magnificent cyclic stability, and superb P and E the prepared ZnS-MnS NC would be the best alternative for the minimal cost SC according to their findings [128].

M. T. Farid et al. (2017) had employed a facile sol-gel procedure to prepare $MnPr_yFe_{2-y}O_4$. The activation energy of samples with high conductivity has been shown to be low. Owing to

the composition of the produced samples, there is a fluctuation in the exponent n, which ensures conductivity via charge hopping. Koop's (theory) and Maxwell-Wagner's (model) had been employed to examine the AC conductivity. The dielectric and electric characteristics of the prepared sample are highly influenced by the doping of the Pr. Chip inductors (high frequency) and power systems may boost from spinel ferrites that have been prepared [129].

C. Wei et al. (2016) had prepared $MnFe_2O_4$, $FeFe_2O_4$, $CoFe_2O_4$, and $NiFe_2O_4$ for employment in the SC working electrode. Owing to the tiny size of the prepared $MnFe_2O_4$, it manifests excellent C_s as compared to its counterparts. To have comprehensive knowledge related to the process that governs spinel C_s, EXAFS and XANES are employed. The shift in the valance state was noticed only for the Mn metal cation. In contrast with the Mn, the valence states of Co, Ni, and Fe remained constant, resulting in substantially lower C_s. The Fe content of the produced ferrite was stable, which contributes very little to the pseudocapacitance. C_s were improved by having more Mn to B locations. However, in $NiFe_2O_4$ and $CoFe_2O_4$, 88 % and 89 % of the Ni and Co respectively are existing in the B location and their capacitances are limited by their inability to change valence state. In the prepared ferrite, the two main factors viz. B location existence and oxidation state change are responsible for the pseudocapacitance [130].

K. V. Sanka et al. (2016) had worked on synthesizing $CoFe_2O_4$ ferrite, reduced graphene (rGO) oxide, and polyaniline (PANI) ternary nanocomposites (CGP) and used it as a negative electrode. The bonding (covalent) formed between PANI-rGO was affirmed by the spectroscopic studies which will ultimately lead to the increase in the electrochemical properties of the ternary CGP nanocomposites. The prepared CGP at 1 mV s^{-1} exhibits C_s of 8.59 F m^{-1}. Moreover, the fabricated SC with the prepared CGP at 1 mA manifests the C_s of 9 mF cm^{-1} and having E of 270×10^{-8} Wh cm^{-1} [131].

B. Bashir et al. (2016) had successfully prepared the $Mn_{0.9}Cu_{0.1}Fe_2O_4$ and rGO NC via simple chemical methods. The electrochemical activity of the prepared samples was examined with the EIS and CV. I-V (two probe) instruments were employed for the investigation of the conductivity of the prepared samples. In contrast to other samples, the prepared NC manifests superb cyclic stability, excellent capability rate, and magnificent C_s of 300 F g^{-1} which make it favorable for SC [132].

S. Sahoo et al. (2016) had worked on developing a ternary nanocomposite material of rGO,

NiMn$_2$O$_4$, and PANI by using a facile chemical process. It had been revealed that the ternary nanocomposites have a higher value of specific capacitance and lower impedance than binary nanocomposites. The above ternary NCs so formed have the higher energy density which is 70 Wh kg^{-1} at 1 A g^{-1} current density and it also showed excellent rate capability and brilliant electrochemical performance at the higher value of current density [133].

B. Bhujun et al. (2016) had employed a sol-gel approach for the preparation of the ternary ferrite. The prepared spinel ferrite characteristics were examined by the electrochemical, SEM, and XRD study. The development of the single-phase (spinel) in the prepared sample was assured by the XRD. The porous structure with micropores that enables the transfer of electrolyte ions was confirmed by SEM micrographs. For the prepared sample at 5 mV s^{-1}, superb C$_s$ were perceived to be 221 F g^{-1} with excellent P and E to be 1711 kW kg^{-1} and 7.9 Wh kg^{-1} respectively [134].

V. Manikandan et al. (2016) had utilized a facile co-precipitation procedure for the preparation of Sn doped CuFe$_2$O$_4$ at different temperatures. It was perceived that the particle size grew as the sintering temperature rose, according to XRD analysis. There is a decrement in the lattice parameter with the enhancement in the temperature as well as doping. The polycrystalline nature is confirmed by the superimposition of bright spots in the SAED pattern of TEM data. The two sharp absorption bands were noticed for the prepared samples in the FTIR and assert the spinel phase. In the 100 KHz to 700 MHz frequency, the prepared samples exhibit a loss and fluctuation in the dielectric constant [135].

K. Praveena et al. (2016) had employed a minimal cost sol-gel approach to preparing the Ni$_{0.4}$Zn$_{0.2}$Mn$_{0.4}$Fe$_2$O$_4$ NPs. All of the samples had grain sizes ranging from 18 to 30 nanometers. The hysteresis loops indicate a high saturation magnetization and low coercivity, indicating that the material is magnetically soft. Permittivity's imaginary and real constituents are almost constant up to 1 GHz, then rise as the frequency is increased. The permeability is governed by Snoek's law, which states that the value of μ′ increases as the temperature rises, and the resonance frequency rises as well. The reflection coefficient, on the other hand, rises with sintering temperature, with the largest loss occurring in the 100 MHz-1 GHz region. The largest reflection loss in the sample sintered at 700 ^{o}C is due to absorption, destructive interference, and many internal reflections in the sample. For all the samples sintered at different temperatures, the quality factor is constant up to 380 MHz and rises with frequency [136].

G. Chandra et al. (2016) had utilized the sol-gel process to synthesize $CoFe_2O_4$ nanoparticles of various sizes. Mossbauer spectroscopy, VSM, TEM, and XRD, were employed for the examination of the magnetic and structural characteristics. The decrement in the H_c and enhancement in the M_s (53 to 85 emu g^{-1}), M_r, and particle size were perceived with the enhancement in the temperature. The ferri-magnetic character of all the samples is shown by Mossbauer spectra. Owing to the Mossbauer research, the prepared $CoFe_2O_4$ stoichiometry was estimated to be $(Co^{2+}_xFe^{3+}_{1-x})[Co^{2+}_{1-x}Fe^{3+}_{1+x}]O_4$. As the sintering temperature rises, the inverse spinel structure progressively converts into the conventional spinel structure [137].

D. Zha et al. (2015) had employed a simple two-step approach to preparing $MnFe_2O_4$-Carbon black-PANI NC. The prepared NC at the 5 A g^{-1} manifests superb capacitive retention of 80 % after 10,000 cycles and at 40 A g^{-1} excellent capability rate of 98 %. Furthermore, this synthesized NC have outstanding C_s, P, and E all of which accounts for its usage as a minimal cost SC material for working electrode [138].

R. Tholkappiyan et al. (2015) had successfully prepared manganese cobaltite nanoparticles under two distinct circumstances. To affirm the phase (spinel) and purity of the prepared sample FTIR and XRD were employed. The elemental analysis and composition of the prepared samples were examined with the XPS. FESEM manifests the sponge-like and flake-like morphology of the Mn (C-C) and Mn (C-H) respectively. The nonporous characteristics of the prepared sample were investigated employing the BET. The two factors viz. state and shape of the prepared material are highly responsible for its electrochemical activity. Because of its flake-like shape, EIS spectra suggest that hydrothermally synthesized $MnCo_2O_4$ has a reduced diffusion resistance. $MnCo_2O_4$ synthesized by a controlled synthesis process has superior capacitance performance and is regarded as a favorable material for the SC as per the electrochemical results [139].

P. Liu et al. (2015) had focused on preparing the Mn-doped spinel ferrite and its usage as a catalyst. The prepared sample, cationic distribution, and structural characteristics were examined by employing TG-DSC, XPS, Raman, and XRD. The temperature-programmed reduction was employed for estimating the decline in the catalytic activity of the prepared sample. The Mn doping enhances the O_2 content of the lattice, accelerates ferrite reduction, and improves the oxidative activity of the Mn and Fe catalyst's surface. In the presence of water vapour, the investigated catalyst exhibits great stability and superior activity, which is

of practical importance. In light of the fluctuation in the physicochemical and microstructural characteristics of the prepared ferrite, the impact of the Mn doping on formaldehyde oxidation was explored [140].

P. Xiong et al. (2014) had worked in successfully synthesizing $CoFe_2O_4$, graphene, and PANI ternary nanocomposites by a two-step approach. The prepared sample characteristics were examined by employing the electrochemical, FESEM, TGA, XPS, and XRD study. The prepared NC at 2 A g^{-1} manifests superb C_s of 1133.3 F g^{-1} and magnificent capacitance retained (96.6 %) beyond 5000 cycles. At 2 A g^{-1} the NC exhibits excellent P and E of 3776.1 W kg^{-1} and 21.5 Wh kg^{-1} respectively [141].

F. Cai et al. (2014) had exploited a facile co-deposition approach for the preparation of 1-D nano-sheets of $NiCo_2O_4$-CNT. The hydroxide nano-sheet precursor was then thermally transformed into $NiCo_2O_4$ nano-sheets, with the overall shape and structure being preserved throughout the process. For $NiCo_2O_4$, the CNT acts as a conducting substrate, thereby resulting in an excellent electrochemical activity. The prepared sample at 0.5 A g^{-1} manifests superb C_s of 1038 F g^{-1} and has capacitive retention of 100 % after 1000 cycles. Moreover, a substantial amount of $NiCo_2O_4$ was deposited onto CNT which makes it favorable for SC [142].

H. Bahiraei et al. (2014) had utilized a sol-gel procedure for the production of MgCuZn ferrite at different temperatures. The magnetic and structural characteristics of the prepared samples were examined at various temperatures. The development of the single-phase (spinel) was assured by the XRD. Microstructural examinations revealed homogenous grains and suggested that sintering temperature change had a substantial impact on the elongation of the grain and density of the prepared specimen. For the prepared samples, with the increment in the sintering temperature, the enhancement in the M_s, permeability, grain size, and density was manifested [143].

R. P. Patil et al. (2013) had exploited the sol-gel approach to prepare $ZnFe_2O_4$, $ZnMnO_4$, $ZnCrO_4$, and $ZnTiO_4$. The development of the tetragonal (by doping Mn) and spinel (by doping Ti and Cr) phase was avowed by the XRD. The two sharp absorption peaks in the wavenumber ranging from 400-800 cm^{-1} in the FTIR ratify the development of the spinel structure. The agglomerated spherical-shaped particles were perceived in the FESEM for all

the prepared specimens. EDX validates the initial composition utilized in the synthesis. VSM revealed the ferromagnetic characteristics of the prepared samples [144].

M. Rahimi et al. (2013) had utilized a sol-gel approach for the preparation of $Ni_{0.3}Zn_{0.7}Fe_2O_4$ ferrite NPs. The prepared sample's magnetic and structural characteristics are highly influenced by the temperature (sintering). The development of the single-phase in the prepared samples was ratified by the XRD. The typical crystallite size was estimated to be between 13 and 58 nm. As crystallite size, the M_s also enhances, whereas H_c first inclined and then declined, according to magnetic investigations of sintered samples at various temperatures. The findings of AC susceptibility studies on $Ni_{0.3}Zn_{0.7}Fe_2O_4$ NPs reveal that the NPs interaction (magnetic) may cause superspin glasses-like behavior [145].

V. S. Kumbhar et al. (2012) had employed a facile chemical procedure to make a thin $CoFe_2O_4$ coating on an SS substrate. The formation of $CoFe_2O_4$ spinel ferrite was confirmed by XRD and FTIR. The nanostructured morphology provides a high surface area which is very helpful for super capacitance. The C_s were observed to be 366 F g^{-1} which might be useful for the energy storage SC [146].

R. P. Patil et al. (2012) had employed the sol-gel process was to prepare Li-Cr ferrite NPs. The prepared samples had been sintered in the air at various temperatures. The magnetic and structural characteristics of the prepared samples were examined by employing P-E loop tracer, FTIR, RAMAN, TEM, SEM, and XRD. The development of the single-phase (spinel) in all the prepared samples was avowed by the XRD. The morphology of the produced specimens was ratified by the TEM and SEM. As per the FTIR and RAMAN, the single-phase development arises at a higher temperature [147].

M. F. Al-Hilli et al. (2011) had adopted a typical chemical solid reaction approach, to prepare $(Li_{0.5}Fe_{0.5})_{0.5}Ni_{0.5}Gd_yFe_{2y}O_4$. The microstructure was studied in relation to sintering temperature. The prepared samples exhibit the development of the single-phase (spinel) as per the XRD spectra. A higher doping concentration of Gd in the grain may limit grain development. However, temperature (sintering), has a substantial influence on the size of the grain as per the SEM. It was noticed that the co-efficient of Seebeck, which would have been computed utilizing thermal electromotive force values, is negative. It shows that n-type charge carriers are the majority, implying that electron hopping is the primary method of

conduction. The resistivity rose as the Gd substitution increased, but it reduced dramatically when the sintering temperature climbed [148].

M. P. Reddy et al. (2010) utilized the traditional mixed oxide approach for the production of $Mg_{0.35}Cu_{0.05}Zn_{0.60}Fe_2O_4$ and $Ni_{0.35}Cu_{0.05}Zn_{0.60}Fe_2O_4$. At 900 and 950 ^oC, the prepared $Mg_{0.35}Cu_{0.05}Zn_{0.60}Fe_2O_4$, and $Ni_{0.35}Cu_{0.05}Zn_{0.60}Fe_2O_4$ respectively have high densities. Both ferrite sample's SEM appears to be almost identical. At all sintering temperatures, the prepared $Mg_{0.35}Cu_{0.05}Zn_{0.60}Fe_2O_4$ would have a high permeability than its counterparts which is on account of the reduction of magnetostrictive and magnetocrystalline constant of $Mg_{0.35}Cu_{0.05}Zn_{0.60}Fe_2O_4$. Because $Ni_{0.35}Cu_{0.05}Zn_{0.60}Fe_2O_4$ have a larger magnetic moment than $Mg_{0.35}Cu_{0.05}Zn_{0.60}Fe_2O_4$, they have a higher M_s. The produced material was favorable for the multilayer chip indicator, based on their findings [149].

P. P. Hankare et al. (2009) had utilized the co-precipitation technique to synthesize $Mg_{0.5}Ni_{0.5}Fe_2O_4$ at a temperature of 110 °C and a pH of 9.5 to obtain a high particle surface area. The powdered materials that resulted were sintered at various temperatures. The prepared sample's structural characteristics were examined by employing the SEM, XRD, and TGA. The high intense peak (311) for the prepared samples is perceived by the XRD patterns. With the enhancement in the temperature (sintering), the enhancement in the peak intensity was avowed by the XRD. With the temperature (sintering), the particle size and M_s were enhanced and ratifies by the SEM and VSM respectively [150].

H. Su et al. (2009) had employed the traditional mixed oxide process to prepare $Mg_{0.4}Cu_{0.2}Zn_{0.4}Fe_{1.96}O_4$ and $Ni_{0.4}Cu_{0.2}Zn_{0.4}Fe_{1.96}O_4$. Both types of ferrite samples attained sufficient density when sintered at 900 °C. Owing to the low weight (atomic) of Mg in contrast to the Ni, the density of $Mg_{0.4}Cu_{0.2}Zn_{0.4}Fe_{1.96}O_4$ ferrite was lower. The microstructures of these two types of ferrite samples did not differ significantly. At all sintering temperatures, the prepared $Mg_{0.35}Cu_{0.05}Zn_{0.60}Fe_2O_4$ would have a high permeability than its counterparts which is on account of the reduction of magnetostrictive and magnetocrystalline constant of $Mg_{0.35}Cu_{0.05}Zn_{0.60}Fe_2O_4$. The contents of Fe^{3+} and Fe^{2+} in the prepared samples really do not tend to be influenced by Mg^{2+} or Ni^{2+}, there were no significant variations in permittivity between the two types of ferrite samples [151].

S. D. Bhame et al. (2008) had investigated the magnetostrictive characteristics of polycrystalline cobalt ferrite produced by the traditional ceramic process in relation to the

sintering temperature and dwell duration. The amount of magnetostriction is highly influenced by the microstructure of the final sintered product, according to the findings of this study. The magnetostrictive strain is increased when tiny, homogeneous grains with a less porous structure are present in the sintered material. For samples sintered at a lower temperature of 1100 ^{o}C, higher magnetostriction is produced. These findings are further supported by an examination of the microstructural and magnetostrictive characteristics of various additives during sintering [152].

2.2. Research Gaps

After surveying numerous pieces of literature in the field of the spinel ferrite for energy storage supercapacitors (SCs), a few research gaps were noted and stated below:

(a) Most of the spinel ferrites utilized as an active material for SC electrodes were synthesized by the conventional solid-state method, co-precipitation method, hydrothermal method, etc. but very few researchers had synthesized spinel ferrite by facile sol-gel auto combustion method.

(b) The spinel ferrite prepared in most of the literature consists of the two divalent metal cations but spinel ferrite consisting of more than two divalent cations are rarely synthesized for energy storage application.

(c) In order to enhance the electrochemical activity of the spinel ferrite material, several nanocomposites (NCs) with carbon material or conducting polymer polyaniline (PANI) can be prepared. In contrast with the carbon material, the PANI-based spinel ferrite NC was very less explored for the SC electrode material.

(d) The literature regarding the spinel ferrite-PANI NC, used for energy storage SC or many other applications had been produced utilizing an in-situ polymerization procedure, whereas the blending procedure was very less exploited.

(e) In most of the literature, the values of power density (P), energy density (E), and specific capacitance (C_s) for spinel ferrite and with conducting polymer PANI NCs were found to be very low, which has to be improved for high-performance energy storage SCs.

To beat these above research gaps, my present research objectives focus on exploring the best possible spinel ferrite material and synthesizing its NC with the conducting polymer PANI using facile techniques for energy storage application. More emphasis is given to preparing the bulk amount, eco-friendly, easy availability, and minimal cost NC material for the welfare of the society.

2.3. Objectives of the Present Work

The main aim and objectives of the study of the present research are:

(a) To synthesis spinel ferrite nano-materials and nanocomposite with conducting material.

(b) To study the effect of metal cation substitution on structural, morphological, and magnetic properties of spinel ferrite.

(c) To investigate the variation in the properties of the doped spinel ferrite with temperature.

(d) To study electrochemical properties of doped spinel ferrite and its conducting nanocomposite for better-performance energy storage devices.

CHAPTER-3

Method of Synthesis

The synthesis method plays an important role in the production of spinel ferrite, polyaniline (PANI), and spinel ferrite-PANI nanocomposite (NC). Various well-known properties of the spinel ferrite viz. structural, morphological, magnetic, and electrochemical were highly influenced by the synthesis methodology utilized. However, these above properties also have a greater impact on the composition, type of the dopant used, and sintering temperature of the prepared material. For the preparation of the conducting PANI, an appropriate selection of dopant, oxidant, and synthesis techniques is required. For preparing the NC (spinel ferrite-PANI) a facile and quick synthesis procedure should be chosen for excellent entanglement of PANI with spinel ferrite nanoparticles (NPs). Furthermore, for the supercapacitor electrode preparation, the electrochemical performance of the prepared materials relies heavily on the type of the substrate, binder, conducting material, and electrolyte utilized. As discussed earlier in chapter 1, about the best synthesis techniques out of the several known techniques, the sol-gel auto combustion, chemical oxidative polymerization (COP), and physical blending have been employed for the synthesis of the spinel ferrite, PANI, and spinel ferrite-PANI NC respectively. The detailed procedures for the preparation of the materials by these above-selected techniques along with the properties to be studied are discussed below one by one in the form of a table.

3.1. Synthesis of Zinc Doped Magnesium Spinel Ferrite
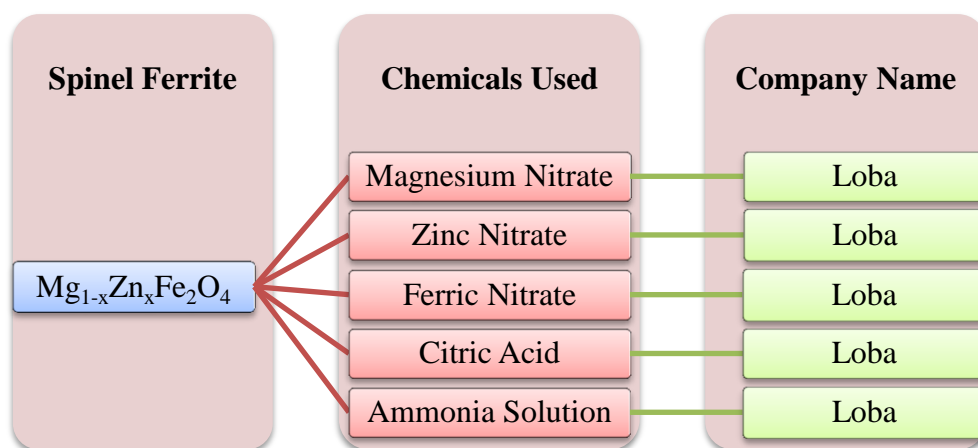
Fig. 3.1. Chemicals along with their company for $Mg_{1-x}Zn_xFe_2O_4$ preparation.

For the preparation of $Mg_{1-x}Zn_xFe_2O_4$ (x = 0.0, 0.2, and 0.4), AR grade chemicals were utilized as illustrated in Fig. 3.1, and the detailed steps for the preparation of spinel ferrite along with the properties studied using various characterization techniques are mentioned in Table 3.1.

Table 3.1. Detailed procedure for the synthesis of $Mg_{1-x}Zn_xFe_2O_4$.

Material name: Zinc doped magnesium spinel ferrite				
Chemical formulae: $Mg_{1-x}Zn_xFe_2O_4$		**Synthesis method:** Sol-gel method		
Cations to citric acid ratio: 1:1		**Doping concentration (x):** 0.0, 0.2, and 0.4		
Molar ratio of Mg:Zn:Fe = 1-x:x:2				
Chemicals used		$Mg(NO_3)_2 \cdot 6H_2O$	$Zn(NO_3)_2 \cdot 6H_2O$	$Fe(NO_3)_3 \cdot 9H_2O$	Citric acid (Anhydrous)
Mol. Wt. (in g)		256.41	297.48	404	192.13
Chemicals amount used (in g)	**x = 0.0**	12.82	0.00	40.40	28.81
	x = 0.2	10.25	2.97	40.40	28.81
	x = 0.4	7.69	5.94	40.40	28.81
Amount of distilled water used for mixing nitrates & citric acid: 100 ml				
Time for which magnetic stirrer is used to obtain a clear solution: 30 min.				
Solution used to balance pH: Ammonia solution				
pH is maintained: 7				
Magnetic stirring and heating are given to make gel: For 4-5 h at 100 ^oC				
Only heating is given to gel for auto combustion process: For 1 h at 100 ^oC				
Further heating of the as burnt powder to form a fluffy powder: For 8-10 h at 80-100 ^oC				
Sintering in muffle furnace is done: For 6 h at 800 ^oC				
Grinding of the powder is done by using a mortar & pestle				
Properties studied: Structural (XRD and FTIR), Morphology (FESEM), Elemental (EDX), and Magnetic (VSM)				

3.2. Synthesis of Manganese Doped Cobalt-Zinc Spinel Ferrite

For the production of $Mn_xCo_{0.5-x}Zn_{0.5}Fe_2O_4$ (x = 0.0, 0.1, 0.2, 0.3, and 0.4), AR grade chemicals were utilized as manifested in the Fig. 3.2. Table 3.2 lists the detailed processes for producing spinel ferrite, as well as the properties studied employing several characterization techniques.
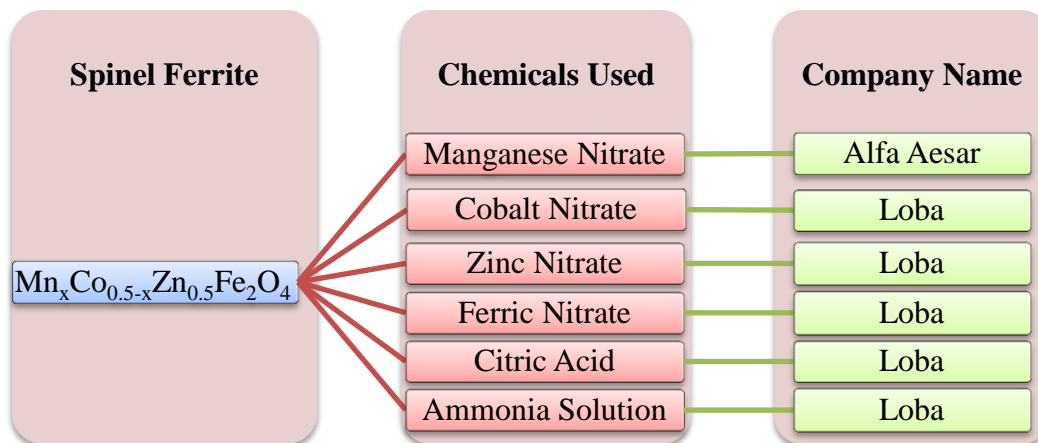
Fig. 3.2. Chemicals along with their company for $Mn_xCo_{0.5-x}Zn_{0.5}Fe_2O_4$ preparation.

Table 3.2. Detailed procedure for the synthesis of $Mn_xCo_{0.5-x}Zn_{0.5}Fe_2O_4$.

Material name : Manganese doped cobalt zinc spinel ferrite					
Chemical formulae: $Mn_xCo_{0.5-x}Zn_{0.5}Fe_2O_4$		**Synthesis method:** Sol-gel method			
Cations to citric acid ratio: 1:1		**Doping concentration (x):** 0.0, 0.1, 0.2, 0.3, and 0.4			
Molar ratio of Mn:Co:Zn:Fe = x:0.5-x:0.5:2					
Chemicals used		$Mn(NO_3)_2$ $\cdot 6H_2O$	$Co(NO_3)_2$ $\cdot 6H_2O$	$Zn(NO_3)_2$ $\cdot 6H_2O$	$Fe(NO_3)_3$ $\cdot 9H_2O$	Citric acid (Anhydrous)
Mol. Wt. (in g)		287.04	291.03	297.48	404	192.13
Chemicals amount used (in g)	**x = 0.0**	0.00	2.91	2.96	16.16	11.52
	x = 0.1	0.57	2.33	2.96	16.16	11.52
	x = 0.2	1.14	1.74	2.96	16.16	11.52
	x = 0.3	1.72	1.16	2.96	16.16	11.52
	x = 0.4	2.28	0.58	2.96	16.16	11.52
Amount of distilled water used for mixing nitrates & citric acid: 100 ml					
Time for which magnetic stirrer is used to obtain a clear solution: 30 min.					
Solution used to balance pH: Ammonia solution					
pH is maintained: 7					
Magnetic stirring and heating are given to make gel: For 4-5 h at 100 ^{o}C					
Only heating is given to gel for auto combustion process: For 1 h at 100 ^{o}C					
Further heating of the as burnt powder to form a fluffy powder: For 8-10 h at 80-100 ^{o}C					
Sintering in muffle furnace is done: For 6 h at 1200 ^{o}C					
Grinding of the powder is done by using a mortar & pestle					
Properties studied: Structural (XRD and FTIR), Morphology (FESEM), Elemental (EDX), and Magnetic (VSM)					

3.3. Synthesis of $Mn_{0.3}Co_{0.2}Zn_{0.5}Fe_2O_4$ at Different Sintering Temperatures

AR grade chemicals have been used to prepare $Mn_{0.3}Co_{0.2}Zn_{0.5}Fe_2O_4$, as shown in Fig. 3.3, and the detailed procedures for the production of spinel ferrite, as well as the characteristics evaluated using different characterization techniques, are included in Table 3.3.
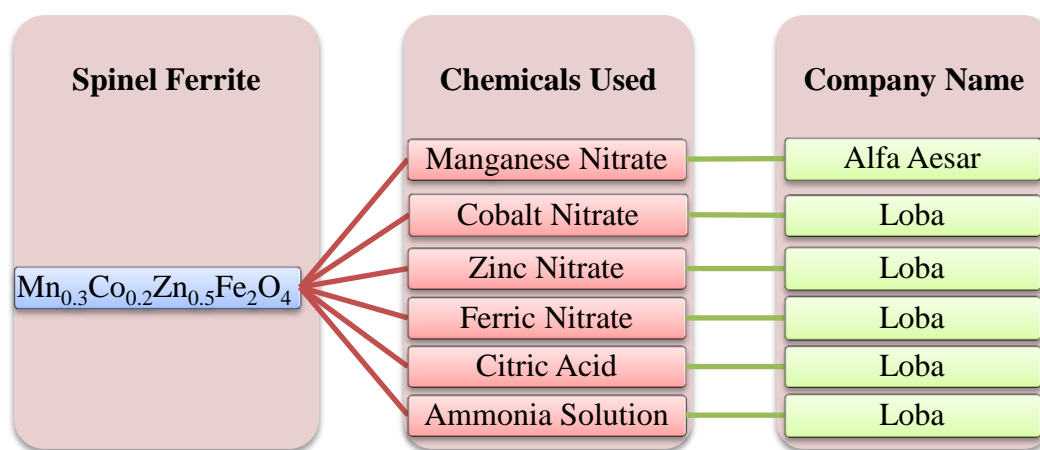
Fig. 3.3. Chemicals along with their company for $Mn_{0.3}Co_{0.2}Zn_{0.5}Fe_2O_4$ preparation.

Table 3.3. Detailed procedure for the synthesis of $Mn_{0.3}Co_{0.2}Zn_{0.5}Fe_2O_4$.

Material name: Manganese cobalt zinc spinel ferrite					
Chemical formulae: $Mn_{0.3}Co_{0.2}Zn_{0.5}Fe_2O_4$		**Synthesis method:** Sol-gel method			
Cations to citric acid ratio: 1:1		**No. of sintering temperatures:** 3			
Chemicals used	$Mn(NO_3)_2$ $\cdot 6H_2O$	$Co(NO_3)_2$ $\cdot 6H_2O$	$Zn(NO_3)_2$ $\cdot 6H_2O$	$Fe(NO_3)_3$ $\cdot 9H_2O$	Citric acid (Anhydrous)
Mol. Wt. (in g)	287.04	291.03	297.48	404	192.13
Chemicals amount used (in g)	1.72	1.16	2.96	16.16	11.52
Amount of distilled water used for mixing nitrates & citric acid: 100 ml					
Time for which magnetic stirrer is used to obtain a clear solution: 30 min.					
Solution used to balance pH: Ammonia solution					
pH is maintained: 7					
Magnetic stirring and heating are given to make gel: For 4 h at 120 ^{o}C					
Only heating is given to gel for auto combustion process: For 1 h at 100 ^{o}C					
Further heating of the as burnt powder to form a fluffy powder: For 8-10 h at 80-100 ^{o}C					
Sintering in muffle furnace is done: For 4 h at 750, 950, and 1150 ^{o}C					
Grinding of the powder is done by using a mortar & pestle					
Properties studied: Structural (XRD and FTIR), Morphology (FESEM), Elemental (EDX), and Magnetic (VSM)					

3.4. Synthesis of Polyaniline (PANI)

The chemical oxidative polymerization (COP) approach, in which polymerization and doping occur concurrently, was used to make conducting polyaniline (PANI). The diagrammatic representation for preparing PANI is displayed in chapter 1 (Fig. 1.15). PANI has three reactants in the COP technique: aniline (monomer), ammonia persulphate (oxidant), and hydrochloric acid (dopant or acidic medium). Aniline (0.5 M) was dispersed in 40 ml of HCl (1 M) to make the PANI. The dispersed solution was agitated in an ice bath to establish a homogenous suspension, and the procedure was repeated for 2 h until anilinium ions were formed. The ammonia persulphate solution (APS) was made by combining 0.4 M ammonia persulphate with 60 ml HCl (1 M). The APS solution was added to the preceding solution drop-wise and stirred constantly in an ice bath for 5 h until the solution became green. The formation of the emeraldine salt (ES), which is PANI's conducting form, is indicated by the green colour. After that, the solution was stored in an ice bath overnight and the precipitates were vacuum filtered. Repeated washings with distilled water and HCl were used to remove the residues adhered to the precipitates. Finally, the PANI green precipitates were dried for 12 h in a hot air oven at 70 ^{o}C and then crushed with the assistance of a mortar and pestle to obtain a fine powder form of PANI as manifested in Fig. 3.4.

Fig. 3.4. Fine powdered PANI prepared by COP technique.

3.5. Synthesis of (Mn$_{0.3}$Co$_{0.2}$Zn$_{0.5}$Fe$_2$O$_4$-PANI) Nanocomposite

A physical blending process as presented in Fig. 3.5 was used to make the Mn$_{0.3}$Co$_{0.2}$Zn$_{0.5}$Fe$_2$O$_4$-PANI nanocomposite. The weight ratio of Mn$_{0.3}$Co$_{0.2}$Zn$_{0.5}$Fe$_2$O$_4$:PANI was chosen at 1:5, and the nanocomposite was physically mixed using a mortar and pestle to achieve a homogeneous mixture.
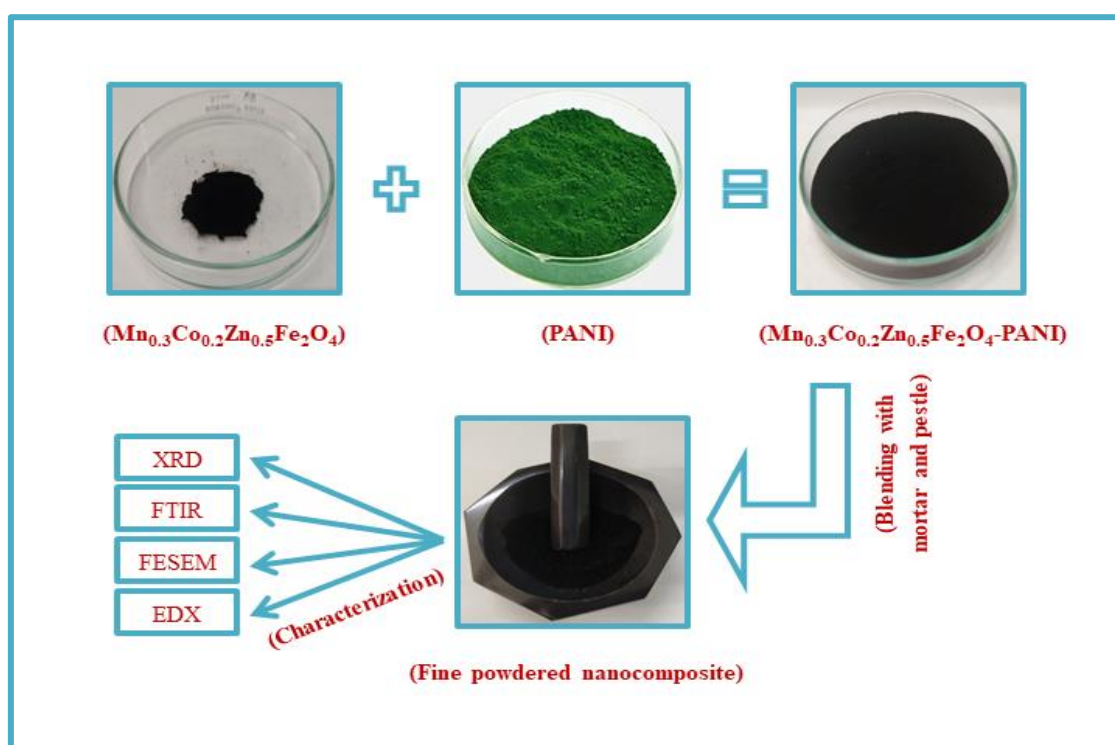
Fig. 3.5. Physical blending process for the production of the nanocomposite.

3.6. Fabrication of Electrochemical Electrode

A three-electrode apparatus was used to conduct the electrochemical examination at room temperature. The working electrode (ink-loaded nickel foam), reference electrode (Ag/AgCl), and counter electrode (platinum wire) were the three electrodes used. The experiment was carried out with 3 M KOH as the electrolyte. To remove the nickel oxide layer, nickel foam (1 cm $\times$ 1 cm) was sonicated in 3 M HCl at 50 ^{o}C for 1 h before being used as a working electrode and manifested in Fig. 3.6. The nickel foam was then repeatedly rinsed with ethanol and distilled water before being dried at 60 ^{o}C for 3 h. Mn$_{0.3}$Co$_{0.2}$Zn$_{0.5}$Fe$_2$O$_4$-PANI nanocomposite (70 Wt. %), acetylene black (20 Wt. %), and polyvinylidene fluoride (PVDF) (10 Wt. %) were used to make the ink, which is to be drop cast on the nickel foam, with n-methyl-2-pyrrolidone (NMP) as a solvent. The ink-soaked

nickel foam was dried for 12 h at 60 $^{\circ}$C. For the relative investigation, the same procedures were used to set up the working electrodes of pure $Mn_{0.3}Co_{0.2}Zn_{0.5}Fe_2O_4$ and PANI as manifested in Fig. 3.7.
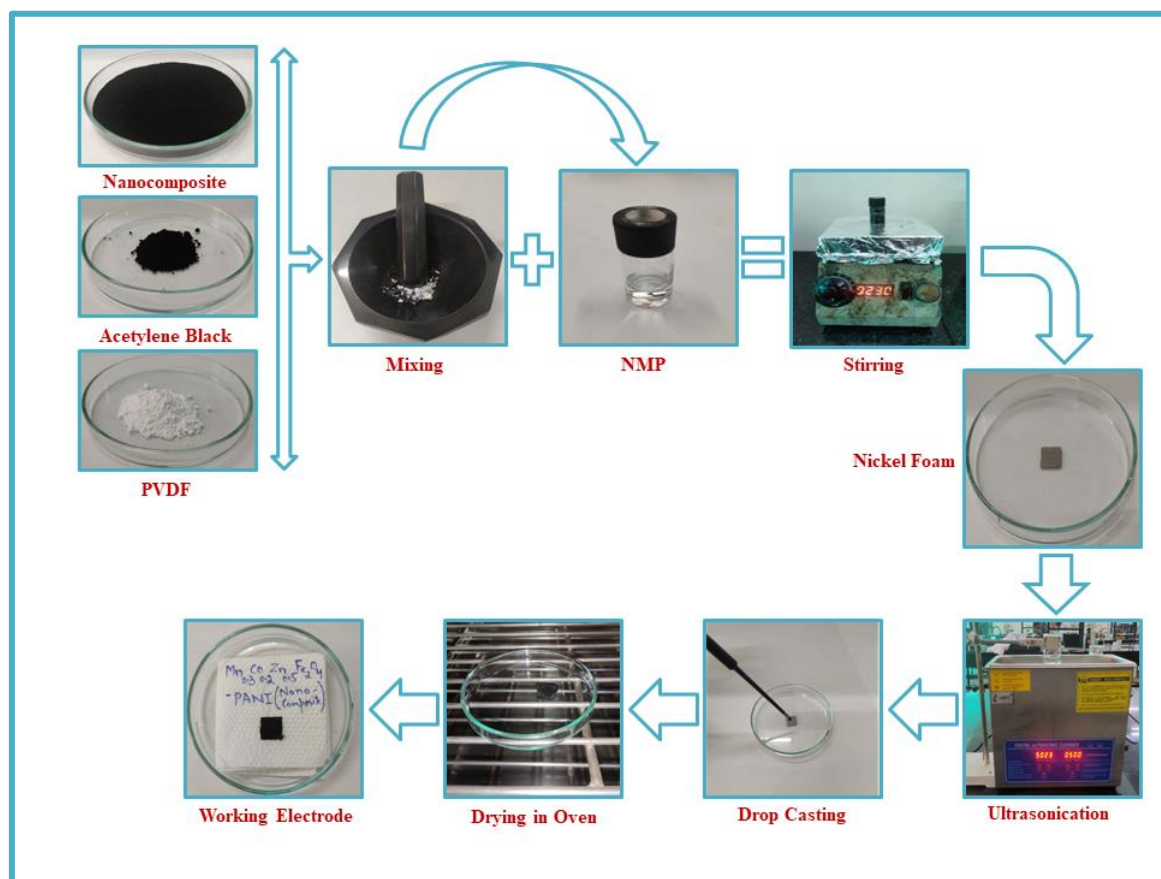
Fig. 3.6. Steps for the fabrication of the nanocomposite working electrode.
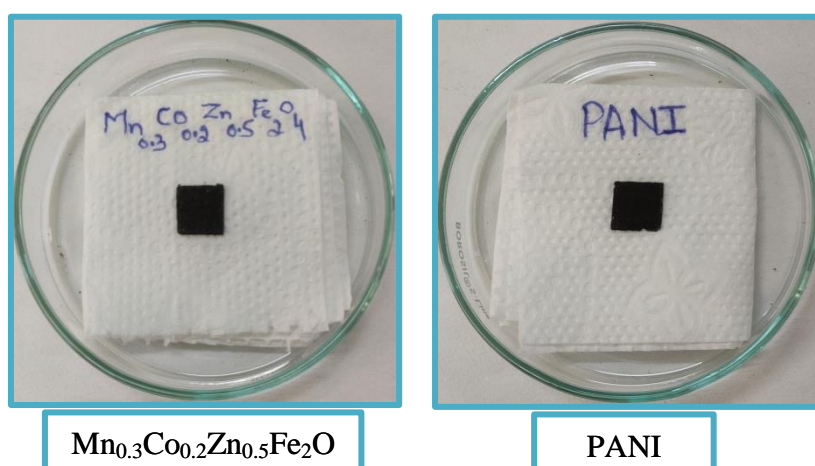
Fig. 3.7. Fabricated working electrode for pure $Mn_{0.3}Co_{0.2}Zn_{0.5}Fe_2O_4$ and PANI.

CHAPTER-4

Characterization Techniques

The structural, morphological, magnetic, and electrochemical characteristics of the produced samples were investigated utilizing the following characterization techniques.

4.1. X-Ray Diffraction (XRD)

X-ray diffraction (XRD) analysis is the most widely utilized analytic tool to determine the crystallinity of a prepared sample and gather information on the phase and dimensions of the unit cell of material [153]. Structure identification, lattice parameters, strain, preferred orientation, structural defect, epitaxy, and grain size of the materials can be determined by the XRD pattern. It is a non-contact and non-destructive, approach that uses the scattering of X-rays from long-range order structures to deliver meaningful information [154]. Due to enhanced detection techniques of X-rays, specific monochromators, and intense micro-focused X-ray beam, the XRD technique has been used to probe crystallite size which is limited to cases where the average crystallite size is ≤ 1 μm. The arrangement of the atoms at the interface (in multilayer) may be quantified as well as accurately determined using XRD intensity measurements [155]. The snapshot of the Bruker D8 Advance X-ray diffractometer is displayed in Fig. 4.1.
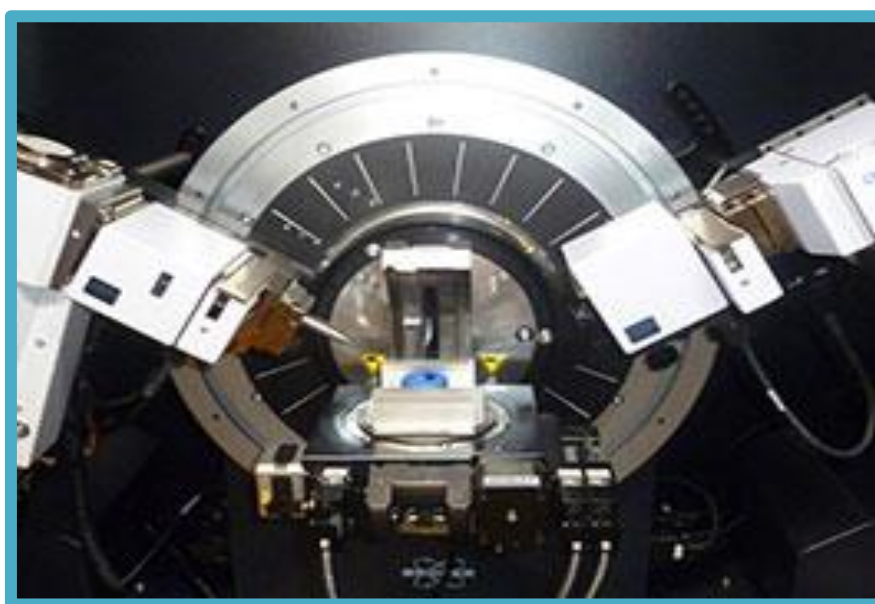
Fig. 4.1. Snapshot of Bruker D8 Advance XRD diffractometer [156].

Fig. 4.2 manifests a schematic of an XRD diffractometer, with the diffraction angle (2θ) representing the angle between diffracted and incident X-rays. The scanning of the X-ray wavelength up to 145° correlates to the energy of the X-ray beam. The XRD technique has been used by numerous researchers to examine the structural properties of powdered samples. In the XRD technique, a diffraction beam provided by chromator is diffracted from the film surface and detected by an oscillating detector around the mean diffraction position. The basic requirement of the XRD technique is monochromatic radiation since the interplanar spacing can be measured from a diffraction angle, according to Bragg's law as exhibited in Eq. (4.1) [157].

$$2d \sin (\theta) = n \lambda \hspace{4cm} (4.1)$$

Here d, θ, n, and, λ signify the interplanar spacing, Bragg's angle, order of the diffraction, and X-ray wavelength respectively. The X-ray powder diffraction data achieved from the diffractometer is compared with Joint Committee Powder Diffraction Standards (JCPDS) or American Standards for Testing of Materials (ASTM) to identify phases of materials [158]. The powder, single crystal, or thin-film sample can be identified by the XRD technique.
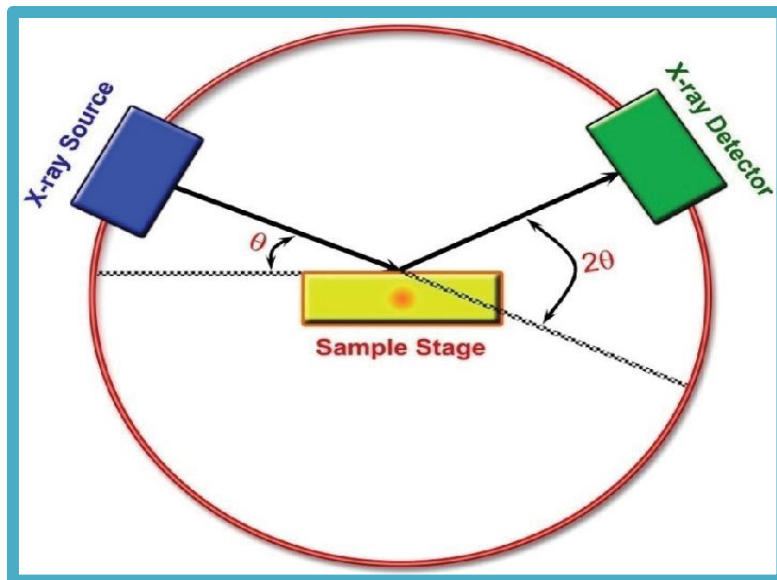
Fig. 4.2. Schematic diagram of XRD diffractometer [159].

Several grains or crystallites with a variety of orientations can be found in powder samples. If somehow the arrangement is entirely haphazard, any crystallite with the proper orientation and meets the diffraction criterion will cause diffraction. The beam of X-rays

which gets diffracted, forms cones with an angle of $2\theta_{hkl}$ around the incident beam, thereby forming a powdered diffracted pattern. Though, the XRD technique effectively investigates the structural properties e.g. structure of a material, lattice dimensions, crystallite size, etc. However, it is unable to determine quantitative compositional analysis.

4.2. Fourier Transform Infrared Spectroscopy (FTIR)

In order to determine the covalent bonds and functional group information of the prepared samples, Fourier-Transform Infrared Spectroscopy (FTIR) is an effective analytic technique. The spontaneous orientation of the dipole moment in materials is studied by the non-destructive tool using infrared spectroscopy that can provide information about inter-atomic forces within the crystal lattice. There are six different ways an organic/inorganic compound can vibrate: symmetrical and anti-symmetrical stretching, wagging, rocking, scissoring, and twisting [160]. FTIR spectrometer; of Perkin Elmer company is used for characterization and the ray diagram of the FTIR is displayed in Fig. 4.3.
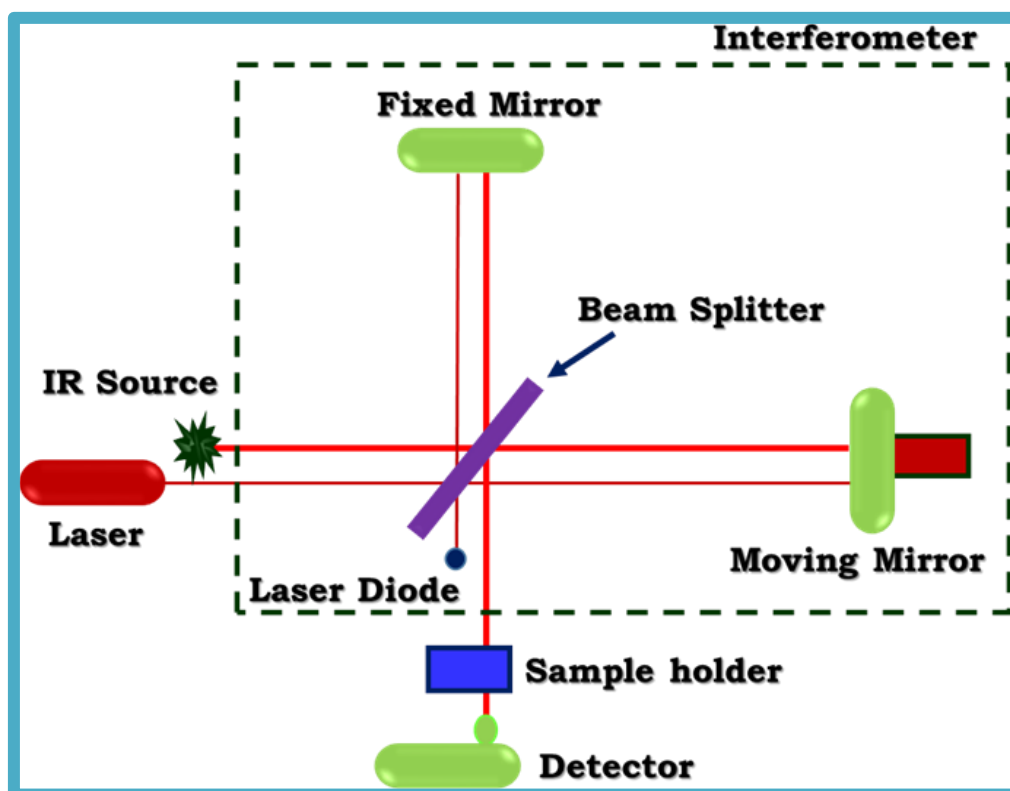
Fig. 4.3. Basic ray diagram of FTIR spectrometer [161].

The infrared vibrational frequencies and inter-atomic forces are correlated and so it is used to investigate functional groups in the material. According to the Planck-Einstein relation, energy transfer between different energy states of molecules can be written as the

following Eq. (4.2).

$$\Delta E = h\nu \qquad\qquad\qquad (4.2)$$

Here ΔE, h, and ν represent the change in energy, Planck constant, and frequency respectively. The positive ΔE means molecule absorbs energy; when ΔE is negative means it emits energy in form of radiation, and thus emission spectrum is obtained. When Eq. (4.2) is satisfied, an absorption spectrum is obtained, which is particular to a molecule under investigation. The spectrum is normally presented as an intensity plot versus frequency and absorption peaks obtain when Eq. (4.2) is satisfied. A spectrum close to a visible region (comparatively small portion) is used for spectroscopic investigations. This portion incorporates UV-VIS and IR regions (10 nm to 1 mm). The different absorption spectra can be observed from atoms and molecules, because of the nature of energy levels in transition. The transition of electrons between orbitals of atoms takes place due to the absorption of energy. However, the atoms vibrate in a molecule and it moves due to the absorption of energy [162]. A few transition energies such as rotational, vibrational, and electronic are possible to measure. Usually, translational energy can be ignored, since it is sufficiently small. The vibrational spectrum is believed to be a unique physical characteristic of molecules. Therefore, the IR spectrum is supposed as a fingerprint for the identification of material [163].

4.3. Field Emission-Scanning Electron Microscopy (FESEM)

In view of its versatility, field emission scanning electron microscopy (FESEM) is the most widely used microscopy technique. Its various imaging techniques and easy interpretation of images make visualize the specimen surface scanned by a focused high-energy electron beam [164]. The FESEM produces clear images, with low electrostatic distortion and spatial resolution of ~1 nm (that means 3-6 times better resolution than regular SEM.

Generally, electrons incident on atoms, and they produce signals which give information about the material's surface topography, elemental analysis, grain size, particle size, etc. [165]. In a vacuum, the electrons are created by the field emission source and accelerate in the field gradient. The bombardment resulted in a variety of emissions from the specimen. The detector captures the secondary electrons, which are useful for the generation of sample surface images. Fig. 4.4 illustrates the FESEM ray diagram. The ray diagram of emitted different types of electrons and X-rays during a scan is presented in Fig. 4.5. The

electron either goes away without any interaction or the electron is dispersed within the cloud with potential. The ejection of electrons from a specimen occurs due to the number of interactions of a specimen with an electron beam. This interaction involves the emission of Auger electrons, back-scattered electrons, secondary electrons, and elemental X-rays (shown in Fig. 4.5). Depending on energies, the secondary electrons and backscattered electrons are separated out. The detector collects secondary electrons and produces electrical signals; these electrical signals are amplified and converted into video scan images that can appear on the monitor screen as a digital image of a sample surface.
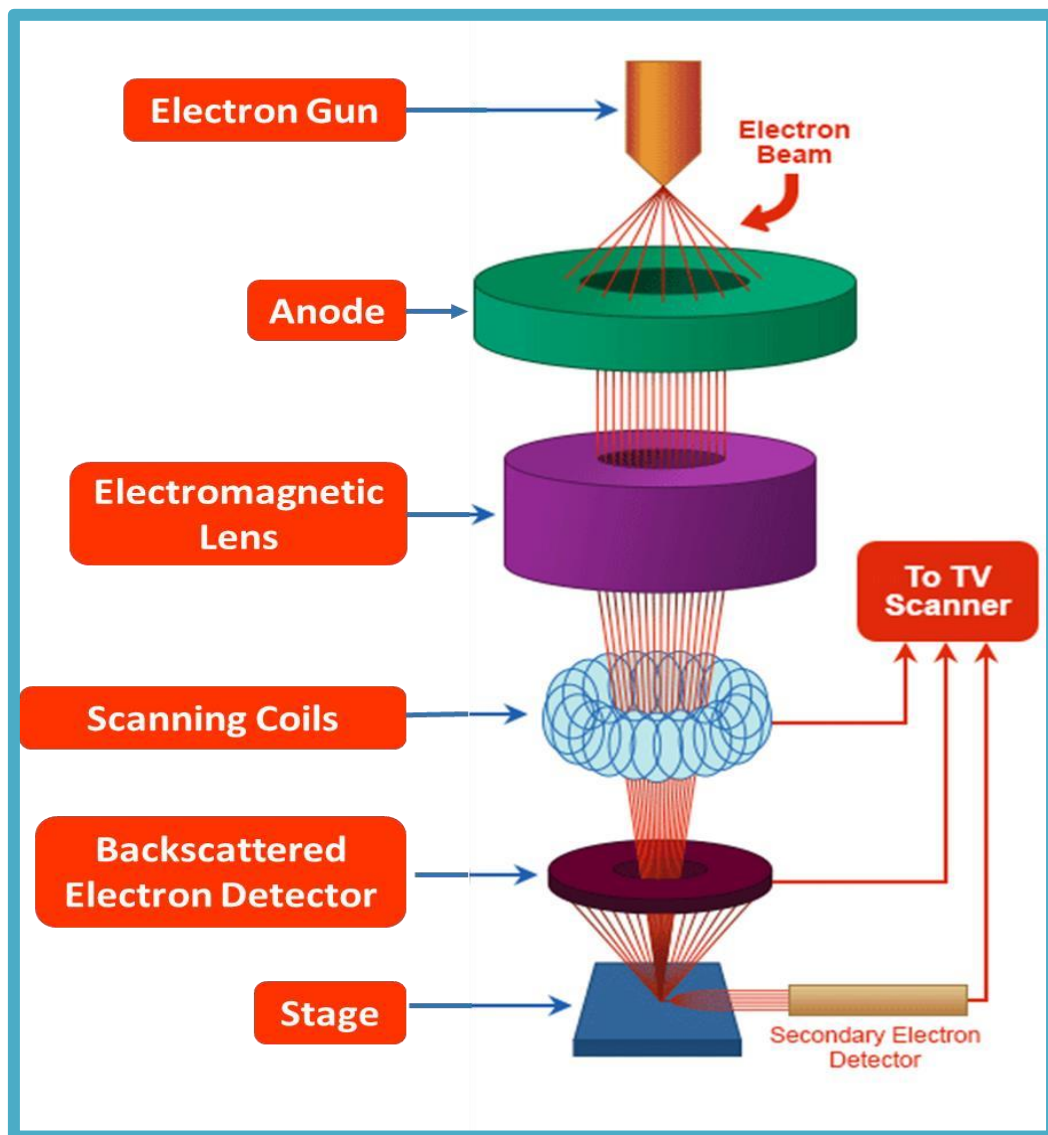
Fig. 4.4. Ray diagram of FESEM [166].

A highly energetic primary electron beam interacts in elastic and inelastic ways, providing a variety of signals. The kinetic energy of an electron does not affect even when its

59

trajectory has been changed, so it is called elastic scattering. However, in inelastic scattering, energy transfer to atoms in a sample from an electron beam, and reduces the energy of the electron with a smaller trajectory deviation. The electrons can leave the sample surface if the transmitted energy exceeds the work function of the test sample. If the energy of an emitted electron is lower than 50 eV, it is classified as a secondary electron. In most cases, secondary electrons are created from the sample's top layer. The emitted electrons that have energy above 50 eV are known as back-scattered electrons [167].
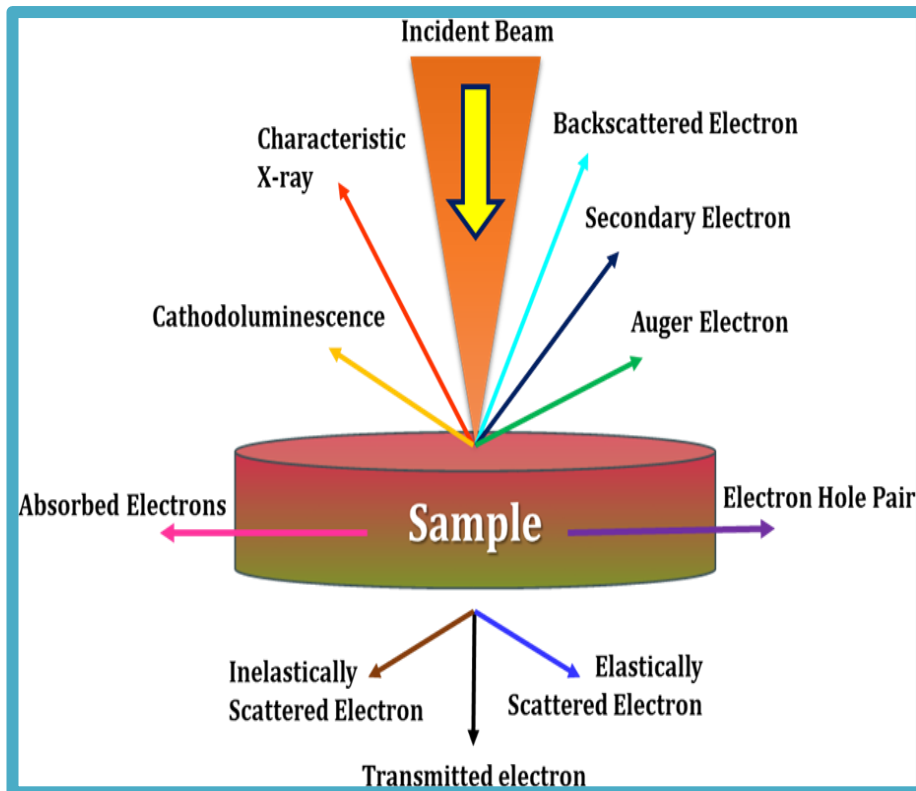
Fig. 4.5. Ray diagram for the emission of diverse forms of electrons during scanning [168].

Low voltage FESEM is used to measure the image without conductive coatings to prevent beam-induced damage to the surface [164]. FESEM equipment consists of the following components; excitation source (electron beam), detector, pulse processor, and analyzer, etc. Information about the underlying structure of the sample cannot be found by FESEM, because it is a surface analysis technique.

4.4. Energy Dispersive X-Ray Spectroscopy (EDX)

The elemental composition along with the stoichiometry of the specimen is determined by energy-dispersive X-ray spectroscopy (EDX or EDS). It's organized in

conjunction with FESEM. Spot analysis, line scanning, and qualitative X-ray mapping are some of the EDX applications. EDX has mainly based on the concept that a specific atomic structure of elements can exhibit a distinct set of peaks in its emission spectrum. The K, L, and M shells of the electron around an atom's nucleus are depicted schematically in Fig. 4.6.
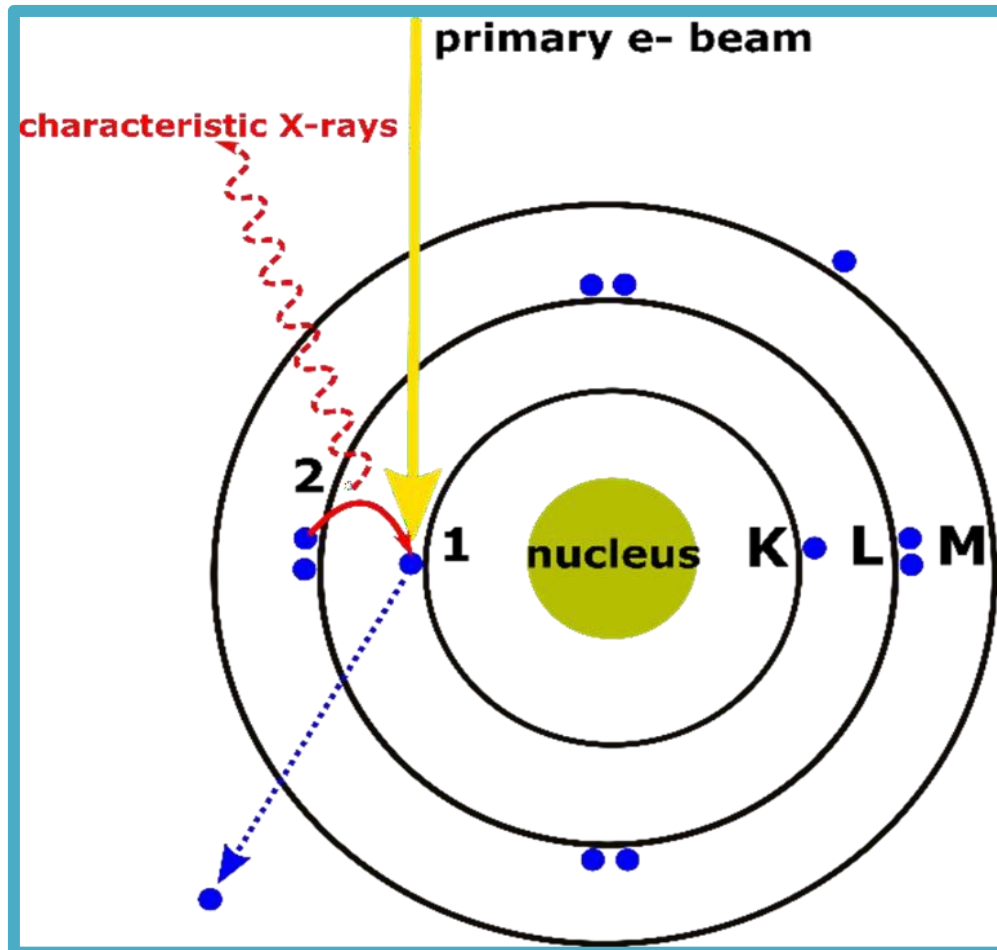
Fig. 4.6. A schematic representation of K, L, and, M electron shells around the nucleus of an atom [169].

To induce the emission of X-rays (characteristic), a high-energy beam of X-rays, or protons, or electrons are allowed to an incident on the sample. Initially, an atom in a specimen consists of unexcited electrons that are ground-state electrons at discrete energy levels. When an electron is incident and emits an electron from the inner shell, the outer shell electron fills the hole and releases energy in the form of X-rays [170]. The energy-dispersive spectrometer measures the energy and amount of X-rays emitted out of a sample. The X-ray emitted has the energy equal to the difference in the energy of the two shells in which electronic transitions undergo and this enables to identify of the elements present in

the test sample. The low detection limit varies from ~ 0.1 to several atomic percentages, depending on the element and sample matrix. An X-ray spectrometer can examine radiation and identify the test sample elements based on their wavelength (characteristic).

4.5. Vibrating Sample Magnetometer (VSM)

Using Faraday's law of electromagnetic induction, which says that a changing magnetic field generates an electric field, the Vibrating Sample Magnetometer (VSM) technique examines the magnetic response of the test sample. The sample under study is placed in a sample holder which is then placed in between two sets of pickup coils that are attached to an electromagnet as manifested in Fig. 4.7. Owing to the uniformity of the electromagnet's magnetic field, the magnetization will be induced in the test sample. The sample holder with the sample inside it is made to mechanically undergo sinusoidal vibration. When a vibrating component produces a change in the magnetic field of the sample, Faraday's law of electromagnetic induction generates an electric field corresponding to the magnetization. Magnetic flux changes induce a voltage in the pickup coils that is proportional to the sample's magnetization. Software in a computer attached to the VSM equipment converts these changes into a graph of magnetization (M) against the applied magnetic field (H) [171].
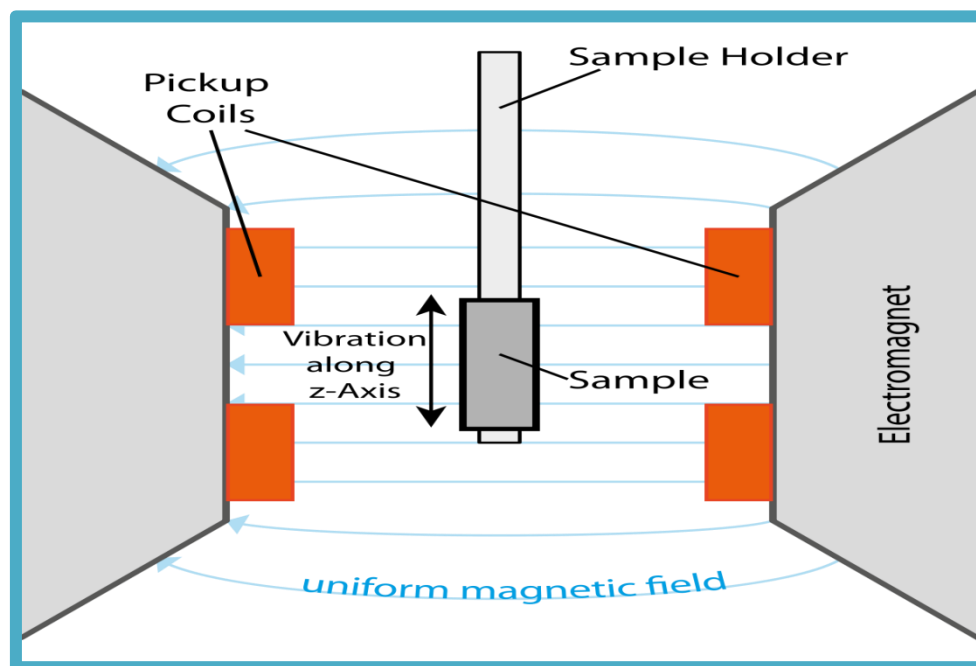
Fig. 4.7. Schematic diagram of VSM [172].

62

4.6. Electrochemical Techniques

Generally, the three-electrode (half-cell) system is used in electrochemical investigations to determine specific electrochemical properties of a material, while a two-electrode (full-cell) system is suggested for performance evaluation of supercapacitor (SC) device [173]. The three electrodes viz. working, reference and counter are immersed in an electrolyte in a half-cell. Fig. 4.8(a) illustrates a schematic of a three-electrode cell system. The electrochemical workstation controller monitors the current flowing from the counter to the working electrode by measuring the potential difference between working and reference electrodes. The resulting current is proportional to the voltage established between the working and the reference electrode, then transformed to a voltage by a current-to-voltage (I/E) converter and recorded by the data-acquisition system with regard to time. It is noted that the electrical resistance of an ideal electrometer should be large enough so that it has zero input current. Since, when current passes through a reference electrode, it can change actual potential which in turn affects the precision of data [174].

In the two-electrode (full-cell) systems, two working electrodes are sandwiched with a solid electrolyte and it acts as a separator. A schematic of a two-electrode configuration that is comparable to a packed SC cell and gives a better representation of the electrode's electrochemical performance in the device [173] is illustrated in Fig. 4.8(b). The working electrodes of the half-cells were double the potential window that was applied to the electrodes in the full cells at the specified potential window on the electrochemical system.
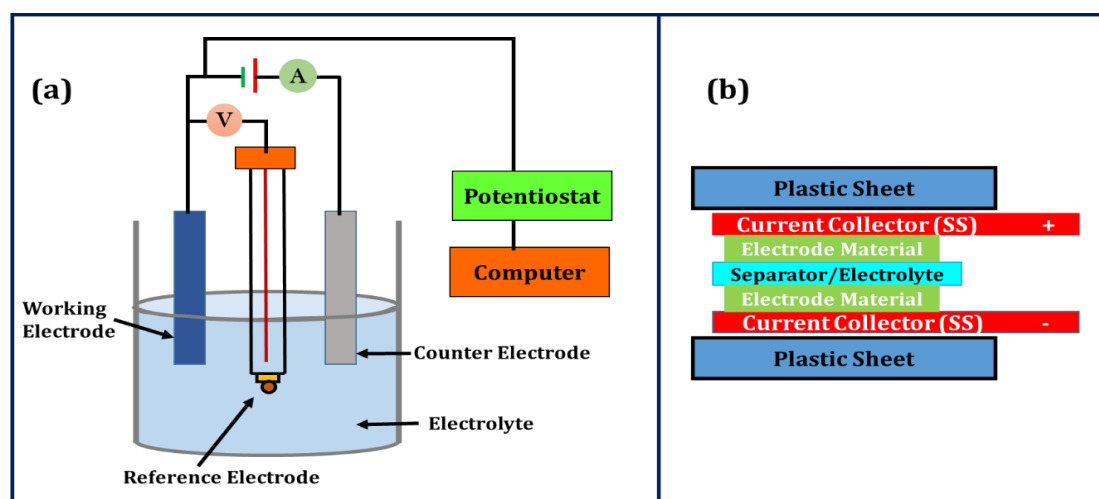
Fig. 4.8. Schematic diagram of (a) three-electrode electrochemical (half-cell) system and, (b) two-electrode (full-cell) systems [175].

The specific capacitance of two or three-electrode-based SCs is calculated by the following relation [111,176] mentioned in Eq. (4.3) and Eq. (4.4).

$$C_s = \frac{1}{m \times v \times \Delta V} \int_{V_i}^{V_f} I(V) dV \qquad \text{[For CV]} \qquad (4.3)$$

Here C_s, m, v, ΔV, and I(V) depict the specific capacitance, loaded mass, scan rate, potential window, and the current response respectively.

$$C_s = \frac{I_m \times \Delta t}{\Delta V} \qquad \text{[For GCD]} \qquad (4.4)$$

Here C_s, I_m, Δt, and ΔV represent the specific capacitance, current density, discharging time, and potential window respectively. The energy (E) and power density (P) of the supercapacitor can be calculated using Eq. (4.5) and Eq. (4.6) respectively [177].

$$E = \frac{1}{2} C_s \Delta V^2 \qquad (4.5)$$

$$P = \frac{E}{\Delta t} \qquad (4.6)$$

To attain the greatest value of specific E, SCs must have a large C_s and operational ΔV. However, the C_s and ΔV of an SC depend on working electrode material and electrolyte.

A number of techniques including CV, GCD, and EIS studies can be employed to probe the electrochemical capacitive performance of developed materials. For the utilization of the thin layer as an active electrode for supercapacitor devices, the electrochemical characteristics of the thin layer are significant.

4.6.1. Cyclic Voltammetry (CV)

Cyclic voltammetry (CV), commonly known as two-way linear sweep voltammetry (LSV), and is regarded as an electro-analytical method to examine the electrochemical activity of active material in an electrolyte solution for a supercapacitor (SC). As manifested in Fig. 4.9, it is a potentiodynamic approach in which the potential of the working electrode sweeps between two voltage limits at a constant voltage scan rate. It produces fundamental data viz. test sample stability, reversibility, charge transfer kinetics, specific capacitance (Cs), and redox behaviour [178].

Firstly, the selection of initial and final potential is a very significant factor for CV measurement. The three-electrode system is utilized to minimize the ohmic resistance. Between a working and reference electrodes, a potential is provided, and between working

and counter electrodes a current is monitored. The range of operating potentials (ΔV) for a CV in the different electrolytes can vary not only depending on electrode material but also on the composition of electrolytes. Furthermore, the operational ΔV of a working electrode is determined by the material's redox potential as well as the electrolyte's decomposition capacity. Generally, high current resulting from electrolyte oxidation causes a positive potential limit, whereas electrolyte reduction causes a negative potential limit.
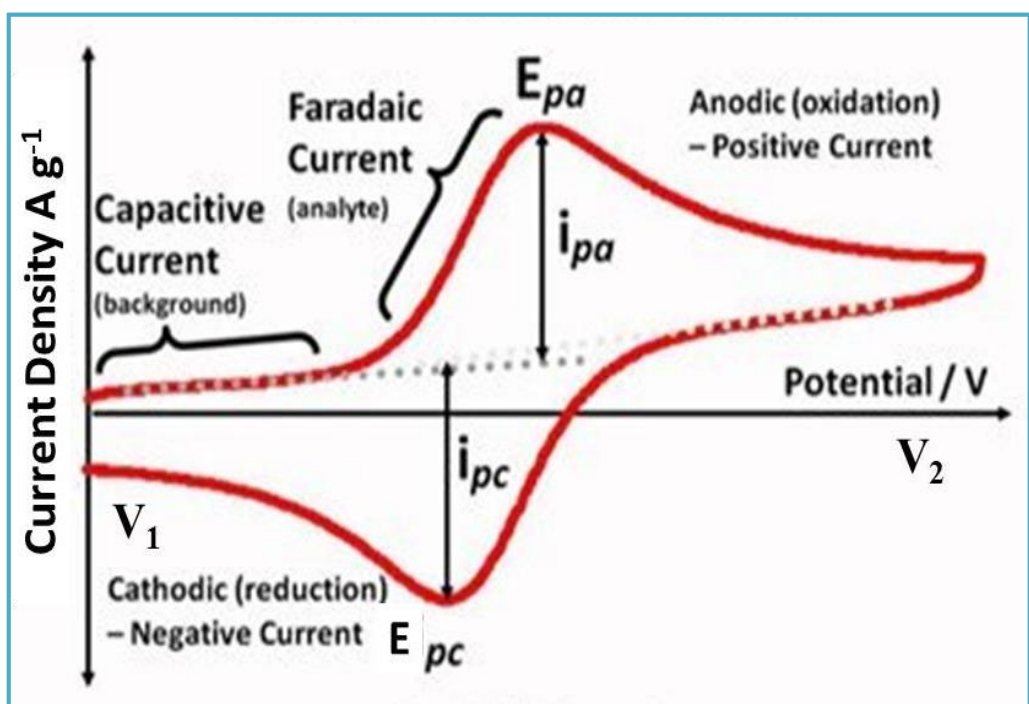
Fig. 4.9. CV curve for a single electrode with a reversible redox process [179].

In CV, the potential is swept within two fixed values (i.e. in a given potential window). The scan swept back and the voltage reverted to point V_1 when the voltage reached point V_2. The potential limits are V_1 and V_2, the cathodic and anodic peak currents are i_{pc} and i_{pa}, and the cathodic and anodic peak voltages of the resultant voltammogram are E_{pc} and E_{pa}. Owing to the large concentration of electrolytic ions at the electro-active sites, the current rises during the forward scan as the potential approaches the oxidation potential of the electrochemically active material, but it drops as the potential rises. The product generated in the initial oxidation step diminishes when a reversible redox couple is supplied with reverse potential, resulting in a reverse polarity current.

4.6.2. Galvanostatic Charge-Discharge (GCD)

The experimental procedure of Galvanostatic charge-discharge (GCD), commonly

described as chronopotentiometry (CP), can offer crucial data on cyclic life, equivalent series resistance (ESR), and energy (E) as well as power (P) densities, and specific capacitance (Cs). In the GCD technique, a constant current is provided to the working electrode, and the corresponding potential with respect to a reference electrode is measured. The amount of charge transmitted between the electrodes remains constant when the working electrode charges and discharges at a fixed current density. The amount of potential change over time is monitored and differs depending on the current density employed. Fig. 4.10 depicts a GCD curve schematic.

However, to characterize the cycle life of supercapacitors (SCs), the two electrode test cell is favorable because it is analogous to the more practical operating conditions. The nature of the charge-discharge curve reveals the charge storage mechanism of a specified electrode. If the charge-discharge curve is linear in nature, then the charges are stored by an electric double-layer capacitance (EDLC) mechanism otherwise non-linear nature indicates that the charges are stored by a pseudocapacitive (PC) mechanism [180].
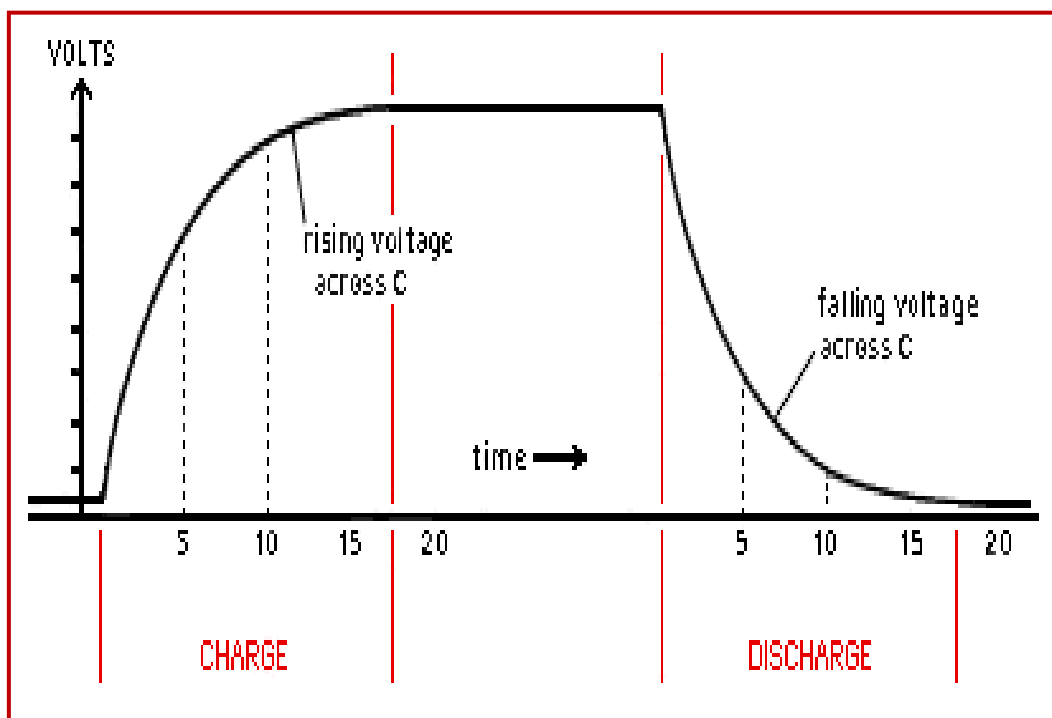
Fig. 4.10. Schematic of GCD curve [181].

4.6.3. Electrochemical Impedance Spectroscopy (EIS)

Electrochemical impedance spectroscopy (EIS) determines the impedance of material in a set of frequencies and is beneficial to provide information about the resistance of the electrode-electrolyte interface and charge transfer process [182]. Over a frequency

range of 10 µHz to 1 MHz, a tiny AC signal (5 to 50 mV) is supplied to the supercapacitor (SC) cell. The output signals are a current response of applied AC signals. The EIS spectra can be analyzed and interpreted by Nyquist and bode plot [183].
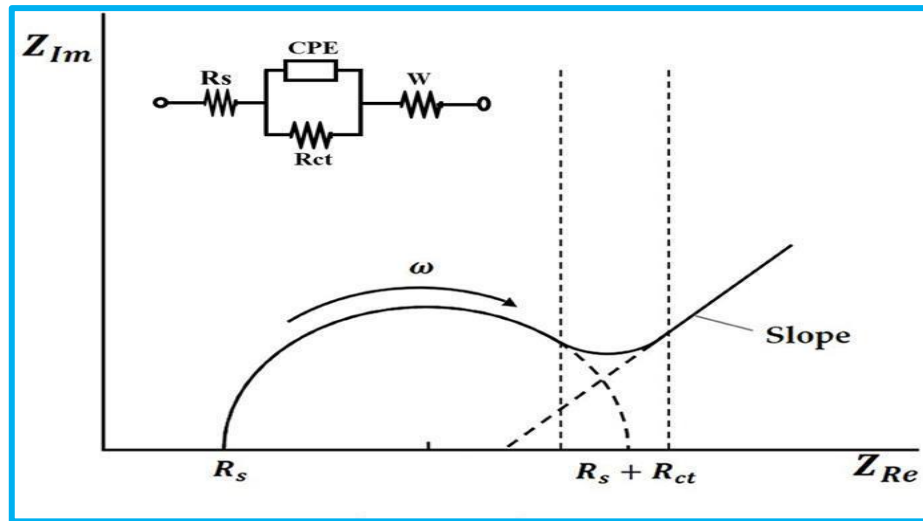
Fig. 4.11. Nyquist plot with an electrical equivalent circuit [184].

A Nyquist plot with equivalent circuits is manifested in Fig. 4.11, which comprises the four circuit elements: R_s (ohmic resistance), R_s+R_{ct} (charge transfer resistance), CPE (constant phase element), and W (Warburg impedance). The EIS technique is essential because it determines the frequency-dependent and independent electrical components from the Nyquist plot. Equivalent circuit models based on basic electric circuit elements such as capacitors and resistors are used to simulate complicated electrochemical processes near the electrode-electrolyte interface [185]. Components of equivalent circuits and the equations of their current-voltage relationships are illustrated in Table 4.1. The resistor is not dependent on the frequency and does not contain imaginary elements. Furthermore, the inductor and capacitor have an imaginary element of impedance [186].

Table 4.1 Common electrical elements.

Component	Current Vs. Voltage	Impedance
Resistor	$E = IR$	$Z = R$
Inductor	$E = L\, di/dt$	$Z = j\omega L$
Capacitor	$I = C\, dE/dt$	$Z = 1/j\omega C$

The imaginary, as well as real impedance components, are described in the Nyquist plot shown in Fig. 4.11. The imaginary and real components of the impedance are shown on the Y and X-axis, respectively, in a Nyquist plot. The inset diagram displays a fitted equivalent circuit associated with the Nyquist plot. In this figure, the semi-circular loop is associated with the resistance of charge transfer. Furthermore, in the impedance of an electrochemical cell, solution resistance is a significant concept. The temperature, the kind of ion present, the amount of ions present, and the geometry of the region through which the electric current passes define the resistance of an electrolytic solution. Also, the transfer of these charges has fixed kinetics and the kinetics depend on reaction type, temperature, concentration, and potential of reaction products. Ionic diffusion can also cause a phenomenon known as Warburg impedance. Impedance is also influenced by the potential irritability frequency.

The Warburg impedance is smaller at higher frequencies because the diffusing reactant does not need to go very far. Also, the real-axis intercept (at high frequencies) corresponds to the ohmic resistance. At lower frequencies, the reactors have to diffuse more distance, increasing the Warburg-impedance. In the Nyquist plot, Warburg impedance is described by a diagonal line with an inclination of 45° arising due to the mass transport of ions [187]. In the EIS study, capacitors are normally not ideally behaved; rather they act as CPE. In short, an SC behaves as a capacitor and pure resistor at low and high frequencies, respectively. Moreover, in the medium-frequency range, the physical and morphological properties of electro-active material play a crucial role in achieving the capacitance value and serving as an association of resistors and capacitors [188]. The impedance response mainly depends on the operating voltage [189]. The obtained data were fitted with different interface parameters by algorithms with minimum chi-square value. EIS is employed as an important characterization technique for applications to many material systems such as plating, corrosion, fuel cells, batteries, etc. Also, EIS gives the opportunity to determine the capacitance as a function of frequency [190].

CHAPTER-5

Structural, Morphological, and Magnetic Investigation of the Zinc Substituted Magnesium Spinel Ferrite

Abstract

By employing the sol-gel auto combustion approach, we have prepared $Mg_{1-x}Zn_xFe_2O_4$ (x = 0.0, 0.2, and 0.4) in the present research. The prepared samples have a cubic single-phase (spinel) structure, according to the XRD study. As Zn^{2+} ions possess a larger ionic radius than Mg^{2+} ions, the lattice constant (a_o) rises with Zn content from 8.390 to 8.417 Å. The nano-sized crystallite (D) has been evaluated utilizing the Debye-Scherrer formula. The spinel structure was verified by bands in the range of 442.93-454.42 cm^{-1} and 554.08-536.45 cm^{-1} in the prepared samples, which correlates to the octahedral (v_2) and tetrahedral (v_1) sites, respectively. Using ImageJ software, FESEM micrographs assess particle size (average) in the nanoscale range, revealing the existence of agglomerated and homogeneous grains. The stoichiometric proportions of the synthesized sample were confirmed by the EDX spectra. With rising Zn content, the VSM study exhibits the increment and decrement in the saturation magnetization (M_s) and coercivity (H_c) respectively. Owing to the lower H_c value, prepared samples possess soft ferromagnetic characteristics, making them favorable for power and electromagnetic applications.

5.1. Introduction

In the family of magnetic materials, the first solid which comes into the picture was the ceramic spinel ferrite. Due to the tremendous advantage in electromagnetic properties, the ceramic spinel ferrite was contemplated over the entire world [191]. Owing to the high surface-to-volume ratio of today's nanomaterials, their physical and chemical characteristics differ from those of bulk materials. The study of characteristics such as size and shape had a substantial influence on the physical and chemical characteristics of the materials, which have attracted a lot of attention due to their scientific and industrial value [192,193]. Presently, ecofriendly nanomaterials (spinel ferrite) have a wide extent of anticipated applications in medical sciences [194], catalysts [140], energy storage devices [195], pollution control [196], sensors [197], data storage systems [198], microwave absorbing materials [199], magnetic resonance imaging (MRI) [200], anticorrosive paints ferrofluids [201], and microelectronics [202]. In spinel ferrites, the existence of the metal cations in the

lattice sites gives rise to various forms of the crystal structure (normal, inverse, or mixed) which has a substantial impact on the structural, morphological, electrical, optical, and magnetic characteristics. Moreover, the cations in the lattice site had been contingent upon some key benchmarks, viz. sintering temperature, composition, stoichiometry, and production technique [203-207].

Amongst the numerous ferrites (spinel) reported, magnesium spinel ferrite ($MgFe_2O_4$) is found to be eco-friendly in nature, whose physical and chemical properties can be varied by embracing different synthesis techniques and their circumstances [208]. The presence of the different metal cations (divalent) viz. Ba^{2+}, Ca^{2+}, Cd^{2+}, Cr^{2+}, Zr^{2+}, Zn^{2+}, Al^{2+}, Ti^{2+} etc. into the magnesium spinel ferrite ($MgFe_2O_4$) may help in enhancing the electric, magnetic and dielectric properties [209-212]. Out of these divalent metal cations, Zn^{2+} is found to be a very exciting and promising candidate doping material. The Zn^{2+} doped spinel ferrite materials have a wide range of importance for soft magnetic applications and high-frequency devices [213]. Although Mg^{2+} and Zn^{2+} divalent metal cations exhibit non-magnetic behavior, they have a strong ability to enhance the magnetic properties by occupying the different lattice sites. Magnesium spinel ferrite ($MgFe_2O_4$) has an inverse structure, whereas zinc spinel ferrite ($ZnFe_2O_4$) has a normal structure [214,215]. The magnesium zinc spinel ferrite ($Mg_{1-x}Zn_xFe_2O_4$) exhibits a soft n-type semiconducting behavior and found its potential application in magneto-optical equipment, electromagnetic wave absorbers, magnetic refrigeration, gas-based sensors, core materials, microwave appliances, and magnetic recording gadgets because of the low magnetic losses and high permeability, and resistivity value [216-218].

The sol-gel auto combustion procedure has been chosen over the other nanomaterials preparation procedures reported [219-224] because of its nano-scale size, pristine product, minimal time, low-temperature formation, bulk production, and homogeneity [225,226]. However, the use of deionized water ensures this procedure to be ecologically friendly. Keeping this into consideration, the present study intends to shed light on the production of $Mg_{1-x}Zn_xFe_2O_4$ (x = 0.0, 0.2, and 0.4) by employing the sol-gel auto combustion procedure. The structural, morphological, and magnetic characteristics of the nanoparticles (NPs) produced were contrasted and examined by employing XRD, FTIR, FESEM, EDX, and VSM.

5.2. Experimental Procedures

The $Mg_{1-x}Zn_xFe_2O_4$ NPs were prepared using Loba AR grade reagents viz. magnesium nitrate, zinc nitrate, ferric nitrate, citric acid, and ammonia solution. To achieve a clear solution, firstly all of the metal nitrates and citric acid in the ratio of 1:1 as per the desired stoichiometry were taken and mixed in 100 ml of deionized water for around 30 minutes with the aid of a magnetic stirrer. Citric acid has been preferred over all other existing fuels owing to its superior complexing capabilities and low ignition temperature [227]. To retain the pH level at 7, the ammonia solution has been added drop by drop to the aforesaid solution. To yield a xerogel, the solution was agitated for 4-5 h at 100 °C. Heating the xerogel to 100 °C initiated the auto-combustion process. The as-burnt powder was then heated for another 8-10 h at 80-100 °C to obtain a fluffy powder, which was then mashed using a mortar and pestle to produce a fine powder. After sintering this fine powder at 800 °C for 6 h, single-phase (spinel ferrite) NPs were produced. The single-phase, spinel structure, surface morphology, composition, and magnetic examination of the prepared samples were assured by the XRD (Bruker D8 Advance), FTIR (Perkin Elmer Spectrum 2), FESEM (JEOL JSM-7610F), EDX (OXFORD EDX LN2 free), and VSM (Lake Shore) respectively.

5.3. Results and Discussions
5.3.1. XRD Study

The prepared samples phase and structural parameters viz. lattice constant (a_0), unit cell volume (V), and crystallite size (D) were examined by employing the X-ray diffraction (XRD) study and presented in Table 5.1. The diffraction pattern for $Mg_{1-x}Zn_xFe_2O_4$ (x = 0.0, 0.2, and 0.4) with a wavelength (λ) of 1.5406 Å and diffraction angle (2θ) in the range of 10° to 70° is manifested in Fig. 5.1. The characteristic diffraction peaks in accordance with the JCPDS card no. 22-1012 viz. (111), (220), (311), (222), (400), (422), (511), and (440) were inspected from the XRD pattern, thereby affirming the pristine spinel phase, face-centered cubic (fcc) configuration and Fd-3m space group of the prepared specimens [228]. The variation in the a_0 values causes a minor shift in the characteristic diffraction peak. The a_0, V, and D were evaluated utilizing Eq. (5.1), (5.2), and (5.3) respectively [229-231].

$$a_o = d\sqrt{h^2 + k^2 + l^2} \qquad\qquad (5.1)$$

$$V = (a_0)^3 \qquad\qquad (5.2)$$

$$D = \frac{K\lambda}{\beta \cos\theta} \qquad (5.3)$$

Here d, (hkl), K, λ, β, and θ represent interlayer spacing, miller indices, shape factor, wavelength of the X-ray source, full width at half maximum, and higher intensity peak angle respectively.
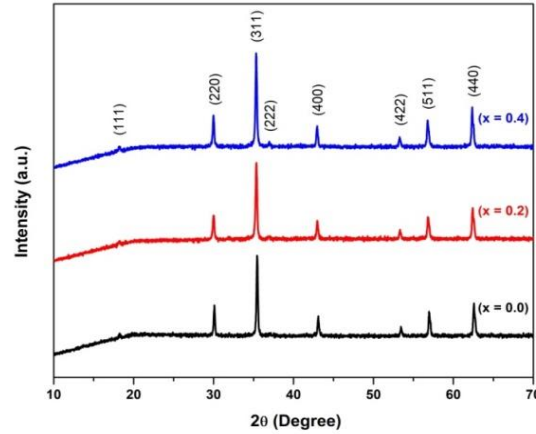
Fig. 5.1. XRD pattern of $Mg_{1-x}Zn_xFe_2O_4$ samples.

Table 5.1
Structural parameters of $Mg_{1-x}Zn_xFe_2O_4$ samples.

Zn Concentration x	a_o (Å)	V (Å)^3	D (nm)
0.0	8.390	590.647	37.558
0.2	8.413	595.633	32.591
0.4	8.417	596.456	34.391

The variability in the a_o and D as a function of Zn content is manifested in Fig. 5.2. As the Zn content rises, the a_o rises from 8.390 to 8.417 as perceived in Fig. 5.2(a), following Vegard's rule. Because Zn has greater ionic radii [0.60 Å (A-site) and 0.74 Å (B-site)] than Mg [0.57 Å (A-site) and 0.72 Å (B-site)] [232], there is a considerable increment in the a_o, which eventually increases the V and thus expands the unit cell of the produced samples with the Zn content. The nano-sized crystallite (D) was assessed by employing the Debye-Scherrer equation, and it was perceived in Fig. 5.2(b) that the D initially decrements from 37.558 to 32.591 nm and then increments up to 34.391 nm with Zn content. A comparable fluctuation in the D was reported for a similar system prepared by employing a facile sol-gel approach

utilizing coconut water as a fuel [233]. This erratic relationship between D and Zn content illustrates the randomized occurrence of metal cations at the A and B sites, thereby resulting in the non-homogeneous strain in the lattice of the prepared spinel ferrite NPs [97,234].
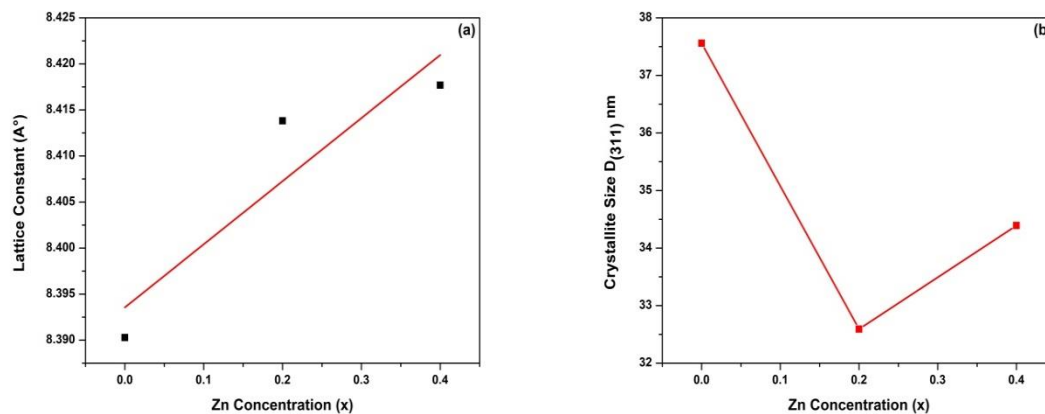
Fig. 5.2. (a) Lattice constant, and (b) Crystallite size as a function of Zn concentration.

5.3.2. FTIR Study

The spinel structure, immaculateness, and chemical bonding in the prepared samples were examined by the FTIR. The FTIR spectra for samples with varying Zn content are presented in Fig. 5.3 with wavenumbers varying from 400 to 4000 cm^{-1}. The prepared Mg$_{1-x}$Zn$_x$Fe$_2$O$_4$ lattice sites are occupied by the metal cations [235]. For all the prepared samples the bands in the range of 442.93-454.42 cm^{-1} and 554.08-536.45 cm^{-1} were noticed which corresponds to the octahedral (v_2) and the tetrahedral (v_1) sites respectively and verifies the spinel structure. As per Waldron [230], these bands exist by virtue of M-O vibrations (stretching) in the lattice sites. The frequency of the two vibrational bands differs owing to the variation in M-O bond length in the lattice sites [227]. The shift in the vibrational bands (v_1 and v_2) was noticed which reveals the distortion of the crystal structure [236]. Because of the occupancy of the Zn ions to the octahedral site, the FTIR spectra show a clear shift of the tetrahedral vibrational band (v_1) towards the lower wavenumber side (red-shift) with the Zn content. The Zn ions had a strong inclination to involve the tetrahedral site and with the increase in value of the Zn content, the reduced mass will be increased thereby reducing the force constant value as they are inversely related to each other and hence undergoes a red-shift [237]. The bands in the 3400-3800 cm^{-1} range have confirmed the adsorbed water in the prepared samples. The elimination of bands at 1100 cm^{-1} proved that all nitrates had been evacuated from our prepared samples. The disappearance of bands at 1385, 1572, and 3137

cm^{-1} reveals the entire removal of the citric acid after sintering, illustrating the quality of our produced spinel ferrite NPs and validating our XRD study [225].
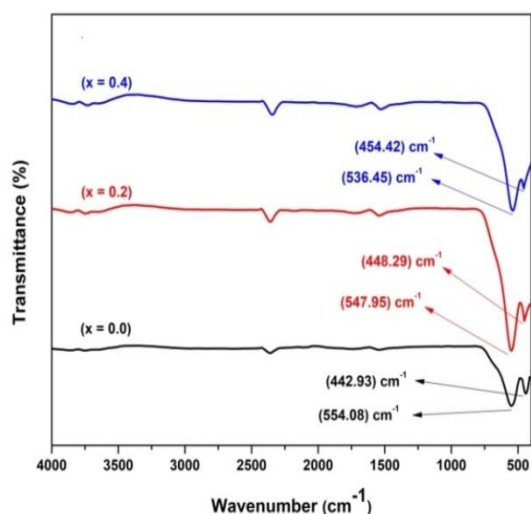
Fig. 5.3. FTIR spectra of $Mg_{1-x}Zn_xFe_2O_4$ samples.

5.3.3. FESEM Study

The FESEM investigation focused on the morphological characteristics and average particle size of the prepared NPs. FESEM micrographs of the prepared samples, as well as a histogram showing particle size, are illustrated in Fig. 5.4. The micrographs in Fig. 5.4 depict a compact arrangement of particles that are homogenous in shape but vary in particle size. FESEM micrographs of doped samples (x = 0.2 and 0.4) were agglomerated and homogenous, exhibiting a spherical form. The magnetic interactions between NPs are mostly responsible for the apparent aggregation in the FESEM micrograph [238,239]. Employing ImageJ software and the histogram obtained from the FESEM micrograph, the average particle size for the prepared samples was estimated and presented in Table 5.2. It was revealed that the particle's average size was greater than D, demonstrating that two or more crystallites are joined together to form a particle, resulting in the particle's massive size.
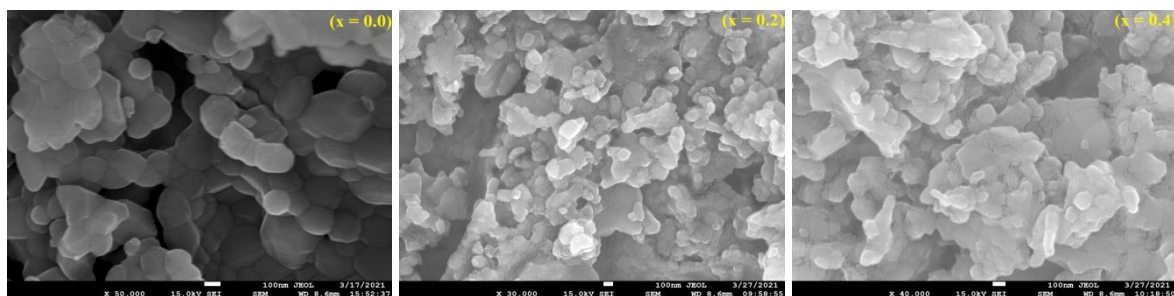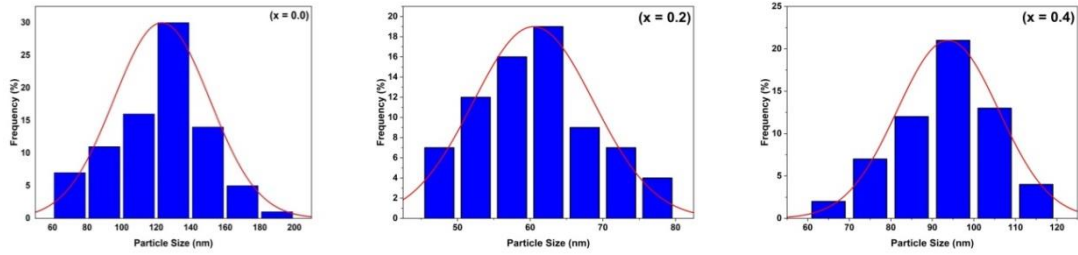
Fig. 5.4. FESEM micrograph and particle size histogram of $Mg_{1-x}Zn_xFe_2O_4$ samples.

Table 5.2
Particle size (average) estimated from FESEM micrograph of $Mg_{1-x}Zn_xFe_2O_4$ samples.

Zn Concentration (x)	Average Particle Size (nm)
0.0	127.867
0.2	60.005
0.4	94.950

5.3.4. EDX Study

EDX spectra represented in Fig. 5.5 have been used to assess the stoichiometric proportions and composition of the prepared samples. The x = 0.0 spectra portrayed the elements viz. Mg, Fe and O, whereas the x = 0.2 and 0.4 spectra portrayed the elements viz. Mg, Zn, Fe, and O. For the undoped sample the elemental mapping is illustrated in Fig. 5.6, revealing that the elements Mg, Fe, and O exist in the associated ferrite NPs and are distributed symmetrically. The experimental At. % and Wt. % values, as noticed in Table 5.3, are in close proximity to the theoretical values, thereby proving the pureness of the prepared ferrite NPs. However the slight variation in the Fe and O content for undoped sample has been noticed and this might be due to the porosity as observed in the FESEM micrograph of the undoped sample.
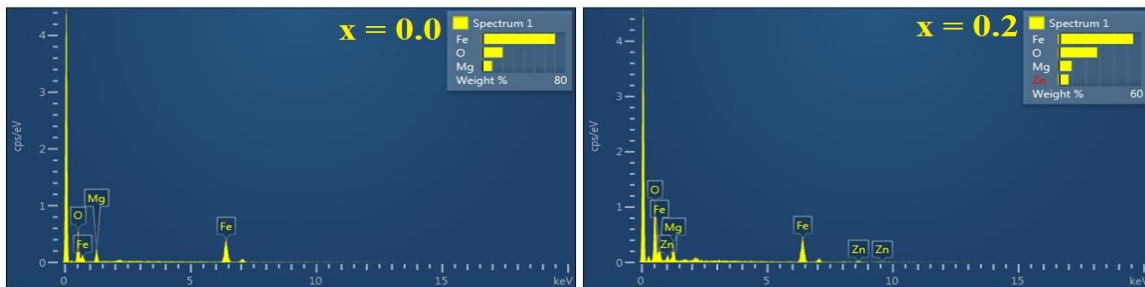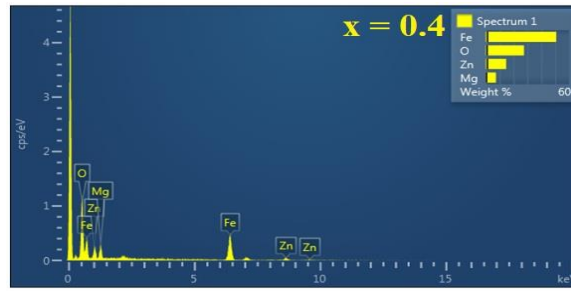
Fig. 5.5. EDX spectra of $Mg_{1-x}Zn_xFe_2O_4$ samples.
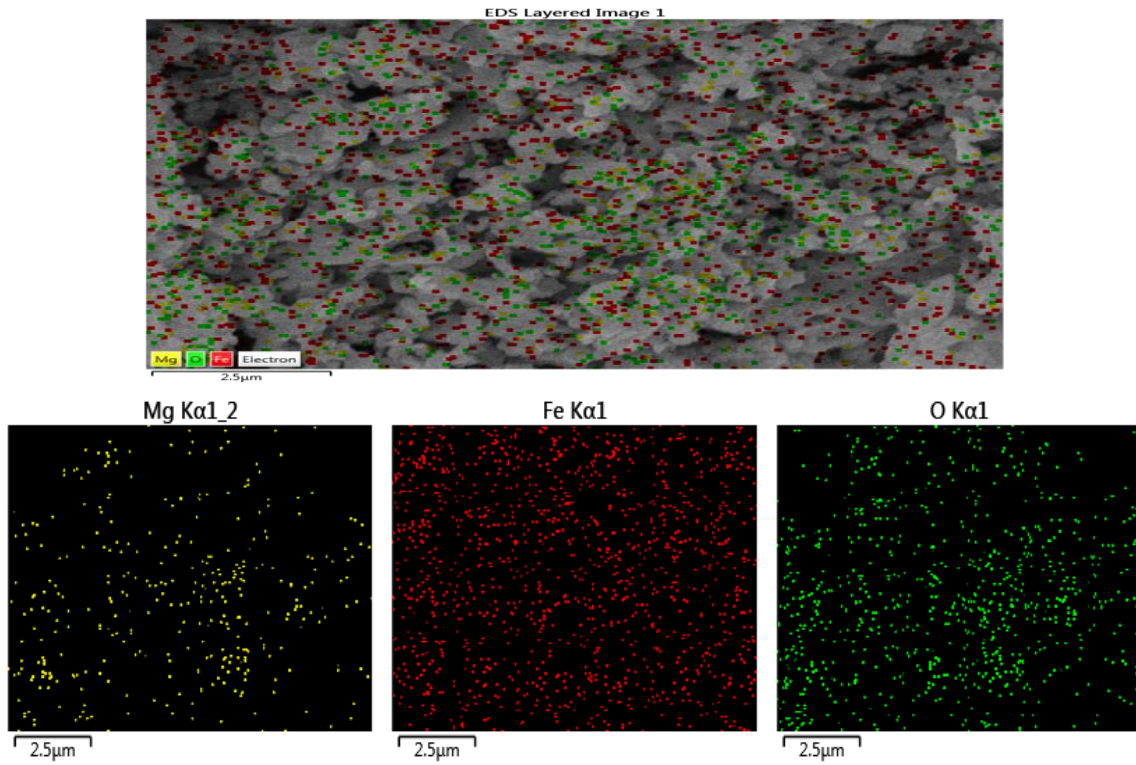
Fig. 5.6. Elemental mapping for undoped sample.

Table 5.3

Experimental and theoretical values of At. % and Wt. % of $Mg_{1-x}Zn_xFe_2O_4$ samples.

Zn Concentration (x)	Atomic % and Weight %	Values	Mg	Zn	Fe	O	Total %
0.0	Atomic %	Experimental	13.72	0	43.26	43.02	100
		Theoretical	14.28	0	28.57	57.14	100
	Weight %	Experimental	9.70	0	70.27	20.02	100
		Theoretical	12.15	0	55.84	31.99	100

0.2	Atomic %	Experimental	11.86	3.54	30.64	53.97	100
		Theoretical	11.42	2.85	28.57	57.14	100
	Weight %	Experimental	9.32	7.47	55.30	27.91	100
		Theoretical	9.33	6.28	53.64	30.73	100
0.4	Atomic %	Experimental	9.46	7.10	28.88	54.56	100
		Theoretical	8.57	5.71	28.57	57.14	100
	Weight %	Experimental	7.23	14.59	50.72	27.45	100
		Theoretical	6.73	12.08	51.60	29.57	100

5.3.5. VSM Study

The VSM approach with a magnetic field of $\pm$ 20 KOe is being used to examine the magnetic characteristics of the prepared samples at room temperature. The values of magnetic characteristics such as saturation magnetization (M_s), magnetic moment (n_B), remnant magnetization (M_r), coercivity (H_c), squareness ratio (R), and anisotropy constant (K_1) are listed in Table 5.4. The prepared sample's M-H curve (Fig. 5.7) exhibits an S-shaped hysteresis curve with features comparable to ferromagnetic materials [240]. In the prepared $Mg_{1-x}Zn_xFe_2O_4$ (x = 0.0) sample (inverse structure), all Mg^{2+} cations were present in the octahedral site, whereas Fe^{3+} cations were equally prevalent in the tetrahedral and octahedral sites. The Fe^{3+} cations in the tetrahedral and octahedral sites are imbalanced when the NPs crystallize, forming a partly inverted structure [214,241]. The super-exchange interaction between the two lattice sites is enhanced by the Fe^{3+} cation imbalance, resulting in net magnetization [242]. The magnetic moment (n_B) for the incorporated samples is assessed by the formulae given in Eq. (5.4) [243,244].

$$n_B = \frac{M_s \times MW}{5585} \qquad (5.4)$$

The rising trend in M_s with Zn (x = 0.2) content is perceived in Fig. 5.8(a). Owing to the replacement of non-magnetic Zn^{2+} cations (0 μ_B) to the tetrahedral site results in the movement of Fe^{3+} cations (5 μ_B) from the tetrahedral to the octahedral site. This enhances the difference in magnetization between the two sites as predicted by Eq. (5.5) [237,245] and, as a result, intensifies the M_s from 41.232 to 45.180 emu/g.

$$M_s = |M_B - M_A| \qquad\qquad (5.5)$$

Here the magnetizations of octahedral and tetrahedral sites are shown by M_B and M_A, respectively. Exceeding Zn content to x = 0.4, furthermore of the Fe^{3+} cations move to the octahedral site which brings about the increment in the M_S from 45.180 to 91 emu/g. A comparable increasing trend in the M_S was reported by P.Y. Reyes-Rodriguez et. al [246]. The H_c estimated via Eq. (5.6) varies based on K_1, M_s, size, and morphology of the prepared samples [247].

$$H_c = \frac{0.96 \times K_1}{M_S} \qquad\qquad (5.6)$$

The significant decline of H_c with Zn content is manifested in Fig. 5.8(b). The Browns relation is assured by the M_s and H_c, which exhibit an inverse proportionate relationship with Zn content. The magnetic soft nature of the prepared sample is revealed by the H_c value presented in Table 5.4, which make it valuable for power and electromagnetic [248,249] applications. The formulae in Eq. (5.7) [240] can be utilized to compute the R of the prepared samples.

$$R = \frac{M_r}{M_S} \qquad\qquad (5.7)$$

The prepared sample's R-value was perceived to be lesser than 0.5, thereby indicating the presence of sporadically aligned tiny single domain assemblies of NPs [225,227,250] and revealing magnetostatic interactions between them [243].

Table 5.4
Magnetic parameters of $Mg_{1-x}Zn_xFe_2O_4$ samples.

Zn Concentration (x)	M_s (emu/g)	n_B (μ_B)	M_r (emu/g)	H_c (Oe)	R	K_1 (erg/cc)
0.0	41.232	1.476	10.985	59.199	0.266	2542.627
0.2	45.180	1.684	6.691	49.392	0.148	2324.557
0.4	91	3.526	8.569	30.323	0.094	2874.367
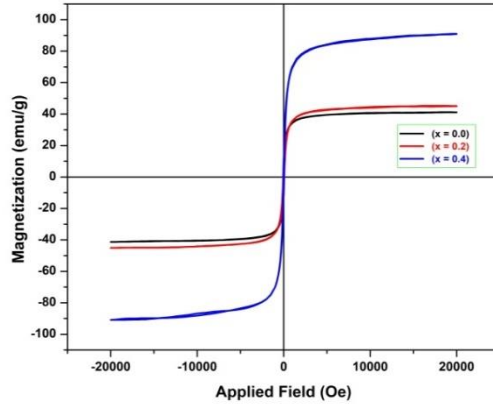
Fig. 5.7. M-H curve of $Mg_{1-x}Zn_xFe_2O_4$ samples.
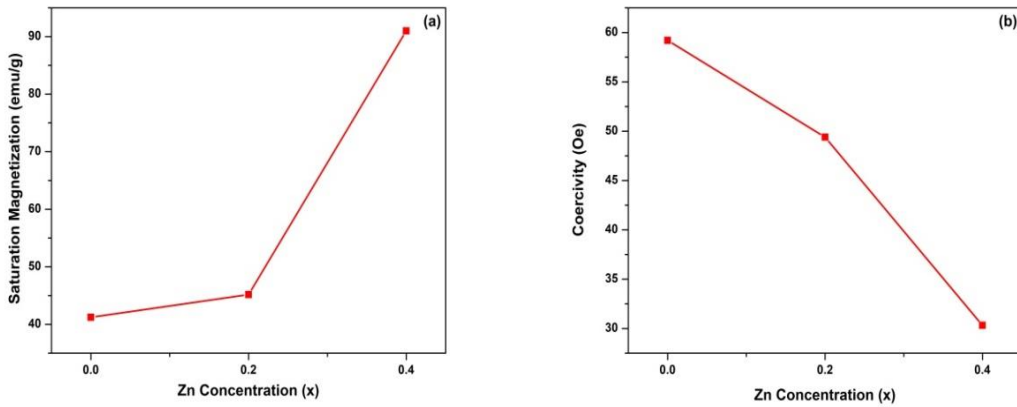
Fig. 5.8. (a) Saturation magnetization (M_s), and (b) Coercivity (H_c) as a function of Zn concentration.

5.4. Conclusion

$Mg_{1-x}Zn_xFe_2O_4$ (spinel ferrite) nanoparticles with various stoichiometric ratios and having crystallite size (D) in the nanoscale range of 32.591 to 37.558 nm were effectively synthesized by the sol-gel auto combustion technique. FTIR spectra display the red-shift of the tetrahedral vibrational peak with the zinc content. FESEM micrographs depict the agglomerated grains due to the magnetic interaction between the nanoparticles. EDX spectra avow the elements present in the incorporated samples without any extra impurity peak present in the spectra. The Atomic percent (At. %) and Weight percent (Wt. %) values, determined utilizing EDX spectra were in close concurrence with the theoretical values, thus affirms the immaculateness of the synthesized samples. The increment in the saturation magnetization (M_s) is because of the substitution of non-magnetic Zn^{2+} (divalent) metal

cations (0 μ_B) to the tetrahedral or A-site. The synthesized samples exhibit soft ferromagnetic properties due to the low coercivity (H_c) value which makes them suitable for electromagnetic radiation material and power application.

CHAPTER-6

Synthesis and Investigation of Structural, Morphological, and Magnetic Properties of the Manganese doped Cobalt-Zinc Spinel Ferrite

Abstract

The current work involves the synthesis of $Mn_xCo_{0.5-x}Zn_{0.5}Fe_2O_4$ (x = 0.0, 0.1, 0.2, 0.3, and 0.4) by adopting sol-gel auto combustion technique. For all the samples, the single-phase spinel structure with cubic symmetry was assured by the XRD studies. The crystallite size lies in the nanoscale range of 35.4 to 43.6 nm as estimated by utilizing Debye-Scherrer formula. FTIR spectroscopy affirms the formation of spinel structure due to the appearance of characteristic vibrational bands near 400 and 600 cm^{-1} which corresponds to the octahedral and tetrahedral sites respectively. FESEM micrographs reveal the presence of non-uniform grain growth which was agglomerated, in-homogenous in size and shape, and having porous morphology. VSM study exhibits soft ferromagnetic nature due to the low coercivity value. There is a decrement in the saturation magnetization with increasing Mn^{2+} concentration which is due to the decrease in the crystallite size and non-magnetic nature of the Mn^{2+}.

6.1. Introduction

Spinel ferrite ceramics are significant rivals in various electronic devices. Presently, ecofriendly nanomaterials such as spinel ferrite, having good thermal and chemical stability, exhibits amazing properties viz. structural and magnetic, due to which it has a wide extent of anticipated applications in energy storage devices [195], magnetic recording [251], catalysts [140], drug delivery system [252], sensors [197], microelectronics [202], data storage system [198], magnetic resonance imaging (MRI) [200], pollution control [196], anticorrosive paints ferrofluids [201], medical sciences [194] and many more. The spinel ferrite has a cubic structure and exhibits an Fd-3m space group. The spinel structure is made up of a closely packed oxygen anion in which thirty-two oxygen anions form a complete structure unit cell. These oxygen anions form a face-centered cubic arrangement leaving two sorts of spaces between these oxygen anions: tetrahedral or A-site, encircled by four oxygen particles, and octahedral or B-site, encircled by six oxygen particles. The single crystallographic unit cell of spinel ferrite contains eight formulae units of MFe_2O_4 (where M is one or more divalent metal cations). Every unit cell of spinel ferrite has sixty-four tetrahedral sites, eight of which

are involved, and thirty-two octahedral sites, sixteen of which are involved. The difference in the magnetization of these lattice sites gives the net value of magnetization of the spinel structure [204]. The presence of metal (divalent or trivalent) cations to the lattice sites have pored over, utilizing the crystal field theory, which results in the different types of crystal structure such as normal, inverse, or mixed. Moreover, these cations emphatically influence the physical properties viz. structural, electrical, optical, and magnetic. Further, this occupancy of metal (divalent or trivalent) cations to these tetrahedral and octahedral sites relied on a few key factors viz. preparation method, elemental composition, and sintering temperature [205-207,253].

The spinel ferrites can be synthesized by several techniques which include the co-precipitation method, hydrothermal method, microwave combustion, sol-gel auto combustion, spray pyrolysis, ceramic, etc. [254-273]. The structural properties such as size, morphology, state of the surface, and chemical homogeneity relied heavily on the preparation method. Out of these above synthesis techniques, the sol-gel auto combustion method has been preferred because of homogeneity, large-scale production, lowering of the crystallization temperature, short time, stoichiometrically pure product formulation, and nanosize formulation of compound [225,226]. Additionally, the utilization of water as a solvent makes this technique eco-friendly according to the natural perspective.

Among the various spinel ferrites present, the $CoFe_2O_4$ and $ZnFe_2O_4$ have drawn an impressive interest in view of their wide scope of uses [274-276]. The $CoFe_2O_4$ exhibits an inverse structure, wherein divalent Co^{2+} cations occupy the octahedral sites and trivalent Fe^{3+} cations equally occupy the tetrahedral and octahedral sites. The $ZnFe_2O_4$ exhibits a normal structure wherein divalent Zn^{2+} cations occupy the tetrahedral sites and trivalent Fe^{3+} cations occupy the octahedral sites [277]. In addition, Mn-Zn ferrite (inverse structure) and Co-Zn ferrite (normal structure) have been researched broadly [278-281]. To the best of our knowledge, several doped spinel ferrites have been developed, but no information is available on the substitution of Mn in Co-Zn spinel ferrite nanoparticles (NPs) for the structural, morphological, and magnetic properties.

Taking into account this, the current work plans to reveal insight into the synthesis of the Mn doped Co-Zn spinel ferrite in different stoichiometric ratios i.e. $Mn_xCo_{0.5-x}Zn_{0.5}Fe_2O_4$ (x = 0.0, 0.1, 0.2, 0.3, and 0.4) by adopting the sol-gel auto combustion technique. Various characterization techniques viz. XRD, FTIR, FESEM, EDX, and VSM were performed for investigating the structural, morphological, and magnetic properties of the spinel ferrite NPs.

6.2. Experimental Procedures

The AR grade chemicals viz. manganese (II) nitrate hexahydrate from Alfa Aesar, cobalt (II) nitrate hexahydrate, zinc (II) nitrate hexahydrate, ferric (III) nitrate nonahydrate, citric acid anhydrous, and ammonium hydroxide from Loba Chemie Pvt. Ltd. were used for the synthesis of $Mn_xCo_{0.5-x}Zn_{0.5}Fe_2O_4$ by adopting the sol-gel auto-combustion technique. Based on the stoichiometric proportions of the spinel ferrite, all the metal nitrates (oxidants) and citric acid (chelating agent or fuel) in the ratio of 1:1 were weighed accordingly and dissolved in 100 ml of distilled water. The solution was stirred for about 30 min. with the help of a magnetic stirrer to obtain a clear solution. Out of the various fuels used in the sol-gel auto-combustion technique, citric acid was preferred because of the low ignition temperature and having excellent complexing ability [227]. The ammonium hydroxide solution was added in a drop-wise manner to the above solution to maintain the pH value at 7. The solution was then persistently stirred at 100 ^{o}C for 4 to 5 h to form a xerogel. The xerogel so formed was heated at 100 ^{o}C to undergo the auto combustion process. The as burnt ferrite powder so obtained was further heated at 80 ^{o}C to 100 ^{o}C for 8 to 10 h to form a fluffy powder which was then crushed with the assistance of mortar and pestle to get a fine powder. Finally, black powder of the $Mn_xCo_{0.5-x}Zn_{0.5}Fe_2O_4$ spinel ferrite NPs was obtained by sintering the fluffy powder under the atmosphere in the muffle furnace. The phase of the synthesized samples was assured by the XRD studies which were performed by Powder X-ray diffractometer (Bruker D8 Advance). In XRD Cu-Kα was used as a radiation source having wavelength λ = 1.5406 Å with diffraction angles of 20° to 70° in increments of 0.02°. The FTIR spectra which are helpful for structural determination of the synthesized spinel ferrite have been performed by using FTIR with diamond ATR and pellet accessories (Perkin Elmer Spectrum 2). The FESEM micrograph and EDX spectra affirm the surface morphology and composition respectively of the synthesized NPs which were performed by using FESEM coupled with EDX detector, Au sputter coater (FE-SEM: JEOL JSM-7610F Plus EDX: OXFORD EDX LN2 free, Au Coater: JEOL Smart Coater). The magnetic studies of the synthesized spinel ferrite have been performed at room temperature by using a vibrating sample magnetometer (VSM-EZ9) in a magnetic field range of ± 20 kOe.

6.3. Results and Discussions

6.3.1. XRD Study

One of the vital steps for the preparation of the spinel ferrite by the sol-gel technique is the sintering. The sintering temperature plays a significant part in influencing the various structural properties viz. phase, crystallinity, crystallite size, density, porosity, etc. To track down the reasonable sintering temperature for obtaining the single-phase spinel structure of the synthesized samples, the undoped Co-Zn spinel ferrite was sintered at 800 ^oC, 1000 ^oC, and 1200 ^oC for 6 h. Fig. 6.1(a) presents XRD pattern for undoped Co-Zn spinel ferrite in which crystalline spinel phase peaks along with the α-Fe_2O_3 were observed for the lower temperatures viz. 800 ^oC and 1000 ^oC. The presence of α-Fe_2O_3 peaks demonstrates that the incomplete sol-gel auto-combustion reaction of CoO, ZnO, and Fe_2O_3 to form a $Co_{0.5}Zn_{0.5}Fe_2O_4$ ferrite NP. At 1200 ^oC the α-Fe_2O_3 peaks were completely disappeared and only spinel phase peaks were present [282]. As per the above XRD investigation, a reasonable sintering temperature of 1200 ^oC for 6 h was employed to synthesize the Mn doped Co-Zn spinel ferrite. The X-ray diffraction studies of the synthesized Mn doped Co-Zn samples were performed to examine the phase structure, and evaluate various lattice parameters for the maximum intensity characteristic diffraction peak (311). The lattice parameters viz. lattice constant (a_0), unit cell volume (V_{cell}), crystallite size (D), dislocation density (δ), and lattice strain (ε) are reported in Table 6.1.
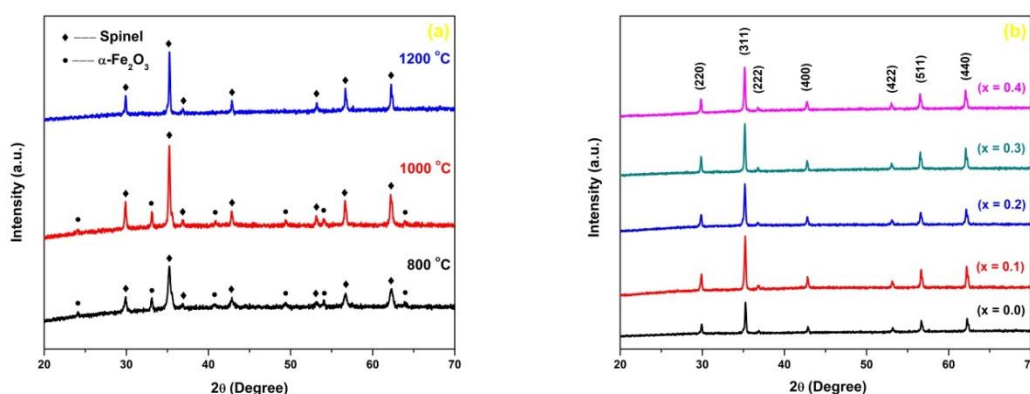
Fig. 6.1. X-ray diffraction pattern of (a) $Co_{0.5}Zn_{0.5}Fe_2O_4$, and (b) $Mn_xCo_{0.5-x}Zn_{0.5}Fe_2O_4$ samples.

From the X-ray diffraction pattern Fig. 6.1(b) (220), (311), (222), (400), (422), (511), and (440) characteristic diffraction peaks are present which is as per the ICDD no. 22-1086

(Co-ferrite) and 89-1009 (Zn-ferrite) [97,283] and affirms the face-centered cubic (fcc) arrangement of the synthesized samples. The X-ray diffraction pattern of all the samples with different Mn concentrations exhibits symmetry of the Fd-3m space group and affirms the single-phase crystalline structure without the presence of any impurity diffraction peak (Fe_2O_3 or ZnO). The slight shifting of the characteristic diffraction peak towards a lower 2θ side (Fig. 6.2) demonstrates an expansion in lattice constant (a_0) which likewise gets affirmed by the determined value of lattice constant (a_0) as reported in Table 6.1.
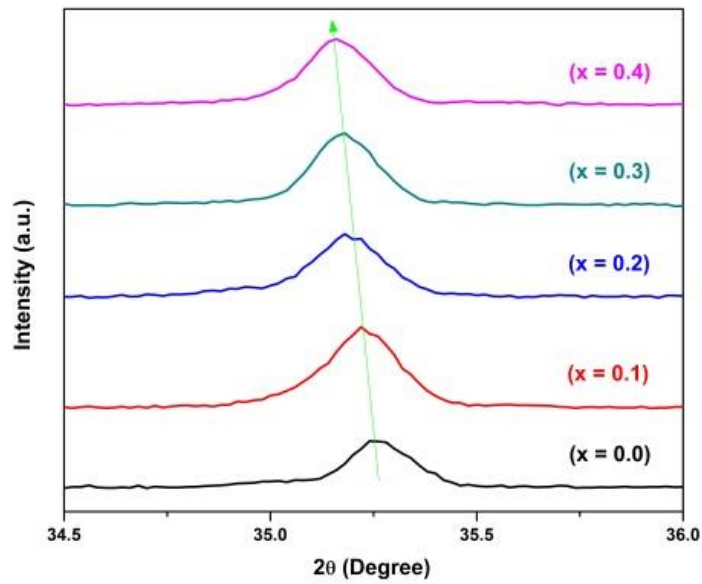
Fig. 6.2. Shift in 2θ ($\sim 35.25^0$) value of $Mn_xCo_{0.5-x}Zn_{0.5}Fe_2O_4$ samples.

The value of the lattice constant (a_0) can be calculated by the interlayer spacing (d) and characteristic diffracting peak values (hkl) given by Eq. (6.1) [229].

$$a_o = d\sqrt{h^2 + k^2 + l^2} \qquad (6.1)$$

The interplanar spacing (theoretically) was determined by Bragg's law given in Eq. (6.2) [284].

$$d = \frac{n\,\lambda}{2\,Sin\theta} \qquad (6.2)$$

Where n represents the order of the characteristic diffraction peak and is normally taken as 1, λ represents the wavelength of Cu-Kα radiation equivalent to 1.5406 Å, and θ represents the angle for the maximum intensity characteristic diffraction peak. The interplanar spacing (d) for the distinctive hkl planes of the incorporated samples are

determined by utilizing XPowder software and appeared in Table 6.2. The crystallite size (D) for all the samples with different Mn concentrations can be calculated for the maximum intensity characteristic diffraction peak (311) by the Debye-Scherrer formula given in Eq. (6.3) [230,231].

$$D = \frac{K\lambda}{\beta\,Cos\theta} \qquad (6.3)$$

Where K represents the shape factor of crystallite which is taken to be 0.9, and β represents full width at half maximum (FWHM) of the maximum intensity characteristic diffraction peak. The dislocation density (δ) can be determined by Eq. (6.4).

$$\delta = \frac{1}{D^2} \qquad (6.4)$$

and the lattice strain (ε) can be assessed by utilizing the Eq. (6.5).

$$\varepsilon = \frac{\beta}{4\,Tan\theta} \qquad (6.5)$$

Table 6.1
Lattice parameters of $Mn_xCo_{0.5-x}Zn_{0.5}Fe_2O_4$ samples.

Mn Concentration (x)	a_0 (Å)	V_{cell} (Å)^3	D (nm)	δ (m)$^{-2}$	ε
0.0	8.434	599.98	42.5	5.53×10^{14}	0.0026
0.1	8.444	602.12	36.3	7.55×10^{14}	0.0031
0.2	8.452	603.86	35.4	7.95×10^{14}	0.0032
0.3	8.454	604.21	43.6	5.25×10^{14}	0.0026
0.4	8.457	604.98	40.5	6.08×10^{14}	0.0028

Table 6.2
Interplanar spacing (d) for hkl planes of $Mn_xCo_{0.5-x}Zn_{0.5}Fe_2O_4$ samples.

(hkl)	d (Å)				
	x = 0.0	x = 0.1	x = 0.2	x = 0.3	x = 0.4
(220)	2.984	2.987	2.991	2.989	2.991
(311)	2.543	2.546	2.549	2.549	2.550
(222)	2.434	2.437	2.440	2.440	2.440
(400)	2.107	2.109	2.112	2.112	2.113
(422)	1.720	1.721	1.723	1.724	1.725
(511)	1.622	1.623	1.624	1.625	1.626
(440)	1.490	1.490	1.492	1.493	1.493

With the increase in the Mn content, the variability in the value of the lattice constant (a_0) was plotted and displayed in Fig. 6.3. The increasing trend of the lattice constant (a_0) from 8.434 to 8.457 Å with Mn content was noticed and follows Vegard's law [227,261,285]. The increase in the value of the lattice constant (a_0) with the Mn content is because the ionic radius of the Mn^{2+} ion (0.80 Å) being larger than the ionic radius of the Co^{2+} ion (0.78 Å) [286,287]. This ionic radius difference results in enhancing the unit cell volume (V_{cell}) and subsequent expansion in the unit cell of the synthesized spinel ferrite.
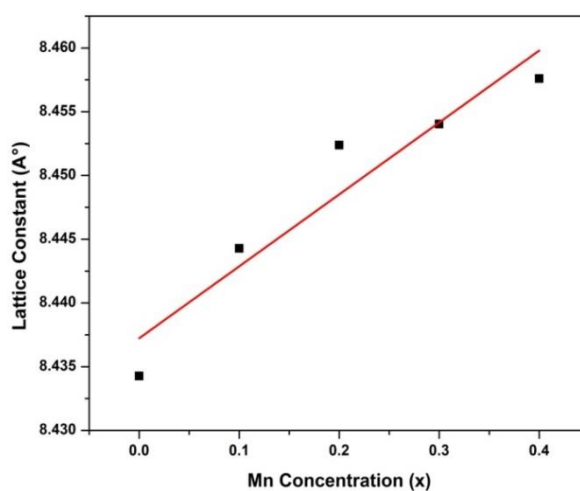
Fig. 6.3. Lattice constant as a function of Mn concentration.

Fig. 6.4 uncovers the Gaussian profile fit of $Co_{0.5}Zn_{0.5}Fe_2O_4$ (x = 0.0) sample for the maximum intensity characteristic diffraction peak (311). The Gaussian fit was utilized for the computation of Full Width at Half Maximum (FWHM) for the estimation of crystallite size (D). Table 6.1 reveals the variability in the crystallite size (D) with Mn content for all the incorporated samples. The crystallite size (D) assessed by utilizing the Debye-Scherrer formulae was found to be in the nanoscale range. It was noticed that the crystallite size (D) first decreased from 42.5 (x = 0.0) to 35.4 (x = 0.2) nm it further increased to the 43.6 (x = 0.3) nm and finally reduced to 40.5 (x = 0.4) nm. A comparative pattern for crystallite size (D) was accounted for a similar system prepared by the co-precipitation method [286]. This irregular trend or variation of the crystallite size (D) with the Mn content reveals the random presence of the metal (divalent or trivalent) cations at the tetrahedral and octahedral sites. This randomness of the metal cations creates inhomogeneous strain in the lattice of the synthesized spinel ferrite [97,288,289], breaking them into irregular particles of sporadic shape. Due to the distinction in ionic radii of the metal (divalent or trivalent) cations (Mn^{2+} = 0.80 Å, Co^{2+} = 0.78 Å, Zn^{2+} = 0.74 Å, and Fe^{3+} = 0.64 Å) [285,286], the inhomogeneous strain was predicted and reported in Table 6.1. The value of dislocation density (δ) and lattice strain (ε) initially increments from x = 0.0 to x = 0.2 as displayed in Table 6.1. The maximum value of the dislocation density (δ) and lattice strain (ε) was determined to be 7.95×10^{14} m^{-2} and 0.0032 respectively for x = 0.2 sample which implies plainly that the maximum deformation and failure of the crystallographic system in the incorporated samples would take at x = 0.2.
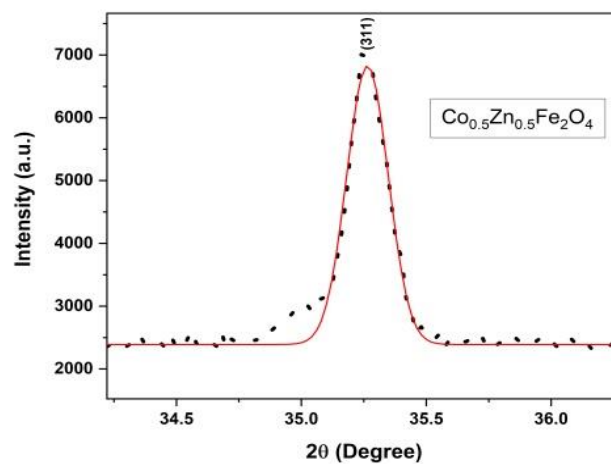
Fig. 6.4. Gaussian profile fit for x = 0.0 sample.

6.3.2. FTIR Study

The infrared spectroscopy technique is particularly helpful in inspecting the quality, chemical bonds, and affirms the spinel structure of the synthesized samples. Fig. 6.5 illustrates the FTIR spectra at room temperature for the incorporated samples with different Mn content in the wavenumber ranging from 400 to 4000 cm^{-1}.
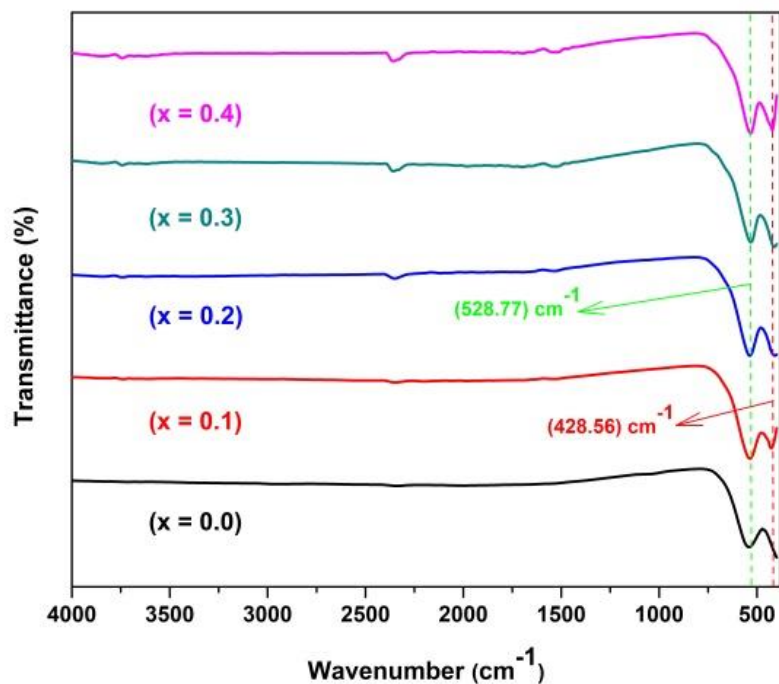
Fig. 6.5. FTIR spectra of $Mn_xCo_{0.5-x}Zn_{0.5}Fe_2O_4$ samples.

In ferrite, the metal (divalent or trivalent) cations exist in two independent lattice sites (tetrahedral and octahedral sites) as demonstrated by the spatial positioning of the nearest neighbor of oxygen ions [290]. The vibrational bands present in the FTIR spectra help in elucidating the position of the cations in these lattice sites. For all samples with different Mn concentrations, two vibrational bands were noticed in the wavenumber ranging from 400 to 600 cm^{-1}. According to Waldron [230], in the spinel ferrite, because of the stretching vibration of the metal-oxygen ion in the tetrahedral and octahedral sites gives rise to the vibrational band v_1 (near to the 600 cm^{-1}) and v_2 (near to the 400 cm^{-1}) respectively [291]. In the present FTIR spectra, the vibrational band v_1 and v_2 were present near to the wavenumber 528.77 cm^{-1} and 428.56 cm^{-1} respectively and hence verifies the spinel structure of the synthesized NPs [110]. Due to the distinction in the bond length of metal-oxygen ions in the tetrahedral and octahedral sites, it leads to the difference in the frequency of the vibrational

89

bands (v_1 and v_2) [227,292]. The vibrational bands present in the wavenumber range of 3400-3800 cm^{-1} reveal the presence of the absorbed water molecules in the synthesized samples. The vibrational band due to the stretching vibration of the hydrogen-bonded OH appeared near the wavenumber 2346.48 cm^{-1}. Moreover, the vibrational band present near the wavenumber 1527.82 cm^{-1} might be due to the bonding interaction between O-H and synthesized ferrite NPs [244]. The complete evacuation of the nitrates (N-O stretching vibration) in our synthesized samples was affirmed by the nonappearance of vibrational bands near the wavenumber 1100 cm^{-1}. The complete evacuation of the citric acid during sintering was affirmed by the nonappearance of vibrational bands near to the wavenumber 1385, 1572, and 3137 cm^{-1} hence portraying the faultlessness of our synthesized spinel ferrite and verifies our XRD results [225].

6.3.3. FESEM Study

The FESEM was utilized to contemplate the morphological characteristics and particle size (average) of the synthesized spinel ferrite. Fig. 6.6 (x = 0.0 - Co-Zn spinel ferrite , x = 0.1, 0.2, 0.3, and 0.4 - Mn doped Co-Zn spinel ferrite) displays the FESEM micrographs along with the particle size histogram of the incorporated samples. The micrographs of all the incorporated samples reveal the compact arrangement of the grains which were agglomerated, inhomogeneous in size and shape, and having non-uniform grain growth, which is by all accounts a mark of gel formation after subsequent heating a solution during spinel ferrite synthesis [97]. The observed agglomeration in the FESEM micrograph is mainly because of the magnetic interaction between the NPs and due to the inaccessibility of surfactant during the synthesis process [238]. As apparent from FESEM micrographs, the grains of all the samples were in nanoscale range with distinctive voids and pores which could be ascribed to the emission of gases (CO_2, NO_2, H_2O, etc.) during the synthesis [293,294]. These pores in the synthesized spinel ferrite were helpful for the gas detecting applications on account of the huge explicit surface area of the (nanosized) grains. For the incorporated samples with different Mn content, the particle size (average) was assessed from the histogram which is formed from the FESEM micrograph using ImageJ software. The particle size (average) of all the samples lies in the nanoscale range. The particle size (average), determined by the histogram was noticed out to be larger than the crystallite size (D) which uncovers that, the crystallites of different sizes with strong magnetic interaction agglomerates to form a particle of different sizes [261,295].
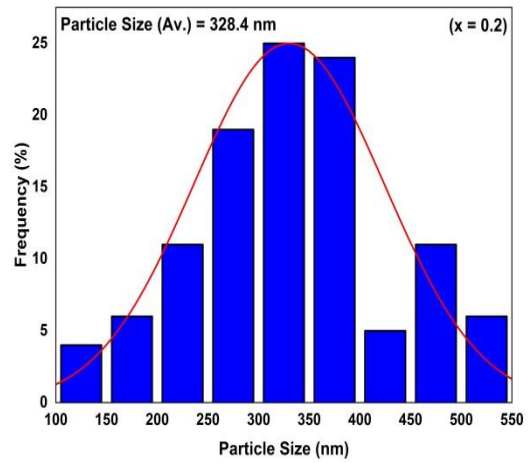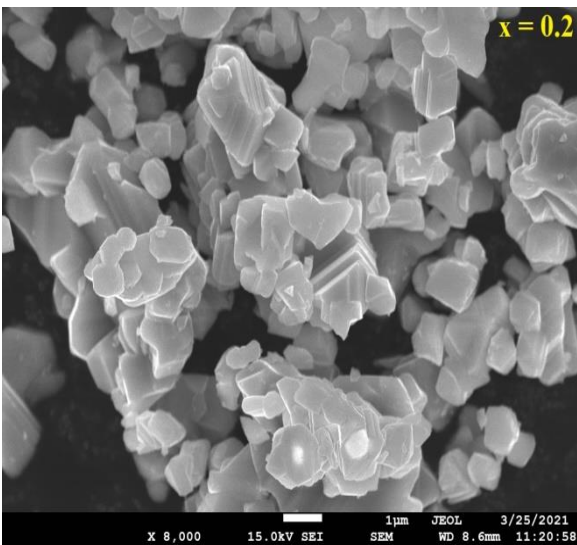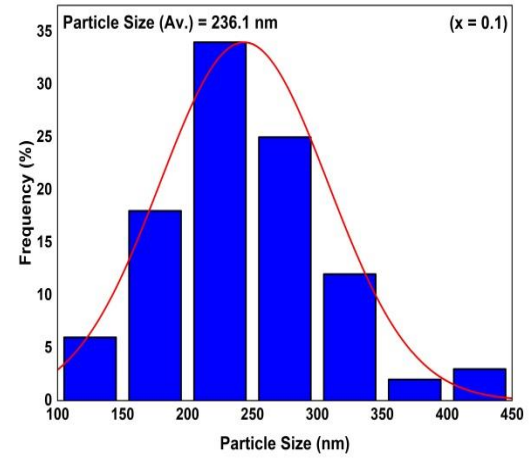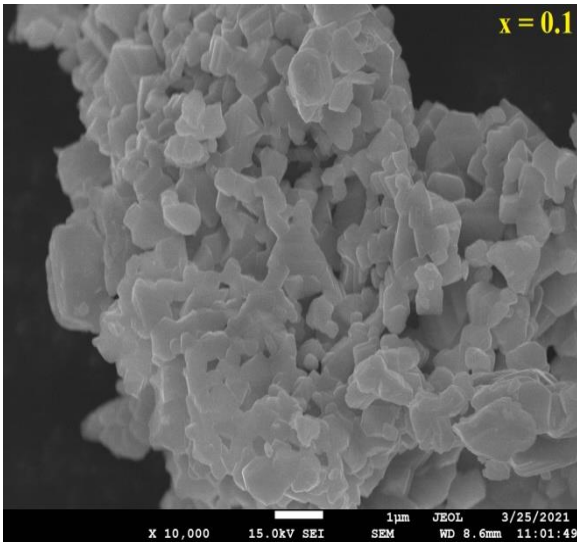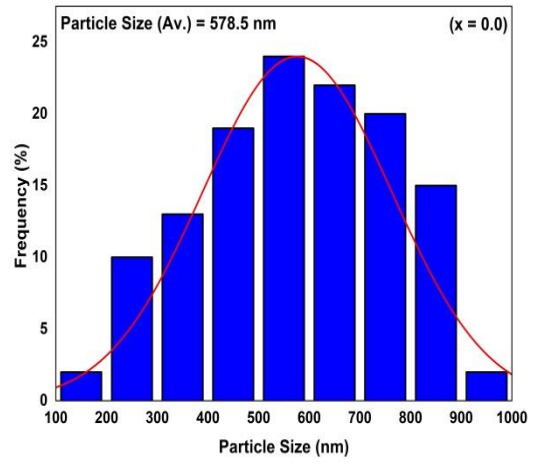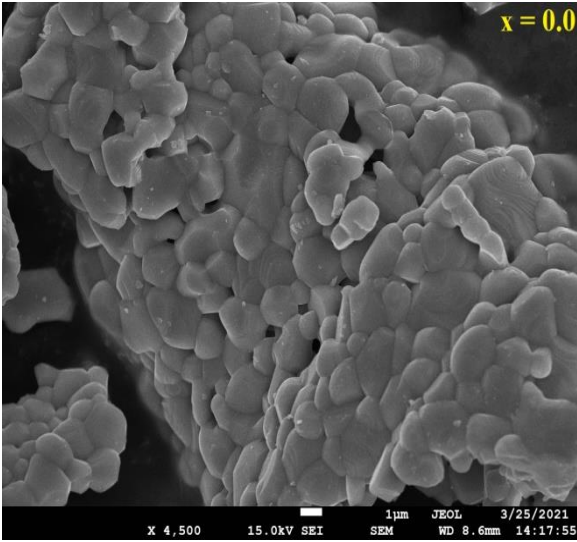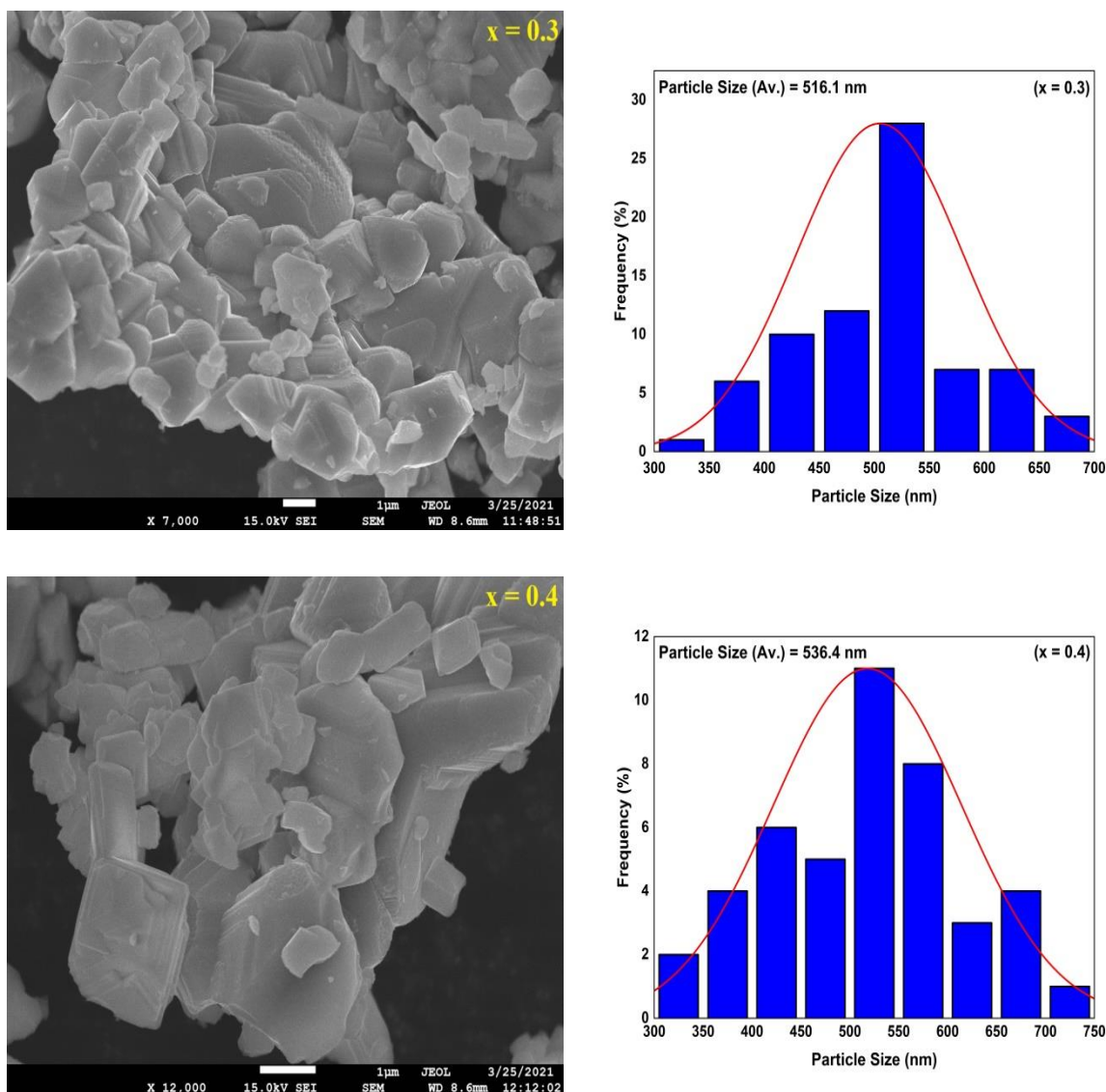
Fig. 6.6. FESEM micrograph and particle size histogram of $Mn_xCo_{0.5-x}Zn_{0.5}Fe_2O_4$ samples.

6.3.4. EDX Study

EDX spectra (Fig. 6.7) certify the composition and the stoichiometric proportion of the incorporated samples. Undoped Co-Zn ferrite (x = 0.0) exhibits peak for elements viz. Co, Zn, Fe and O and for Mn doped Co-Zn ferrite (x = 0.1, 0.2, 0.3, and 0.4) exhibits peak for elements viz. Mn, Co, Zn, Fe, and O. Fig. 6.8 delineates the elemental mapping for an undoped sample which avows the existence of the elements viz. Co, Zn, Fe. and O and their uniform dissemination in the specific spinel ferrite. Table 6.3 reports the atomic percent (At. %) values of the incorporated samples, theoretically and experimentally from EDX spectra. The crystalline defect in the incorporated samples results to a slight variation in the theoretical and experimental values of the atomic percent (At. %) [243,296]. For all the

samples it was scrutinized that the theoretical values of the atomic percent (At. %) were in close concordance with the experimental values from EDX spectra and hence affirms the impeccability of our synthesized (spinel ferrite) NPs.
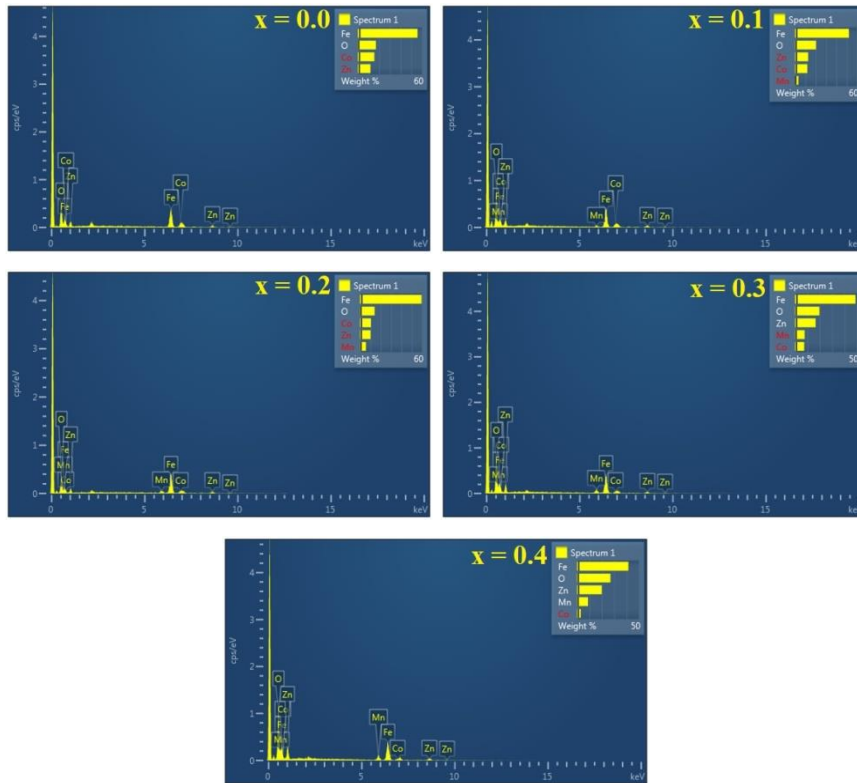
Fig. 6.7. EDX spectra of $Mn_xCo_{0.5-x}Zn_{0.5}Fe_2O_4$ samples.
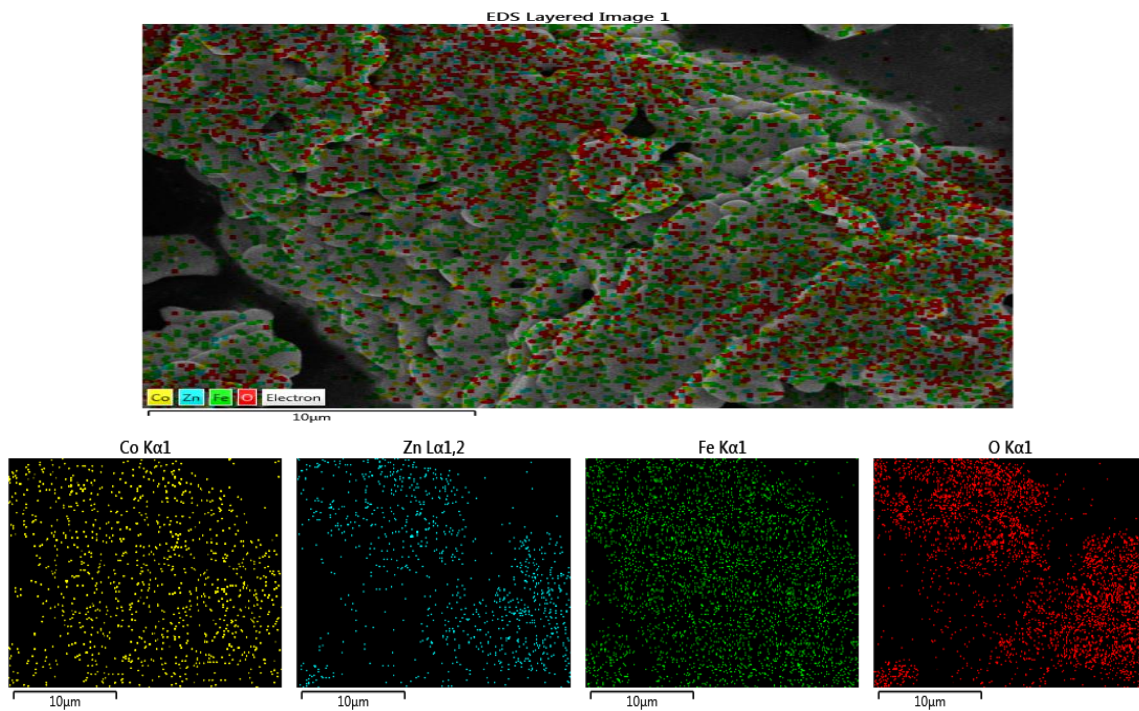
Fig. 6.8. Elemental mapping for undoped sample.

Table 6.3
Experimental and theoretical values of At. % of $Mn_xCo_{0.5-x}Zn_{0.5}Fe_2O_4$ samples.

Mn Concentration (x)	Value	Elements At. %					Total At. %
		Mn	Co	Zn	Fe	O	
0.0	Experimental	0	10.50	7.22	39.97	42.30	100
	Theoretical	0	7.14	7.14	28.57	57.14	100
0.1	Experimental	2.18	7.54	7.26	35.22	47.80	100
	Theoretical	1.42	5.71	7.14	28.57	57.14	100
0.2	Experimental	4.31	7.49	6.51	44.80	36.89	100
	Theoretical	2.85	4.28	7.14	28.57	57.14	100
0.3	Experimental	5.35	4.77	9.68	33.39	46.82	100
	Theoretical	4.28	2.85	7.14	28.57	57.14	100
0.4	Experimental	5.45	1.70	10.37	25.24	57.24	100
	Theoretical	5.71	1.42	7.14	28.57	57.14	100

6.3.5. VSM Study

Magnetic investigation at the room temperature of the incorporated samples has been performed by the vibrating sample magnetometer (VSM), having the magnetic field in the range of $\pm$ 20 KOe. Table 6.4 interprets the values of magnetic parameters [saturation magnetization (M_s), remnant magnetization (M_r), coercivity (H_c), squareness ratio (R), anisotropy constant (K_1), and magnetic moment (n_B)]. These parameters were typically influenced by the microstructure, non-alignment of magnetic moments at the octahedral site, grain size, exchange interactions, and presence of the metal (divalent or trivalent) cations at the lattice sites [297-299]. The M-H curve of the incorporated samples (Fig. 6.9) with different Mn content presents an S-shaped hysteresis curve, which uncovers the attributes like that of the ferromagnetic material. The undoped Co-Zn sample achieves the saturation magnetization of 77.31 (emu/g) which is particularly higher than the Mn doped Co-Zn samples and is all around concurred with the revealed values of Co-Zn (spinel ferrite) NP prepared by sol-gel technique. Table 6.4 presents variability in the saturation magnetization with the Mn content and noticed the decrement from 77.31 (x = 0.0) (emu/g) to 56.28 (x =

0.4) (emu/g), the lowest value observed to be 54.80 (x = 0.3) (emu/g). This abatement in the saturation magnetization is a direct result of the crystallite size miniaturization. When the size of the particle changes from bulk to nanoscale, the saturation magnetization diminishes with diminishing the size of the NPs because of the presence of some level of the spin canting in the entire volume of the NPs [300]. Within this critical size, the magnetic domains of the structure changes from multi-domain to single-domain state [301]. Hence the decline in the saturation magnetization can be clarified by the speculation of the magnetic dead sheets (disarray of spins) on the surface of the incorporated NPs [302]. In addition, this diminishing in the saturation magnetization with the Mn content can likewise be clarified dependent on the superexchange interaction (A-A, B-B, and A-B) which occurs in the crystal lattice, and is reliable with Neel's sublattice model. As Mn exhibits non-magnetic behavior, so it can possess any of the site (A or B), yet it has a solid inclination to possess the B-site [303,304], which will bring about the reduction in the magnetization of the B-site whereas, the magnetization of the A-site would stay as before. This will cause the comprehensive decline in the magnetization of the incorporated samples as net saturation magnetization (M_s) is the difference of magnetization between the two lattice sites, $M = |M_A - M_B|$. M_A and M_B represent the magnetizations for tetrahedral and octahedral sites respectively [237,245]. The value of coercivity obtained from VSM results varies with several factors viz. size, morphology, microstrain, and anisotropy constant of the incorporated samples. The Browns relation presented in Eq. (6.6) uncovers the inverse connection of coercivity (H_c) and saturation magnetization (M_S) [227,249,286].

$$H_c = \frac{0.96 \times K_1}{M_S} \qquad\qquad (6.6)$$

Table 6.4 displays the increasing and decreasing pattern of coercivity (H_c) with Mn content because of the anomalous behavior in the anisotropy constant determined by Eq. (6.6). The value of the coercivity is higher for the undoped sample when contrasted with the doped samples which can be clarified dependent on the electronic configuration of metal (divalent) cations viz. Mn ($3d^5$) and Co ($3d^7$). The Mn metal (divalent) cation prompts in quenching of the orbital angular momentum (l = 0) and the reduction in the anisotropy constant will happen which will reduce the coercivity of the doped samples. The value of the coercivity reported in Table 6.4 reveals the magnetic soft nature of the synthesized sample due to which it is helpful in electromagnetic radiation material, sensors, switching, multilayer

chip indicators, hyperthermia, and power application. The squareness ratio for all the samples can be calculated by the formulae given in Eq. (6.7).

$$R = \frac{M_r}{M_S} \qquad (6.7)$$

The value of squareness ratio for all the samples in Table 6.4 was found to be under 0.5 which demonstrates the existence of haphazardly or randomly oriented small single domain assembly of (spinel ferrite) NPs [225,227] and reveals the magnetostatic interaction between the NPs [244]. Eq. (6.8) uncovers the direct connection of magnetic moment (n_B) and saturation magnetization (M_s) [227,243,244].

$$n_B = \frac{M_s \times MW}{5585} \qquad (6.8)$$

As saturation magnetization reduces with the Mn content, the reduction in the magnetic moment will occur which brings about debilitating of the A-B exchange interaction [97,227,249] and cause the disorder of consecutive magnetic spin in the crystal structure of the incorporated (spinel ferrite) NP.
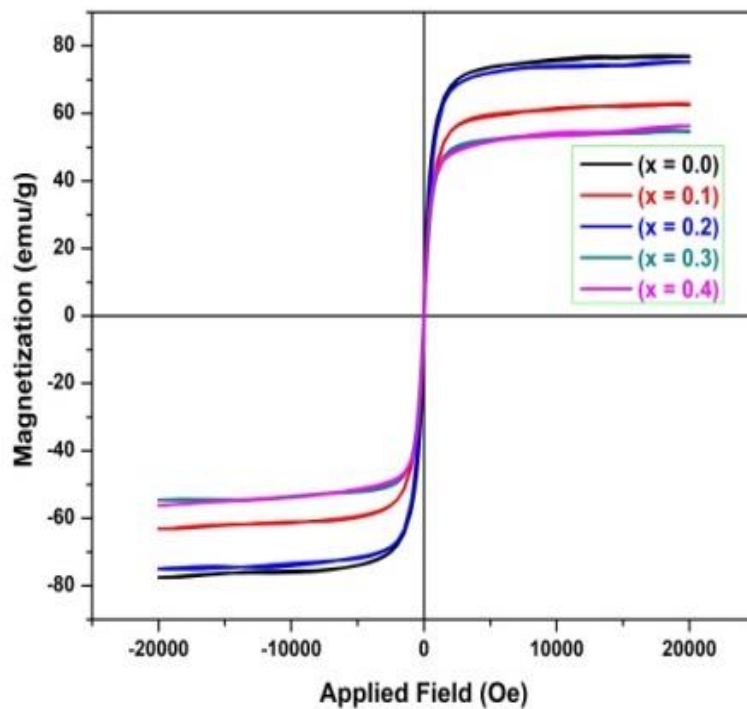
Fig. 6.9. M-H curve of $Mn_xCo_{0.5-x}Zn_{0.5}Fe_2O_4$ samples.

Table 6.4

Magnetic parameters of $Mn_xCo_{0.5-x}Zn_{0.5}Fe_2O_4$ samples.

Mn Concentration (x)	M_s (emu/g)	M_r (emu/g)	H_c (Oe)	R	K_1 (erg/cc)	n_B (μ_B)
0.0	77.31	5.32	34.63	0.06	2789.61	3.29
0.1	63.03	2.38	28.80	0.03	1890.93	2.67
0.2	75.30	3.34	31.31	0.04	2456.58	3.19
0.3	54.80	1.54	18.07	0.02	1032.18	2.32
0.4	56.28	1.94	16.01	0.03	938.97	2.38

6.4. Conclusion

$Mn_xCo_{0.5-x}Zn_{0.5}Fe_2O_4$ (spinel ferrite) nanoparticles with various stoichiometric ratios were effectively synthesized by the sol-gel auto combustion technique. The increase in the lattice constant from 8.434 to 8.457 Å with the Mn content may be ascribed to the ionic radius of Mn^{2+} ions being larger than that of Co^{2+} ions. The complete evacuation of the nitrates and citric acid from the incorporated samples was avowed by the FTIR spectra. The synthesized samples can be valuable for the gas sensing application because of the porous morphology exhibited by all the FESEM micrographs. The atomic percent (At. %) values, determined utilizing EDX spectra were in close concordance with the theoretical values, thus affirms the impeccability of the synthesized samples. The magnetic soft nature of the incorporated samples makes them suitable for electromagnetic radiation material, sensors, switching, multilayer chip indicators, hyperthermia, and power application. The squareness ratio for all the samples was noticed to be less than 0.5 which affirms the existence of the random oriented small single domain assembly of (spinel ferrite) nanoparticles and reveals the magnetostatic interaction between the nanoparticles. Moreover, the synthesized ferrite has a large surface area, appropriate pore size, pore size dissemination, and the presence of the functional group which complements its utilization in the supercapacitor electrode material.

CHAPTER-7

Effect of Sintering Temperature on Structural, Morphological, and Magnetic Properties of $Mn_{0.3}Co_{0.2}Zn_{0.5}Fe_2O_4$ Ferrite

Abstract

The sol-gel methodology was exploited for the preparation of $Mn_{0.3}Co_{0.2}Zn_{0.5}Fe_2O_4$ ferrite nanoparticles (NPs), at different sintering temperatures (750, 950, and 1150 ^{o}C). The nanometer size crystallites were evaluated utilizing the Debye Scherrer formulae. The two bands manifested in FTIR spectra near 600 cm^{-1} (tetrahedral site) and 400 cm^{-1} (octahedral site) ratify the formation of spinel structure for all sintering temperatures. The FESEM micrographs measure the average particle size by using ImageJ software and reveal the agglomerated grains, which are inhomogeneous in shape and size. EDX study confirms the stoichiometry and composition of the synthesized samples. With the enhancement in the sintering temperature, the enhancement in the saturation magnetization was perceived in the magnetic studies by using VSM. For all incorporated samples the squareness ratio was assessed to be under 0.5 that assimilates to a multi-domain structure.

7.1. Introduction

Throughout the ongoing years, our general public is overseeing unbelievable issues related to energy storage in reduced size [305]. Nonetheless, the improvement of energy storage systems is lingering behind the fast progression in electrical-powered industries [306]. Nowadays the energy storage system in, convenient electronic gadgets like smartphones, smartwatches, cameras, portable PCs, headphones, calculators, tablets, and so forth request the utilization of those energy storage systems which have featherweight, pliable, cost-efficient, and eco-friendly [307]. The energy storage systems viz. batteries and the conventional capacitors had broadly utilized, inferable from the minimal expense and better execution, yet these storage systems are not able to satisfy the genuine energy demands of hand-held electronic gadgets, hybrid automobiles, and various end-user electrical appliances, and so forth [308]. In addition, these energy storage systems viz. batteries and conventional capacitors both have their astounding benefits and negative marks [309]. The batteries have high energy density than the conventional capacitors while the conventional capacitors have high power density than the batteries [310]. In a conventional capacitor, the

maximum energy storage is not possible due to the small surface area [311]. Therefore the researchers are too much concentrating on finding those materials which have high energy storage capacity and which can deliver maximum power [9]. In light of this, one of the best contenders to the above-mentioned systems are the supercapacitors (SCs) which form a bridge between the batteries and conventional capacitors [312]. Moreover, these SCs are cost-effective as well as environmentally safe and have superior efficiency, longer charge-discharge cycle, greater shelf life, and excellent power density [10,313,314].

The three main factors viz. electrolyte, substrate, and active material are mainly accountable for the electrochemical activity of the SCs [315,316]. In SCs, the energy can be stored in two ways as capacitive (electrolytic double-layer capacitor) nature and pseudocapacitive (pseudocapacitor) nature contingent on the active material and charge storage procedure [317]. Carbon-based materials (active material) are utilized in the electrolytic double-layer capacitor and the storage is attributable to the adsorption of the electrolytic ion on the electrode-electrolyte interface which does not involve faradic reaction and hence leads to high power density [318]. Metal oxides (active material) are utilized in the pseudocapacitor and the storage is attributable to the reverse faradic reaction which emerges at the electrode-electrolyte interface as well as because of the incalation of cations from the electrolyte material used which helps in achieving greater capacitance and energy densities than an electric double-layer capacitor [319].

Among the several metal oxides, RuO_2 is the most incredible known material for the pseudocapacitive electrode which yields an excellent value of specific capacitance, high electrical conductivity, and reversible charge-discharge properties but there arise some difficulties in the use of RuO_2 as an electrode material because it is highly toxic and too much expensive [38]. These above difficulties can be developed by the use of the potential candidate spinel ferrite (MFe_2O_4, M = divalent metal) or doped spinel ferrite material because of the large-scale production, low cost, flexibility in the structure, morphology, and eco-friendly nature [134]. Besides the spinel ferrites had anticipated applications in various fields viz. medical sciences [194], catalysts [140], pollution control [196], sensors [197], data storage system [198], microwave absorbing materials [199], microelectronics [202], etc, but it can also be used as active material in the SC electrode for superior electrochemical activity as compared to single metal oxide [114,117,146,320]. In spinel ferrite, various factors viz. composition, synthesis procedure, temperature, etc. are responsible for the existence of cations in the tetrahedral and octahedral sites [206,207]. Out of the several nanomaterials synthesis procedure [219,221-224,321], the sol-gel procedure is favored on account of the

ease of synthesis, cost-effective, minimal time, uniformity, low temperature, reliability, facile formation of films, superior deposition, and nanoscale formation of the product [225,226].

Several spinel ferrites, such as $Ni_{0.6}Cu_{0.2}Zn_{0.2}Fe_2O_4$, $Al_{0.2}Cu_{0.4}Co_{0.4}Fe_2O_4$, $Ni_{0.8}Zn_{0.2}Al_{0.1}Fe_{1.9}O_4$, etc. were synthesized at various sintering temperatures and subsequently examined for use in the SCs. However, for $Mn_{0.3}Co_{0.2}Zn_{0.5}Fe_2O_4$ no structural, morphological, magnetic, or electrochemical research have been conducted so far. Before investigating the material for energy storage application it is vital to first investigate its structural, morphological, and magnetic properties at different temperatures. With this in mind, the current work uses a facile sol-gel procedure to synthesize and investigate the structural, morphological, and magnetic properties of $Mn_{0.3}Co_{0.2}Zn_{0.5}Fe_2O_4$ ferrite NPs at varied sintering temperatures (750, 950, and 1150 ^{o}C).

7.2. Experimental Procedures

For the preparation of $Mn_{0.3}Co_{0.2}Zn_{0.5}Fe_2O_4$ AR grade chemicals were utilized. The metal nitrates (viz. $Mn(NO_3)_2 \cdot 6H_2O$, $Co(NO_3)_2 \cdot 6H_2O$, $Zn(NO_3)_2 \cdot 6H_2O$, and $Fe(NO_3)_3 \cdot 9H_2O$) and citric acid in 1:1 proportion were weighted as per the required stoichiometry and mixed in 100 ml of distilled water. The pH of the above solution was maintained at 7 by adding NH_4OH in a drop-wise manner. After continual stirring and heating, the solution at 120 ^{o}C for 4 h the gel was formed. The fluffy brown powder was procured by heating the gel at 100 ^{o}C until self-ignition and then blended utilizing mortar and pestle. The blended powder so obtained was sintered in the muffle furnace at three different temperatures viz. 750, 950, and 1150 ^{o}C for 4 h. XRD (PANalytical X'Pert Pro) having Cu-Kα (1.5406 Å) target was exploited for the phase investigation of the incorporated samples. FTIR (SHIMADZU) was employed for the examination of the various molecular bonds, spinel structure, and purity of the prepared samples. The surface morphological properties and stoichiometry of the samples were inspected with FESEM (JEOL) and EDX (OXFORD) respectively. The magnetic properties of the samples were scrutinized at room temperature with VSM (Lake Shore).

7.3. Results and Discussion

7.3.1. XRD Study

7.3.1.1. Phase Investigation

The X-ray diffraction pattern for the samples sintered at 750, 950, and 1150 ^{o}C was illustrated in Fig. 7.1 having a diffraction angle between 20° to 70° with 0.02^o step size. For lower temperatures viz. 750 and 950 ^{o}C two types of peaks were perceived which relate to spinel and α-Fe$_2$O$_3$ (marked with asterisk * symbol) phases [322]. The incompletion of the self-ignition process at lower temperatures prompts to the α-Fe$_2$O$_3$ phase [323]. The α-Fe$_2$O$_3$ phase totally vanished at 1150 ^{o}C and the one and only spinel phase with fcc arrangement was manifested, having diffraction peaks indexed as (220), (311), (222), (400), (422), (511), and (440). These peaks evince the space group of Fd-3m and are ascribed with the single-phase cobalt and zinc spinel ferrite bearing ICDD no. 22-1086 and 89-1009 respectively [97,283]. The existence of the pure spinel phase at 1150 ^{o}C indicates that increasing sintering temperature leads to the crystallization formation, homogeneity, and completion of the self-ignition process. Moreover, with the increase in sintering temperature, it was noticed that the intensity of the diffraction peaks also increases which reveals that high sintering temperature is required for the crystallization of the Mn$_{0.3}$Co$_{0.2}$Zn$_{0.5}$Fe$_2$O$_4$ ferrite.
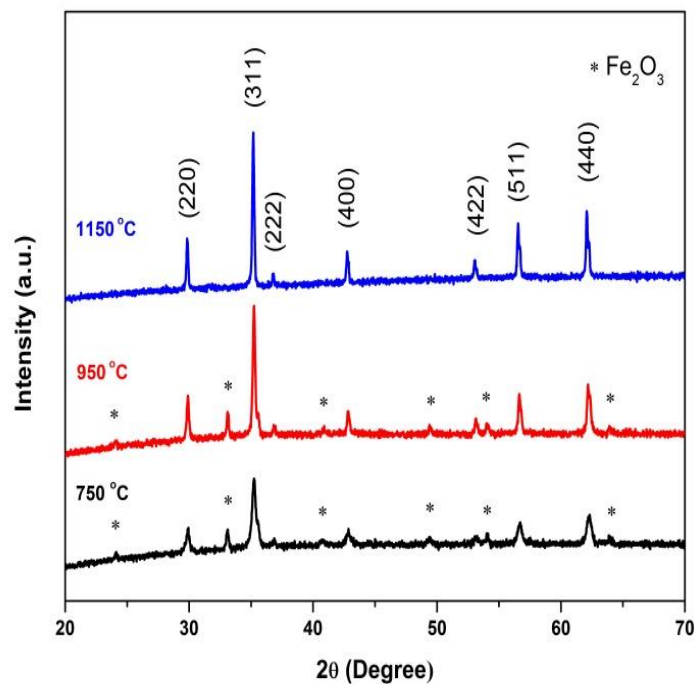
Fig. 7.1. X-ray diffraction pattern of Mn$_{0.3}$Co$_{0.2}$Zn$_{0.5}$Fe$_2$O$_4$ samples.

7.3.1.2. Lattice Parameters

For all incorporated samples Table 7.1 records the lattice parameters viz. interlayer spacing (d), lattice constant (a_o), unit cell volume (V_{cell}), and crystallite size (D). Bragg's law was utilized for the evaluation of interlayer spacing (d) and lattice constant (a_o) mentioned in Eq. (7.1) and Eq. (7.2) respectively [229,284].

$$D = \frac{n\,\lambda}{2\,Sin\theta} \tag{7.1}$$

$$a_o = d\sqrt{h^2 + k^2 + l^2} \tag{7.2}$$
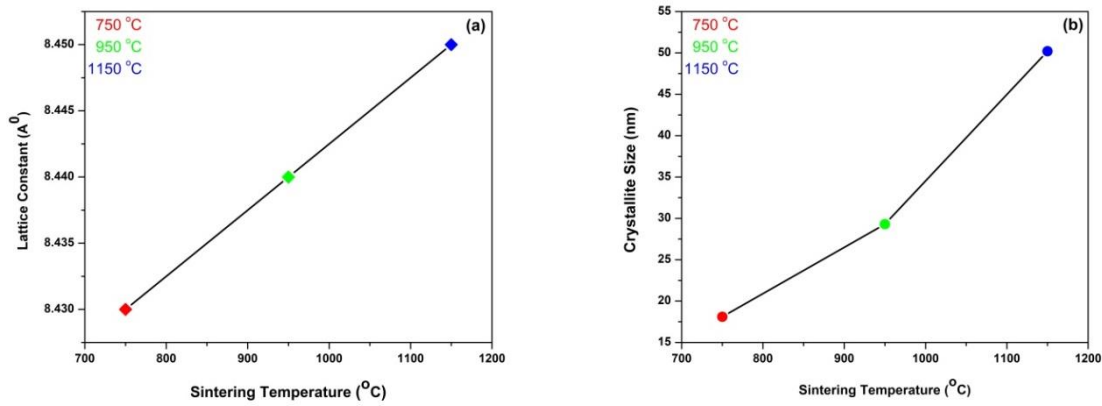
Fig. 7.2. (a) Lattice constant, and (b) Crystallite size as a function of sintering temperature.

Here n (1) depicts the order of the diffraction, λ (1.5406 Å) signifies the wavelength of the X-ray, θ corresponds to high intense peak angle, and (hkl) represents the miller indices. With the enhancement in the sintering temperature the enhancement in the lattice constant from 8.43 Å (750 ^{o}C) to 8.45 Å (1150 ^{o}C) was perceived in Fig. 7.2(a) which subsequently enhances the volume of the unit cell as $V_{cell} = (a_o)^3$. This connotes that the sintering temperature prompts the expansion of $Mn_{0.3}Co_{0.2}Zn_{0.5}Fe_2O_4$ unit cell. The change in the oxidation state and distribution of cations in the lattice sites were responsible for the increment in the lattice constant. During sintering, the reduction of iron (Fe) takes place from Fe^{3+} (0.64 Å) to Fe^{2+} (0.76 Å) thereby enhancing the lattice constant [324]. The Debye-Scherrer formula referred in Eq. (7.3) was employed to higher intensity peak (311) for the evaluation of crystallite size (D) [230].

$$D = \frac{0.9\,\lambda}{\beta\,Cos\theta} \tag{7.3}$$

Here β signifies full width at half maximum (FWHM) of the higher intensity peak. Fig. 7.2(b) displays an increasing trend of crystallite size (D) from 18.1 to 50.2 nm with temperature. With the enhancement in the sintering temperature agglomeration may occur which was accountable for the enhancement of the crystallite size.

7.3.1.3. Porosity

The porosity in the sample arises due to the difference in the X-ray density (D_x) and the bulk density (D_b). For all incorporated samples Table 7.1 records the value of X-ray density, bulk density, and porosity by utilizing Eq. (7.4), Eq. (7.5), and Eq. (7.6) respectively [91,325-327].

$$D_x = \frac{Z(MW)}{N_A V} \tag{7.4}$$

$$D_b = \frac{m}{\pi r^2 t} \tag{7.5}$$

$$P = \left(\frac{D_x - D_b}{D_x}\right) \times 100 \tag{7.6}$$

In X-ray density Z, MW, N_A, and V signifies the number of molecules in the unit cell, molecular weight of the synthesized spinel ferrite, Avogadro's number (6.023×10^{23}), and unit cell volume respectively. Whereas in bulk density m, r, and t depicts the mass, radius, and thickness of the prepared pellets. With the increment in the sintering temperature, the decrement in the X-ray density from 5.233 (750 ^{o}C) to 5.202 (1150 ^{o}C) g/cm^3 was perceived which may be due to the expansion of the crystal lattice. The bulk density was noticed to be higher (2.770 g/cm^3) for the sample sintered at 1150 ^{o}C. The defect in the grain shape by virtue of the sintering and several synthesis parameters was responsible for porosity in the synthesized spinel ferrite. For all incorporated samples the excellent porosity (%) in the range of 46.75 to 61.10 % was achieved. These pores were beneficial for the energy storage application on account of the ease of access of electrolyte to the electrode.

7.3.1.4. Specific Surface Area

For all incorporated samples, the specific surface area (S) was tabulated in Table 7.1 utilizing Eq. (7.7) [328].

$$S = \frac{6000}{DD_x} \tag{7.7}$$

The outstanding specific surface area was procured for all the samples, resulting in additional active sites for the ion-electron transport and adsorption-desorption process in the SCs. With the increment in the sintering temperature, the decrement in the specific surface area from 63.156×10^7 (750 °C) to 22.933×10^7 (1150 °C) cm^2/g was noticed. The predominant factor accountable for the variety of the specific surface area is the crystallite size (D). This signifies that increasing the sintering temperature of the synthesized spinel ferrite leads to a decrease in the appearance of the atom on the surface of the sample [329].

7.3.1.5. Lattice Strain

The lattice strain (ε) in the incorporated samples arises during the synthesis and sintering treatment process. The lattice strain (ε) was evaluated by Eq. (7.8) [330] and presented in Table 7.1.

$$\beta Cos(\theta) = \frac{0.9 \lambda}{D} + 4\varepsilon Sin(\theta) \qquad (7.8)$$

With the expansion in the sintering temperature, the strain in the lattice diminishes, which may be credited to the development and improvement towards the pure spinel phase structure without any extra impurity present in it.

Table 7.1
Structural parameters of $Mn_{0.3}Co_{0.2}Zn_{0.5}Fe_2O_4$ samples.

T (°C)	2θ (°)	d (Å)	β (°)	a_0 (Å)	V (Å)^3	D (nm)	Phase	D_x (g/cm^3)	D_b (g/cm^3)	P (%)	S×10^7 (cm^2/g)	ε×10^{-3}
750	35.25	2.544	0.4591	8.43	600.70	18.1	Spinel + Fe$_2$O$_3$	5.233	2.085	60.16	63.156	6.305
950	35.24	2.545	0.2837	8.44	601.25	29.3	Spinel + Fe$_2$O$_3$	5.228	2.033	61.10	39.064	3.898
1150	35.18	2.549	0.1657	8.45	604.23	50.2	Spinel	5.202	2.770	46.75	22.933	2.281

7.3.2. FTIR Study

The structural investigation along with the presence of the various functional groups and molecular bonds which remain during the synthesis were studied with FTIR, possess wavenumber of 400 to 4000 cm^{-1}. Fig. 7.3 manifest FTIR spectra for $Mn_{0.3}Co_{0.2}Zn_{0.5}Fe_2O_4$ samples sintered at 750, 950, and 1150 ^oC for 4 h. On account of the M-O vibrations, two absorption bands were observed near 541.11 cm^{-1} and 404.66 cm^{-1} which were designated with ν_1 (tetrahedral site) and ν_2 (octahedral site) respectively, and affirms the spinel structure of $Mn_{0.3}Co_{0.2}Zn_{0.5}Fe_2O_4$ samples [291]. The variability in the position of the bands emerges by virtue of the variety in the bond length of M-O [292]. For all the samples the band near 2400 cm^{-1} was observed, which is attributed to the presence of the CO_2 even for high sintering temperature (1150 ^oC). The band observed near the 3700 cm^{-1} is attributed to the stretching vibration (O-H) in water molecules which get diminished with the sintering temperature. The bands perceived near 1100 cm^{-1} and 2900 cm^{-1} ascribes to the existence of nitrates and moisture respectively in the samples sintered at 750 ^oC and 950 ^oC [329,331,332]. These bands (near 1100 cm^{-1} and 2900 cm^{-1}) were disappeared for the sample sintered above the 950 ^oC, which clarifies that the expansion in the sintering temperature prompts the development of the unadulterated spinel ferrite as likewise affirmed from the XRD.
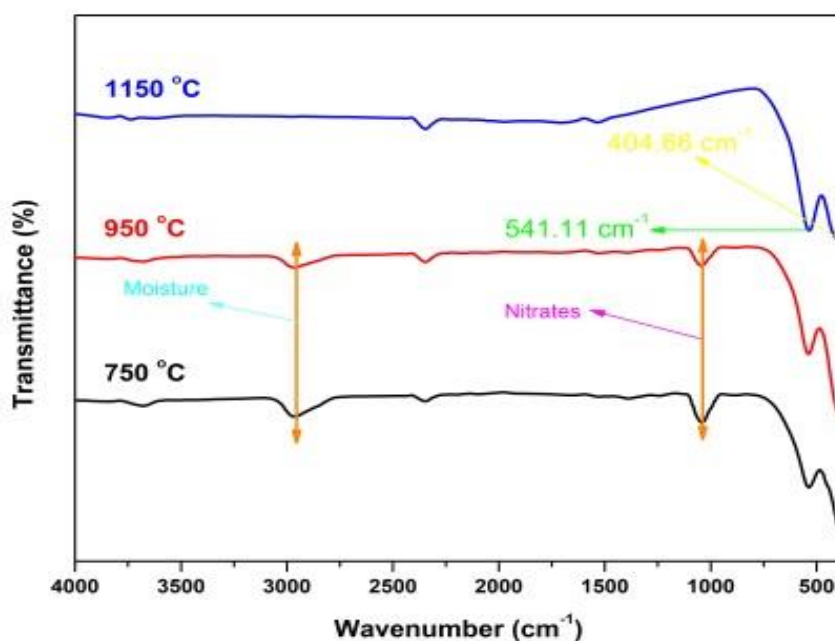
Fig. 7.3. FTIR spectra of $Mn_{0.3}Co_{0.2}Zn_{0.5}Fe_2O_4$ samples.

7.3.3. FESEM Study

FESEM micrograph and particle size histogram of $Mn_{0.3}Co_{0.2}Zn_{0.5}Fe_2O_4$ samples (Fig. 7.4) were employed for the examination of surface morphological properties and evaluation of the average size of the particle respectively. FESEM micrographs display the grains which were irregular in shape and size and had porous morphology. In the sol-gel procedure, the gas discharge during self-ignition leads to the existence of pores in $Mn_{0.3}Co_{0.2}Zn_{0.5}Fe_2O_4$ samples [293]. These pores strengthen the electrochemical activity and beneficial for the gas sensing application. The grains in the micrographs were appeared to agglomerate with the enhancement in the sintering temperature which might be the reason for the formation of larger particles at higher temperature (1150 ^oC). The interaction between magnetic NPs was responsible for these agglomerations [238]. The FESEM micrographs were utilized to calculate the particle size (average) with the help of ImageJ software. For all incorporated samples, the histogram was plotted for the estimation of the particle size (average). The increasing trend in the particle size (average) with temperature was perceived in Table 7.2. For all sintering temperature, it was observed that the particle size have a larger value than the crystallite size which is a clear indication that a large no of crystallites agglomerates, thereby resulting in the large particle size.
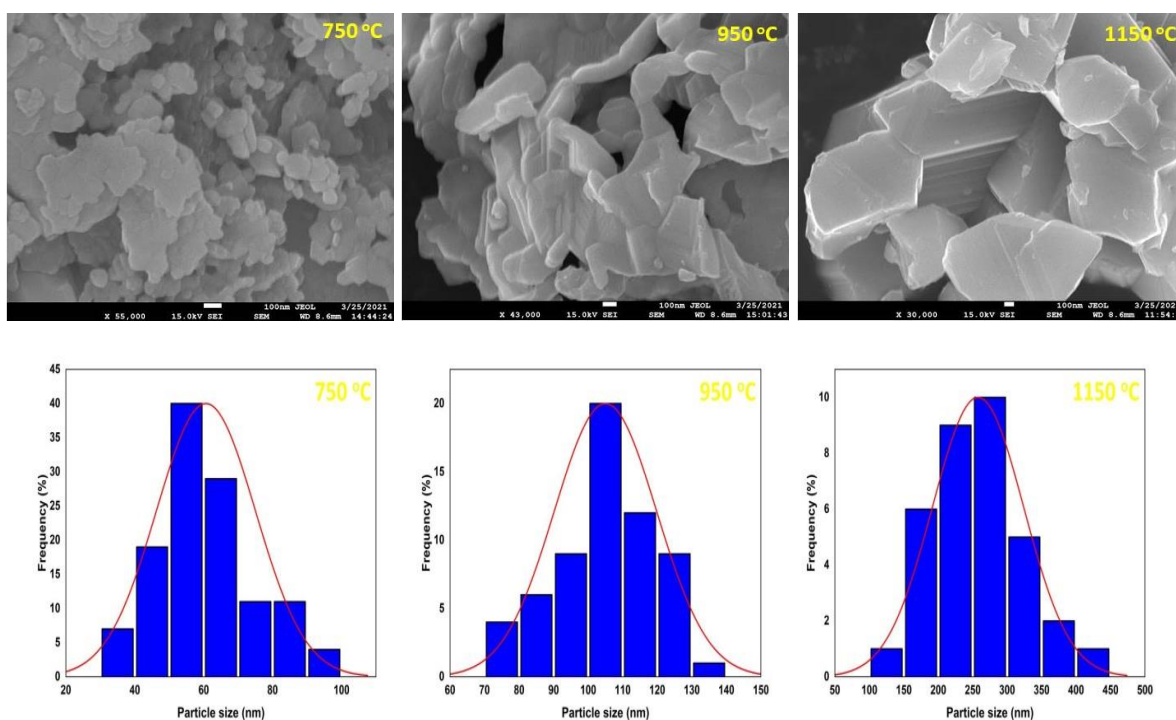
Fig. 7.4. FESEM micrograph and particle size histogram of $Mn_{0.3}Co_{0.2}Zn_{0.5}Fe_2O_4$ samples.

Table 7.2
Particle size (average) estimated from FESEM micrograph of $Mn_{0.3}Co_{0.2}Zn_{0.5}Fe_2O_4$ samples.

Sintering Temperature (^oC)	Particle Size (nm)
750	57.3
950	106.9
1150	250.4

7.3.4. EDX Study

The stoichiometry along with the elemental composition of the synthesized samples was investigated utilizing the EDX technique. Fig. 7.5 presents the EDX spectra of single-phase $Mn_{0.3}Co_{0.2}Zn_{0.5}Fe_2O_4$ sintered at 1150 ^oC. Peaks corresponding to Mn, Co, Zn, Fe, and O elements were manifested by the EDX spectra without the existence of any extra impurity peaks. These elements were uniformly distributed over the entire ferrite sample which gets affirmed with the elemental mapping as presented in Fig. 7.6. Table 7.3 reports the experimental along with the theoretical values of the Wt. % and At. % for the sample sintered at 1150 ^oC. The experimental Wt. % and At. % values had close estimation with the theoretical values as perceived in Table 7.3. Subsequently, EDX affirms the immaculateness of the ferrite NPs sintered at 1150 ^oC.
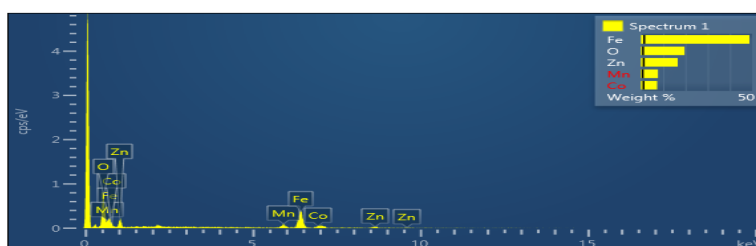
Fig. 7.5. EDX spectra of $Mn_{0.3}Co_{0.2}Zn_{0.5}Fe_2O_4$ sample at 1150 ^oC.
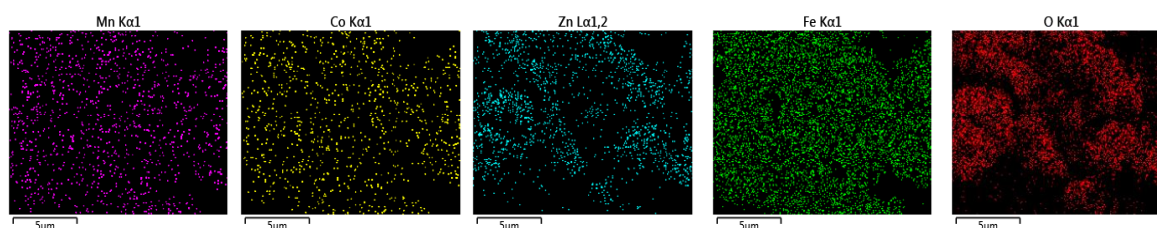
Fig. 7.6. Elemental mapping of $Mn_{0.3}Co_{0.2}Zn_{0.5}Fe_2O_4$ sample at 1150 ^oC.

Table 7.3

Experimental and theoretical values of Wt. % and At. % of $Mn_{0.3}Co_{0.2}Zn_{0.5}Fe_2O_4$ sample.

Sintering Temperature (^{o}C)	Wt. % and At. %	Values	Elements					Total %
			Mn	Co	Zn	Fe	O	
1150	Wt. %	Experimental	7.69	7.35	16.55	48.80	19.60	100
		Theoretical	6.96	4.98	13.81	47.19	27.04	100
	At. %	Experimental	4.24	3.66	8.57	32.28	51.26	100
		Theoretical	4.28	2.85	7.14	28.57	57.14	100

7.3.5. VSM Study

The magnetic investigation of the spinel ferrite synthesized at different sintering temperatures was performed utilizing the VSM technique. The M-H curve (Fig. 7.7) for all the samples under an applied field of $\pm$ 20 KOe, displays S-shaped symmetry which is attributed to the ferromagnetic material [333]. Table 7.4 reports the magnetic parameters [saturation magnetization (M_s), magnetic moment (n_B), remnant magnetization (M_r), coercivity (H_c), squareness ratio (R), and anisotropy constant (K_1)] of the sample at different sintering temperatures which are influenced by the composition of the incorporated samples, porosity and grain size. Fig. 7.8(a) displays an increase in the value of saturation magnetization from 23.163 to 53.695 emu/g with an increase in the sintering temperature. This enhancement in the saturation magnetization with temperature could be on account of the superexchange interaction (Fe-O-Fe) increment, grain boundaries abatement, and grain size inflation [325]. The saturation magnetization is also influenced by porosity. As porosity decreases, agglomeration occurs by virtue of the interaction between the magnetic particles, causing more and more magnetic moments to align, thereby resulting in saturation magnetization enhancement. As shown in Eq. (7.9) [244], the magnetic moment is determined by saturation magnetization. The magnetic moment also exhibits an increasing trend with the sintering temperature, just like saturation magnetization.

$$n_B = \frac{M_s \times MW}{5585} \qquad (7.9)$$

The variability in coercivity as a function of temperature was manifested in Fig. 7.8(b), with the highest value of coercivity being 21.348 Oe. This upgrade of the coercivity at 950 °C can be clarified based on the porosity as assessed in the XRD studies. The porosity for the sample sintered at 950 °C was found to be larger (61.10 %). These pores block the movement of the domain walls which requires a large magnetic field for their alignment, thereby causing the high coercivity at 950 °C. Owing to the low coercivity value presented in Table 7.4, all incorporated samples have a magnetic soft character, making them suitable for power applications, microwave absorbers, and electromagnetic radiation materials [248,249]. The squareness ratio was estimated by applying the formula referred in Eq. (7.10). The squareness ratio in all of the samples was under 0.5, indicating that the produced spinel ferrites had a multi-domain structure and strong interaction between the magnetic NPs [334].

$$R = \frac{M_r}{M_s} \qquad\qquad (7.10)$$
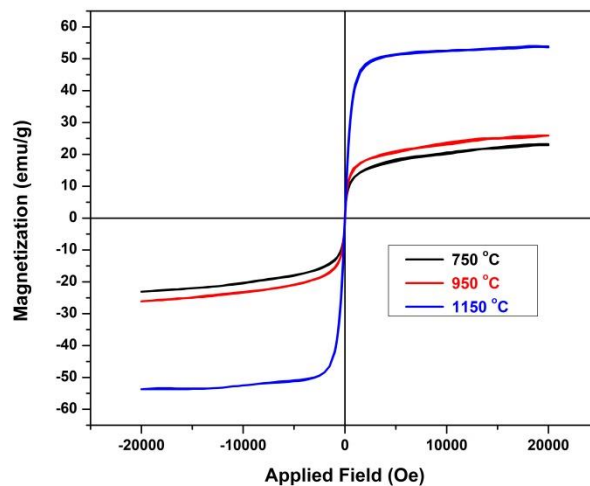
Fig. 7.7. M-H curve of $Mn_{0.3}Co_{0.2}Zn_{0.5}Fe_2O_4$ samples.

Due to the anisotropic morphology of the spinel ferrites at different temperatures, there arises the variation in the anisotropic constant as observed from Table 7.4. The maximum value of anisotropic constant, evaluated utilizing Brown's relation mentioned in Eq. (7.11) [247], was noticed to be 960.695 erg/cc at 1150 °C. The high value of saturation magnetization at 1150 °C may be the reason for achieving the high value of the anisotropic constant.

$$K_1 = \frac{M_s \times H_c}{0.96} \qquad\qquad (7.11)$$

Thus the magnetic characteristics of the prepared $Mn_{0.3}Co_{0.2}Zn_{0.5}Fe_2O_4$ could be controlled by adjusting the sintering temperature, and it can meet the criteria of hyper frequency application such as electrical filters, multi-layer chip indicators, and circulators [325].
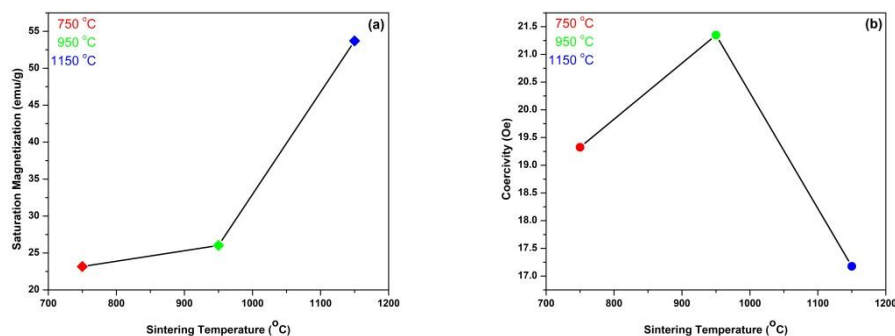
Fig. 7.8. (a) Saturation magnetization, and (b) Coercivity as a function of sintering temperature.

Table 7.4
Magnetic parameters of $Mn_{0.3}Co_{0.2}Zn_{0.5}Fe_2O_4$ samples.

Sintering Temperature (^{o}C)	M_s (emu/g)	n_B (μ_B)	M_r (emu/g)	H_c (Oe)	R	K_1 (erg/cc)
750	23.163	0.981	1.226	19.324	0.053	466.255
950	26.021	1.103	1.481	21.348	0.057	578.651
1150	53.695	2.275	1.449	17.176	0.026	960.695

7.4. Conclusion

$Mn_{0.3}Co_{0.2}Zn_{0.5}Fe_2O_4$ (spinel ferrite) was successfully synthesized at different sintering temperatures. Using the XRD technique, the enhancement in the lattice constant was detected as the sintering temperature increased, which is attributable to the reduction of iron (Fe) from Fe^{3+} (0.64 Å) to Fe^{2+} (0.76 Å). The pure spinel phase formation at 1150 ^{o}C was affirmed from the FTIR analysis due to the non-appearance of the nitrates, citric acid, and moisture peaks. With the increment in the sintering temperature, the agglomeration of the gains in the FESEM micrographs was observed due to the magnetic interaction between the

ferrite nanoparticle. Crystallite size was incremented from 18.1 to 50.2 nm by virtue of these agglomerations. FESEM study reveals, the increasing trend of particle size (average) in the nanoscale range with temperature, as estimated by the ImageJ software. The experimental Wt. % and At. % values had close approximation with the theoretical values as estimated by the EDX. For all incorporated samples, the ferromagnetic behavior was perceived on account of the S-shaped symmetry as per the M-H curve in the VSM study. Owing to low coercivity value, all samples have a magnetic soft character, making them suitable for power applications, microwave absorbers, and electromagnetic radiation materials. Our prepared spinel ferrites, magnetic characteristics can be modified by adjusting the sintering temperature, making them useful for high-frequency applications. Furthermore, these prepared ferrites had functional group availability, porous morphology, pore size dissemination, suitable pore size, and wide surface area, all of which contribute to its suitability for use as an active material for supercapacitor electrodes.

CHAPTER-8

Structural, Morphological, and Electrochemical Investigation of $Mn_{0.3}Co_{0.2}Zn_{0.5}Fe_2O_4$-Polyaniline Nanocomposite for Supercapacitor Application

Abstract

The present research deals in preparing $Mn_{0.3}Co_{0.2}Zn_{0.5}Fe_2O_4$ (spinel ferrite) by sol-gel procedure, polyaniline (PANI) by chemical oxidative method, and $Mn_{0.3}Co_{0.2}Zn_{0.5}Fe_2O_4$-PANI nanocomposite (NC) by physical blending method. X-ray diffraction (XRD) study affirms the formation of $Mn_{0.3}Co_{0.2}Zn_{0.5}Fe_2O_4$-PANI NC owing to the appearance of two different types of peaks: sharp $Mn_{0.3}Co_{0.2}Zn_{0.5}Fe_2O_4$ peaks, and broader PANI peaks. Fourier transform infrared spectroscopy (FTIR) of $Mn_{0.3}Co_{0.2}Zn_{0.5}Fe_2O_4$-PANI NC shows all characteristic vibrational bands, which are observed in the $Mn_{0.3}Co_{0.2}Zn_{0.5}Fe_2O_4$ and PANI spectra. Field emission scanning electron microscopy (FESEM) micrographs have been used to measure the average particle size by using ImageJ software. The encapsulation of the synthesized ferrite nanoparticle (NP) with the PANI matrix is exhibited by the FESEM micrograph of $Mn_{0.3}Co_{0.2}Zn_{0.5}Fe_2O_4$-PANI NC. The electrochemical activity of the novel $Mn_{0.3}Co_{0.2}Zn_{0.5}Fe_2O_4$-PANI NC is manifested to be higher as compared to their counterparts on account of synergistic impact, continual movement of electrons towards the electrode, and multiple redox reactions.

8.1. Introduction

The tremendous upgrades in ecological contamination and the ineluctable lack of fossil fuels are compelling researchers to foster perfect and economical energy storage gadgets. The quickly developing business sectors for portable electronic gadgets (smartphones, smartwatches, cameras, portable computers, headphones, calculators, tablets, and so forth), and electric as well as hybrid electric automobiles demand the usage of those energy storage systems which have a featherweight, pliable, cost-efficient, and eco-friendly [307]. The expanding interest in inexhaustible and eco-friendly energy is one of the incredible difficulties of the 21st century. At the present juncture, the most used energy storage gadgets are batteries, fuel cells, conventional capacitors, and supercapacitors (SCs) [335]. The usage of batteries and fuel cells for high-energy applications is principally a direct

result of their higher energy density. Nevertheless, it has the deficiencies of significant expense, short cycle life, complex gadget manufacturing process, lower power density, and shoddy security [336]. The fundamental benefits of the conventional capacitors are long cycle life and higher power density, yet it experiences lower-energy density than batteries and fuel cells. In this manner, the SC is considered as the superior decision in the energy storage application as it channels the batteries and conventional capacitors through their higher energy and power densities with a quick dynamic reaction, quick charge-discharge rate, superb cycling life expectancy, featherweight, eco-friendly, minimal expense, and functional security [313].

The SCs are fundamentally classified as electric double-layer capacitors, pseudocapacitors, and hybrid capacitors depending on the type of active material and charge storage strategy. In an electric double-layer capacitor carbon-based material (viz. carbon nanotubes, carbon aerogel, activated carbon, carbon fiber cloth, graphene, etc.) were utilized as an active material for the electrode. In this SC, the charge storage is a direct result of the electrostatic attraction which segregates the charge (electronic and ionic) across the electrode-electrolyte interface and results in the formation of the double-layer on each electrode. Whereas in the pseudocapacitor conducting polymer and metal oxides were utilized as an active material for the electrode. In the pseudocapacitor, the charge storage is a result of the electrochemical reverse faradic reaction which undergoes at the electrode-electrolyte interface. The hybrid capacitor is a combination of the electric double-layer capacitor and pseudocapacitor. This capacitor utilized composite material (either two or more than two components) as an active material for the electrode. In the hybrid capacitor, the charge storage is a result of the electrostatic double-layer formation and electrochemical reverse faradic reaction [318]. Notwithstanding, these active materials have their own shortcomings such as low energy density of electric double-layer capacitors, low electronic conductivity of pseudocapacitors, and small cyclic life of the hybrid capacitors. These above-specified properties can be enhanced by preparing the various binary NCs viz. metal oxide-carbon, conducting polymer-carbon, and metal oxide-conducting polymer. Out of these binary composites, the metal oxide-conducting polymer was favored as an active material for pseudocapacitor electrodes in light of their faradic reactions [47].

Various metal oxides viz. Fe_2O_3, Co_3O_4, ZnO_2, MnO_2, RuO_2, NiO, V_2O_5, SnO_2, etc. were examined for the energy storage application. Out of these above-specified metal oxides, RuO_2 was observed to be the most amazing active material for pseudocapacitor electrodes which exhibits reverse charge-discharge properties, excellent specific capacitance,

and extremely high electrical conductivity. Despite that, there emerge a few difficulties with the utilization of RuO_2 as an active material for electrodes because it is highly toxic and too much expensive [38]. Moreover, the single transition metal oxides have lower specific capacitance and lower electrical conductivity which needs to be improved. These above troubles can be eliminated by the utilization of the mixed metal oxides viz. cobaltites (MCo_2O_4), aluminates (MAl_2O_4), spinel ferrites (MFe_2O_4), etc. These mixed metal oxides have been contemplated as a possible contestants for superior SCs in light of the fact that they exhibit magnificent electrochemical performance due to the synergetic impact of different metal cations [39]. One of the most outstanding known, the mixed metal oxide is the spinel ferrite (MFe_2O_4) because it imparts surprising properties viz. electrochemical stability, different oxidation states, electronic, magnetic, optical, and catalytic [40,225]. Furthermore, these spinel ferrites are easily available, have minimal cost, massive productivity, ecologically innocuous, and convenient to synthesize on an industrial scale. Several spinel ferrites were examined for electrochemical execution, but till now there is no information available on the structural, morphological, and electrochemical properties of $Mn_{0.3}Co_{0.2}Zn_{0.5}Fe_2O_4$ (spinel ferrite).

Several known electrical conducting polymers viz. polypyrrole (PPy), polythiophene (PTh), poly (3,4-ethylenedioxythiophene) (PEDOT), and polyaniline (PANI) were investigated for the electrochemical execution. These above-demonstrated polymers had drawn in much consideration because of their minimal cost, and high electrical conductivity [337]. As of late, scientists have escalated examinations about the conducting PANI as an active material for SC electrodes due to the excellent electrical conductivity, numerous redox reactions, large capacitance value, facile synthesis, and quick doping-dedoping of the ions during the charge-discharge cycles [72]. Despite that, the conducting PANI itself displays poor cyclic stability due to the swelling and shrinking, which prohibits its usage as an active material for the electrode [73]. To beat this above issue, it is necessary to formulate a composite of conducting PANI with those active materials having excellent cyclic stability. Thus the mixed metal oxide viz. $Mn_{0.3}Co_{0.2}Zn_{0.5}Fe_2O_4$ was utilized for the synthesis of novel $Mn_{0.3}Co_{0.2}Zn_{0.5}Fe_2O_4$-PANI NC.

Considering this, the present work intends to synthesize the $Mn_{0.3}Co_{0.2}Zn_{0.5}Fe_2O_4$ (spinel ferrite) by utilizing the facile auto combustion technique, conducting polyaniline (PANI) by adopting the chemical oxidative technique, and $Mn_{0.3}Co_{0.2}Zn_{0.5}Fe_2O_4$-PANI NC by employing the physical blending technique. The structural, morphological, and electrochemical properties were investigated utilizing X-ray diffraction (XRD), Fourier

transform infrared spectroscopy (FTIR), Field emission scanning electron microscopy (FESEM), Energy dispersive X-ray analysis (EDX), Cyclic voltammetry (CV), Galvanostatic charge-discharge (GCD), and Electrochemical impedance spectroscopy (EIS). Despite breakthroughs, research on $Mn_{0.3}Co_{0.2}Zn_{0.5}Fe_2O_4$-PANI NC to serve as an active material for pseudocapacitor electrodes has not been accounted so far.

8.2. Materials and Methods

8.2.1. Material Used

The AR-grade chemicals were utilized for the synthesis of $Mn_{0.3}Co_{0.2}Zn_{0.5}Fe_2O_4$-PANI NC. The tetrahydrate nitrates of Mn (II), Co (II), and Zn (II) were bought from Sigma-Aldrich, nonahydrate nitrate of Fe (III), monohydrate $C_6H_8O_7$ (citric acid), NH_4OH (ammonia solution), $C_6H_5NH_2$ (aniline), $N_2H_8S_2O_8$ (ammonia persulphate), HCl (hydrochloric acid), and C_3H_6O (acetone) were bought from Loba Chemie Pvt. Ltd, polyvinylidene fluoride was received from Merck, conducting acetylene black was bought from MTI Corporation, and nickel metal foam was purchased from Nanoshel.

8.2.2. Synthesis of $Mn_{0.3}Co_{0.2}Zn_{0.5}Fe_2O_4$

For the synthesis of $Mn_{0.3}Co_{0.2}Zn_{0.5}Fe_2O_4$, the metal nitrates and citric acid in the required stoichiometry were weighted and mixed in 150 ml of distilled water. The cationic (oxidant) to citric acid (fuel) proportion was taken to be 1:2. To maintain the pH at 7 of the above reaction mixture, ammonia solution was added in a drop-wise fashion. The solution was thoroughly stirred and heated at 120 ^{o}C for 4.5 h till the xerogel formation. The auto combustion phenomenon occurs on heating xerogel at 100 ^{o}C for 3 h. The ferrite powder acquired while auto combustion was then further heated at 100 ^{o}C for 8 h and grinded by utilizing mortar and pestle to form a soft brown powder. The procured $Mn_{0.3}Co_{0.2}Zn_{0.5}Fe_2O_4$ ferrite powder was then sintered at 1100 ^{o}C for 5 h in a muffle furnace.

8.2.3. Synthesis of PANI

For the synthesis of conducting PANI, the chemical oxidative technique was utilized in which polymerization and doping occur simultaneously. In the chemical oxidative technique, there are three reactants of PANI viz. aniline (monomer), ammonia persulphate (oxidant), and hydrochloric acid (dopant or acidic medium). The PANI was synthesized by dispersing aniline (0.5 M) in 40 ml of the HCl (1 M). The dispersed solution was stirred in an

ice bath to form a homogeneous suspension and this process continue for 2 h till the formation of anilinium ions. The ammonia persulphate solution (APS) was prepared by mixing ammonia persulphate (0.4 M) with 60 ml of HCl (1 M). The APS solution was added in a dropwise manner to the above solution and stirred continuously in an ice bath for 5 h till the green colour solution was observed. The green colour indicates the formation of the emeraldine salt which is the conducting form of PANI. The solution was then kept overnight in an ice bath and precipitates were vacuum filtered. The residues attached with precipitates were removed by repeated washing with distilled water and HCl. Finally, the green-colored precipitates of PANI were dried in a hot air oven at 70 ^{o}C for 12 h.

8.2.4. Synthesis of $Mn_{0.3}Co_{0.2}Zn_{0.5}Fe_2O_4$-PANI Nanocomposite

For the synthesis of $Mn_{0.3}Co_{0.2}Zn_{0.5}Fe_2O_4$-PANI NC, a physical blending technique was utilized. The weight ratio of $Mn_{0.3}Co_{0.2}Zn_{0.5}Fe_2O_4$:PANI was taken to be 1:5, which was physically blended using mortar and pestle to obtain a homogenous mixture of the synthesized NC.

8.2.5. Fabrication of Electrochemical Electrode

The electrochemical investigation at room temperature was carried out utilizing a three-electrode system. The three electrodes were designated as working electrode (ink-loaded nickel foam), reference electrode (Ag/AgCl), and counter electrode (platinum wire). The experiment was performed involving 3 M KOH as an electrolyte. Prior to utilizing nickel foam (1 cm × 1 cm) as a working electrode, it was initially sonicated using 3 M HCl at 50 ^{o}C for 1 h to eliminate the nickel oxide layer. Then, the nickel foam was washed over and over with ethanol and distilled water followed by drying at 60 ^{o}C for 3h. The ink drop cast on the nickel foam was prepared with $Mn_{0.3}Co_{0.2}Zn_{0.5}Fe_2O_4$-PANI NC (70 Wt. %), acetylene black (20 Wt. %), and polyvinylidene fluoride (10 Wt. %) utilizing n-methyl-2-pyrrolidone (NMP) as a solvent. The ink-loaded nickel foam was dried at 60 ^{o}C for 12 h. Similar strategies were applied to set up the working electrodes of pure $Mn_{0.3}Co_{0.2}Zn_{0.5}Fe_2O_4$ and PANI for the relative study.

8.2.6. Characterization Techniques

The XRD (BRUKER) was utilized to examine the phase and the crystalline nature of the incorporated samples. The type of structure, functional groups, molecular bonds, and

immaculateness of the incorporated samples were investigated utilizing FTIR (PERKIN ELMER). The FESEM (JEOL) was employed to investigate the surface morphology and EDX (OXFORD) measures the elemental composition of the incorporated samples. The CV, GCD, and EIS were employed in the electrochemical workstation (METROHM) for the electrochemical investigation of the prepared electrodes.

8.3. Results and Discussion
8.3.1. XRD Study

The non-destructive XRD technique that utilizes Cu-Kα as a radiation source was employed on pure $Mn_{0.3}Co_{0.2}Zn_{0.5}Fe_2O_4$, PANI, and $Mn_{0.3}Co_{0.2}Zn_{0.5}Fe_2O_4$-PANI NC for the investigation of phase, structure, and crystallinity. Fig. 8.1 illustrates the XRD pattern of the incorporated samples having diffraction angle (2θ) of 10° to 70° with 0.02^o step size. For $Mn_{0.3}Co_{0.2}Zn_{0.5}Fe_2O_4$ the characteristics diffraction peaks were indexed as (111), (220), (311), (222), (400), (422), (511), and (440) having diffraction angle (2θ) of 18.1^o, 29.9^o, 35.2^o, 36.8^o, 42.8^o, 53.1^o, 56.6^o, and 62.2^o respectively. These indexed peaks were in accordance with the single-phase cobalt and zinc spinel ferrite bearing ICDD no. 22-1086 and 89-1009 respectively [97]. These characteristic diffraction peaks of the incorporated samples assure face-centered cubic (fcc) arrangement and possess a space group of Fd-3m. The appearance of a single phase of $Mn_{0.3}Co_{0.2}Zn_{0.5}Fe_2O_4$ at 1100 ^{o}C is a clear indication of homogeneity, crystallization formation, and completion of the auto combustion process. The crystalline nature of $Mn_{0.3}Co_{0.2}Zn_{0.5}Fe_2O_4$ was affirmed from sharp peaks in the diffraction pattern. The XRD pattern of the conducting PANI exhibits a semi-crystalline structure by virtue of the occurrence of broader peaks. For conducting PANI the characteristics diffraction peaks were indexed as (110) and (111) having diffraction angles (2θ) of 20.1^o and 25.2^o respectively. The densely packed phenyl rings in the conducting PANI prompt the overlapping of π–π orbitals and are responsible for the broadening of the peaks. Meanwhile, the XRD pattern of the $Mn_{0.3}Co_{0.2}Zn_{0.5}Fe_2O_4$-PANI NC exhibits two different types of peaks, sharp $Mn_{0.3}Co_{0.2}Zn_{0.5}Fe_2O_4$ ferrite peaks, and broader PANI peaks. The presence of two types of peaks in the $Mn_{0.3}Co_{0.2}Zn_{0.5}Fe_2O_4$-PANI NC results in the effective intercalation between $Mn_{0.3}Co_{0.2}Zn_{0.5}Fe_2O_4$ and PANI matrix [338]. The higher intensity peaks of the incorporated samples were employed for the computation of the crystallite size (D) (Table 8.1) by the Debye-Scherrer formula mentioned in Eq. (8.1).

$$D = \frac{0.9\,\lambda}{\beta\,Cos\theta} \qquad\qquad (8.1)$$

Here λ (1.5406 Å) signifies the wavelength of the X-ray, and β signifies full width at half maximum (FWHM) of the higher intensity peaks.
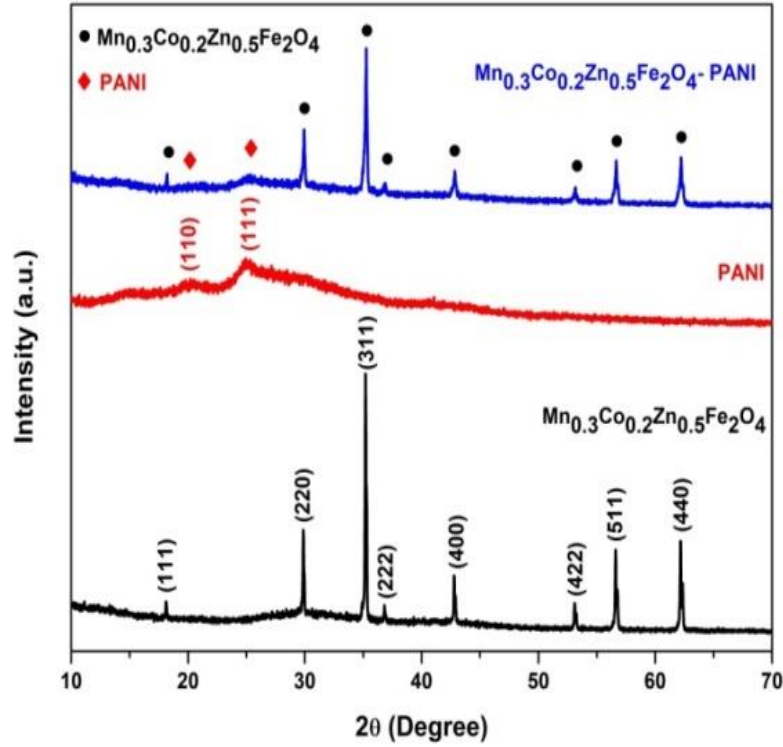
Fig. 8.1. XRD pattern of $Mn_{0.3}Co_{0.2}Zn_{0.5}Fe_2O_4$, PANI, and $Mn_{0.3}Co_{0.2}Zn_{0.5}Fe_2O_4$-PANI nanocomposite.

Table 8.1
Structural parameters of $Mn_{0.3}Co_{0.2}Zn_{0.5}Fe_2O_4$, PANI, and $Mn_{0.3}Co_{0.2}Zn_{0.5}Fe_2O_4$-PANI nanocomposite.

Sample	2θ (Degree)	β (Degree)	D (nm)
$Mn_{0.3}Co_{0.2}Zn_{0.5}Fe_2O_4$	35.2	0.155	53.8
PANI	25.2	0.237	34.3
$Mn_{0.3}Co_{0.2}Zn_{0.5}Fe_2O_4$-PANI	35.2	0.196	42.52

For all the incorporated samples, the crystallite size was found to be in the nanometer range. The crystallite size of $Mn_{0.3}Co_{0.2}Zn_{0.5}Fe_2O_4$-PANI NC was noticed to be smaller than the $Mn_{0.3}Co_{0.2}Zn_{0.5}Fe_2O_4$. This decrement in the crystallite size of $Mn_{0.3}Co_{0.2}Zn_{0.5}Fe_2O_4$-PANI NC affirms the encapsulation of ferrite NPs with the PANI matrix which avoid agglomeration [339].

8.3.2. FTIR Study

The purity of the synthesized samples was confirmed by utilizing the FTIR analysis having wavenumber in the range of 400 to 4000 cm^{-1}. The structural investigation along with the presence of the various functional groups and molecular bonds which remain during the synthesis were studied using FTIR. Fig. 8.2 delineates the FTIR spectra for $Mn_{0.3}Co_{0.2}Zn_{0.5}Fe_2O_4$, PANI, and $Mn_{0.3}Co_{0.2}Zn_{0.5}Fe_2O_4$-PANI NC. In $Mn_{0.3}Co_{0.2}Zn_{0.5}Fe_2O_4$ due to the vibration of metal-oxygen (M-O) bonds, two absorption bands were perceived near 550 cm^{-1} (tetrahedral site) and 405 cm^{-1} (octahedral site) which assert the formation of spinel structure. This variation in the position of the bands was due to the variation in the bond length of metal-oxygen (M-O) [292]. The immaculateness of the synthesized $Mn_{0.3}Co_{0.2}Zn_{0.5}Fe_2O_4$ was assured by the nonexistence of the bands near 1100 cm^{-1} (nitrates), 1385 cm^{-1} (citric acid), and 3700 cm^{-1} (moisture). In conducting PANI, the strong absorption band that appeared at 3689 cm^{-1} is attributed to the stretching vibration (N-H) in the amino group. The (symmetric as well as the asymmetric) stretching vibration (C-H) in the methyl group gives rise to the band near 2965 cm^{-1}. The band at 1562 cm^{-1}, 1474 cm^{-1}, and 1292 cm^{-1} were ascribed to the stretching vibration in the quinoid ring (C=N), benzenoid ring (C=C), and aromatic amine (C=N) respectively and portrays the oxidation state of the conducting PANI [39]. The crystalline nature of the conducting PANI was asserted by these benzenoid and quinoid rings. The bending vibration (C-H) in the (P-disubstituted) aromatic ring gives rise to the bands at 1129 cm^{-1}, 1040 cm^{-1}, 789 cm^{-1}, and 456 cm^{-1}. The bands at 1129 cm^{-1} and 456 cm^{-1} assure the conductivity of the synthesized PANI and substitutions present in the aromatic benzene ring during the polymerization process respectively [340]. In $Mn_{0.3}Co_{0.2}Zn_{0.5}Fe_2O_4$-PANI NC all characteristic vibrational bands were present, which were observed in the $Mn_{0.3}Co_{0.2}Zn_{0.5}Fe_2O_4$ and PANI spectra. As contrasted with the $Mn_{0.3}Co_{0.2}Zn_{0.5}Fe_2O_4$ spectra, the absorption bands of $Mn_{0.3}Co_{0.2}Zn_{0.5}Fe_2O_4$-PANI at 550 cm^{-1} and 405 cm^{-1} were comparatively weak which reveals the lower concentration of $Mn_{0.3}Co_{0.2}Zn_{0.5}Fe_2O_4$ interfaced with the PANI matrix. Moreover, the vibrational bands of the

PANI in $Mn_{0.3}Co_{0.2}Zn_{0.5}Fe_2O_4$-PANI NC were slightly shifted towards the higher wavenumber which might be due to the hydrogen bonding between the $Mn_{0.3}Co_{0.2}Zn_{0.5}Fe_2O_4$ and PANI [341]. This decrease in the intensity ($Mn_{0.3}Co_{0.2}Zn_{0.5}Fe_2O_4$) and shifting (PANI) of the vibrational bands in $Mn_{0.3}Co_{0.2}Zn_{0.5}Fe_2O_4$-PANI NC affirms the successful intercalation and chemical interaction of $Mn_{0.3}Co_{0.2}Zn_{0.5}Fe_2O_4$ with the PANI matrix [342]. The NC formation was assured by the FTIR spectra and ratifies our XRD study.
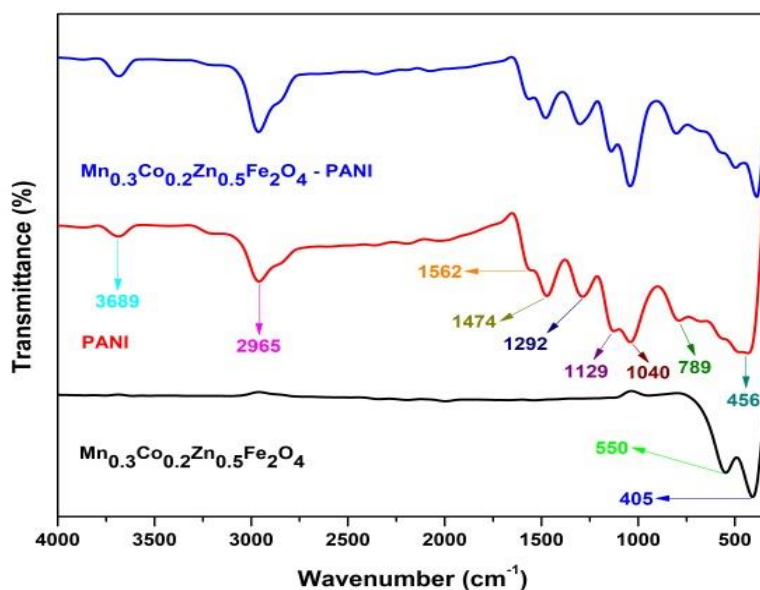
Fig. 8.2. FTIR spectra of $Mn_{0.3}Co_{0.2}Zn_{0.5}Fe_2O_4$, PANI, and $Mn_{0.3}Co_{0.2}Zn_{0.5}Fe_2O_4$-PANI nanocomposite.

8.3.3. FESEM Study

The surface morphology along with the particle size (average) was investigated with the FESEM micrographs. The FESEM micrographs of $Mn_{0.3}Co_{0.2}Zn_{0.5}Fe_2O_4$, PANI, and $Mn_{0.3}Co_{0.2}Zn_{0.5}Fe_2O_4$-PANI NC were depicted in Fig. 8.3. FESEM micrograph of $Mn_{0.3}Co_{0.2}Zn_{0.5}Fe_2O_4$ displays the grains which were irregular in shape and size and had porous morphology. The discharge of gases during auto combustion gives rise to the existence of pores [293]. The FESEM micrograph of PANI reveals the interconnected worm-like fiber network. The encapsulation of the synthesized ferrite NP with the PANI matrix was exhibited by the FESEM micrograph of $Mn_{0.3}Co_{0.2}Zn_{0.5}Fe_2O_4$-PANI NC. The hydrogen bonding formed between the amino group (PANI) and oxygen (ferrite) was responsible for the encapsulation [39]. Due to the surface absorption feature of conducting PANI, the synthesized NC appeared to coalesce. Moreover, the incorporated PANI controls the

agglomeration of $Mn_{0.3}Co_{0.2}Zn_{0.5}Fe_2O_4$ NPs in $Mn_{0.3}Co_{0.2}Zn_{0.5}Fe_2O_4$-PANI NC which ultimately leads to the enhancement of the pores [342]. These pores were helpful in strengthening the electrochemical activity because of the ease of access of electrolyte to the electrode. The FESEM micrographs were utilized to calculate the particle size (average) with the help of ImageJ software. For all incorporated samples, the histogram was plotted in Fig. 8.3 for the estimation of the average particle size in the nanosize range. The particle size of $Mn_{0.3}Co_{0.2}Zn_{0.5}Fe_2O_4$-PANI NC was evaluated to be less as compared to the $Mn_{0.3}Co_{0.2}Zn_{0.5}Fe_2O_4$ NPs due to the presence of PANI. During synthesis, PANI was washed with HCl as a result PANI surface attains a positive charge. This positive charge prompts electrostatic repulsion so as to avoid agglomeration and affirms the formation of the NC [343].
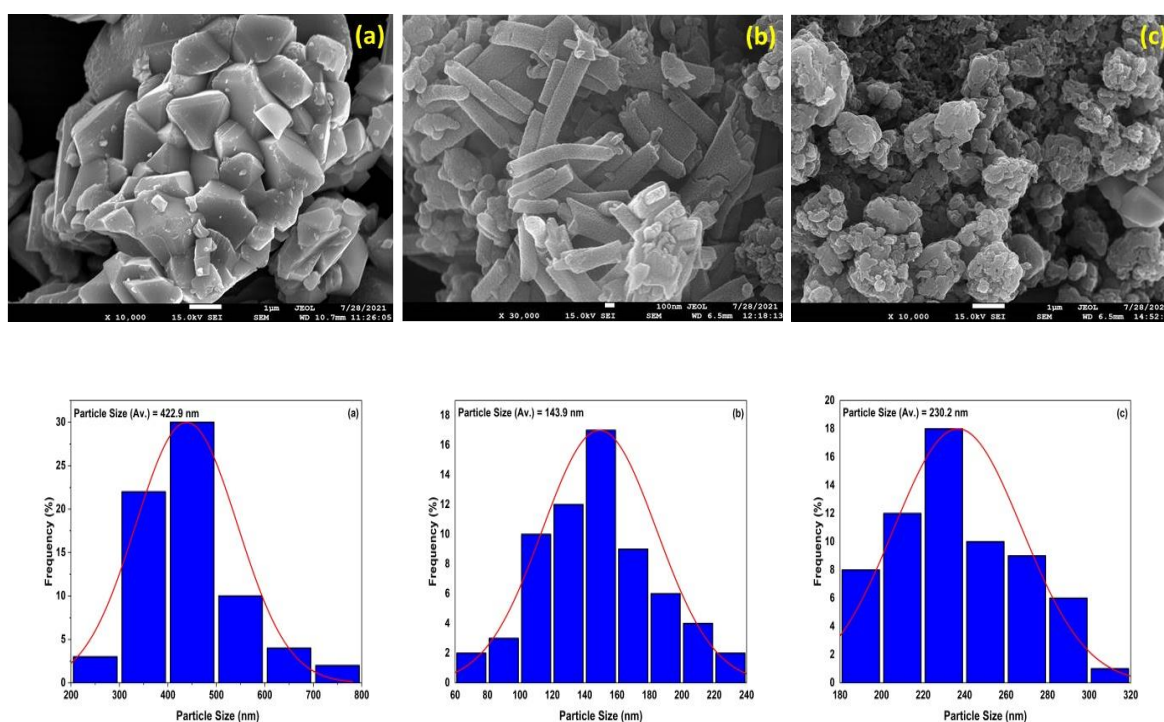
Fig. 8.3. FESEM micrograph and particle size histogram of (a) $Mn_{0.3}Co_{0.2}Zn_{0.5}Fe_2O_4$, (b) PANI, and (c) $Mn_{0.3}Co_{0.2}Zn_{0.5}Fe_2O_4$-PANI nanocomposite.

8.3.4. EDX Study

The stoichiometry along with the elemental composition of the synthesized samples was investigated utilizing the EDX technique. Fig. 8.4 presents the EDX spectra of $Mn_{0.3}Co_{0.2}Zn_{0.5}Fe_2O_4$, PANI, and $Mn_{0.3}Co_{0.2}Zn_{0.5}Fe_2O_4$-PANI NC. The EDX spectra, of $Mn_{0.3}Co_{0.2}Zn_{0.5}Fe_2O_4$ NP display Mn, Co, Zn, Fe, and O peaks, PANI displays C, N, and O peaks and $Mn_{0.3}Co_{0.2}Zn_{0.5}Fe_2O_4$-PANI NC displays Mn, Co, Zn, Fe, C, N, and O peaks [344].

For all the samples, no extra higher intensity peak was observed. The extra small intensity peaks in the EDX spectra might be due to the carbon tape utilized during the EDX analysis. The elemental mapping as presented in Fig. 8.5 affirms the uniform distribution of elements over the entire NC sample. Table 8.2 reports the values of the Wt. % and At. % for all the incorporated samples and reflects the actual weight ratios of $Mn_{0.3}Co_{0.2}Zn_{0.5}Fe_2O_4$ to PANI in the synthesized NC. Subsequently, EDX affirms the impeccability of our synthesized samples.
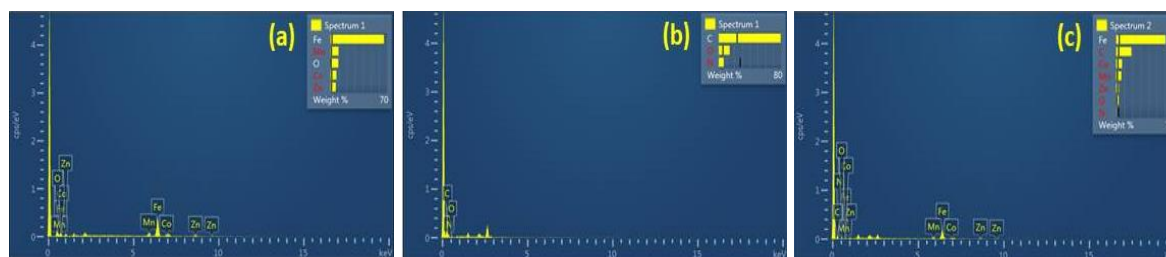
Fig. 8.4. EDX spectra of (a) $Mn_{0.3}Co_{0.2}Zn_{0.5}Fe_2O_4$, (b) PANI, and (c) $Mn_{0.3}Co_{0.2}Zn_{0.5}Fe_2O_4$-PANI nanocomposite.
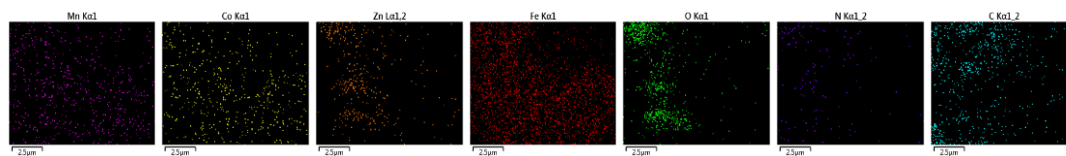
Fig. 8.5. Elemental mapping of $Mn_{0.3}Co_{0.2}Zn_{0.5}Fe_2O_4$-PANI nanocomposite.

Table 8.2
Wt. % and At. % of $Mn_{0.3}Co_{0.2}Zn_{0.5}Fe_2O_4$, PANI, and $Mn_{0.3}Co_{0.2}Zn_{0.5}Fe_2O_4$-PANI nanocomposite.

Sample	Weight % & Atomic %	Elements							Total %
		Mn	Co	Zn	Fe	O	N	C	
$Mn_{0.3}Co_{0.2}Zn_{0.5}Fe_2O_4$	Weight %	9.91	7.47	6.75	66.21	9.67	0	0	100
	Atomic %	8.20	5.76	4.69	53.89	27.46	0	0	100
PANI	Weight %	0	0	0	0	13.96	6.41	79.63	100
	Atomic %	0	0	0	0	10.96	5.75	83.29	100
$Mn_{0.3}Co_{0.2}Zn_{0.5}Fe_2O_4$-PANI	Weight %	6.35	7.32	3.24	61.03	2.94	0.26	18.84	100
	Atomic %	3.67	3.94	1.57	34.65	5.83	0.60	49.75	100

8.3.5. Electrochemical Study

8.3.5.1. CV Study

The CV of the incorporated samples was conducted under the potential ranging from 0 to 0.5 V with respect to Ag/AgCl at different scan rates (10 to 100 mV s^{-1}) utilizing 3 M KOH as an electrolyte. The CV curves at 10 mV s^{-1} for $Mn_{0.3}Co_{0.2}Zn_{0.5}Fe_2O_4$, PANI, and $Mn_{0.3}Co_{0.2}Zn_{0.5}Fe_2O_4$-PANI NC were depicted in Fig. 8.6(a). These CV curves manifest faradic (battery) comportment by virtue of the appearance of redox peaks [345]. As familiar that the capacitance varies in a direct proportion to the area of the CV curve. In contrast with $Mn_{0.3}Co_{0.2}Zn_{0.5}Fe_2O_4$ and PANI, the $Mn_{0.3}Co_{0.2}Zn_{0.5}Fe_2O_4$-PANI NC exhibits a larger area, thereby demonstrating higher capacitance for the synthesized NC. Fig. 8.6(b) delineates CV curves for $Mn_{0.3}Co_{0.2}Zn_{0.5}Fe_2O_4$-PANI NC at different scan rates viz. 10, 20, 40, 60, and 100 mV s^{-1}. With the increment in the scan rate, it was perceived that the peak current increases without substantial modification in the shape of the CV curve. This property of the NC is convenient for fast redox reactions (reversible). Furthermore, the redox reactions (reversible) and high electrical polarization give rise to the shifting of the cathodic and anodic peaks towards lower and higher potential respectively [346,347]. The specific capacitance (C_s) of the incorporated samples at different scan rates were recorded in Table 8.3 utilizing Eq. (8.2) [348].

$$C_s = \frac{1}{m \upsilon \Delta V} \int_{V_i}^{V_f} I(V) dV \qquad (8.2)$$

Here m, υ, ΔV, and integral part signifies loaded mass, scan rate, potential window, and area of the CV curve respectively.
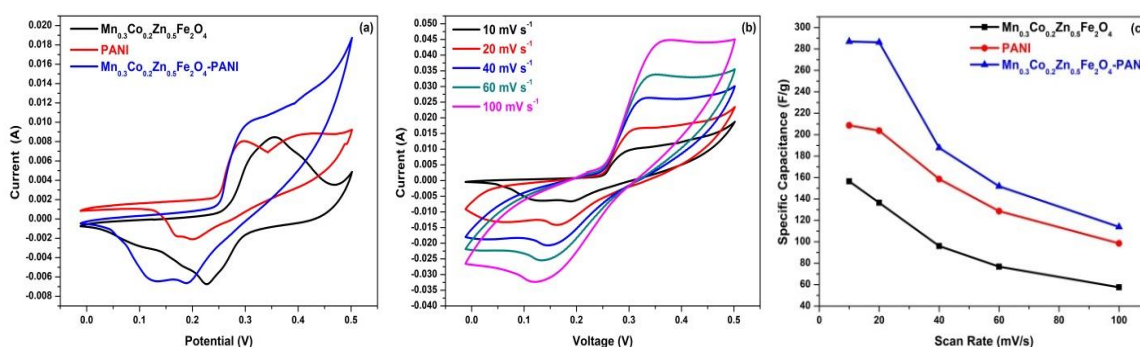
Fig. 8.6. (a) CV curve of $Mn_{0.3}Co_{0.2}Zn_{0.5}Fe_2O_4$, PANI, and $Mn_{0.3}Co_{0.2}Zn_{0.5}Fe_2O_4$-PANI nanocomposite at 10 mV s^{-1}, (b) CV curve of $Mn_{0.3}Co_{0.2}Zn_{0.5}Fe_2O_4$-PANI nanocomposite at different scan rates, and (c) Specific capacitance as a function of scan rate.

Table 8.3

Electrochemical parameters from CV curve of $Mn_{0.3}Co_{0.2}Zn_{0.5}Fe_2O_4$, PANI, and $Mn_{0.3}Co_{0.2}Zn_{0.5}Fe_2O_4$-PANI nanocomposite.

Sample	υ (mV s^{-1})	m (mg)	ΔV (V)	$\int_{V_i}^{V_f} I(V)dV$ (AV)	C_s (F g^{-1})
	10	1.5	0.5	0.001175	156.46
	20	1.5	0.5	0.002045	136.47
$Mn_{0.3}Co_{0.2}Zn_{0.5}Fe_2O_4$	40	1.5	0.5	0.002885	96.08
	60	1.5	0.5	0.003455	76.82
	100	1.5	0.5	0.004315	57.57
	10	1	0.5	0.001045	208.65
	20	1	0.5	0.002040	203.76
PANI	40	1	0.5	0.003170	158.56
	60	1	0.5	0.003860	128.67
	100	1	0.5	0.004930	98.57
	10	1	0.5	0.001435	286.91
	20	1	0.5	0.002860	286.20
$Mn_{0.3}Co_{0.2}Zn_{0.5}Fe_2O_4$ -PANI	40	1	0.5	0.003755	187.70
	60	1	0.5	0.004555	151.83
	100	1	0.5	0.005695	113.93

The specific capacitance at the scan rate of 10 mV s^{-1} for $Mn_{0.3}Co_{0.2}Zn_{0.5}Fe_2O_4$, PANI, and $Mn_{0.3}Co_{0.2}Zn_{0.5}Fe_2O_4$-PANI NC was evaluated to be 156.46, 208.65, and 286.91 F g^{-1} respectively. The specific capacitance of the $Mn_{0.3}Co_{0.2}Zn_{0.5}Fe_2O_4$-PANI NC was subsequently higher (286.91 F g^{-1} at 10 mV s^{-1}) than that of previously published studies such as $CoFe_2O_4$-PANI (60 F g^{-1} at 1 mV s^{-1}), $NiFe_2O_4$-PANI (51 F g^{-1} at 1 mV s^{-1}), Fe_3O_4-PANI (14.5 F g^{-1} at 1 mV s^{-1}), $CoFe_2O_4$-Graphene (256 F g^{-1} at 1 mV s^{-1}), $NiFe_2O_4$-Graphene (81 F g^{-1} at 1 mV s^{-1}), and Fe_3O_4-Graphene (23 F g^{-1} at 1 mV s^{-1}) [340]. With the increment in the scan rate, the decrement in the specific capacitance was noticed for all the incorporated samples. This decrement in the specific capacitance at a higher scan rate emerges on account of the limited time available for OH^{-1} ions to penetrate in the depth of the synthesized electrode. Meanwhile, these OH^{-1} ions were extensively available to the inner as well as the outer surface of the synthesized electrode at the lower scan rate thereby resulting in the

higher value of the specific capacitance [349]. For all scan rates, the synthesized $Mn_{0.3}Co_{0.2}Zn_{0.5}Fe_2O_4$-PANI NC had higher specific capacitance than the unitary samples as perceived from Fig. 8.6(c).

8.3.5.2. GCD Study

The GCD of the incorporated samples were conducted at the different current densities (1 to 5 A g^{-1}) under the potential range of 0 to 0.4 V. The GCD curves at 1 A g^{-1} for $Mn_{0.3}Co_{0.2}Zn_{0.5}Fe_2O_4$, PANI, and $Mn_{0.3}Co_{0.2}Zn_{0.5}Fe_2O_4$-PANI NC was presented in Fig. 8.7(a). For all incorporated samples the internal resistance drop (IR$_{drop}$) was noticed at the turning point by virtue of the equivalent series resistance (ESR) which will ultimately loose energy [350,351]. The active material, electrolytic ions, and electrode-electrolyte interface resistances were responsible for ESR [352,353]. The specific capacitance (C$_s$) of the incorporated samples at different current densities were recorded in Table 8.4 utilizing Eq. (8.3) [176].

$$C_s = \frac{I_m \times \Delta t}{\Delta V}$$ (8.3)

Here I$_m$, Δt, and ΔV signifies the current density, discharge time, and potential window respectively of the incorporated samples.
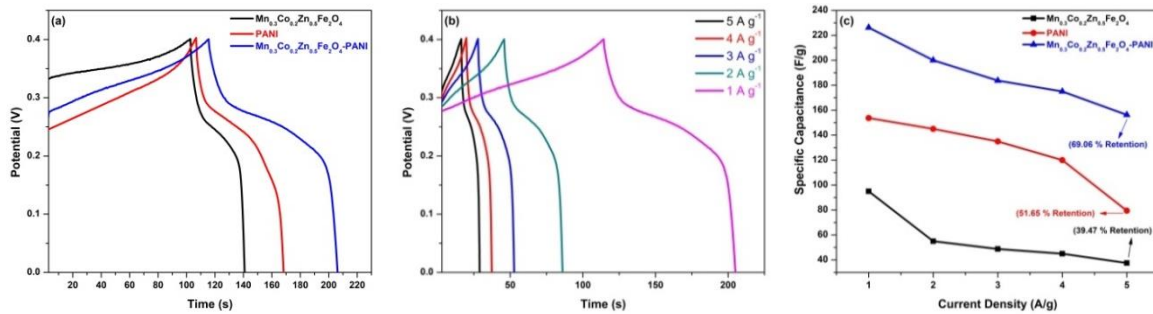
Fig. 8.7. (a) GCD curve of $Mn_{0.3}Co_{0.2}Zn_{0.5}Fe_2O_4$, PANI, and $Mn_{0.3}Co_{0.2}Zn_{0.5}Fe_2O_4$-PANI nanocomposite at 1A g^{-1}, (b) GCD curve of $Mn_{0.3}Co_{0.2}Zn_{0.5}Fe_2O_4$-PANI nanocomposite at different current densities, and (c) Specific capacitance as a function of current density.

The specific capacitance at the current density of 1 A g^{-1} for $Mn_{0.3}Co_{0.2}Zn_{0.5}Fe_2O_4$, PANI, and $Mn_{0.3}Co_{0.2}Zn_{0.5}Fe_2O_4$-PANI NC was evaluated to be 95, 153.75, and 226.25 F g^{-1} respectively. The specific capacitance of the $Mn_{0.3}Co_{0.2}Zn_{0.5}Fe_2O_4$-PANI NC was subsequently higher (226.25 F g^{-1} at 1 A g^{-1}) than that of previously published studies such as $CoFe_2O_4$-PANI (53 F g^{-1} at 1 A g^{-1}), $NiFe_2O_4$-PANI (46 F g^{-1} at 1 A g^{-1}), Fe_3O_4-PANI (15.5 F g^{-1} at 1 A g^{-1}), $CoFe_2O_4$-Graphene (196 F g^{-1} at 1 A g^{-1}), $NiFe_2O_4$-Graphene (70 F g^{-1} at 1 A

g^{-1}), and Fe_3O_4-Graphene (15 F g^{-1} at 1 A g^{-1}) [340]. The lower internal resistance in $Mn_{0.3}Co_{0.2}Zn_{0.5}Fe_2O_4$-PANI NC was attributed to its higher specific capacitance value [134]. Fig. 8.7(b) portrays GCD curves for $Mn_{0.3}Co_{0.2}Zn_{0.5}Fe_2O_4$-PANI NC at different current densities viz. 1, 2, 3, 4, and 5 A g^{-1}. With the increment in the current density, the decrement in the discharging time of the $Mn_{0.3}Co_{0.2}Zn_{0.5}Fe_2O_4$-PANI NC was noticed which reduced the specific capacitance as evaluated in Table 8.4. This decrement in the specific capacitance at higher current density arises on account of the diffusion which impedes the mobility of electrolytic ions to permeate in the depth of the synthesized electrode [133].

Table 8.4
Electrochemical parameters from GCD curve of $Mn_{0.3}Co_{0.2}Zn_{0.5}Fe_2O_4$, PANI, and $Mn_{0.3}Co_{0.2}Zn_{0.5}Fe_2O_4$-PANI nanocomposite.

Sample	I_m (A g^{-1})	Δt (s)	ΔV (V)	C_s (F g^{-1})
$Mn_{0.3}Co_{0.2}Zn_{0.5}Fe_2O_4$	1	38	0.4	95
	2	11	0.4	55
	3	6.5	0.4	48.75
	4	4.5	0.4	45
	5	3	0.4	37.50
PANI	1	61.5	0.4	153.75
	2	29	0.4	145
	3	18	0.4	135
	4	12	0.4	120
	5	6.4	0.4	79.42
$Mn_{0.3}Co_{0.2}Zn_{0.5}Fe_2O_4$-PANI	1	90.5	0.4	226.25
	2	40	0.4	200
	3	24.5	0.4	183.75
	4	17.5	0.4	175
	5	12.5	0.4	156.25

For all current densities, $Mn_{0.3}Co_{0.2}Zn_{0.5}Fe_2O_4$-PANI NC exhibits non-linear charge-discharge curves due to the redox reaction between the $Mn_{0.3}Co_{0.2}Zn_{0.5}Fe_2O_4$-PANI NC and electrolytic ions [354]. For all current densities, the synthesized $Mn_{0.3}Co_{0.2}Zn_{0.5}Fe_2O_4$-PANI NC had higher specific capacitance than the unitary samples as perceived from Fig. 8.7(c) and affirms the CV results. The capacitance retention of $Mn_{0.3}Co_{0.2}Zn_{0.5}Fe_2O_4$, PANI, and

$Mn_{0.3}Co_{0.2}Zn_{0.5}Fe_2O_4$-PANI NC at the current density of 5 A g^{-1} was achieved to be 39.47, 51.65, and 69.06 % respectively. This enhancement in the electrochemical performance of the NC is because of the following aspects; [355,356] (i) In $Mn_{0.3}Co_{0.2}Zn_{0.5}Fe_2O_4$-PANI NC large number of the redox reaction undergoes by virtue of the conducting PANI which avoids agglomeration and enhances the surface area. (ii) The worm-like fiber network of the conducting PANI supports the $Mn_{0.3}Co_{0.2}Zn_{0.5}Fe_2O_4$ NPs by supplying interrelated pathways to assist the continual movement of electrons towards the electrode. (iii) In alkaline electrolyte concurrently both of the $Mn_{0.3}Co_{0.2}Zn_{0.5}Fe_2O_4$ and PANI were electrochemically active consequently manifesting larger specific capacitance relative to their counterparts.

8.3.5.3. EIS Study

The EIS was conducted under an applied potential of 5 mV to examine the response of the incorporated samples in the frequency range of 100 kHz-10 MHz [188]. Fig. 8.8 delineates the Nyquist plots for $Mn_{0.3}Co_{0.2}Zn_{0.5}Fe_2O_4$, PANI, and $Mn_{0.3}Co_{0.2}Zn_{0.5}Fe_2O_4$-PANI NC. The two regions perceived in Fig. 8.8 viz. low-frequency (straight line) and high-frequency (semi-circle) demonstrate the ionic diffusion in the electrolyte and charge transfer at the interface of electrode-electrolyte respectively [357]. The equivalent series resistance (ESR) for $Mn_{0.3}Co_{0.2}Zn_{0.5}Fe_2O_4$, PANI, and $Mn_{0.3}Co_{0.2}Zn_{0.5}Fe_2O_4$-PANI NC was examined by the semi-circle intercept (along X-axis) and evaluated to be 1.25, 1.12, and 0.57 Ω respectively [358]. As EIS of the incorporated samples were performed utilizing the same electrolyte (KOH) as well as concentration (3 M) thereby resulting in the least variety in the ESR values. At the interface of the electrode-electrolyte, the charge transfer resistance (R_{ct}) due to the ions were determined by the semi-circle diameter (along X-axis) [359]. The higher R_{ct} was exhibited by the $Mn_{0.3}Co_{0.2}Zn_{0.5}Fe_2O_4$ NPs on account of the larger diameter than their counterparts. Due to the diffusion of OH^{-1} inside the synthesized active materials, the straight line was perceived and infers Warburg impedance [360]. $Mn_{0.3}Co_{0.2}Zn_{0.5}Fe_2O_4$-PANI NC exhibits the most vertical line whose slope is nearly close to 90° indicating better capacitance behavior than their counterparts and ratifies CV and GCD results. Consequently, the physical blending of $Mn_{0.3}Co_{0.2}Zn_{0.5}Fe_2O_4$ with PANI prompts the synergistic impact subsequently boosting the electrochemical activity of the synthesized NC electrode. Furthermore, investigation to enhance the specific capacitance involves the synthesis of ternary NC with rGO is underway.
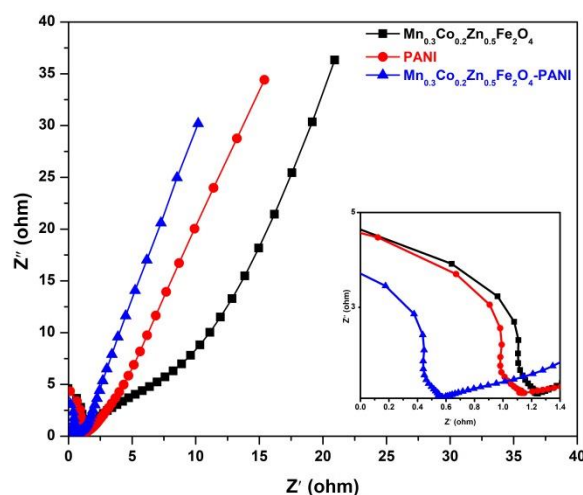
Fig. 8.8. Nyquist plot of $Mn_{0.3}Co_{0.2}Zn_{0.5}Fe_2O_4$, PANI, and $Mn_{0.3}Co_{0.2}Zn_{0.5}Fe_2O_4$-PANI nanocomposite.

8.4. Conclusion

The sol-gel procedure was adopted for the successful preparation of novel $Mn_{0.3}Co_{0.2}Zn_{0.5}Fe_2O_4$ spinel ferrite which was then blended with PANI to form $Mn_{0.3}Co_{0.2}Zn_{0.5}Fe_2O_4$-PANI nanocomposite. Scherrer's formula evaluates the crystallite size in the nanosize range. The decrement in the crystallite size of $Mn_{0.3}Co_{0.2}Zn_{0.5}Fe_2O_4$-PANI NC affirms the encapsulation of ferrite NPs with the PANI matrix which avoid agglomeration. The FTIR spectra of $Mn_{0.3}Co_{0.2}Zn_{0.5}Fe_2O_4$-PANI nanocomposite exhibits decrement in the intensity of $Mn_{0.3}Co_{0.2}Zn_{0.5}Fe_2O_4$ bands and shifting of PANI bands which affirms the successful intercalation and chemical interaction of $Mn_{0.3}Co_{0.2}Zn_{0.5}Fe_2O_4$ with the PANI matrix. The porous morphology exhibited by FESEM micrograph of the nanocomposite is helpful in strengthening the electrochemical activity because of the ease of access of electrolyte to the electrode. EDX study affirms the stoichiometry along with the elemental composition of the incorporated samples. The excellent electrochemical activity of the $Mn_{0.3}Co_{0.2}Zn_{0.5}Fe_2O_4$-PANI nanocomposite was exhibited by the CV, GCD, and EIS. The higher specific capacitance was achieved to be 286.91 F g^{-1} at 10 mV s^{-1} with capacitance retention of 69.06 % at 5 A g^{-1}.

CHAPTER-9

Summary and Conclusion

The current research deals with the sol-gel auto combustion approach to efficiently prepare $Mg_{1-x}Zn_xFe_2O_4$ NPs with concentrations of x = 0.0, 0.2, and 0.4 and crystallite size (D) in the nano-meter level of 32.591 to 37.558 nm. The prepared samples have a cubic single-phase (spinel) structure, according to the XRD study. As Zn^{2+} ions possess a larger ionic radius than Mg^{2+} ions, the lattice constant (a_o) rises with Zn content from 8.390 to 8.417 Å. The spinel structure was verified by bands in the range of 442.93-454.42 cm^{-1} and 554.08-536.45 cm^{-1} in the prepared samples, which correlates to the octahedral (v_2) and tetrahedral (v_1) sites, respectively. The Zn content causes the tetrahedral band to undergo a red shift in FTIR spectra. Using ImageJ software, FESEM micrographs assess particle size (average) in the nanoscale range, revealing the existence of agglomerated and homogeneous grains. Owing to the magnetic interaction between the prepared NPs, FESEM micrographs exhibit aggregation of the grains. EDX spectra avow the elements present in the incorporated samples without any extra impurity peak present in the spectra. The experimental At. % and Wt. % values are quite close to the theoretical values, demonstrating that the prepared ferrite NPs are pristine. The addition of non-magnetic Zn^{2+} cations (0 μ_B) to the tetrahedral site enhances the M_s. The R value of the prepared samples has been less than 0.5, indicating the presence of sporadic single domain NP assemblies with magnetostatic interactions between them. Owing to the lower H_c value, prepared samples possess soft ferromagnetic characteristics, making them favorable for power and electromagnetic applications.

Further the $Mn_xCo_{0.5-x}Zn_{0.5}Fe_2O_4$ (x = 0.0, 0.1, 0.2, 0.3, and 0.4) NPs were efficiently produced by using sol-gel auto combustion approach. The increase in the lattice constant from 8.434 to 8.457 Å with the Mn content may be ascribed to the ionic radius of Mn^{2+} ions being larger than that of Co^{2+} ions. For all the samples, the single-phase spinel structure with cubic symmetry was assured by the XRD studies. The crystallite size lies in the nanoscale range of 35.4 to 43.6 nm as estimated by utilizing the Debye-Scherrer formula. The complete evacuation of the nitrates and citric acid from the incorporated samples was avowed by the FTIR spectra. FESEM micrographs reveal the presence of non-uniform grain growth which was agglomerated, in-homogenous in size and shape, and had porous morphology. The synthesized samples can be valuable for the gas sensing application because of the porous

morphology exhibited by all the FESEM micrographs. The atomic percent (At. %) values, determined utilizing EDX spectra were in close concordance with the theoretical values, thus affirming the impeccability of the synthesized samples. There is a decrement in the saturation magnetization with increasing Mn^{2+} concentration which is due to the decrease in the crystallite size and non-magnetic nature of the Mn^{2+}. VSM study exhibits soft ferromagnetic nature due to the low coercivity value. The magnetic soft nature of the incorporated samples makes them suitable for electromagnetic radiation material, sensors, switching, multilayer chip indicators, hyperthermia, and power application. The squareness ratio for all the samples was noticed to be less than 0.5 which affirms the existence of the random oriented small single domain assembly of (spinel ferrite) NPs and reveals the magneto-static interaction between the NPs. Moreover, the synthesized ferrite has a large surface area, appropriate pore size, pore size dissemination, and the presence of the functional group which complements its utilization in the supercapacitor electrode material.

Owing to the magnificent properties of the prepared $Mn_xCo_{0.5-x}Zn_{0.5}Fe_2O_4$ (x = 0.0, 0.1, 0.2, 0.3, and 0.4) samples for supercapacitor electrode material as described above, the sample at x = 0.3, viz. $Mn_{0.3}Co_{0.2}Zn_{0.5}Fe_2O_4$ were sintered at three different temperatures to track down the reasonable sintering temperature for better structural, morphological, elemental, and magnetic characteristics. The α-Fe_2O_3 phase has totally vanished at 1150 ^{o}C. Using the XRD technique, the enhancement in the lattice constant was detected as the sintering temperature increased, which is attributable to the reduction of iron (Fe) from Fe^{3+} (0.64 Å) to Fe^{2+} (0.76 Å). The pure spinel phase formation at 1150 ^{o}C was affirmed from the FTIR analysis due to the non-appearance of the nitrates, citric acid, and moisture peaks. With the increment in the sintering temperature, the agglomeration of the gains in the FESEM micrographs was observed due to the magnetic interaction between the ferrite NP. Crystallite size was incremented from 18.1 to 50.2 nm by virtue of these agglomerations. FESEM study reveals the increasing trend of particle size (average) in the nanoscale range with temperature, as estimated by the ImageJ software. The experimental Wt. % and At. % values had close approximation with the theoretical values as estimated by the EDX. Our prepared spinel ferrites, magnetic characteristics can be modified by adjusting the sintering temperature, making them useful for high-frequency applications such as electrical filters, multi-layer chip indicators, and circulators.

Taking into consideration the findings of the above studies, the conducting polymer PANI and novel $Mn_{0.3}Co_{0.2}Zn_{0.5}Fe_2O_4$-PANI nanocomposite (NC) have been produced effectively by employing the chemical oxidative polymerization and physical blending

procedures respectively. XRD study affirms the formation of $Mn_{0.3}Co_{0.2}Zn_{0.5}Fe_2O_4$-PANI NC owing to the appearance of two different types of peaks: sharp $Mn_{0.3}Co_{0.2}Zn_{0.5}Fe_2O_4$ peaks, and broader PANI peaks. The decrement in the crystallite size of $Mn_{0.3}Co_{0.2}Zn_{0.5}Fe_2O_4$-PANI NC affirms the encapsulation of ferrite NPs with the PANI matrix which avoid agglomeration. FTIR of $Mn_{0.3}Co_{0.2}Zn_{0.5}Fe_2O_4$-PANI NC shows all characteristic vibrational bands, which are observed in the $Mn_{0.3}Co_{0.2}Zn_{0.5}Fe_2O_4$ and PANI spectra. The FTIR spectra of $Mn_{0.3}Co_{0.2}Zn_{0.5}Fe_2O_4$-PANI NC exhibit decrement in the intensity of $Mn_{0.3}Co_{0.2}Zn_{0.5}Fe_2O_4$ bands and shifting of PANI bands which affirms the successful intercalation and chemical interaction of $Mn_{0.3}Co_{0.2}Zn_{0.5}Fe_2O_4$ with the PANI matrix. The encapsulation of the synthesized ferrite nanoparticle (NP) with the PANI matrix is exhibited by the FESEM micrograph of $Mn_{0.3}Co_{0.2}Zn_{0.5}Fe_2O_4$-PANI NC. The porous morphology exhibited by the FESEM micrograph of the NC is helpful in strengthening the electrochemical activity because of the ease of access of electrolytes to the electrode. EDX study affirms the stoichiometry along with the elemental composition of the incorporated samples. The excellent electrochemical activity of the $Mn_{0.3}Co_{0.2}Zn_{0.5}Fe_2O_4$-PANI NC was exhibited by the CV, GCD, and EIS. The higher specific capacitance was achieved to be 286.91 F g^{-1} at 10 mV s^{-1} with capacitance retention of 69.06 % at 5 A g^{-1}. The electrochemical activity of the novel $Mn_{0.3}Co_{0.2}Zn_{0.5}Fe_2O_4$-PANI NC is manifested to be higher as compared to their counterparts on account of synergistic impact, continual movement of electrons towards the electrode, and multiple redox reactions.

Future Scope

➤ Obtaining pure phase of other novel spinel ferrites is necessary to use them as potential candidate for the supercapacitor applications.

➤ Citric acid is used as fuel in the present synthesis of spinel ferrites while use of other fuels like urea, glycine, tartaric acid etc. can be explored.

➤ The particle size, porosity and morphology of the synthesized materials significantly affect the electrochemical measurements therefore other methods of synthesis can be explored.

➤ Electrochemical measurement studies can be performed on the ternary nanocomposite (especially with rGO and MXene) to strengthen the specific capacitance.

We believe that the aforementioned aspects will provide researchers working in this field more chances to look at cutting-edge spinel ferrite-based nanocomposites for use in supercapacitors in the future.

CHAPTER-10

Bibliography

[1] J. Castro-Gutiérrez, A. Celzard, and V. Fierro, "Energy Storage in Supercapacitors: Focus on Tannin-Derived Carbon Electrodes," *Front. Mater.*, vol. 7, no. July, pp. 1–25, 2020, doi: 10.3389/fmats.2020.00217.

[2] M. Lazarus and H. van Asselt, "Fossil fuel supply and climate policy: exploring the road less taken," *Clim. Change*, vol. 150, no. 1–2, pp. 1–13, 2018, doi: 10.1007/s10584-018-2266-3.

[3] A. Månberger, "Reduced Use of Fossil Fuels can Reduce Supply of Critical Resources," *Biophys. Econ. Sustain.*, vol. 6, no. 2, pp. 1–15, 2021, doi: 10.1007/s41247-021-00088-5.

[4] B. K. Saikia, S. M. Benoy, M. Bora, J. Tamuly, M. Pandey, and D. Bhattacharya, "A brief review on supercapacitor energy storage devices and utilization of natural carbon resources as their electrode materials," *Fuel*, vol. 282, no. July, p. 118796, 2020, doi: 10.1016/j.fuel.2020.118796.

[5] L. Guan *et al.*, "Green and scalable synthesis of porous carbon nanosheet-assembled hierarchical architectures for robust capacitive energy harvesting," *Carbon N. Y.*, vol. 152, pp. 537–544, 2019, doi: 10.1016/j.carbon.2019.06.059.

[6] O. Krishan and S. Suhag, "An updated review of energy storage systems: Classification and applications in distributed generation power systems incorporating renewable energy resources," *Int. J. Energy Res.*, vol. 43, no. 12, pp. 6171–6210, 2019, doi: 10.1002/er.4285.

[7] H. Sun *et al.*, "Hierarchical 3D electrodes for electrochemical energy storage," *Nat. Rev. Mater.*, vol. 4, no. 1, pp. 45–60, 2019, doi: 10.1038/s41578-018-0069-9.

[8] F. Tao, Y. Q. Zhao, G. Q. Zhang, and H. L. Li, "Electrochemical characterization on cobalt sulfide for electrochemical supercapacitors," *Electrochem. commun.*, vol. 9, no. 6, pp. 1282–1287, 2007, doi: 10.1016/j.elecom.2006.11.022.

[9] L. Nikzad, S. Alibeigi, M. R. Vaezi, B. Yazdani, and M. R. Rahimipour, "Synthesis of a graphite-polyaniline nanocomposite and evaluation of its electrochemical properties," *Chem. Eng. Technol.*, vol. 32, no. 6, pp. 861–866, 2009, doi: 10.1002/ceat.200800470.

[10]   M. Nagao *et al.*, "All-solid-state lithium–sulfur batteries with three-dimensional mesoporous electrode structures," *J. Power Sources*, vol. 330, pp. 120–126, 2016, doi: 10.1016/j.jpowsour.2016.09.009.

[11]   H. Ayornu, S. Anwar, and Y. Thakur, "Fabrication and Characterization of Semi-Crystalline and Amorphous Dielectric Polymer Films for Energy Storage," no. Figure 1, pp. 559–568, 2022, doi: 10.4236/msa.2022.1311034.

[12]   M. Winter and R. J. Brodd, "What are batteries, fuel cells, and supercapacitors?," *Chem. Rev.*, vol. 104, no. 10, pp. 4245–4269, 2004, doi: 10.1021/cr020730k.

[13]   L. Yu and G. Z. Chen, "Supercapatteries as High-Performance Electrochemical Energy Storage Devices," *Electrochem. Energy Rev.*, vol. 3, no. 2, pp. 271–285, 2020, doi: 10.1007/s41918-020-00063-6.

[14]   S. D. Perera *et al.*, "Enhanced Supercapacitor Performance for Equal Co-Mn Stoichiometry in Colloidal Co 3-x Mn x O 4 Nanoparticles, in Additive-Free Electrodes," *Chem. Mater.*, vol. 27, no. 23, pp. 7861–7873, 2015, doi: 10.1021/acs.chemmater.5b02106.

[15]   P. J. Hall *et al.*, "Energy storage in electrochemical capacitors: Designing functional materials to improve performance," *Energy Environ. Sci.*, vol. 3, no. 9, pp. 1238–1251, 2010, doi: 10.1039/c0ee00004c.

[16]   W. G. Pell, B. E. Conway, W. A. Adams, and J. De Oliveira, "Electrochemical efficiency in multiple discharge/recharge cycling of supercapacitors in hybrid EV applications," *J. Power Sources*, vol. 80, no. 1, pp. 134–141, 1999, doi: 10.1016/S0378-7753(98)00257-2.

[17]   R. R. Zhang, Y. M. Xu, D. Harrison, J. Fyson, F. L. Qiu, and D. Southee, "Flexible strip supercapacitors for future energy storage," *Int. J. Autom. Comput.*, vol. 12, no. 1, pp. 43–49, 2015, doi: 10.1007/s11633-014-0866-6.

[18]   H. Du, Z. Wu, Y. Xu, S. Liu, and H. Yang, "Poly(3,4-ethylenedioxythiophene) based solid-state polymer supercapacitor with ionic liquid gel polymer electrolyte," *Polymers (Basel).*, vol. 12, no. 2, 2020, doi: 10.3390/polym12020297.

[19]   M. Yassine and D. Fabris, "Performance of commercially available supercapacitors," *Energies*, vol. 10, no. 9, 2017, doi: 10.3390/en10091340.

[20]   Y. Hu and T. S. Fisher, "Suggested standards for reporting power and energy density in supercapacitor research," *Bull. Mater. Sci.*, vol. 41, no. 5, pp. 10–13, 2018, doi: 10.1007/s12034-018-1641-z.

[21] Z. Qi and G. M. Koenig, "Review Article: Flow battery systems with solid electroactive materials," *J. Vac. Sci. Technol. B, Nanotechnol. Microelectron. Mater. Process. Meas. Phenom.*, vol. 35, no. 4, p. 040801, 2017, doi: 10.1116/1.4983210.

[22] P. Forouzandeh, V. Kumaravel, and S. C. Pillai, "Electrode materials for supercapacitors: A review of recent advances," *Catalysts*, vol. 10, no. 9, pp. 1–73, 2020, doi: 10.3390/catal10090969.

[23] B. Pal, S. Yang, S. Ramesh, V. Thangadurai, and R. Jose, "Electrolyte selection for supercapacitive devices: A critical review," *Nanoscale Adv.*, vol. 1, no. 10, pp. 3807–3835, 2019, doi: 10.1039/c9na00374f.

[24] Bharti *et al.*, "Theories and models of supercapacitors with recent advancements: impact and interpretations," *Nano Express*, vol. 2, no. 2, p. 022004, 2021, doi: 10.1088/2632-959x/abf8c2.

[25] H. D. Abruña, Y. Kiya, and J. C. Henderson, "Batteries and electrochemical capacitors," *Phys. Today*, vol. 61, no. 12, pp. 43–47, 2008, doi: 10.1063/1.3047681.

[26] P. R. Ferrer, A. Mace, S. N. Thomas, and J. W. Jeon, "Nanostructured porous graphene and its composites for energy storage applications," *Nano Converg.*, vol. 4, no. 1, 2017, doi: 10.1186/s40580-017-0123-0.

[27] M. Vangari, T. Pryor, and L. Jiang, "Supercapacitors: Review of Materials and Fabrication Methods," *J. Energy Eng.*, vol. 139, no. 2, pp. 72–79, 2013, doi: 10.1061/(asce)ey.1943-7897.0000102.

[28] M. V. Kiamahalleh, S. H. S. Zein, G. Najafpour, S. A. Sata, and S. Buniran, "Multiwalled carbon nanotubes based nanocomposites for supercapacitors: A review of electrode materials," *Nano*, vol. 7, no. 2, pp. 1–27, 2012, doi: 10.1142/S1793292012300022.

[29] M. Jayalakshmi and K. Balasubramanian, "Simple capacitors to supercapacitors - An overview," *Int. J. Electrochem. Sci.*, vol. 3, no. 11, pp. 1196–1217, 2008.

[30] H. Choi and H. Yoon, "Nanostructured electrode materials for electrochemical capacitor applications," *Nanomaterials*, vol. 5, no. 2, pp. 906–936, 2015, doi: 10.3390/nano5020906.

[31] S. M. Chen, R. Ramachandran, V. Mani, and R. Saraswathi, "Recent advancements in electrode materials for the high-performance electrochemical supercapacitors: A review," *Int. J. Electrochem. Sci.*, vol. 9, no. 8, pp. 4072–4085, 2014.

[32] T. Chen and L. Dai, "Carbon nanomaterials for high-performance supercapacitors," *Mater. Today*, vol. 16, no. 7–8, pp. 272–280, 2013, doi: 10.1016/j.mattod.2013.07.002.

[33] M. I. A. Abdel Maksoud *et al.*, *Advanced materials and technologies for supercapacitors used in energy conversion and storage: a review*, vol. 19, no. 1. Springer International Publishing, 2021.

[34] A. Burke, "R&D considerations for the performance and application of electrochemical capacitors," *Electrochim. Acta*, vol. 53, no. 3 SPEC. ISS., pp. 1083–1091, 2007, doi: 10.1016/j.electacta.2007.01.011.

[35] H. Yang, S. Kannappan, A. S. Pandian, J. H. Jang, Y. S. Lee, and W. Lu, "Graphene supercapacitor with both high power and energy density," *Nanotechnology*, vol. 28, no. 44, 2017, doi: 10.1088/1361-6528/aa8948.

[36] Z. Bo, Z. Wen, H. Kim, G. Lu, K. Yu, and J. Chen, "One-step fabrication and capacitive behavior of electrochemical double layer capacitor electrodes using vertically-oriented graphene directly grown on metal," *Carbon N. Y.*, vol. 50, no. 12, pp. 4379–4387, 2012, doi: 10.1016/j.carbon.2012.05.014.

[37] A. P. Singh, N. K. Tiwari, P. B. Karandikar, and A. Dubey, "Effect of electrode shape on the parameters of supercapacitor," *2015 Int. Conf. Ind. Instrum. Control. ICIC 2015*, no. Icic, pp. 669–673, 2015, doi: 10.1109/IIC.2015.7150826.

[38] M. A. A. Mohd Abdah, N. H. N. Azman, S. Kulandaivalu, and Y. Sulaiman, "Review of the use of transition-metal-oxide and conducting polymer-based fibres for high-performance supercapacitors," *Mater. Des.*, vol. 186, p. 108199, 2020, doi: 10.1016/j.matdes.2019.108199.

[39] N. Arsalani, A. G. Tabrizi, and L. S. Ghadimi, "Novel PANI/MnFe2O4 nanocomposite for low-cost supercapacitors with high rate capability," *J. Mater. Sci. Mater. Electron.*, vol. 29, no. 7, pp. 6077–6085, 2018, doi: 10.1007/s10854-018-8582-6.

[40] S. Liu, L. Hu, X. Xu, A. A. Al-Ghamdi, and X. Fang, "Nickel Cobaltite Nanostructures for Photoelectric and Catalytic Applications," *Small*, vol. 11, no. 34, pp. 4267–4283, 2015, doi: 10.1002/smll.201500315.

[41] C. Paper *et al.*, "Fabrication of Graphene / Polyaniline," *ACS Nano*, vol. 3, no. 7, pp. 1745–1752, 2009.

[42] Z. S. Iro, C. Subramani, and S. S. Dash, "A brief review on electrode materials for supercapacitor," *Int. J. Electrochem. Sci.*, vol. 11, no. 12, pp. 10628–10643, 2016, doi: 10.20964/2016.12.50.

[43] P. Sharma and T. S. Bhatti, "A review on electrochemical double-layer capacitors," *Energy Convers. Manag.*, vol. 51, no. 12, pp. 2901–2912, 2010, doi: 10.1016/j.enconman.2010.06.031.

[44] T. Liangliang and J. Chunyang, "Conducting polymers as electrode materials for supercapacitors," *Prog. Chem.*, vol. 22, no. 8, pp. 1610–1618, 2010.

[45] Q. Cheng, J. Tang, N. Shinya, and L. C. Qin, "Polyaniline modified graphene and carbon nanotube composite electrode for asymmetric supercapacitors of high energy density," *J. Power Sources*, vol. 241, pp. 423–428, 2013, doi: 10.1016/j.jpowsour.2013.04.105.

[46] J. Li, H. Xie, Y. Li, J. Liu, and Z. Li, "Electrochemical properties of graphene nanosheets/polyaniline nanofibers composites as electrode for supercapacitors," *J. Power Sources*, vol. 196, no. 24, pp. 10775–10781, 2011, doi: 10.1016/j.jpowsour.2011.08.105.

[47] G. Singh and S. Chandra, "Nano-flowered manganese doped ferrite@PANI composite as energy storage electrode material for supercapacitors," *J. Electroanal. Chem.*, vol. 874, p. 114491, 2020, doi: 10.1016/j.jelechem.2020.114491.

[48] J. L. Snoek, "Gyromagnetic resonance in ferrites [8]," *Nature*, vol. 160, no. 4055. p. 90, 1947, doi: 10.1038/160090a0.

[49] R. A. Pawar, S. S. Desai, S. M. Patange, S. S. Jadhav, and K. M. Jadhav, "Inter-atomic bonding and dielectric polarization in Gd3+ incorporated Co-Zn ferrite nanoparticles," *Phys. B Condens. Matter*, vol. 510, pp. 74–79, 2017, doi: 10.1016/j.physb.2017.01.011.

[50] S. K. Gore, S. S. Jadhav, U. B. Tumberphale, S. M. Shaikh, M. Naushad, and R. S. Mane, "Cation distribution, magnetic properties and cubic-perovskite phase transition in bismuth-doped nickel ferrite," *Solid State Sci.*, vol. 74, pp. 88–94, 2017, doi: 10.1016/j.solidstatesciences.2017.10.009.

[51] Á. B. Sifontes *et al.*, "Chitosan templated synthesis of strontium–iron–oxygen nanocrystalline system," *Ceram. Int.*, vol. 41, no. 10, pp. 13250–13256, 2015, doi: 10.1016/j.ceramint.2015.07.104.

[52] V. Tsurkan, H. A. Krug von Nidda, J. Deisenhofer, P. Lunkenheimer, and A. Loidl, "On the complexity of spinels: Magnetic, electronic, and polar ground states," *Phys. Rep.*, vol. 926, pp. 1–86, 2021, doi: 10.1016/j.physrep.2021.04.002.

[53] K. K. Kefeni, B. B. Mamba, and T. A. M. Msagati, "Application of spinel ferrite nanoparticles in water and wastewater treatment: A review," *Sep. Purif. Technol.*, vol. 188, pp. 399–422, 2017, doi: 10.1016/j.seppur.2017.07.015.

[54] A. El khanchaoui *et al.*, "Structural, morphological, and magnetic studies of spinel ferrites derived from layered double hydroxides," *Appl. Phys. A*, vol. 128, no. 5, pp. 1–12, 2022, doi: 10.1007/s00339-022-05547-4.

[55] H. Mahajan, S. K. Godara, and A. K. Srivastava, "Synthesis and investigation of structural, morphological, and magnetic properties of the manganese doped cobalt-zinc spinel ferrite," *J. Alloys Compd.*, vol. 896, p. 162966, 2022, doi: 10.1016/j.jallcom.2021.162966.

[56] A. Sutka and G. Mezinskis, "Sol-gel auto-combustion synthesis of spinel-type ferrite nanomaterials," *Front. Mater. Sci.*, vol. 6, no. 2, pp. 128–141, 2012, doi: 10.1007/s11706-012-0167-3.

[57] P. Innocenzi, "Understanding sol–gel transition through a picture. A short tutorial," *J. Sol-Gel Sci. Technol.*, vol. 94, no. 3, pp. 544–550, 2020, doi: 10.1007/s10971-020-05243-w.

[58] H. Shirakawa, E. J. Louis, A. G. MacDiarmid, C. K. Chiang, and A. J. Heeger, "Synthesis of electrically conducting organic polymers: Halogen derivatives of polyacetylene, (CH)x," *J. Chem. Soc. Chem. Commun.*, no. 16, pp. 578–580, 1977, doi: 10.1039/C39770000578.

[59] C. H. B. Silva, N. A. Galiote, F. Huguenin, É. Teixeira-Neto, V. R. L. Constantino, and M. L. A. Temperini, "Spectroscopic, morphological and electrochromic characterization of layer-by-layer hybrid films of polyaniline and hexaniobate nanoscrolls," *J. Mater. Chem.*, vol. 22, no. 28, pp. 14052–14060, 2012, doi: 10.1039/c2jm31531a.

[60] S. Bhadra, D. Khastgir, N. K. Singha, and J. H. Lee, "Progress in preparation, processing and applications of polyaniline," *Prog. Polym. Sci.*, vol. 34, no. 8, pp. 783–810, 2009, doi: 10.1016/j.progpolymsci.2009.04.003.

[61] Z. A. Boeva and V. G. Sergeyev, "Polyaniline: Synthesis, properties, and application," *Polym. Sci. - Ser. C*, vol. 56, no. 1, pp. 144–153, 2014, doi: 10.1134/S1811238214010032.

[62]   S. Bhandari, *Polyaniline*. Elsevier Inc., 2018.

[63]   P. Kong *et al.*, "Conjugated HCl-doped polyaniline for photocatalytic oxidative coupling of amines under visible light," *Catal. Sci. Technol.*, vol. 9, no. 3, pp. 753–761, 2019, doi: 10.1039/c8cy02280a.

[64]   M. R. Saeb, P. Zarrintaj, P. Khandelwal, and N. P. S. Chauhan, *Synthetic route of polyaniline (I): Conventional oxidative polymerization*, no. I. Elsevier Inc., 2019.

[65]   B. Qiu, J. Wang, Z. Li, X. Wang, and X. Li, "Influence of acidity and oxidant concentration on the nanostructures and electrochemical performance of polyaniline during fast microwave-assisted chemical polymerization," *Polymers (Basel).*, vol. 12, no. 2, 2020, doi: 10.3390/polym12020310.

[66]   J. Stejskal, I. Sapurina, J. Prokeš, and J. Zemek, "In-situ polymerized polyaniline films," *Synth. Met.*, vol. 105, no. 3, pp. 195–202, 1999, doi: 10.1016/S0379-6779(99)00105-8.

[67]   M. F. Shakir *et al.*, "EMI shielding properties of polymer blends with inclusion of graphene nano platelets," *Results Phys.*, vol. 14, no. April, p. 102365, 2019, doi: 10.1016/j.rinp.2019.102365.

[68]   G. Ciric-Marjanovic, "Recent advances in polyaniline research: Polymerization mechanisms, structural aspects, properties and applications," *Synth. Met.*, vol. 177, no. 3, pp. 1–47, 2013, doi: 10.1016/j.synthmet.2013.06.004.

[69]   S. Tan *et al.*, "Property influence of polyanilines on photovoltaic behaviors of dye-sensitized solar cells," *Langmuir*, vol. 20, no. 7, pp. 2934–2937, 2004, doi: 10.1021/la036260m.

[70]   M. Beygisangchin, S. A. Rashid, S. Shafie, and A. R. Sadrolhosseini, "Polyaniline Thin Films — A Review," *Polymers (Basel).*, vol. 13, pp. 1–46, 2021.

[71]   N. Kumari Jangid, S. Jadoun, and N. Kaur, "A review on high-throughput synthesis, deposition of thin films and properties of polyaniline," *Eur. Polym. J.*, vol. 125, no. August 2019, p. 109485, 2020, doi: 10.1016/j.eurpolymj.2020.109485.

[72]   A. Khosrozadeh, M. A. Darabi, Q. Wang, and M. Xing, "Polyaniline nanoflowers grown on vibration-isolator-mimetic polyurethane nanofibers for flexible supercapacitors with prolonged cycle life," *J. Mater. Chem. A*, vol. 5, no. 17, pp. 7933–7943, 2017, doi: 10.1039/c7ta00591a.

[73]   K. V. Sankar and R. K. Selvan, "The preparation of MnFe2O4 decorated flexible graphene wrapped with PANI and its electrochemical performances for hybrid

supercapacitors," *RSC Adv.*, vol. 4, no. 34, pp. 17555–17566, 2014, doi: 10.1039/c3ra47681b.

[74] M. O. Akharame, O. S. Fatoki, B. O. Opeolu, D. I. Olorunfemi, and O. U. Oputu, "Polymeric nanocomposites (Pncs) for wastewater remediation: An overview," *Polym. - Plast. Technol. Eng.*, vol. 57, no. 17, pp. �1801–1827, 2018, doi: 10.1080/03602559.2018.1434666.

[75] S. Kango, S. Kalia, A. Celli, J. Njuguna, Y. Habibi, and R. Kumar, "Surface modification of inorganic nanoparticles for development of organic-inorganic nanocomposites - A review," *Prog. Polym. Sci.*, vol. 38, no. 8, pp. 1232–1261, 2013, doi: 10.1016/j.progpolymsci.2013.02.003.

[76] T. Dippong, E. A. Levei, I. G. Deac, I. Petean, and O. Cadar, "Dependence of Structural, Morphological and Magnetic Properties of Manganese Ferrite on Ni-Mn Substitution," *Int. J. Mol. Sci.*, vol. 23, no. 6, 2022, doi: 10.3390/ijms23063097.

[77] S. A. Al Kiey, R. Ramadan, and M. M. El-Masry, "Synthesis and characterization of mixed ternary transition metal ferrite nanoparticles comprising cobalt, copper and binary cobalt–copper for high-performance supercapacitor applications," *Appl. Phys. A Mater. Sci. Process.*, vol. 128, no. 6, pp. 1–13, 2022, doi: 10.1007/s00339-022-05590-1.

[78] S. Balideh, A. Aavazpour, G. Rezaei, and A. Nikzad, "Structural and magnetic properties of spinel nickel-cobalt ferrite nanoparticles substituted by dysprosium cation synthesized by hydrothermal method," *Acta Phys. Pol. A*, vol. 140, no. 1, pp. 14–19, 2021, doi: 10.12693/APHYSPOLA.140.14.

[79] B. Nawaz, G. Ali, M. O. Ullah, S. Rehman, and F. Abbas, "Investigation of the electrochemical properties of ni0.5zn0.5fe2o4 as binder-based and binder-free electrodes of supercapacitors," *Energies*, vol. 14, no. 11, 2021, doi: 10.3390/en14113297.

[80] E. Samuel, A. Aldalbahi, M. El-Newehy, H. El-Hamshary, and S. S. Yoon, "Nickel ferrite beehive-like nanosheets for binder-free and high-energy-storage supercapacitor electrodes," *J. Alloys Compd.*, vol. 852, p. 156929, 2021, doi: 10.1016/j.jallcom.2020.156929.

[81] K. Sathiyamurthy, C. Rajeevgandhi, L. Guganathan, S. Bharanidharan, and S. Savithiri, "Enhancement of magnetic, supercapacitor applications and theoretical

approach on cobalt-doped zinc ferrite nanocomposites," *J. Mater. Sci. Mater. Electron.*, vol. 32, no. 9, pp. 11593–11606, 2021, doi: 10.1007/s10854-021-05764-2.

[82]   M. Safari and J. Mazloom, "Electrochemical performance of spindle-like Fe2Co-MOF and derived magnetic yolk-shell CoFe2O4 microspheres for supercapacitor applications," *J. Solid State Electrochem.*, vol. 25, no. 8–9, pp. 2189–2200, 2021, doi: 10.1007/s10008-021-04989-9.

[83]   W. Raza, G. Nabi, A. Shahzad, N. Malik, and N. Raza, "Electrochemical performance of lanthanum cerium ferrite nanoparticles for supercapacitor applications," *J. Mater. Sci. Mater. Electron.*, vol. 32, no. 6, pp. 7443–7454, 2021, doi: 10.1007/s10854-021-05457-w.

[84]   A. Anwar *et al.*, "The impact of highly paramagnetic Gd3+ cations on structural, spectral, magnetic and dielectric properties of spinel nickel ferrite nanoparticles," *J. Saudi Chem. Soc.*, vol. 25, no. 9, p. 101306, 2021, doi: 10.1016/j.jscs.2021.101306.

[85]   I. Petrila and F. Tudorache, "Effects of sintering temperature on the microstructure, electrical and magnetic characteristics of copper-zinc spinel ferrite with possibility use as humidity sensors," *Sensors Actuators A Phys.*, vol. 332, p. 113060, 2021, doi: 10.1016/j.sna.2021.113060.

[86]   S. A. Mazen, H. M. Elsayed, and N. I. Abu-Elsaad, "Effect of divalent metal ions substitution on structural and magnetic properties of Li0.25Mn0.5-xMxFe2.25O4 (M = Co2+, Ni2+, Cu2+) spinel ferrites," *Mater. Chem. Phys.*, vol. 256, no. March, pp. 1–10, 2020, doi: 10.1016/j.matchemphys.2020.123676.

[87]   S. J. Uke, S. P. Mardikar, D. R. Bambole, Y. Kumar, and G. N. Chaudhari, "Sol-gel citrate synthesized Zn doped MgFe2O4 nanocrystals: A promising supercapacitor electrode material," *Mater. Sci. Energy Technol.*, vol. 3, pp. 446–455, 2020, doi: 10.1016/j.mset.2020.02.009.

[88]   M. Barakzehi, M. Montazer, F. Sharif, T. Norby, and A. Chatzitakis, "MOF-modified polyester fabric coated with reduced graphene oxide/polypyrrole as electrode for flexible supercapacitors," *Electrochim. Acta*, vol. 336, p. 135743, 2020, doi: 10.1016/j.electacta.2020.135743.

[89]   J. P. Cheng, W. D. Wang, X. C. Wang, and F. Liu, "Recent research of core–shell structured composites with NiCo2O4 as scaffolds for electrochemical capacitors," *Chem. Eng. J.*, vol. 393, no. December 2019, p. 124747, 2020, doi: 10.1016/j.cej.2020.124747.

[90] R. Awata, M. Shehab, A. El Tahan, M. Soliman, and S. Ebrahim, "High performance supercapacitor based on camphor sulfonic acid doped polyaniline/multiwall carbon nanotubes nanocomposite," *Electrochim. Acta*, vol. 347, p. 136229, 2020, doi: 10.1016/j.electacta.2020.136229.

[91] S. Gul *et al.*, "Al-substituted zinc spinel ferrite nanoparticles: Preparation and evaluation of structural, electrical, magnetic and photocatalytic properties," *Ceram. Int.*, vol. 46, no. 9, pp. 14195–14205, 2020, doi: 10.1016/j.ceramint.2020.02.228.

[92] S. B. Somvanshi, S. A. Jadhav, M. V. Khedkar, P. B. Kharat, S. D. More, and K. M. Jadhav, "Structural, thermal, spectral, optical and surface analysis of rare earth metal ion (Gd3+) doped mixed Zn–Mg nano-spinel ferrites," *Ceram. Int.*, vol. 46, no. 9, pp. 13170–13179, 2020, doi: 10.1016/j.ceramint.2020.02.091.

[93] Y. Slimani *et al.*, "Investigation of structural and physical properties of Eu3+ ions substituted Ni0.4Cu0.2Zn0.4Fe2O4 spinel ferrite nanoparticles prepared via sonochemical approach," *Results Phys.*, vol. 17, no. February, p. 103061, 2020, doi: 10.1016/j.rinp.2020.103061.

[94] M. F. Warsi *et al.*, "Erbium substituted nickel–cobalt spinel ferrite nanoparticles: Tailoring the structural, magnetic and electrical parameters," *Ceram. Int.*, vol. 46, no. 15, pp. 24194–24203, 2020, doi: 10.1016/j.ceramint.2020.06.199.

[95] S. Ikram *et al.*, "A Kinetic study of Tb3+ and Dy3+ co-substituted CoFe2O4 spinel ferrites using temperature dependent XRD, XPS and SQUID measurements," *Ceram. Int.*, vol. 46, no. 10, pp. 15943–15948, 2020, doi: 10.1016/j.ceramint.2020.03.143.

[96] S. Ikram *et al.*, "Role of Rare Earth Metal Ions Doping on Structural, Electrical, Magnetic, and Dielectric Behavior of Spinel Ferrites: a Comparative Study," *J. Supercond. Nov. Magn.*, vol. 34, no. 7, pp. 1833–1842, 2021, doi: 10.1007/s10948-020-05688-8.

[97] S. V. Bhandare *et al.*, "Effect of Mg-substitution in Co–Ni-Ferrites: Cation distribution and magnetic properties," *Mater. Chem. Phys.*, vol. 251, no. December 2019, p. 123081, 2020, doi: 10.1016/j.matchemphys.2020.123081.

[98] C. Murugesan, K. Ugendar, L. Okrasa, J. Shen, and G. Chandrasekaran, "Zinc substitution effect on the structural, spectroscopic and electrical properties of nanocrystalline MnFe2O4 spinel ferrite," *Ceram. Int.*, vol. 47, no. 2, pp. 1672–1685, 2021, doi: 10.1016/j.ceramint.2020.08.284.

[99] R. P. Patil, P. N. Nikam, S. B. Patil, R. K. Dhokale, V. S. Sawant, and S. B. Shelke, "Effect of Sintering Temperature on Structural and Morphological Properties of Mn-

Substituted Lithium Ferrite," *Macromol. Symp.*, vol. 393, no. 1, pp. 2–6, 2020, doi: 10.1002/masy.202000173.

[100] K. Tanbir, M. P. Ghosh, R. K. Singh, M. Kar, and S. Mukherjee, "Effect of doping different rare earth ions on microstructural, optical, and magnetic properties of nickel–cobalt ferrite nanoparticles," *J. Mater. Sci. Mater. Electron.*, vol. 31, no. 1, pp. 435–443, 2020, doi: 10.1007/s10854-019-02546-9.

[101] N. Mechi, A. Mallah, S. Hcini, M. L. Bouazizi, M. Boudard, and A. Dhahri, "Effects of Sintering Temperature on Microstructural, Magnetic, and Impedance Spectroscopic Properties of Ni0.4Cd0.3Zn0.3Fe2O4 Ferrites," *J. Supercond. Nov. Magn.*, vol. 33, no. 5, pp. 1547–1557, 2020, doi: 10.1007/s10948-019-05416-x.

[102] F. Hcini, S. Hcini, B. Alzahrani, S. Zemni, and M. L. Bouazizi, "Effects of sintering temperature on structural, infrared, magnetic and electrical properties of Cd0.5Zn0.5FeCrO4 ferrites prepared by sol–gel route," *J. Mater. Sci. Mater. Electron.*, vol. 31, no. 17, pp. 14986–14997, 2020, doi: 10.1007/s10854-020-04061-8.

[103] M. A. Almessiere *et al.*, "Impact of Eu3+ ion substitution on structural, magnetic and microwave traits of Ni–Cu–Zn spinel ferrites," *Ceram. Int.*, vol. 46, no. 8, pp. 11124–11131, 2020, doi: 10.1016/j.ceramint.2020.01.132.

[104] R. R. Chilwar, A. R. Chavan, M. K. Babrekar, and K. M. Jadhav, "Impact of trivalent metal ion substitution on structural, optical, magnetic and dielectric properties of Li0.5Fe2.5O4 thin films," *Phys. B Condens. Matter*, vol. 566, no. April, pp. 43–49, 2019, doi: 10.1016/j.physb.2019.04.031.

[105] P. Bandyopadhyay, G. Saeed, N. H. Kim, and J. H. Lee, "Zinc-nickel-cobalt oxide@NiMoO4 core-shell nanowire/nanosheet arrays for solid state asymmetric supercapacitors," *Chem. Eng. J.*, vol. 384, p. 123357, 2020, doi: 10.1016/j.cej.2019.123357.

[106] Y. Z. Cai, W. Q. Cao, Y. L. Zhang, P. He, J. C. Shu, and M. S. Cao, "Tailoring rGO-NiFe2O4 hybrids to tune transport of electrons and ions for supercapacitor electrodes," *J. Alloys Compd.*, vol. 811, p. 152011, 2019, doi: 10.1016/j.jallcom.2019.152011.

[107] J. Bhagwan, S. Khaja Hussain, and J. S. Yu, "Aqueous asymmetric supercapacitors based on ZnCo2O4 nanoparticles via facile combustion method," *J. Alloys Compd.*, vol. 815, p. 152456, 2020, doi: 10.1016/j.jallcom.2019.152456.

[108] J. Acharya, B. G. S. Raj, T. H. Ko, M. S. Khil, H. Y. Kim, and B. S. Kim, "Facile one pot sonochemical synthesis of CoFe2O4/MWCNTs hybrids with well-dispersed

MWCNTs for asymmetric hybrid supercapacitor applications," *Int. J. Hydrogen Energy*, vol. 45, no. 4, pp. 3073–3085, 2020, doi: 10.1016/j.ijhydene.2019.11.169.

[109] T. Das and B. Verma, "Synthesis of polymer composite based on polyaniline-acetylene black-copper ferrite for supercapacitor electrodes," *Polymer (Guildf).*, vol. 168, pp. 61–69, 2019, doi: 10.1016/j.polymer.2019.01.058.

[110] H. Javed, F. Iqbal, P. O. Agboola, M. A. Khan, M. F. Warsi, and I. Shakir, "Structural, electrical and magnetic parameters evaluation of nanocrystalline rare earth Nd 3+ -substituted nickel-zinc spinel ferrite particles," *Ceram. Int.*, vol. 45, no. 8, pp. 11125–11130, 2019, doi: 10.1016/j.ceramint.2019.02.176.

[111] B. J. Rani *et al.*, "Pure and cobalt-substituted zinc-ferrite magnetic ceramics for supercapacitor applications," *Appl. Phys. A Mater. Sci. Process.*, vol. 124, no. 7, pp. 1–12, 2018, doi: 10.1007/s00339-018-1936-3.

[112] M. Chandel, D. Moitra, P. Makkar, H. Sinha, H. S. Hora, and N. N. Ghosh, "Synthesis of multifunctional CuFe2O4-reduced graphene oxide nanocomposite: An efficient magnetically separable catalyst as well as high performance supercapacitor and first-principles calculations of its electronic structures," *RSC Adv.*, vol. 8, no. 49, pp. 27725–27739, 2018, doi: 10.1039/c8ra05393f.

[113] S. Hcini, N. Kouki, A. Omri, A. Dhahri, and M. L. Bouazizi, "Effect of sintering temperature on structural, magnetic, magnetocaloric and critical behaviors of Ni-Cd-Zn ferrites prepared using sol-gel method," *J. Magn. Magn. Mater.*, vol. 464, pp. 91–102, 2018, doi: 10.1016/j.jmmm.2018.05.045.

[114] F. M. Ismail, M. Ramadan, A. M. Abdellah, I. Ismail, and N. K. Allam, "Mesoporous spinel manganese zinc ferrite for high-performance supercapacitors," *J. Electroanal. Chem.*, vol. 817, pp. 111–117, 2018, doi: 10.1016/j.jelechem.2018.04.002.

[115] A. Shokri, S. F. Shayesteh, and K. Boustani, "The role of Co ion substitution in SnFe2O4 spinel ferrite nanoparticles: Study of structural, vibrational, magnetic and optical properties," *Ceram. Int.*, vol. 44, no. 18, pp. 22092–22101, 2018, doi: 10.1016/j.ceramint.2018.08.319.

[116] X. Feng, Y. Huang, X. Chen, C. Wei, X. Zhang, and M. Chen, "Hierarchical CoFe2O4/NiFe2O4 nanocomposites with enhanced electrochemical capacitive properties," *J. Mater. Sci.*, vol. 53, no. 4, pp. 2648–2657, 2018, doi: 10.1007/s10853-017-1735-9.

[117] H. Kennaz *et al.*, "Synthesis and electrochemical investigation of spinel cobalt ferrite magnetic nanoparticles for supercapacitor application," *J. Solid State Electrochem.*, vol. 22, no. 3, pp. 835–847, 2018, doi: 10.1007/s10008-017-3813-y.

[118] V. Vignesh, K. Subramani, M. Sathish, and R. Navamathavan, "Electrochemical investigation of manganese ferrites prepared via a facile synthesis route for supercapacitor applications," *Colloids Surfaces A Physicochem. Eng. Asp.*, vol. 538, no. November 2017, pp. 668–677, 2018, doi: 10.1016/j.colsurfa.2017.11.045.

[119] S. R. Bhongale, H. R. Ingawale, T. J. Shinde, and P. N. Vasambekar, "Effect of Nd3+ substitution on structural and magnetic properties of Mg–Cd ferrites synthesized by microwave sintering technique," *J. Rare Earths*, vol. 36, no. 4, pp. 390–397, 2018, doi: 10.1016/j.jre.2017.11.003.

[120] E. Ranjith Kumar *et al.*, "Synergistic effect of heat treatment on structural, magnetic and dielectric properties of spinel ferrite nanoparticles," *J. Mater. Sci. Mater. Electron.*, vol. 29, no. 24, pp. 20968–20977, 2018, doi: 10.1007/s10854-018-0241-4.

[121] M. N. Akhtar and M. A. Khan, "Effect of rare earth doping on the structural and magnetic features of nanocrystalline spinel ferrites prepared via sol gel route," *J. Magn. Magn. Mater.*, vol. 460, pp. 268–277, 2018, doi: 10.1016/j.jmmm.2018.03.069.

[122] F. S. Omar, A. Numan, N. Duraisamy, S. Bashir, K. Ramesh, and S. Ramesh, "A promising binary nanocomposite of zinc cobaltite intercalated with polyaniline for supercapacitor and hydrazine sensor," *J. Alloys Compd.*, vol. 716, pp. 96–105, 2017, doi: 10.1016/j.jallcom.2017.05.039.

[123] R. Singh Yadav *et al.*, "Structural, magnetic, elastic, dielectric and electrical properties of hot-press sintered Co1−xZnxFe2O4 (x = 0.0, 0.5) spinel ferrite nanoparticles," *J. Magn. Magn. Mater.*, vol. 447, pp. 48–57, 2018, doi: 10.1016/j.jmmm.2017.09.033.

[124] M. A. Mousa, M. Khairy, and M. Shehab, "Nanostructured ferrite/graphene/polyaniline using for supercapacitor to enhance the capacitive behavior," *J. Solid State Electrochem.*, vol. 21, no. 4, pp. 995–1005, 2017, doi: 10.1007/s10008-016-3446-6.

[125] A. E. Elkholy, F. El-Taib Heakal, and N. K. Allam, "Nanostructured spinel manganese cobalt ferrite for high-performance supercapacitors," *RSC Adv.*, vol. 7, no. 82, pp. 51888–51895, 2017, doi: 10.1039/c7ra11020k.

[126] P. Thakur, R. Sharma, V. Sharma, and P. Sharma, "Structural and optical properties of Mn0.5Zn0.5Fe2O4 nano ferrites: Effect of sintering temperature," *Mater. Chem. Phys.*, vol. 193, pp. 285–289, 2017, doi: 10.1016/j.matchemphys.2017.02.043.

[127] S. A. Ansari, H. Fouad, S. G. Ansari, M. P. Sk, and M. H. Cho, "Mechanically exfoliated MoS2 sheet coupled with conductive polyaniline as a superior supercapacitor electrode material," *J. Colloid Interface Sci.*, vol. 504, pp. 276–282, 2017, doi: 10.1016/j.jcis.2017.05.064.

[128] N. S. Arul, L. S. Cavalcante, and J. In Han, "Facile synthesis of ZnS/MnS nanocomposites for supercapacitor applications," *J. Solid State Electrochem.*, vol. 22, no. 1, pp. 303–313, 2018, doi: 10.1007/s10008-017-3782-1.

[129] M. T. Farid, I. Ahmad, M. Kanwal, and I. Ali, "Effect of praseodymium ions on manganese based spinel ferrites," *Chinese J. Phys.*, vol. 55, no. 3, pp. 813–824, 2017, doi: 10.1016/j.cjph.2017.02.011.

[130] C. Wei *et al.*, "Valence Change Ability and Geometrical Occupation of Substitution Cations Determine the Pseudocapacitance of Spinel Ferrite XFe2O4(X = Mn, Co, Ni, Fe)," *Chem. Mater.*, vol. 28, no. 12, pp. 4129–4133, 2016, doi: 10.1021/acs.chemmater.6b00713.

[131] K. Vijaya Sankar and R. Kalai Selvan, "Fabrication of flexible fiber supercapacitor using covalently grafted CoFe2O4/reduced graphene oxide/polyaniline and its electrochemical performances," *Electrochim. Acta*, vol. 213, pp. 469–481, 2016, doi: 10.1016/j.electacta.2016.07.056.

[132] B. Bashir *et al.*, "Copper doped manganese ferrites nanoparticles anchored on graphene nano-sheets for high performance energy storage applications," *J. Alloys Compd.*, vol. 695, pp. 881–887, 2017, doi: 10.1016/j.jallcom.2016.10.183.

[133] S. Sahoo, S. Zhang, and J. J. Shim, "Porous Ternary High Performance Supercapacitor Electrode Based on Reduced graphene oxide, NiMn2O4, and Polyaniline," *Electrochim. Acta*, vol. 216, pp. 386–396, 2016, doi: 10.1016/j.electacta.2016.09.030.

[134] B. Bhujun, M. T. T. Tan, and A. S. Shanmugam, "Study of mixed ternary transition metal ferrites as potential electrodes for supercapacitor applications," *Results Phys.*, vol. 7, no. May, pp. 345–353, 2017, doi: 10.1016/j.rinp.2016.04.010.

[135] V. Manikandan, A. Vanitha, E. Ranjith Kumar, and J. Chandrasekaran, "Effect of sintering temperature on Structural and Dielectric properties of Sn substituted

CuFe2O4 Nanoparticles," *J. Magn. Magn. Mater.*, vol. 423, pp. 250–255, 2017, doi: 10.1016/j.jmmm.2016.09.077.

[136] K. Praveena, K. Sadhana, S. Matteppanavar, and H. L. Liu, "Effect of sintering temperature on the structural, dielectric and magnetic properties of Ni0.4Zn0.2Mn0.4Fe2O4 potential for radar absorbing," *J. Magn. Magn. Mater.*, vol. 423, pp. 343–352, 2017, doi: 10.1016/j.jmmm.2016.09.129.

[137] G. Chandra, R. C. Srivastava, V. R. Reddy, and H. M. Agrawal, "Effect of sintering temperature on magnetization and Mössbauer parameters of cobalt ferrite nanoparticles," *J. Magn. Magn. Mater.*, vol. 427, pp. 225–229, 2017, doi: 10.1016/j.jmmm.2016.10.082.

[138] D. Zha, P. Xiong, and X. Wang, "Strongly coupled manganese ferrite/carbon black/polyaniline hybrid for low-cost supercapacitors with high rate capability," *Electrochim. Acta*, vol. 185, pp. 218–228, 2015, doi: 10.1016/j.electacta.2015.10.139.

[139] R. Tholkappiyan, A. N. Naveen, S. Sumithra, and K. Vishista, "Investigation on spinel MnCo2O4 electrode material prepared via controlled and uncontrolled synthesis route for supercapacitor application," *J. Mater. Sci.*, vol. 50, no. 17, pp. 5833–5843, 2015, doi: 10.1007/s10853-015-9132-8.

[140] P. Liu *et al.*, "Effect of Mn substitution on the promoted formaldehyde oxidation over spinel ferrite: Catalyst characterization, performance and reaction mechanism," *Appl. Catal. B Environ.*, vol. 182, pp. 476–484, 2016, doi: 10.1016/j.apcatb.2015.09.055.

[141] P. Xiong, H. Huang, and X. Wang, "Design and synthesis of ternary cobalt ferrite/graphene/polyaniline hierarchical nanocomposites for high-performance supercapacitors This work is dedicated to Professor MIN Enze on the occasion of his 90th birthday.," *J. Power Sources*, vol. 245, pp. 937–946, 2014, doi: 10.1016/j.jpowsour.2013.07.064.

[142] F. Cai, Y. Kang, H. Chen, M. Chen, and Q. Li, "Hierarchical CNT@NiCo2O4 core-shell hybrid nanostructure for high-performance supercapacitors," *J. Mater. Chem. A*, vol. 2, no. 29, pp. 11509–11515, 2014, doi: 10.1039/c4ta01235f.

[143] H. Bahiraei, M. Z. Shoushtari, K. Gheisari, and C. K. Ong, "The effect of sintering temperature on the electromagnetic properties of nanocrystalline MgCuZn ferrite prepared by sol-gel auto combustion method," *Mater. Lett.*, vol. 122, pp. 129–132, 2014, doi: 10.1016/j.matlet.2014.02.027.

[144] R. P. Patil, S. D. Delekar, D. R. Mane, and P. P. Hankare, "Synthesis, structural and magnetic properties of different metal ion substituted nanocrystalline zinc ferrite," *Results Phys.*, vol. 3, no. 3, pp. 129–133, 2013, doi: 10.1016/j.rinp.2013.08.002.

[145] M. Rahimi, P. Kameli, M. Ranjbar, and H. Salamati, "The effect of sintering temperature on evolution of structural and magnetic properties of nanostructured Ni0.3Zn0.7Fe 2O4 ferrite," *J. Nanoparticle Res.*, vol. 15, no. 9, 2013, doi: 10.1007/s11051-013-1865-1.

[146] V. S. Kumbhar, A. D. Jagadale, N. M. Shinde, and C. D. Lokhande, "Chemical synthesis of spinel cobalt ferrite (CoFe 2 O 4) nano-flakes for supercapacitor application," *Appl. Surf. Sci.*, vol. 259, pp. 39–43, 2012, doi: 10.1016/j.apsusc.2012.06.034.

[147] R. P. Patil, P. P. Hankare, K. M. Garadkar, and R. Sasikala, "Effect of sintering temperature on structural, magnetic properties of lithium chromium ferrite," *J. Alloys Compd.*, vol. 523, pp. 66–71, 2012, doi: 10.1016/j.jallcom.2012.01.025.

[148] M. F. Al-Hilli, S. Li, and K. S. Kassim, "Gadolinium substitution and sintering temperature dependent electronic properties of Li-Ni ferrite," *Mater. Chem. Phys.*, vol. 128, no. 1–2, pp. 127–132, 2011, doi: 10.1016/j.matchemphys.2011.02.064.

[149] M. Penchal Reddy *et al.*, "Effect of sintering temperature on structural and magnetic properties of NiCuZn and MgCuZn ferrites," *J. Magn. Magn. Mater.*, vol. 322, no. 19, pp. 2819–2823, 2010, doi: 10.1016/j.jmmm.2010.04.036.

[150] P. P. Hankare, S. D. Jadhav, U. B. Sankpal, S. S. Chavan, K. J. Waghmare, and B. K. Chougule, "Synthesis, characterization and effect of sintering temperature on magnetic properties of MgNi ferrite prepared by co-precipitation method," *J. Alloys Compd.*, vol. 475, no. 1–2, pp. 926–929, 2009, doi: 10.1016/j.jallcom.2008.08.082.

[151] H. Su, H. Zhang, X. Tang, B. Liu, and Z. Zhong, "Study on low-temperature sintered NiCuZn and MgCuZn spinel ferrites," *J. Alloys Compd.*, vol. 475, no. 1–2, pp. 683–685, 2009, doi: 10.1016/j.jallcom.2008.07.112.

[152] S. D. Bhame and P. A. Joy, "Effect of sintering conditions and microstructure on the magnetostrictive properties of cobalt ferrite," *J. Am. Ceram. Soc.*, vol. 91, no. 6, pp. 1976–1980, 2008, doi: 10.1111/j.1551-2916.2008.02367.x.

[153] D. Gal, G. Hodes, D. Lincot, and H. Schock, *Chemical Solution Deposition of*, vol. 362. 2000.

[154] C. Hu, X. Dang, and S. Hu, "Studies on adsorption of cetyltrimethylammonium bromide at carbon paste electrode and the enhancement effect in thyroxine reduction

by voltammetry and electrochemical impedance spectroscopy," *J. Electroanal. Chem.*, vol. 572, no. 1, pp. 161–171, 2004, doi: 10.1016/j.jelechem.2004.06.009.

[155] R. S. Almenares Reyes *et al.*, "Clay Deposits from the Northeastern of Cuba: Characterization, Evaluation, and Use as a Source of Supplementary Cementitious Materials," *RILEM Bookseries*, vol. 25, no. 617, pp. 49–56, 2020, doi: 10.1007/978-981-15-2806-4_6.

[156] https://www.lpu.in/cif/powder-x-ray-diffractometer.php.

[157] A. A. Bunaciu, E. gabriela Udriştioiu, and H. Y. Aboul-Enein, "X-Ray Diffraction: Instrumentation and Applications," *Crit. Rev. Anal. Chem.*, vol. 45, no. 4, pp. 289–299, 2015, doi: 10.1080/10408347.2014.949616.

[158] P. B. Hirsch, "Elements of X-Ray Diffraction," *Phys. Bull.*, vol. 8, no. 7, pp. 237–238, 1957, doi: 10.1088/0031-9112/8/7/008.

[159] https://www.semanticscholar.org/paper/3.-GROWTH-METHODOLOGY-OF-PURE-AND-DOPED-METAL/528d83f73dc4e051c0cc0cf61c606e6cb015e382/figure/7.

[160] "Handbook of Instrumental Techniques for Analytical Chemistry," *J. Liq. Chromatogr. Relat. Technol.*, vol. 21, no. 19, pp. 3072–3076, 1998, doi: 10.1080/10826079808006889.

[161] D. Sundeep, "Spectroscopic Investigations of MoO3 / CuO Nanocomposites : Mechanical Synthesis , Spectroscopic Characterization and Thermal Analysis," no. October 2017, 2018.

[162] J. Preudhomme and P. Tarte, "Infrared studies of spinels-III. The normal II-III spinels," *Spectrochim. Acta Part A Mol. Spectrosc.*, vol. 27, no. 9, pp. 1817–1835, 1971, doi: 10.1016/0584-8539(71)80235-0.

[163] A. Ramírez-Hernández, C. Aguilar-Flores, and A. Aparicio-Saguilán, "Fingerprint analysis of ftir spectra of polymers containing vinyl acetate," *DYNA*, vol. 86, no. 209, pp. 198–205, 2019, doi: 10.15446/dyna.v86n209.77513.

[164] A. Alyamani and O. M., "FE-SEM Characterization of Some Nanomaterial," *Scan. Electron Microsc.*, no. 1, 2012, doi: 10.5772/34361.

[165] A. Mayeen, L. K. Shaji, A. K. Nair, and N. Kalarikkal, *Morphological characterization of nanomaterials*. Elsevier Ltd., 2018.

[166] https://www.nanoimages.com/sem-technology-overview/sem_img2/.

[167] K. Mikroskop, E. Imbasan, P. Medan, and D. I. Bti, "47111897."

[168] https://www.azom.com/article.aspx?ArticleID=16256.

[169] https://www.thermofisher.com/blog/materials/edx-analysis-with-sem-how-does-it work/.

[170] R. K. Mishra, A. K. Zachariah, and S. Thomas, *Energy-Dispersive X-ray Spectroscopy Techniques for Nanomaterial*. Elsevier Inc., 2017.

[171] A. O. Adeyeye and G. Shimon, *Growth and Characterization of Magnetic Thin Film and Nanostructures*, 1st ed., vol. 5. Elsevier B.V., 2015.

[172] https://upload.wikimedia.org/wikipedia/commons/f/f2/VSM_en.svg.

[173] M. D. Stoller and R. S. Ruoff, "Best practice methods for determining an electrode material's performance for ultracapacitors," *Energy Environ. Sci.*, vol. 3, no. 9, pp. 1294–1301, 2010, doi: 10.1039/c0ee00074d.

[174] B. K. Kim, S. Sy, A. Yu, and J. Zhang, "Electrochemical Supercapacitors for Energy Storage and Conversion," *Handb. Clean Energy Syst.*, pp. 1–25, 2015, doi: 10.1002/9781118991978.hces112.

[175] M. H. F. Taha, H. Ashraf, and W. Caesarendra, "A brief description of cyclic voltammetry transducer-based non-enzymatic glucose biosensor using synthesized graphene electrodes," *Appl. Syst. Innov.*, vol. 3, no. 3, pp. 1–33, 2020, doi: 10.3390/asi3030032.

[176] M. M. Vadiyar *et al.*, "Mechanochemical growth of a porous ZnFe2O4 nano-flake thin film as an electrode for supercapacitor application," *RSC Adv.*, vol. 5, no. 57, pp. 45935–45942, 2015, doi: 10.1039/c5ra07588b.

[177] M. Mandal *et al.*, "Simple and Cost-Effective Synthesis of Activated Carbon Anchored by Functionalized Multiwalled Carbon Nanotubes for High-Performance Supercapacitor Electrodes with High Energy Density and Power Density," *J. Electron. Mater.*, vol. 50, no. 5, pp. 2879–2889, 2021, doi: 10.1007/s11664-021-08796-w.

[178] V. Climent and J. M. Feliu, *Cyclic voltammetry*. Elsevier Inc., 2018.

[179] M. S. Khan, A. Asif, S. Khawaldeh, and A. Tekin, "Dopamine detection using mercaptopropionic acid and cysteamine for electrodes surface modification," *J. Electr. Bioimpedance*, vol. 9, no. 1, pp. 3–9, 2018, doi: 10.2478/joeb-2018-0002.

[180] L. M. Da Silva *et al.*, "Reviewing the fundamentals of supercapacitors and the difficulties involving the analysis of the electrochemical findings obtained for porous electrode materials," *Energy Storage Mater.*, vol. 27, pp. 555–590, 2020, doi: 10.1016/j.ensm.2019.12.015.

[181] https://superuser.com/questions/698421/is-there-an-acer-battery-management-tool that-limits-the-battery-charge-should.

[182] P. S. Nnamchi and C. S. Obayi, *Electrochemical characterization of nanomaterials*. Elsevier Ltd., 2018.

[183] Y. Li, S. M. Chen, M. A. Ali, and F. M. A. AlHemaid, "Biosynthesis and electrochemical characterization of silver nanoparticles from leaf extract of adenium obesum and its application to antibacterial effect," *Int. J. Electrochem. Sci.*, vol. 8, no. 2, pp. 2691–2701, 2013.

[184] C. Song *et al.*, "Study on Interaction Between TATA-Box Binding Protein (TBP), TATA-Box and Multiprotein Bridging Factor 1(MBF1) in Beauveria bassiana by Graphene-Based Electrochemical Biosensors," *Front. Chem.*, vol. 8, no. April, pp. 1–9, 2020, doi: 10.3389/fchem.2020.00278.

[185] R. D. Levie, "On porous electrodes," *Electrochim. Acta*, vol. 9, no. November 1963, p. 1231, 1964.

[186] H. Herrera Hernández *et al.*, "Electrochemical Impedance Spectroscopy (EIS): A Review Study of Basic Aspects of the Corrosion Mechanism Applied to Steels," *Electrochem. Impedance Spectrosc.*, pp. 1–35, 2020, doi: 10.5772/intechopen.94470.

[187] R. Vedalakshmi, V. Saraswathy, H. W. Song, and N. Palaniswamy, "Determination of diffusion coefficient of chloride in concrete using Warburg diffusion coefficient," *Corros. Sci.*, vol. 51, no. 6, pp. 1299–1307, 2009, doi: 10.1016/j.corsci.2009.03.017.

[188] V. Ganesh, S. Pitchumani, and V. Lakshminarayanan, "New symmetric and asymmetric supercapacitors based on high surface area porous nickel and activated carbon," *J. Power Sources*, vol. 158, no. 2 SPEC. ISS., pp. 1523–1532, 2006, doi: 10.1016/j.jpowsour.2005.10.090.

[189] J. Y. Chang, Y. Der Kuan, and S. M. Lee, "Experimental investigation of a direct methanol fuel cell with Hilbert fractal current collectors," *J. Chem.*, vol. 2014, 2014, doi: 10.1155/2014/371616.

[190] H. S. Magar, R. Y. A. Hassan, and A. Mulchandani, "Electrochemical impedance spectroscopy (Eis): Principles, construction, and biosensing applications," *Sensors*, vol. 21, no. 19, 2021, doi: 10.3390/s21196578.

[191] D. S. Mathew and R. S. Juang, "An overview of the structure and magnetism of spinel ferrite nanoparticles and their synthesis in microemulsions," *Chem. Eng. J.*, vol. 129, no. 1–3, pp. 51–65, 2007, doi: 10.1016/j.cej.2006.11.001.

[192] B. S. Murty, P. Shankar, B. Raj, B. B. Rath, and J. Murday, *Textbook of Nanoscience and Nanotechnology*. 2013.

[193] S. K. Kulkarni, *Nanotechnology - Principles and Practices 3rd ed (Springer, CP, 2015).pdf*. 2014.

[194] M. Amiri, M. Salavati-Niasari, and A. Akbari, "Magnetic nanocarriers: Evolution of spinel ferrites for medical applications," *Adv. Colloid Interface Sci.*, vol. 265, pp. 29–44, 2019, doi: 10.1016/j.cis.2019.01.003.

[195] E. M. Masoud, "Improved initial discharge capacity of nanostructured Ni-Co spinel ferrite as anode material in lithium ion batteries," *Solid State Ionics*, vol. 253, pp. 247–252, 2013, doi: 10.1016/j.ssi.2013.10.017.

[196] L. Satyanarayana, K. M. Reddy, and S. V. Manorama, "Nanosized spinel NiFe2O4: A novel material for the detection of liquefied petroleum gas in air," *Mater. Chem. Phys.*, vol. 82, no. 1, pp. 21–26, 2003, doi: 10.1016/S0254-0584(03)00170-6.

[197] A. Šutka and K. A. Gross, "Spinel ferrite oxide semiconductor gas sensors," *Sensors Actuators, B Chem.*, vol. 222, pp. 95–105, 2016, doi: 10.1016/j.snb.2015.08.027.

[198] W. Hu, N. Qin, G. Wu, Y. Lin, S. Li, and D. Bao, "Opportunity of spinel ferrite materials in nonvolatile memory device applications based on their resistive switching performances," *J. Am. Chem. Soc.*, vol. 134, no. 36, pp. 14658–14661, 2012, doi: 10.1021/ja305681n.

[199] J. L. Xie, M. Han, L. Chen, R. Kuang, and L. Deng, "Microwave-absorbing properties of NiCoZn spinel ferrites," *J. Magn. Magn. Mater.*, vol. 314, no. 1, pp. 37–42, 2007, doi: 10.1016/j.jmmm.2007.02.124.

[200] S. Amiri and H. Shokrollahi, "The role of cobalt ferrite magnetic nanoparticles in medical science," *Mater. Sci. Eng. C*, vol. 33, no. 1, pp. 1–8, 2013, doi: 10.1016/j.msec.2012.09.003.

[201] Y. M. A. Ayana, S. M. El-Sawy, and S.H.Salah, "Contributed papers Zinc-ferrite pigment for corrosion protection," *Anti-Corrosion Methods Mater.*, vol. 44, no. 6, pp. 381–388, 1997.

[202] R. Matz, D. Götsch, R. Karmazin, R. Männer, and B. Siessegger, "Low temperature cofirable MnZn ferrite for power electronic applications," *J. Electroceramics*, vol. 22, no. 1–3, pp. 209–215, 2009, doi: 10.1007/s10832-007-9334-9.

[203] F. Naaz, H. K. Dubey, C. Kumari, and P. Lahiri, "Structural and magnetic properties of MgFe2O4 nanopowder synthesized via co-precipitation route," *SN Appl. Sci.*, vol. 2, no. 5, pp. 1–8, 2020, doi: 10.1007/s42452-020-2611-9.

[204] C. N. Chinnasamy et al., "Mixed spinel structure in nanocrystalline NiFe2O4," *Phys. Rev. B - Condens. Matter Mater. Phys.*, vol. 63, no. 18, pp. 2–7, 2001, doi: 10.1103/PhysRevB.63.184108.

[205] T. Zeeshan, S. Anjum, S. Waseem, and L. Mustufa, "Tailoring of structural and magnetic properties by substitution of copper in cobalt chromium ferrites," *Ceram. Int.*, vol. 44, no. 15, pp. 17709–17715, 2018, doi: 10.1016/j.ceramint.2018.06.235.

[206] M. Stefanescu, M. Bozdog, C. Muntean, O. Stefanescu, and T. Vlase, "Synthesis and magnetic properties of Co1-xZnxFe2O4 (x=0÷1) nanopowders by thermal decomposition of Co(II), Zn(II) and Fe(III) carboxylates," *J. Magn. Magn. Mater.*, vol. 393, pp. 92–98, 2015, doi: 10.1016/j.jmmm.2015.05.048.

[207] M. A. Willard, L. K. Kurihara, E. E. Carpenter, S. Calvin, and V. G. Harris, "Chemically prepared magnetic nanoparticles," *Int. Mater. Rev.*, vol. 49, no. 3–4, pp. 125–170, 2004, doi: 10.1179/095066004225021882.

[208] S. Thankachan, B. P. Jacob, S. Xavier, and E. M. Mohammed, "Effect of neodymium substitution on structural and magnetic properties of magnesium ferrite nanoparticles," *Phys. Scr.*, vol. 87, no. 2, 2013, doi: 10.1088/0031-8949/87/02/025701.

[209] M. Kaur, S. Rana, and P. S. Tarsikka, "Comparative analysis of cadmium doped magnesium ferrite Mg (1-x) Cd x Fe 2O 4 (x = 0.0, 0.2, 0.4, 0.6) nanoparticles," *Ceram. Int.*, vol. 38, no. 5, pp. 4319–4323, 2012, doi: 10.1016/j.ceramint.2012.02.013.

[210] E. E. Ateia, E. Takla, and A. T. Mohamed, "Physical and magnetic properties of (Ba/Sr) substituted magnesium nano ferrites," *Appl. Phys. A Mater. Sci. Process.*, vol. 123, no. 10, 2017, doi: 10.1007/s00339-017-1246-1.

[211] M. Raghasudha, D. Ravinder, and P. Veerasomaiah, "Electrical resistivity studies of Cr doped Mg nano-ferrites," *Mater. Discov.*, vol. 2, pp. 50–54, 2015, doi: 10.1016/j.md.2016.05.001.

[212] Y. Diao, Z. Yan, M. Guo, and X. Wang, "Magnetic multi-metal co-doped magnesium ferrite nanoparticles: An efficient visible light-assisted heterogeneous Fenton-like catalyst synthesized from saprolite laterite ore," *J. Hazard. Mater.*, vol. 344, pp. 829–838, 2018, doi: 10.1016/j.jhazmat.2017.11.029.

[213] C. Choodamani, B. Rudraswamy, and G. T. Chandrappa, "Structural, electrical, and magnetic properties of Zn substituted magnesium ferrite," *Ceram. Int.*, vol. 42, no. 9, pp. 10565–10571, 2016, doi: 10.1016/j.ceramint.2016.03.120.

[214] K. Nadeem, S. Rahman, and M. Mumtaz, "Effect of annealing on properties of Mg doped Zn-ferrite nanoparticles," *Prog. Nat. Sci. Mater. Int.*, vol. 25, no. 2, pp. 111–116, 2015, doi: 10.1016/j.pnsc.2015.02.001.

[215] A. Manikandan, J. Judith Vijaya, M. Sundararajan, C. Meganathan, L. J. Kennedy, and M. Bououdina, "Optical and magnetic properties of Mg-doped ZnFe2O4 nanoparticles prepared by rapid microwave combustion method," *Superlattices Microstruct.*, vol. 64, pp. 118–131, 2013, doi: 10.1016/j.spmi.2013.09.021.

[216] Y. Y. Meng *et al.*, "Structure and magnetic properties of Mn(Zn)Fe 2-xRE xO 4 ferrite nano-powders synthesized by co-precipitation and refluxing method," *Powder Technol.*, vol. 229, pp. 270–275, 2012, doi: 10.1016/j.powtec.2012.06.050.

[217] J. Hu, G. Shi, Z. Ni, L. Zheng, and A. Chen, "Effects of V 2O 5 addition on NiZn ferrite synthesized using two-step sintering process," *Phys. B Condens. Matter*, vol. 407, no. 12, pp. 2205–2210, 2012, doi: 10.1016/j.physb.2012.02.042.

[218] D. C. Bharti, K. Mukherjee, and S. B. Majumder, "Wet chemical synthesis and gas sensing properties of magnesium zinc ferrite nano-particles," *Mater. Chem. Phys.*, vol. 120, no. 2–3, pp. 509–517, 2010, doi: 10.1016/j.matchemphys.2009.11.050.

[219] S. Rahman, K. Nadeem, M. Anis-Ur-Rehman, M. Mumtaz, S. Naeem, and I. Letofsky-Papst, "Structural and magnetic properties of ZnMg-ferrite nanoparticles prepared using the co-precipitation method," *Ceram. Int.*, vol. 39, no. 5, pp. 5235–5239, 2013, doi: 10.1016/j.ceramint.2012.12.023.

[220] J. Zhang, J. Shi, and M. Gong, "Synthesis of magnetic nickel spinel ferrite nanospheres by a reverse emulsion-assisted hydrothermal process," *J. Solid State Chem.*, vol. 182, no. 8, pp. 2135–2140, 2009, doi: 10.1016/j.jssc.2009.05.032.

[221] M. Sundararajan, L. John Kennedy, P. Nithya, J. Judith Vijaya, and M. Bououdina, "Visible light driven photocatalytic degradation of rhodamine B using Mg doped cobalt ferrite spinel nanoparticles synthesized by microwave combustion method," *J. Phys. Chem. Solids*, vol. 108, pp. 61–75, 2017, doi: 10.1016/j.jpcs.2017.04.002.

[222] S. Hajarpour, A. Honarbakhsh Raouf, and K. Gheisari, "Structural evolution and magnetic properties of nanocrystalline magnesium-zinc soft ferrites synthesized by glycine-nitrate combustion process," *J. Magn. Magn. Mater.*, vol. 363, pp. 21–25, 2014, doi: 10.1016/j.jmmm.2014.03.027.

[223] D. Kotsikau, M. Ivanovskaya, V. Pankov, and Y. Fedotova, "Structure and magnetic properties of manganese-zinc-ferrites prepared by spray pyrolysis method," *Solid State Sci.*, vol. 39, pp. 69–73, 2015, doi: 10.1016/j.solidstatesciences.2014.11.013.

[224] K. A. Mohammed *et al.*, "Infrared and structural studies of Mg 1-xZn xFe 2O 4 ferrites," *Phys. B Condens. Matter*, vol. 407, no. 4, pp. 795–804, 2012, doi: 10.1016/j.physb.2011.12.097.

[225] V. Verma, M. Kaur, and J. M. Greneche, "Tailored structural, optical and magnetic properties of ternary nanohybrid Mn 0.4 Co 0.6-x Cu x Fe 2 O 4 (x= 0, 0.2, 0.4, 0.6) spinel ferrites," *Ceram. Int.*, vol. 45, no. 8, pp. 10865–10875, 2019, doi: 10.1016/j.ceramint.2019.02.164.

[226] N. Murali *et al.*, "Effect of Al substitution on the structural and magnetic properties of Co-Zn ferrites," *Phys. B Condens. Matter*, vol. 522, no. May, pp. 1–6, 2017, doi: 10.1016/j.physb.2017.07.043.

[227] A. V. Raut, R. S. Barkule, D. R. Shengule, and K. M. Jadhav, "Synthesis, structural investigation and magnetic properties of Zn 2+ substituted cobalt ferrite nanoparticles prepared by the sol-gel auto-combustion technique," *J. Magn. Magn. Mater.*, vol. 358–359, pp. 87–92, 2014, doi: 10.1016/j.jmmm.2014.01.039.

[228] H. Saqib, S. Rahman, R. Susilo, B. Chen, and N. Dai, "Structural, vibrational, electrical, and magnetic properties of mixed spinel ferrites Mg1-xZnxFe2O4 nanoparticles prepared by co-precipitation," *AIP Adv.*, vol. 9, no. 5, 2019, doi: 10.1063/1.5093221.

[229] D. V. Kurmude, R. S. Barkule, A. V. Raut, D. R. Shengule, and K. M. Jadhav, "X-ray diffraction and cation distribution studies in zinc-substituted nickel ferrite nanoparticles," *J. Supercond. Nov. Magn.*, vol. 27, no. 2, pp. 547–553, 2014, doi: 10.1007/s10948-013-2305-2.

[230] R. Sharma, P. Thakur, P. Sharma, and V. Sharma, "Ferrimagnetic Ni2+doped Mg-Zn spinel ferrite nanoparticles for high density information storage," *J. Alloys Compd.*, vol. 704, pp. 7–17, 2017, doi: 10.1016/j.jallcom.2017.02.021.

[231] M. Bhuvaneswari, S. Sendhilnathan, M. Kumar, R. Tamilarasan, and N. V. Giridharan, "Synthesis, investigation on structural and electrical properties of cobalt doped Mn-Zn ferrite nanocrystalline powders," *Mater. Sci. Pol.*, vol. 34, no. 2, pp. 344–353, 2016, doi: 10.1515/msp-2016-0046.

[232] P. Hartman and H. K. Chan, "Application of the Periodic Bond Chain (PBC) Theory and Attachment Energy Consideration to Derive the Crystal Morphology of Hexamethylmelamine," *Pharm. Res. An Off. J. Am. Assoc. Pharm. Sci.*, vol. 10, no. 7, pp. 1052–1058, 1993, doi: 10.1023/A:1018927109487.

[233] P. P. Khirade, A. R. Chavan, S. B. Somvanshi, J. S. Kounsalye, and K. M. Jadhav, "Tuning of physical properties of multifunctional Mg-Zn spinel ferrite nanocrystals: A comparative investigations manufactured via conventional ceramic versus green approach sol-gel combustion route," *Mater. Res. Express*, vol. 7, no. 11, p. 116102, 2020, doi: 10.1088/2053-1591/abca6c.

[234] M. Raghasudha, D. Ravinder, and P. Veerasomaiah, "Characterization of nano-structured magnesium-chromium ferrites synthesized by citrate-gel auto combustion method," *Adv. Mater. Lett.*, vol. 4, no. 12, pp. 910–916, 2013, doi: 10.5185/amlett.2013.5479.

[235] D. R. Kumar, S. I. Ahmad, C. A. Lincoln, and D. Ravinder, "Structural, optical, room-temperature and low-temperature magnetic properties of Mg–Zn nanoferrite ceramics," *J. Asian Ceram. Soc.*, vol. 7, no. 1, pp. 53–68, 2019, doi: 10.1080/21870764.2018.1563036.

[236] R. Kumar and M. Kar, "Correlation between lattice strain and magnetic behavior in non-magnetic Ca substituted nano-crystalline cobalt ferrite," *Ceram. Int.*, vol. 42, no. 6, pp. 6640–6647, 2016, doi: 10.1016/j.ceramint.2016.01.007.

[237] M. Kaur, P. Jain, and M. Singh, "Studies on structural and magnetic properties of ternary cobalt magnesium zinc (CMZ) Co0.6-xMgxZn0.4 Fe2O4 (x = 0.0, 0.2, 0.4, 0.6) ferrite nanoparticles," *Mater. Chem. Phys.*, vol. 162, pp. 332–339, 2015, doi: 10.1016/j.matchemphys.2015.05.075.

[238] U. Naresh, R. J. Kumar, and K. C. B. Naidu, "Hydrothermal synthesis of barium copper ferrite nanoparticles: Nanofiber formation, optical, and magnetic properties," *Mater. Chem. Phys.*, vol. 236, no. March, p. 121807, 2019, doi: 10.1016/j.matchemphys.2019.121807.

[239] R. Jasrotia, Suman, V. Pratap Singh, R. Kumar, R. Verma, and A. Chauhan, "Effect of Y3+, Sm3+ and Dy3+ ions on the microstructure, morphology, optical and magnetic properties NiCoZn magnetic nanoparticles," *Results Phys.*, vol. 15, no. August, p. 102544, 2019, doi: 10.1016/j.rinp.2019.102544.

[240] A. Rajeshwari, I. Kartharinal Punithavthy, S. Johnson Jeyakumar, N. Lenin, and B. Vigneshwaran, "Dependance of lanthanum ions on structural, magnetic and electrical of manganese based spinel nanoferrites," *Ceram. Int.*, vol. 46, no. 5, pp. 6860–6870, 2020, doi: 10.1016/j.ceramint.2019.11.180.

[241] A. Pradeep, P. Priyadharsini, and G. Chandrasekaran, "Sol- gel route of synthesis of nanoparticles of MgFe2O 4 and XRD, FTIR and VSM study," *J. Magn. Magn. Mater.*, vol. 320, no. 21, pp. 2774–2779, 2008, doi: 10.1016/j.jmmm.2008.06.012.

[242] H. Dutta, M. Sinha, Y. C. Lee, and S. K. Pradhan, "Microstructure characterization and phase transformation kinetics of ball-mill prepared nanocrystalline Mg-Zn-ferrite by Rietveld's analysis and electron microscopy," *Mater. Chem. Phys.*, vol. 105, no. 1, pp. 31–37, 2007, doi: 10.1016/j.matchemphys.2007.04.019.

[243] A. A. H. El-Bassuony, "A Comparative Study of Physical Properties of Er and Yb Nanophase Ferrite for Industrial Application," *J. Supercond. Nov. Magn.*, vol. 31, no. 9, pp. 2829–2840, 2018, doi: 10.1007/s10948-017-4543-1.

[244] A. A. H. El-Bassuony and H. K. Abdelsalam, "Synthesis, characterization, magnetic and antimicrobial properties of silver chromite nanoparticles," *J. Mater. Sci. Mater. Electron.*, vol. 31, no. 4, pp. 3662–3673, 2020, doi: 10.1007/s10854-020-02924-8.

[245] S. J. Haralkar *et al.*, "Substitutional effect of Cr 3+ ions on the properties of Mg-Zn ferrite nanoparticles," *Phys. B Condens. Matter*, vol. 407, no. 21, pp. 4338–4346, 2012, doi: 10.1016/j.physb.2012.07.030.

[246] P. Y. Reyes-Rodríguez *et al.*, "Structural and magnetic properties of Mg-Zn ferrites (Mg1−xZnxFe2O4) prepared by sol-gel method," *J. Magn. Magn. Mater.*, vol. 427, no. October, pp. 268–271, 2017, doi: 10.1016/j.jmmm.2016.10.078.

[247] R. Nongjai, S. Khan, K. Asokan, H. Ahmed, and I. Khan, "Magnetic and electrical properties of in doped cobalt ferrite nanoparticles," *J. Appl. Phys.*, vol. 112, no. 8, 2012, doi: 10.1063/1.4759436.

[248] J. Azadmanjiri and S. A. S. Ebrahimi, "Influence of stoichiometry and calcination condition on the microstructure and phase constitution of NiFe2O4 powders prepared by sol-gel autocombustion method," *Phys. Status Solidi C Conf.*, vol. 1, no. 12, pp. 3414–3417, 2004, doi: 10.1002/pssc.200405468.

[249] R. Jasrotia, P. Puri, A. Verma, and V. P. Singh, "Magnetic and electrical traits of sol-gel synthesized Ni-Cu-Zn nanosized spinel ferrites for multi-layer chip inductors application," *J. Solid State Chem.*, vol. 289, no. April, p. 121462, 2020, doi: 10.1016/j.jssc.2020.121462.

[250] K. Praveena, K. Sadhana, and H. S. Virk, "Structural and magnetic properties of MN-ZN ferrites synthesized by microwave-hydrothermal process," *Solid State Phenom.*, vol. 232, pp. 45–64, 2015, doi: 10.4028/www.scientific.net/SSP.232.45.

[251] W. Zhang, X. Zuo, D. Zhang, C. Wu, and S. R. P. Silva, "Cr3+ substituted spinel ferrite nanoparticles with high coercivity," *Nanotechnology*, vol. 27, no. 24, pp. 1–8, 2016, doi: 10.1088/0957-4484/27/24/245707.

[252] P. Chen, B. Cui, X. Cui, W. Zhao, Y. Bu, and Y. Wang, "A microwave-triggered controllable drug delivery system based on hollow-mesoporous cobalt ferrite magnetic nanoparticles," *J. Alloys Compd.*, vol. 699, pp. 526–533, 2017, doi: 10.1016/j.jallcom.2016.12.304.

[253] C. Singh, A. Goyal, and S. Singhal, "Nickel-doped cobalt ferrite nanoparticles: Efficient catalysts for the reduction of nitroaromatic compounds and photo-oxidative degradation of toxic dyes," *Nanoscale*, vol. 6, no. 14, pp. 7959–7970, 2014, doi: 10.1039/c4nr01730g.

[254] K. Marathe and P. Doshi, "Magnetic nanoparticles: preparation, physical properties, and applications in biomedicine," *IEEE Int. Conf. Intell. Robot. Syst.*, vol. 2015-Decem, pp. 2550–2555, 2015, doi: 10.1109/IROS.2015.7353724.

[255] S. Majidi, F. Z. Sehrig, S. M. Farkhani, M. S. Goloujeh, and A. Akbarzadeh, "Current methods for synthesis of magnetic nanoparticles," *Artif. Cells, Nanomedicine Biotechnol.*, vol. 44, no. 2, pp. 722–734, 2016, doi: 10.3109/21691401.2014.982802.

[256] R. Arulmurugan, B. Jeyadevan, G. Vaidyanathan, and S. Sendhilnathan, "Effect of zinc substitution on Co-Zn and Mn-Zn ferrite nanoparticles prepared by co-precipitation," *J. Magn. Magn. Mater.*, vol. 288, pp. 470–477, 2005, doi: 10.1016/j.jmmm.2004.09.138.

[257] C. Rath *et al.*, "Dependence on cation distribution of particle size, lattice parameter, and magnetic properties in nanosize Mn-Zn ferrite," *J. Appl. Phys.*, vol. 91, no. 3, pp. 2211–2215, 2002, doi: 10.1063/1.1432474.

[258] J. M. Yang and F. S. Yen, "Evolution of intermediate phases in the synthesis of zinc ferrite nanopowders prepared by the tartrate precursor method," *J. Alloys Compd.*, vol. 450, no. 1–2, pp. 387–394, 2008, doi: 10.1016/j.jallcom.2006.10.139.

[259] L. I. Liangchao, Q. I. U. Haizhen, and W. Yuping, "JOURNAL OF RARE EARTHS, Vol. 26, No. 4, Aug. 2008, p. 558," vol. 26, no. 4, pp. 558–562, 2008.

[260] E. J. Verwey, P. W. Haayman, and F. C. Romeijn, "Physical properties and cation arrangement of oxides with spinel structures II. Electronic conductivity," *J. Chem. Phys.*, vol. 15, no. 4, pp. 181–187, 1947, doi: 10.1063/1.1746466.

[261] C. Sang, S. Jin, G. Li, and Y. Luo, "Preparation of copper ferrite by sol–gel method and the synergistic catalytic for the thermal decomposition of ammonium

perchlorate," *J. Sol-Gel Sci. Technol.*, vol. 98, no. 3, pp. 559–567, 2021, doi: 10.1007/s10971-021-05509-x.

[262] L. Zhao *et al.*, "Studies on the magnetism of cobalt ferrite nanocrystals synthesized by hydrothermal method," *J. Solid State Chem.*, vol. 181, no. 2, pp. 245–252, 2008, doi: 10.1016/j.jssc.2007.10.034.

[263] D. H. Chen and X. R. He, "Synthesis of nickel ferrite nanoparticles by sol-gel method," *Mater. Res. Bull.*, vol. 36, no. 7–8, pp. 1369–1377, 2001, doi: 10.1016/S0025-5408(01)00620-1.

[264] M. Kishimoto, Y. Sakurai, and T. Ajima, "Magneto-optical properties of Ba-ferrite particulate media," *J. Appl. Phys.*, vol. 76, no. 11, pp. 7506–7509, 1994, doi: 10.1063/1.357981.

[265] M. M. Rashad and M. I. Nasr, "Controlling the microstructure and magnetic properties of Mn-Zn ferrites nanopowders synthesized by co-precipitation method," *Electron. Mater. Lett.*, vol. 8, no. 3, pp. 325–329, 2012, doi: 10.1007/s13391-012-1104-4.

[266] M. A. Ahmed, H. H. Afify, I. K. El Zawawia, and A. A. Azab, "Novel structural and magnetic properties of Mg doped copper nanoferrites prepared by conventional and wet methods," *J. Magn. Magn. Mater.*, vol. 324, no. 14, pp. 2199–2204, 2012, doi: 10.1016/j.jmmm.2012.02.025.

[267] A. E. Saba, E. M. Elsayed, M. M. Moharam, M. M. Rashad, and R. M. Abou-Shahba, "Structure and magnetic properties of Ni x Zn1-x Fe2O4 thin films prepared through electrodeposition method," *J. Mater. Sci.*, vol. 46, no. 10, pp. 3574–3582, 2011, doi: 10.1007/s10853-011-5271-8.

[268] M. M. Rashad, R. M. Mohamed, and H. El-Shall, "Magnetic properties of nanocrystalline Sm-substituted CoFe2O4 synthesized by citrate precursor method," *J. Mater. Process. Technol.*, vol. 198, no. 1–3, pp. 139–146, 2008, doi: 10.1016/j.jmatprotec.2007.07.012.

[269] J. Bennet, R. Tholkappiyan, K. Vishista, N. V. Jaya, and F. Hamed, "Attestation in self-propagating combustion approach of spinel AFe 2 O 4 (A = Co, Mg and Mn) complexes bearing mixed oxidation states: Magnetostructural properties," *Appl. Surf. Sci.*, vol. 383, pp. 113–125, 2016, doi: 10.1016/j.apsusc.2016.04.177.

[270] T. Vigneswari and P. Raji, "Structural and magnetic properties of calcium doped nickel ferrite nanoparticles by co-precipitation method," *J. Mol. Struct.*, vol. 1127, pp. 515–521, 2017, doi: 10.1016/j.molstruc.2016.07.116.

[271] Y. Feng, S. Li, Y. Zheng, Z. Yi, Y. He, and Y. Xu, "Preparation and characterization of MgFe2O4nanocrystallites via PVA sol-gel route," *J. Alloys Compd.*, vol. 699, pp. 521–525, 2017, doi: 10.1016/j.jallcom.2016.12.432.

[272] J. Kurian and M. Jacob Mathew, "A facile approach to the elucidation of magnetic parameters of CuFe2O4 nanoparticles synthesized by hydrothermal route," *J. Magn. Magn. Mater.*, vol. 428, pp. 204–212, 2017, doi: 10.1016/j.jmmm.2016.12.027.

[273] F. Özel, O. Karaagac, E. Tokay, F. Köçkar, and H. Köçkar, "A simple way to synthesize tartaric acid, ascorbic acid and their mixture coated superparamagnetic iron oxide nanoparticles with high saturation magnetisation and high stability against oxidation: Characterizations and their biocompatibility studies," *J. Magn. Magn. Mater.*, vol. 474, pp. 654–660, 2019, doi: 10.1016/j.jmmm.2018.11.025.

[274] D. R. Mane, D. D. Birajdar, S. Patil, S. E. Shirsath, and R. H. Kadam, "Redistribution of cations and enhancement in magnetic properties of sol-gel synthesized Cu0.7-x Co x Zn0.3Fe 2O4 (0 ≤ x ≤ 0.5)," *J. Sol-Gel Sci. Technol.*, vol. 58, no. 1, pp. 70–79, 2011, doi: 10.1007/s10971-010-2357-8.

[275] H. Search, C. Journals, A. Contact, M. Iopscience, C. Phys, and I. P. Address, "of Co 1 − x Zn x Fe 2 O 4 nanoparticles," vol. 1858, 2008.

[276] X. Q. Shen, J. Xiang, F. Z. Song, and M. Q. Liu, "Characterization and magnetic properties of electrospun Co 1-xZnxFe2O4 nanofibers," *Appl. Phys. A Mater. Sci. Process.*, vol. 99, no. 1, pp. 189–195, 2010, doi: 10.1007/s00339-009-5494-6.

[277] A. Franco and F. C. E Silva, "Effect of the Zn content in the magnetic properties of Co 1-xZnxFe2O4 mixed ferrites," *J. Appl. Phys.*, vol. 113, no. 17, pp. 4–7, 2013, doi: 10.1063/1.4796173.

[278] Y. Chen, X. Y. Zhang, C. Vittoria, and V. G. Harris, "Giant magnetodielectric effect and magnetic field tunable dielectric resonance in spinel MnZn ferrite," *Appl. Phys. Lett.*, vol. 94, no. 10, 2009, doi: 10.1063/1.3095498.

[279] K. Sun *et al.*, "Temperature and frequency characteristics of low-loss MnZn ferrite in a wide temperature range," *J. Appl. Phys.*, vol. 109, no. 10, pp. 88–91, 2011, doi: 10.1063/1.3583551.

[280] Y. Liu *et al.*, "Structure and magnetic properties of MnZn nanoferrites synthesized under a high magnetic field," *J. Appl. Phys.*, vol. 110, no. 7, pp. 1–5, 2011, doi: 10.1063/1.3646558.

[281] S. S. Jadhav, S. E. Shirsath, S. M. Patange, and K. M. Jadhav, "Effect of Zn substitution on magnetic properties of nanocrystalline cobalt ferrite," *J. Appl. Phys.*, vol. 108, no. 9, 2010, doi: 10.1063/1.3499346.

[282] G. Raju *et al.*, "Effect of chromium substitution on the structural and magnetic properties of cobalt ferrite," *Mater. Sci. Energy Technol.*, vol. 2, no. 1, pp. 78–82, 2019, doi: 10.1016/j.mset.2018.11.001.

[283] K. Rajasekhar Babu, M. Purnachandra Rao, P. S. V. Subba Rao, K. Rama Rao, B. Kishore Babu, and B. Rajesh Babu, "Structural and Magnetic Properties of Cu2+ Substituted Co–Zn Ferrite Nanoparticles, Synthesized by Sol–Gel Combustion Method," *J. Inorg. Organomet. Polym. Mater.*, vol. 27, no. 3, pp. 612–621, 2017, doi: 10.1007/s10904-017-0499-7.

[284] A. Amirabadizadeh and T. Amirabadi, "Effect of Substitution of Al for Fe on Magnetic Properties and Particle Size of Ni-Co Nanoferrite," *World J. Condens. Matter Phys.*, vol. 03, no. 03, pp. 131–135, 2013, doi: 10.4236/wjcmp.2013.33021.

[285] K. Raju, G. Venkataiah, and D. H. Yoon, "Effect of Zn substitution on the structural and magnetic properties of Ni-Co ferrites," *Ceram. Int.*, vol. 40, no. 7 PART A, pp. 9337–9344, 2014, doi: 10.1016/j.ceramint.2014.01.157.

[286] I. Sharifi and H. Shokrollahi, "Structural, magnetic and Mössbauer evaluation of Mn substituted Co-Zn ferrite nanoparticles synthesized by co-precipitation," *J. Magn. Magn. Mater.*, vol. 334, pp. 36–40, 2013, doi: 10.1016/j.jmmm.2013.01.021.

[287] H. Mohseni, H. Shokrollahi, I. Sharifi, and K. Gheisari, "Magnetic and structural studies of the Mn-doped Mg-Zn ferrite nanoparticles synthesized by the glycine nitrate process," *J. Magn. Magn. Mater.*, vol. 324, no. 22, pp. 3741–3747, 2012, doi: 10.1016/j.jmmm.2012.06.009.

[288] M. Augustin and T. Balu, "Estimation of Lattice Stress and Strain in Zinc and Manganese Ferrite Nanoparticles by Williamson-Hall and Size-Strain Plot Methods," *Int. J. Nanosci.*, vol. 16, no. 3, pp. 1–7, 2017, doi: 10.1142/S0219581X16500356.

[289] H. Moradmard, S. Farjami Shayesteh, P. Tohidi, Z. Abbas, and M. Khaleghi, "Structural, magnetic and dielectric properties of magnesium doped nickel ferrite nanoparticles," *J. Alloys Compd.*, vol. 650, pp. 116–122, 2015, doi: 10.1016/j.jallcom.2015.07.269.

[290] T. M. Hammad, S. Kuhn, A. A. Amsha, N. K. Hejazy, and R. Hempelmann, "Comprehensive Study of the Impact of Mg2+ Doping on Optical, Structural, and

Magnetic Properties of Copper Nanoferrites," *J. Supercond. Nov. Magn.*, vol. 33, no. 10, pp. 3065–3075, 2020, doi: 10.1007/s10948-020-05559-2.

[291]   S. Jandl and J. Deslandes, "Infrared spectra of HfS3," *Phys. Rev. B*, vol. 24, no. 2, pp. 1040–1044, 1981, doi: 10.1103/PhysRevB.24.1040.

[292]   A. Faraz *et al.*, "Synthesis, structural, and magnetic characterization of Mn 1-x Ni x Fe 2O 4 spinel nanoferrites," *J. Supercond. Nov. Magn.*, vol. 25, no. 1, pp. 91–100, 2012, doi: 10.1007/s10948-011-1212-7.

[293]   Hirthna and S. Sendhilnathan, "Enhancement in dielectric and magnetic properties of Mg2+ substituted highly porous super paramagnetic nickel ferrite nanoparticles with Williamson-Hall plots mechanistic view," *Ceram. Int.*, vol. 43, no. 17, pp. 15447–15453, 2017, doi: 10.1016/j.ceramint.2017.08.090.

[294]   N. M. Deraz, "Effects of magnesia addition on structural, morphological and magnetic properties of nano-crystalline nickel ferrite system," *Ceram. Int.*, vol. 38, no. 1, pp. 511–516, 2012, doi: 10.1016/j.ceramint.2011.07.036.

[295]   S. A. V. Prasad *et al.*, "Synthesis of MFe2O4 (M=Mg2+, Zn2+, Mn2+) spinel ferrites and their structural, elastic and electron magnetic resonance properties," *Ceram. Int.*, vol. 44, no. 9, pp. 10517–10524, 2018, doi: 10.1016/j.ceramint.2018.03.070.

[296]   A. A. H. El-Bassuony, "Enhancement of structural and electrical properties of novelty nanoferrite materials," *J. Mater. Sci. Mater. Electron.*, vol. 28, no. 19, pp. 14489–14498, 2017, doi: 10.1007/s10854-017-7312-9.

[297]   C. Srinivas *et al.*, "Journal of Magnetism and Magnetic Materials Study of magnetic behavior in co-precipitated Ni – Zn ferrite nanoparticles and their potential use for gas sensor applications," *J. Magn. Magn. Mater.*, vol. 502, no. February, p. 166534, 2020, doi: 10.1016/j.jmmm.2020.166534.

[298]   C. S. Babu, K. S. Ramakrishna, and D. L. Sastry, "Author ' s Accepted Manuscript," *J. Magn. Magn. Mater.*, 2016, doi: 10.1016/j.jmmm.2016.01.060.

[299]   B. V. Tirupanyam *et al.*, "Investigation of structural and magnetic properties of co-precipitated Mn-Ni ferrite nanoparticles in the presence of α-Fe2O3 phase," *J. Magn. Magn. Mater.*, vol. 392, pp. 101–106, 2015, doi: 10.1016/j.jmmm.2015.05.010.

[300]   H. Fakhr Nabavi, M. Aliofkhazraei, M. Hasanpoor, and A. Seyfoori, "Combustion and Coprecipitation Synthesis of Co–Zn Ferrite Nanoparticles: Comparison of Structure and Magnetic Properties," *Int. J. Appl. Ceram. Technol.*, vol. 13, no. 6, pp. 1112–1118, 2016, doi: 10.1111/ijac.12580.

[301] J. M. D. Coey, "Noncollinear spin arrangement in ultrafine ferrimagnetic crystallites," *Phys. Rev. Lett.*, vol. 27, no. 17, pp. 1140–1142, 1971, doi: 10.1103/PhysRevLett.27.1140.

[302] M. Yousaf, M. N. Akhtar, B. Wang, and A. Noor, "Preparations, optical, structural, conductive and magnetic evaluations of RE's (Pr, Y, Gd, Ho, Yb) doped spinel nanoferrites," *Ceram. Int.*, vol. 46, no. 4, pp. 4280–4288, 2020, doi: 10.1016/j.ceramint.2019.10.149.

[303] M. Arshad *et al.*, "Structural and magnetic properties variation of manganese ferrites via Co-Ni substitution," *J. Magn. Magn. Mater.*, vol. 474, pp. 98–103, 2019, doi: 10.1016/j.jmmm.2018.10.141.

[304] M. H. R. Khan and A. K. M. A. Hossain, "Reentrant spin glass behavior and large initial permeability of Co 0.5-xMnxZn0.5Fe2O4," *J. Magn. Magn. Mater.*, vol. 324, no. 4, pp. 550–558, 2012, doi: 10.1016/j.jmmm.2011.08.039.

[305] A. Z. AL Shaqsi, K. Sopian, and A. Al-Hinai, "Review of energy storage services, applications, limitations, and benefits," *Energy Reports*, vol. 6, no. xxxx, pp. 288–306, 2020, doi: 10.1016/j.egyr.2020.07.028.

[306] L. Yao, B. Yang, H. Cui, J. Zhuang, J. Ye, and J. Xue, "Challenges and progresses of energy storage technology and its application in power systems," *J. Mod. Power Syst. Clean Energy*, vol. 4, no. 4, pp. 519–528, 2016, doi: 10.1007/s40565-016-0248-x.

[307] N. R. Chodankar, D. P. Dubal, G. S. Gund, and C. D. Lokhande, "Flexible all-solid-state MnO2 thin films based symmetric supercapacitors," *Electrochim. Acta*, vol. 165, pp. 338–347, 2015, doi: 10.1016/j.electacta.2015.02.246.

[308] S. J. Uke, G. N. Chaudhari, A. B. Bodade, and S. P. Mardikar, "Morphology dependant electrochemical performance of hydrothermally synthesized NiCo2O4 nanomorphs," *Mater. Sci. Energy Technol.*, vol. 3, pp. 289–298, 2020, doi: 10.1016/j.mset.2019.11.004.

[309] Y. Kim, J. Koh, Q. Xie, Y. Wang, N. Chang, and M. Pedram, "A scalable and flexible hybrid energy storage system design and implementation," *J. Power Sources*, vol. 255, pp. 410–422, 2014, doi: 10.1016/j.jpowsour.2013.12.102.

[310] J. R. Rani, R. Thangavel, M. Kim, Y. S. Lee, and J. H. Jang, "Ultra-high energy density hybrid supercapacitors using mno2/reduced graphene oxide hybrid nanoscrolls," *Nanomaterials*, vol. 10, no. 10, pp. 1–16, 2020, doi: 10.3390/nano10102049.

[311] P. K. Panda, A. Grigoriev, Y. K. Mishra, and R. Ahuja, "Progress in supercapacitors: Roles of two dimensional nanotubular materials," *Nanoscale Adv.*, vol. 2, no. 1, pp. 70–108, 2020, doi: 10.1039/c9na00307j.

[312] P. Lu, D. Xue, H. Yang, and Y. Liu, "Supercapacitor and nanoscale research towards electrochemical energy storage," *Int. J. Smart Nano Mater.*, vol. 4, no. 1, pp. 2–26, 2013, doi: 10.1080/19475411.2011.652218.

[313] S. Vijayakumar, S. Nagamuthu, and G. Muralidharan, "Supercapacitor studies on NiO nanoflakes synthesized through a microwave route," *ACS Appl. Mater. Interfaces*, vol. 5, no. 6, pp. 2188–2196, 2013, doi: 10.1021/am400012h.

[314] V. D. Patake, S. M. Pawar, V. R. Shinde, T. P. Gujar, and C. D. Lokhande, "The growth mechanism and supercapacitor study of anodically deposited amorphous ruthenium oxide films," *Curr. Appl. Phys.*, vol. 10, no. 1, pp. 99–103, 2010, doi: 10.1016/j.cap.2009.05.003.

[315] A. Soam, R. Kumar, M. C, M. Singh, D. Thatoi, and R. O. Dusane, "Development of paper-based flexible supercapacitor: Bismuth ferrite/graphene nanocomposite as an active electrode material," *J. Alloys Compd.*, vol. 813, p. 152145, 2020, doi: 10.1016/j.jallcom.2019.152145.

[316] M. Fu *et al.*, "Facile synthesis of strontium ferrite nanorods/graphene composites as advanced electrode materials for supercapacitors," *J. Colloid Interface Sci.*, vol. 588, no. xxxx, pp. 795–803, 2021, doi: 10.1016/j.jcis.2020.11.114.

[317] M. Mortazavi and A. Ivanov, "µECM process investigation considering pulse signal features and EDL capacitance," *Int. J. Adv. Manuf. Technol.*, vol. 105, no. 11, pp. 4621–4632, 2019, doi: 10.1007/s00170-019-03864-2.

[318] P. A. Shinde *et al.*, "Layered manganese metal-organic framework with high specific and areal capacitance for hybrid supercapacitors," *Chem. Eng. J.*, vol. 387, p. 122982, 2020, doi: 10.1016/j.cej.2019.122982.

[319] Y. Sun *et al.*, "Improved pseudocapacitances of supercapacitors based on electrodes of nitrogen-doped Ti3C2Tx nanosheets with in-situ growth of carbon nanotubes," *J. Alloys Compd.*, vol. 859, p. 158347, 2021, doi: 10.1016/j.jallcom.2020.158347.

[320] B. Bhujun, M. T. T. Tan, and A. S. Shanmugam, "Evaluation of aluminium doped spinel ferrite electrodes for supercapacitors," *Ceram. Int.*, vol. 42, no. 5, pp. 6457–6466, 2016, doi: 10.1016/j.ceramint.2015.12.118.

[321] K. Mukherjee and S. B. Majumder, "Promising methane-sensing characteristics of hydrothermal synthesized magnesium zinc ferrite hollow spheres," *Scr. Mater.*, vol. 67, no. 6, pp. 617–620, 2012, doi: 10.1016/j.scriptamat.2012.06.025.

[322] C. F. Zhang, X. C. Zhong, H. Y. Yu, Z. W. Liu, and D. C. Zeng, "Effects of cobalt doping on the microstructure and magnetic properties of Mn-Zn ferrites prepared by the co-precipitation method," *Phys. B Condens. Matter*, vol. 404, no. 16, pp. 2327–2331, 2009, doi: 10.1016/j.physb.2008.12.044.

[323] G. Xi, Y. Li, and Y. M. Liu, "Study on preparation of manganese-zinc ferrites using spent Zn-Mn batteries," *Mater. Lett.*, vol. 58, no. 7–8, pp. 1164–1167, 2004, doi: 10.1016/j.matlet.2003.08.029.

[324] F. L. Zabotto, A. J. Gualdi, and J. A. Eiras, "Influence of the sintering temperature on the magnetic and electric properties of NiFe2O4 ferrites," *Mater. Res.*, vol. 15, no. 3, pp. 428–433, 2012, doi: 10.1590/S1516-14392012005000043.

[325] T. Kaur, B. Kaur, B. H. Bhat, S. Kumar, and A. K. Srivastava, "Effect of calcination temperature on microstructure, dielectric, magnetic and optical properties of Ba0.7La0.3Fe11.7Co0.3O19hexaferrites," *Phys. B Condens. Matter*, vol. 456, pp. 206–212, 2015, doi: 10.1016/j.physb.2014.09.003.

[326] M. J. Iqbal and M. N. Ashiq, "Physical and electrical properties of Zr-Cu substituted strontium hexaferrite nanoparticles synthesized by co-precipitation method," *Chem. Eng. J.*, vol. 136, no. 2–3, pp. 383–389, 2008, doi: 10.1016/j.cej.2007.05.046.

[327] T. Kaur, S. Kumar, B. H. Bhat, and A. K. Srivastava, "Enhancement in physical properties of barium hexaferrite with substitution," *J. Mater. Res.*, vol. 30, no. 18, pp. 2753–2762, 2015, doi: 10.1557/jmr.2015.244.

[328] A. Thakur, R. R. Singh, and P. B. Barman, "Synthesis and characterizations of Nd3+ doped SrFe 12O19 nanoparticles," *Mater. Chem. Phys.*, vol. 141, no. 1, pp. 562–569, 2013, doi: 10.1016/j.matchemphys.2013.05.063.

[329] T. Kaur, S. Kumar, B. H. Bhat, B. Want, and A. K. Srivastava, "Effect on dielectric, magnetic, optical and structural properties of Nd–Co substituted barium hexaferrite nanoparticles," *Appl. Phys. A Mater. Sci. Process.*, vol. 119, no. 4, pp. 1531–1540, 2015, doi: 10.1007/s00339-015-9134-z.

[330] G. Dixit, J. Pal Singh, R. C. Srivastava, and H. M. Agrawal, "Magnetic resonance study of Ce and Gd doped NiFe2O4 nanoparticles," *J. Magn. Magn. Mater.*, vol. 324, no. 4, pp. 479–483, 2012, doi: 10.1016/j.jmmm.2011.08.027.

[331] J. P. Singh, G. Dixit, R. C. Srivastava, H. M. Agrawal, and K. Asokan, "Looking for the possibility of multiferroism in NiGd0.04Fe 1.96O4 nanoparticle system," *J. Phys. D. Appl. Phys.*, vol. 44, no. 43, 2011, doi: 10.1088/0022-3727/44/43/435306.

[332] S. Kumar, T. Kaur, S. Kumar, and A. K. Srivastava, "Effect of Heat Treatment on Properties of Sr0.7Nd0.3Co0.3Fe11.7O19," *J. Supercond. Nov. Magn.*, vol. 28, no. 10, pp. 2935–2940, 2015, doi: 10.1007/s10948-015-3105-7.

[333] M. A. Gabal and A. A. Al-Juaid, "Structural and electromagnetic studies of Mg1-xZnxFe2O4 nanoparticles synthesized via a sucrose autocombustion route," *J. Mater. Sci. Mater. Electron.*, vol. 31, no. 13, pp. 10055–10071, 2020, doi: 10.1007/s10854-020-03551-z.

[334] M. A. Almessiere *et al.*, "Sonochemical synthesis of Eu3+ substituted CoFe2O4 nanoparticles and their structural, optical and magnetic properties," *Ultrason. Sonochem.*, vol. 58, no. May, p. 104621, 2019, doi: 10.1016/j.ultsonch.2019.104621.

[335] P. Xiong, J. Zhu, and X. Wang, "Recent advances on multi-component hybrid nanostructures for electrochemical capacitors," *J. Power Sources*, vol. 294, pp. 31–50, 2015, doi: 10.1016/j.jpowsour.2015.06.062.

[336] B. K. Roy, I. Tahmid, and T. U. Rashid, "Chitosan-based materials for supercapacitor applications: A review," *J. Mater. Chem. A*, vol. 9, no. 33, pp. 17592–17642, 2021, doi: 10.1039/d1ta02997e.

[337] A. Mohammadi, S. J. Peighambardoust, A. A. Entezami, and N. Arsalani, "High performance of covalently grafted poly(o-methoxyaniline) nanocomposite in the presence of amine-functionalized graphene oxide sheets (POMA/f-GO) for supercapacitor applications," *J. Mater. Sci. Mater. Electron.*, vol. 28, no. 8, pp. 5776–5787, 2017, doi: 10.1007/s10854-016-6248-9.

[338] R. Bolagam, R. Boddula, and P. Srinivasan, "Nanosphere of Semicrystalline Polyaniline Powder: An Effective, Versatile, and Reusable Catalyst for Hantzsch Reaction," *J. Catal.*, vol. 2014, pp. 1–6, 2014, doi: 10.1155/2014/984730.

[339] A. M. A. Henaish *et al.*, "Synthesize, characterization, dielectric, linear and nonlinear optical properties of Ni–Al Ferrite/PANI nanocomposite film," *Opt. Mater. (Amst).*, vol. 119, no. July, p. 111397, 2021, doi: 10.1016/j.optmat.2021.111397.

[340] M. A. Mousa, M. Khairy, and M. Shehab, "Nanostructured ferrite/graphene/polyaniline using for supercapacitor to enhance the capacitive behavior," *J. Solid State Electrochem.*, vol. 21, no. 4, pp. 995–1005, 2017, doi: 10.1007/s10008-016-3446-6.

[341] K. V. Sankar and R. K. Selvan, "The ternary MnFe2O4/graphene/polyaniline hybrid composite as negative electrode for supercapacitors," *J. Power Sources*, vol. 275, pp. 399–407, 2015, doi: 10.1016/j.jpowsour.2014.10.183.

[342] N. Dong, M. Zhong, P. Fei, Z. Lei, and B. Su, "Magnetic and electrochemical properties of PANI-CoFe2O4 nanocomposites synthesized via a novel one-step solvothermal method," *J. Alloys Compd.*, vol. 660, pp. 382–386, 2016, doi: 10.1016/j.jallcom.2015.11.175.

[343] W. Wang, S. P. Gumfekar, Q. Jiao, and B. Zhao, "Ferrite-grafted polyaniline nanofibers as electromagnetic shielding materials," *J. Mater. Chem. C*, vol. 1, no. 16, pp. 2851–2859, 2013, doi: 10.1039/c3tc00757j.

[344] A. H. A. Aziz, T. S. Jamil, M. S. Shalaby, A. M. Shaban, E. R. Souaya, and N. A. A. Ghany, "Application of (Polyaniline/zeolite X) composite as anticorrosion coating for energy recovery devices in ro desalination water plants," *Int. J. Ind. Chem.*, vol. 10, no. 2, pp. 175–191, 2019, doi: 10.1007/s40090-019-0182-7.

[345] T. Brousse, D. Bélanger, and J. W. Long, "To Be or Not To Be Pseudocapacitive?," *J. Electrochem. Soc.*, vol. 162, no. 5, pp. A5185–A5189, 2015, doi: 10.1149/2.0201505jes.

[346] E. Umeshbabu, G. Rajeshkhanna, P. Justin, and G. Ranga Rao, "Synthesis of mesoporous NiCo2O4-rGO by a solvothermal method for charge storage applications," *RSC Adv.*, vol. 5, no. 82, pp. 66657–66666, 2015, doi: 10.1039/c5ra11239g.

[347] G. Jiang, M. Zhang, X. Li, and H. Gao, "NiMoO4@Ni(OH)2 core/shell nanorods supported on Ni foam for high-performance supercapacitors," *RSC Adv.*, vol. 5, no. 85, pp. 69365–69370, 2015, doi: 10.1039/c5ra11960j.

[348] B. J. Rani *et al.*, "Pure and cobalt-substituted zinc-ferrite magnetic ceramics for supercapacitor applications," *Appl. Phys. A Mater. Sci. Process.*, vol. 124, no. 7, p. 0, 2018, doi: 10.1007/s00339-018-1936-3.

[349] S. Pilban Jahromi *et al.*, "Influence of particle size on performance of a nickel oxide nanoparticle-based supercapacitor," *RSC Adv.*, vol. 5, no. 18, pp. 14010–14019, 2015, doi: 10.1039/c4ra16776g.

[350] D. Yan *et al.*, "Design and influence of mass ratio on supercapacitive properties of ternary electrode material reduced graphene oxide@MnO2@ poly(3,4-ethylenedioxythiophene)-poly(styrene sulfonate)," *Electrochim. Acta*, vol. 169, pp. 317–325, 2015, doi: 10.1016/j.electacta.2015.04.078.

[351] Z. Fan *et al.*, "Asymmetric supercapacitors based on graphene/MnO2 and activated carbon nanofiber electrodes with high power and energy density," *Adv. Funct. Mater.*, vol. 21, no. 12, pp. 2366–2375, 2011, doi: 10.1002/adfm.201100058.

[352] Y. F. Yuan, X. H. Xia, J. B. Wu, J. L. Yang, Y. B. Chen, and S. Y. Guo, "Nickel foam-supported porous Ni(OH)2/NiOOH composite film as advanced pseudocapacitor material," *Electrochim. Acta*, vol. 56, no. 6, pp. 2627–2632, 2011, doi: 10.1016/j.electacta.2010.12.001.

[353] M. L. Huang, C. D. Gu, X. Ge, X. L. Wang, and J. P. Tu, "NiO nanoflakes grown on porous graphene frameworks as advanced electrochemical pseudocapacitor materials," *J. Power Sources*, vol. 259, pp. 98–105, 2014, doi: 10.1016/j.jpowsour.2014.02.088.

[354] Y. G. Wang, Z. D. Wang, and Y. Y. Xia, "An asymmetric supercapacitor using RuO2/TiO2 nanotube composite and activated carbon electrodes," *Electrochim. Acta*, vol. 50, no. 28, pp. 5641–5646, 2005, doi: 10.1016/j.electacta.2005.03.042.

[355] F. S. Omar, A. Numan, N. Duraisamy, M. M. Ramly, R. Ramesh, and R. Ramesh, "Binary composite of polyaniline/copper cobaltite for high performance asymmetric supercapacitor application," *Electrochim. Acta*, vol. 227, pp. 41–48, 2017, doi: 10.1016/j.electacta.2017.01.006.

[356] S. Xu *et al.*, "Nanofoaming to Boost the Electrochemical Performance of Ni@Ni(OH)2 Nanowires for Ultrahigh Volumetric Supercapacitors," *ACS Appl. Mater. Interfaces*, vol. 8, no. 41, pp. 27868–27876, 2016, doi: 10.1021/acsami.6b10700.

[357] N. Li, D. Shan, and H. Xue, "Electrochemical synthesis and characterization of poly(pyrrole-co-tetrahydrofuran) conducting copolymer," *Eur. Polym. J.*, vol. 43, no. 6, pp. 2532–2539, 2007, doi: 10.1016/j.eurpolymj.2007.01.048.

[358] D. Kalpana, S. H. Cho, S. B. Lee, Y. S. Lee, R. Misra, and N. G. Renganathan, "Recycled waste paper-A new source of raw material for electric double-layer capacitors," *J. Power Sources*, vol. 190, no. 2, pp. 587–591, 2009, doi: 10.1016/j.jpowsour.2009.01.058.

[359] Y. Li, H. Peng, G. Li, and K. Chen, "Synthesis and electrochemical performance of sandwich-like polyaniline/graphene composite nanosheets," *Eur. Polym. J.*, vol. 48, no. 8, pp. 1406–1412, 2012, doi: 10.1016/j.eurpolymj.2012.05.014.

[360] W. Chen, X. Tao, D. Wei, H. Wang, Q. Yu, and Y. Li, "High-performance supercapacitor based on actived carbon–MnO2–polyaniline composite," *J. Mater. Sci.*

Mater. Electron., vol. 27, no. 2, pp. 1357–1362, 2016, doi: 10.1007/s10854-015-3897-z.

Synthesis and investigation of structural, morphological, and magnetic properties of the manganese doped cobalt-zinc spinel ferrite

Hamnesh Mahajan[a], Sachin Kumar Godara[b], A.K. Srivastava[a,*]

[a] *Department of Physics, Lovely Professional University, Phagwara, Punjab 144411, India*
[b] *Department of Chemistry, Guru Nanak Dev University, Amritsar, Punjab 143005, India*

ARTICLE INFO

ABSTRACT

The current work involves the synthesis of $Mn_xCo_{0.5-x}Zn_{0.5}Fe_2O_4$ (x = 0.0, 0.1, 0.2, 0.3, and 0.4) by adopting sol-gel auto combustion technique. For all the samples, the single-phase spinel structure with cubic symmetry was assured by the XRD studies. The crystallite size lies in the nanoscale range of 35.4–43.6 nm as estimated by utilizing Debye-Scherrer formula. FTIR spectroscopy affirms the formation of spinel structure due to the appearance of characteristic vibrational bands near 400 and 600 cm^{-1} which corresponds to the octahedral and tetrahedral sites respectively. FESEM micrographs reveal the presence of non-uniform grain growth which was agglomerated, inhomogenous in size and shape, and having porous morphology. VSM study exhibits soft ferromagnetic nature due to the low coercivity value. There is a decrement in the saturation magnetization with increasing Mn^{2+} concentration which is due to the decrease in the crystallite size and non-magnetic nature of the Mn^{2+}.

1. Introduction

Spinel ferrite ceramics are significant rivals in various electronic devices. Presently, ecofriendly nanomaterials such as spinel ferrite, having good thermal and chemical stability, exhibits amazing properties viz. structural and magnetic, due to which it has a wide extent of anticipated applications in energy storage devices [1], magnetic recording [2], catalysts [3], drug delivery system [4], sensors [5], microelectronics [6], data storage system [7], magnetic resonance imaging (MRI) [8], pollution control [9], anticorrosive paints ferrofluids [10], medical sciences [11] and many more. The spinel ferrite has a cubic structure and exhibits an Fd-3 m space group. The spinel structure is made up of a closely packed oxygen anion in which thirty-two oxygen anions form a complete structure unit cell. These oxygen anions form a face-centered cubic arrangement leaving two sorts of spaces between these oxygen anions: tetrahedral or A-site, encircled by four oxygen particles, and octahedral or B-site, encircled by six oxygen particles. The single crystallographic unit cell of spinel ferrite contains eight formulae units of MFe_2O_4 (where M is one or more divalent metal cations). Every unit cell of spinel ferrite has sixty-four tetrahedral sites, eight of which are involved, and thirty-two octahedral sites, sixteen of which are

involved. The difference in the magnetization of these lattice sites gives the net value of magnetization of the spinel structure [12,13]. The presence of metal (divalent or trivalent) cations to the lattice sites have pored over, utilizing the crystal field theory [14], which results in the different types of crystal structure such as normal, inverse, or mixed. Moreover, these cations emphatically influence the physical properties viz. structural, electrical, optical, and magnetic. Further, this occupancy of metal (divalent or trivalent) cations to these tetrahedral and octahedral sites relied on a few key factors viz. preparation method, elemental composition, and sintering temperature [15–18].

The spinel ferrites can be synthesized by several techniques which include the co-precipitation method, hydrothermal method, microwave combustion, sol-gel auto combustion, spray pyrolysis, ceramic, etc. [19–38]. The structural properties such as size, morphology, state of the surface, and chemical homogeneity relied heavily on the preparation method. Out of these above synthesis techniques, the sol-gel auto combustion method has been preferred because of homogeneity, large-scale production, lowering of the crystallization temperature, short time, stoichiometrically pure product formulation, and nanosize formulation of compound [39,40]. Additionally, the utilization of water as a solvent makes this technique eco-friendly according to the natural perspective.

Among the various spinel ferrites present, the $CoFe_2O_4$ and $ZnFe_2O_4$ have drawn an impressive interest in view of their wide scope of uses [41–43]. The $CoFe_2O_4$ exhibits an inverse structure,

* Corresponding author.
E-mail address: srivastava_phy@yahoo.co.in (A.K. Srivastava).

ORIGINAL PAPER: NANO-STRUCTURED MATERIALS (PARTICLES, FIBERS, COLLOIDS, COMPOSITES, ETC.)

Effect of sintering temperature on structural, morphological, magnetic, and electrochemical properties of $Mn_{0.3}Co_{0.2}Zn_{0.5}Fe_2O_4$ Ferrite

Hamnesh Mahajan[1] · Shammi Kumar[2] · Anjori Sharma[1] · Ibrahim Mohammed[1] · Manisha Thakur[1] · Amarjeet Kaur[3] · A. K. Srivastava [1]

Abstract

The sol-gel methodology was exploited for the production of $Mn_{0.3}Co_{0.2}Zn_{0.5}Fe_2O_4$ ferrite nanoparticles, at different sintering temperatures (750, 950, and 1150 °C). The nanometer size crystallites were evaluated utilizing the Debye Scherrer formulae in the X-ray diffraction (XRD) study. The two bands manifested in Fourier transform infrared (FTIR) spectra near $600\,cm^{-1}$ (tetrahedral site) and $400\,cm^{-1}$ (octahedral site) ratify the formation of spinel structure for all sintering temperatures. Field emission scanning electron microscopy (FESEM) micrographs estimate the average size of the particle by using ImageJ software and reveal the agglomerated grains, which are inhomogeneous in shape and size. Energy dispersive X-ray (EDX) study confirms the stoichiometry and composition of the synthesized specimens. For an enhancement in the sintering temperature, the enhancement in the saturation magnetization was perceived in the magnetic studies by using a vibrating sample magnetometer (VSM). With regard to all incorporated samples, the squareness ratio was assessed to be under 0.5 which assimilates to a multi-domain structure. For all scan rates and current densities, the prepared $Mn_{0.3}Co_{0.2}Zn_{0.5}Fe_2O_4$ (1150 °C) had the higher value of the specific capacitance as portrayed through the electrochemical study.

✉ A. K. Srivastava
    srivastava_phy@yahoo.co.in

1   Department of Physics, Lovely Professional University, Phagwara, Punjab 144411, India

2   Department of Physics, GCET, Chak Bhalwal, Jammu 181122, India

3   Central Instrumentation Facility, Lovely Professional University, Phagwara, Punjab 144411, India

Structural, morphological, and electrochemical investigation of $Mn_{0.3}Co_{0.2}Zn_{0.5}Fe_2O_4$-polyaniline nanocomposite for supercapacitor application

Hamnesh Mahajan[1], Shammi Kumar[2], Anjori Sharma[1], Ibrahim Mohammed[1], Manisha Thakur[1], Simrandeep Kour[1], Amarjeet Kaur[3], and Ajeet Kumar Srivastava[1,*] (iD)

[1] *Department of Physics, Lovely Professional University, Phagwara, Punjab 144411, India*
[2] *Department of Physics, GCET, Chak Bhalwal, Jammu 181122, India*
[3] *Central Instrumentation Facility, Lovely Professional University, Phagwara, Punjab 144411, India*

ABSTRACT

The present research deals in preparing $Mn_{0.3}Co_{0.2}Zn_{0.5}Fe_2O_4$ (spinel ferrite) by sol–gel procedure, polyaniline (PANI) by chemical oxidative method, and $Mn_{0.3}Co_{0.2}Zn_{0.5}Fe_2O_4$-PANI nanocomposite by physical blending method. X-ray diffraction (XRD) study affirms the formation of $Mn_{0.3}Co_{0.2}Zn_{0.5}Fe_2O_4$-PANI nanocomposite owing to the appearance of two different types of peaks: sharp $Mn_{0.3}Co_{0.2}Zn_{0.5}Fe_2O_4$ peaks, and broader PANI peaks. Fourier transform infrared spectroscopy (FTIR) of $Mn_{0.3}Co_{0.2}Zn_{0.5}Fe_2O_4$-PANI nanocomposite shows all characteristic vibrational bands, which are observed in the $Mn_{0.3}Co_{0.2}Zn_{0.5}Fe_2O_4$ and PANI spectra. Field emission scanning electron microscopy (FESEM) micrographs have been employed for measuring the average particle size by using ImageJ software. The encapsulation of the synthesized ferrite nanoparticle with the PANI matrix is exhibited by the FESEM micrograph of $Mn_{0.3}Co_{0.2}Zn_{0.5}Fe_2O_4$-PANI nanocomposite. The electrochemical activity of the novel $Mn_{0.3}Co_{0.2}Zn_{0.5}Fe_2O_4$-PANI nanocomposite is manifested to be higher as compared to their counterparts on account of synergistic impact, continual movement of electrons toward the electrode, and multiple redox reactions.

1 Introduction

The tremendous upgrades in ecological contamination and the ineluctable lack of fossil fuels are compelling researchers to foster perfect and economical energ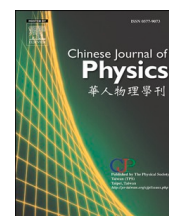y storage gadgets [1]. At the present juncture, the most used energy storage gadgets are batteries, fuel cells, conventional capacitors, and supercapacitors [2]. The usage of batteries and fuel cells for high-energy applications is principally a direct result of their higher energy density. Nevertheless, it has the deficiencies of significant expense, short cycle life,

Structural, morphological, optical, magnetic, and microwave properties of La^{3+}- Mn^{2+} substituted Zn$_2$-Y-type barium-strontium hexaferrite

Ibrahim Mohammed [a], J. Mohammed [b], Anjori Sharma [a], Hamnesh Mahajan [a], Shweta Sharma [a], Manisha Thakur [a], Amarjeet Kaur [c], Neha Aggarwal [d], A.K. Srivastava [a],*

[a] *Department of Physics, School of Physical Sciences and Chemical Engineering, Lovely Professional University, Phagwara-144411, Punjab, India*
[b] *Department of Physics, Faculty of Science, Federal University Dutse, P.M.B. 7156, Dutse, Jigawa, Nigeria*
[c] *Central Instrumentation Facility, Lovely Professional University, Phagwara-144411, Punjab, India*
[d] *Department of Electronics Technology, Guru Nanak Dev University, Amritsar, 143005, India*

ARTICLE INFO

ABSTRACT

This experimental study examines the effects of the La^{3+}-Mn^{2+} substitution on structural, morphological, optical, magnetic, and microwave properties of Ba$_{1.7-x}$Sr$_{0.3}$La$_x$Zn$_2$Fe$_{12-x}$Mn$_x$O$_{22}$ (x = 0.0, 0.1, 0.2) using sol-gel auto combustion. We characterize the as-prepared nanoparticles structurally using XRD and FTIR, and the morphology is determined using FESEM micrographs. Elemental analysis (EDX) verifies the presence of the entire experimental elements. The optical band gap was determined using UV Visible spectroscopy with the help of Tauc theory. VSM and VNA analyses determine the magnetic and microwave properties, respectively. The small coercivity and small area under the hysteresis loop show that the materials are soft magnetic. The microwave properties of the prepared material were affected by the grain size and saturation magnetization. A single absorption peak from the reflection loss graph and high shielding effectiveness of the synthesized nanoparticles indicates that the material may have the potential as an effective EMI shielding material in Ku-band.

1. Introduction

Wireless communication technology has steadily advanced in the information era, and electronic gadgets nearly surround every part of human existence, bringing in overwhelming electromagnetic waves (EMW). Excessive electromagnetic waves pollute the environment and potentially endanger human health [1–5]. Although electromagnetic wave has provided enormous advantages to humanity, the devastation it has caused is immeasurable [6]. There are significant efforts to develop high-performance EMW absorbers to prevent the harm caused by EM pollution to individuals and the environment while also meeting the criteria for electronic security and defensive stealth [7,8]. Due to their wide range of applications and great absorption capacity, EMW absorbers are protective agents against EMW concerns since they can convert EMW to thermal energy and subsequently dissipate it [9–12]. Thus, to convert EMW energy to thermal energy, various absorbers with superior EM wave attenuation performance were investigated [13]. In general,

---

Influence of sintering temperature on impedance and modulus spectroscopy of nickel-substituted cobalt ferrite

Simrandeep Kour[1], Hamnesh Mahajan[1], and Rupam Mukherjee[1,*]

[1]Department of Physics, Lovely Professional University, Phagwara 144411, Punjab, India

ABSTRACT

In this paper, the author reports the productive synthesis of spinel ferrite samples with composition $Ni_{0.5}Co_{0.5}Fe_2O_4$ using the sol–gel auto-combustion method. The crystal structure of inverse spinel ferrite was confirmed by X-ray Diffraction (XRD) for all the $Ni_{0.5}Co_{0.5}Fe_2O_4$ samples. Here, the crystallize size (D) and theoretical density (D_x) calculated are found to be inversely proportional to each other. Crystallize size (D) increases with increasing sintering temperature from 850 °C to 1150 °C. The X-ray Photoelectron Spectroscopy (XPS) confirms the presence of a single-phase of synthesized samples at the highest sintering temperature of 1150 °C. The change in morphology and the elemental composition of $Ni_{0.5}Co_{0.5}Fe_2O_4$ is confirmed by Field Emission Scanning Electron Microscope (FESEM) and Energy-Dispersive X-ray Analysis (EDAX), respectively. Additionally, Transmission Electron Microscopy (TEM) confirms the uniformity of cuboidal shape grains having an average grain size of about 84 nm for the $Ni_{0.5}Co_{0.5}Fe_2O_4$ sample at an optimized temperature of 1150 °C. Also, the Selective Area Electron Diffraction (SAED) pattern designates the regular distribution of bright spots, affirming the high degree of crystallinity and single-phase formation. Furthermore, Complex Impedance Spectroscopy (CIS) along with complex dielectric modulus studies reveal a relaxation phenomenon with non-Debye-type nature originating from grain boundaries. Frequency-dependent complex impedance and modulus studies exhibit space charge polarization effect with increasing sintering temperature. It is suggested that sintering the compound at the requisite temperature is the significant reason for the improved dielectric properties, which can be further useful for magnetodielectric materials, spintronic devices, sensors, and many more.

Address correspondence to E-mail: rupam.23644@lpu.co.in

Influence of Mn²⁺-substitution on the structural, morphological and magnetic properties of Co₂Y strontium hexaferrites

Ibrahim Mohammed [a], J. Mohammed [b], Anjori Sharma [a], Hamnesh Mahajan [a], Amarjeet Kaur [c], A.K. Srivastava [a,*]

[a] Department of Physics, School of Physical Sciences and Chemical Engineering, Lovely Professional University, Phagwara 144411, Punjab, India
[b] Department of Physics, Faculty of Science, Federal University Dutse, P.M.B. 7156, Dutse, Jigawa State, Nigeria
[c] Central Instrumentation Facility, Lovely Professional University, Phagwara 144411, Punjab, India

ARTICLE INFO

ABSTRACT

This research focus on using sol-gel auto combustion method to synthesize Co₂Y strontium hexaferrite with chemical composition $Sr_2Mn_xCo_{2-x}Fe_{12}O_{22}$ (x = 0.0, 0.5, 1.0). Samples were calcinated at 1150 for 6 h. The XRD analysis revealed a single crystalline phase Co₂Y strontium hexaferrites with the absence of secondary phase or impurity. Values of lattice parameters as well as unit cell volume rise with addition of Mn²⁺. The emergence of two peaks at 422 and 580 cm⁻¹ in FTIR analysis suggests the formation of hexaferrites. The morphological analysis show an agglomerated network of grains which is caused by magnetic interaction. EDX spectra shows the entire host as well as substituted elements, this confirm the purity and stoichiometry of the prepared Co₂Y strontium hexaferrites samples. Magnetic parameters: coercivity, saturation magnetization, squareness ratio as well as remnant were calculated using M-H hysteresis loop obtained from the VSM.

Copyright © 2022 Elsevier Ltd. All rights reserved.
Selection and peer-review under responsibility of the scientific committee of the International Conference on Recent Advances in Mechanical Engineering and Nanomaterials.

1. Introduction

Magnetic materials are widely employed in technological and industrial applications, including but not limited to the automobile sector, electronics, data storage and microwave (MW) devices [1]. Hexaferrites are among the most important materials nowadays due to the low cost, ease of manufacture, and fascinating electrical and magnetic properties [2]. Many researchers are interested in Y-type hexaferrites with planar magnetic anisotropy because they have the advantage of having a higher magnetic permeability in the GHz frequency range over other hexagonal ferrites with uniaxial magnetic anisotropy [3]. Also, because they develop good magnetic characteristics in the hyper frequency region when sintered at low temperature, Y-type hexaferrites are considered the best choice [4]. Crystalline structure of the Y-type hexagonal ferrites was said to be an alternating stacking of the S and T blocks along c-axis with space group R-3m [5–9]. Based on the relative direction of magnetic moments in each layer, two distinct magnetic blocks may be described: small (S) and large (L) magnetic moment and

within each block, the magnetic moments of the Fe ions were organized in a collinear manner [10]. Two of Fe₃O₄ formula units formed S block, which has a spinel structure with 2-tetrahedral and also 4-octahedral cation sites [11]. Magnetic as well as structural properties of Y type hexaferrite are substantially influenced by a number of parameters, including sintering duration, chemical composition, ingredient purity, and substitution amount [12–14]. Several researchers have improved the magnetic as well as electric properties of Y-type nanohexaferrites to make them appropriate for microwave applications, including dielectric permittivity, dielectric losses, saturation magnetization, coercivity, and so on [4]. In hyper-frequency, Y-type hexaferrite has good magnetic characteristics and it is expected to address the demand for soft magnetic materials in high frequency chip components [15]. This research work aimed to study influence of Mn²⁺ on morphological and also magnetic properties of $Sr_2Mn_xCo_{2-x}Fe_{12}O_{22}$ (x = 0.0, 0.5, 1.0). The produced samples were analysed by XRD, FESEM/EDX, and VSM. Furthermore, this composition has never been studied before.

2. Material and method

Analytical grade chemicals from LOBA Chemie Pvt Ltd: strontium nitrate, [Sr(NO₃)₂·6H₂O], Ferric nitrate, [Fe(NO₃)₂·9H₂O

---

* Corresponding author.
    E-mail address: srivastava_phy@yahoo.co.in (A.K. Srivastava).

Resume

Name: Hamnesh Mahajan

Stream: Ph.D. Physics (LPU)

Registration No: 11919191

Supervisor: Dr. A. K. Srivastava

Contact: 9797596234

Email: mahajanhamnesh@gmail.com

Present Address: H.No. 549 A, Randhawa Niwas, Dakoha, Jalandhar-144023.

Objective

With 4 years experience in research and 2 years experience in teaching seeking position of Assistant Lecturer in Government College of Engineering & Technology (Jammu) and to gain a good career in Physics research practices.

Areas of Expertise

- My expertise is in the field of Research Methodology, Material Science, Sol-Gel Auto Combustion Method, and Energy Storage Supercapacitors.

- Excellent knowledge of theories and concepts of Physics and Mathematics.

- Good interpersonal skills.

- Good communication skills.

- Polite and patient.

- Excellent relationship builder.

- Keen observer.

- Proficient in FORTRAN 77, MS-Word, MS-Excel, MS-PowerPoint, XRD, FTIR, FESEM, EDX, VSM, CV, GCD, EIS, XPowder, ImageJ, Xpert High Score etc.

Employer

- Assistant Lecturer (Physics) in Government College of Engineering & Technology (JAMMU) from 2017 to 2019

Key Responsibilities Handled

- Plan and present suitable learning experiences for all students.
- Develop course materials and teaching lasers, electrostatics, electrodynamics, quantum mechanics, oscillations, and semiconductors.
- Documenting tools used for physics concept demonstrations.
- Arranging seminars with experts in the field, for enhancing student's interests in physics.
- Grading and administering classroom tests and assignments in the Physics class.
- Maintain and manage apt records and follow needed methods and practices.
- Monitor student's laboratory work.
- Conducting course assessment tests.
- Arranging practical work sessions at the laboratory.
- Guiding students on the procedures of performing specific experiments.
- Using available teaching aids such as digital boards, projectors, charts, PowerPoint presentations, etc.

Education

- Full Time Ph.D. in Physics from Lovely Professional University.
- M.Sc. in Physics from Shri Mata Vaishno Devi University Katra with 80% Marks.
- B.Sc. from Govt. Maulana Azad Memorial College Jammu with 78% Marks.
- 12th from Govt. Higher Sec. School Billawar with 80.2% Marks.
- 10th from Sacred Heart Convent School Phinter with 86% Marks.

Extra-Curricular Activities

- One Year Diploma in Computer Application with Grade 'A' from Global Institute of Information Technology Centre Billawar.

- Participated in the Science Camp under INSPIRE program of department of Science & Technology, Govt. of India at the Department of Geology, University of Jammu.
- Attended the National Level Refresher Course on Mathematical Physics Organized by Indian Academy of Science & Technology.

Paper Published and Communicated

- **Hamnesh Mahajan**, Sachin Kumar Godara, A. K. Srivastava, Synthesis and Investigation of Structural, Morphological, and Magnetic Properties of the Manganese Doped Cobalt-Zinc Spinel Ferrite, J. Alloys Compd. 896 (2021) 162966. https://doi.org/10.1016/j.jallcom.2021.162966 (Impact Factor - 6.371).

- **Hamnesh Mahajan**, Shammi Kumar, Anjori Sharma, Ibrahim Mohammed, Manisha Thakur, Simrandeep Kour, Amarjeet Kaur, Ajeet Kumar Srivastava, Structural, Morphological, and Electrochemical Investigation of $Mn_{0.3}Co_{0.2}Zn_{0.5}Fe_2O_4$-Polyaniline Nanocomposite for Supercapacitor Application, J. Mater. Sci.: Mater. Electron. (2022) 1-14. https://doi.org/10.1007/s10854-022-09335-x (Impact Factor - 2.779).

- **Hamnesh Mahajan**, Shammi Kumar, Anjori Sharma, Ibrahim Mohammed, Manisha Thakur, Amarjeet Kaur, A. K. Srivastava, Effect of Sintering Temperature on Structural, Morphological, and Magnetic Properties of $Mn_{0.3}Co_{0.2}Zn_{0.5}Fe_2O_4$ Ferrite, J. Sol-Gel Sci. Technol. 105 (2023) 388-404. https://doi.org/10.1007/s10971-022-06022-5 (Impact Factor - 2.606).

- Ibrahim Mohammed, J. Mohammed, Anjori Sharma, **Hamnesh Mahajan**, Shweta Sharma, Manisha Thakur, Amarjeet Kaur, Neha Aggarwal, Structural, Morphological, Optical, Magnetic, and Microwave Properties of La^{3+}-Mn^{2+} substituted Zn_2-Y- Type Barium-Strontium Hexaferrite, Chin. J. Phys. (2022) 0577-9073. https://doi.org/10.1016/j.cjph.2022.06.025 (Impact Factor - 3.957).

- Anjori Sharma, **Hamnesh Mahajan**, Ibrahim Mohammed, Sachin Kumar Godara, A. K. Srivastava, Enhanced Dielectric and Magnetic Properties of Garnet-Spinel Ferrite Composite for Microwave Device Application, Appl. Phys. A, 2022 (under review).

- Anjori Sharma, **Hamnesh Mahajan**, Ibrahim Mohammed, Amarjeet Kaur, Neha Aggarwal, Sukhleen Bindra Narang, Ajeet Kumar Srivastava, Investigation of Miniaturization Parameter and Losses of YIG/MgCdCoFe Composite for Antenna Applications in Ku Band, Mater. Res. Bull., 2022 (under review).

- Simrandeep Kour, Nitish Kumar, **Hamnesh Mahajan**, Rupam Mukherjee, Influence of the Sintering Temperature on Impedance and Modulus Spectroscopic Studies of Nickel-Substituted Cobalt Ferrite, J. Mater. Sci.: Mater. Electron. 34 (2023) 594. https://doi.org/10.1007/s10854-023-10030-8 (Impact Factor - 2.779).

Conference Proceedings

- Ibrahim Mohammed, J. Mohammed, Anjori Sharma, **Hamnesh Mahajan**, Amarjeet Kaur, A. K. Srivastava, Influence of Mn^{2+}-Substitution on the Structural, Morphological and Magnetic Properties of Co2Y Strontium Hexaferrites, Mater. Today: Proc., 2022, ISSN: 2214-7853. https://doi.org/10.1016/j.matpr.2021.12.514 (Impact Factor - 1.46).

- **Hamnesh Mahajan**, A. K. Srivastava, Structural, Morphological, and Magnetic Investigation of the Zinc Substituted Magnesium Spinel Ferrite, AIP. Conf. Proc., 2022 (Accepted Manuscript).

Poster Presentations

- **Hamnesh Mahajan** and A. K. Srivastava, Investigation of Structural Magnetic Studies of the Zinc Doped Magnesium Spinel Ferrite, International Conference on "Recent Advances in Fundamental and Applied Sciences" (RAFAS-2021), 25-26 June, 2021, Lovely Professional University, Punjab.

- **Hamnesh Mahajan**, Amarjeet Kaur, A. K. Srivastava, Effect of Sintering Temperature on Structural, Morphological, and Magnetic Properties of $Mn_{0.3}Co_{0.2}Zn_{0.5}Fe_2O_4$ Ferrite, ACS and ECS Sponsored International Conference on Technologies for Smart Green Connected Societies (ICTSGS-2021), 29-30 November, 2021, Yamagata University, Japan.

Oral Presentation

- **Hamnesh Mahajan**, Amarjeet Kaur, and A. K. Srivastava, Effect of Mn Doping on Structural, Morphological, and Magnetic Properties of Co-Zn Spinel Ferrite, International Conference on Materials for Emerging Technologies (ICMET-21), 18-19 February, 2022, Lovely Professional University, Punjab.

Paper Award

- Best Paper Award of the Conference Theme: Materials Science and Nanomaterials on the Topic Influence of Mn^{2+}-Substitution on the Structural, Morphological and Magnetic Properties of Co2Y Strontium Hexaferrites in the International Conference on Recent Advances in Mechanical Engineering and Nanomaterials (ICRAMEN-2022), 19-20 February, 2022, **Research Association of Masters of Engineering, Maharashtra, India.**

Course Award

- Attended and Awarded Elite Class NPTEL Certificate for Successfully Completing the 12 Week Course from July-October (2021) on Experimental Physics-1 by Indian Institute of Technology Kharagpur (Funded by Ministry of Human Resource Development, Govt. of India).
- Attended and Awarded Elite Class NPTEL Certificate for Successfully Completing the 4 Week Course from January-February (2022) on Introduction to Probability and Statistics by Indian Institute of Technology Madras (Funded by Ministry of Education, Govt. of India).

Copyright

- One Copyright granted by the Copyright Office (Government of India), Ministry of Commerce and Industry, Department of Industrial Policy & Promotion under the topic "Investigation of Structural, Magnetic, and Electrochemical Parameters of Spinel Ferrites and its Composites for Energy Storage Application".

Workshop

- Participated in a Five Day Faculty Development Workshop on Design, Development and Delivery of Massive Open Online Course (MOOCs), Organised by the Department of Higher Education Government of J&K at Govt. College for Women, Prade Ground Jammu.
- Participated in Boxberg Sponsored Workshop on "Manuscript Writing" by SPAST Foundation, 23-24 April (2022), Hyderabad, India.

Hobbies

- Reading
- Writing research papers
- Learning new things
- Adventurous sports
- Cooking

Personal Details

DOB: 03/01/1994

Languages Known: English, Hindi, Dogri, and Punjabi.

Permanent Address: VPO – Phinter (near Shiv Temple), Tehsil – Billawar, District – Kathua, State – Jammu and Kashmir, Pin Code – 184203.